Elucidation of Reaction Mechanism of the Oxygen Evolution Reaction for Water Electrolysis

Yadan Ren

Elucidation of Reaction Mechanism of the Oxygen Evolution Reaction for Water Electrolysis

Yadan Ren

Graduate School of Human and Environmental Studies

Kyoto University

Supervised by

Prof. Dr. Yoshiharu Uchimoto

Contents

Chapter 1. General Introduction

1.1 Background

In recent years, development of sustainable energy has become increasingly crucial due to growing environmental concerns and depletion of carbon-based fossil fuels[1, 2]. To achieve the goal of low or even zero carbon emissions, renewable energy forms like solar, wind, and hydrogen energy have been widely studied. H_2, being abundant and one of the energy sources with the highest gravimetric energy densities, is now considered a highly promising energy carrier to convert chemical energy into electricity[3, 4], and is expected to form the basis of a future H_2 society. H_2 is typically extracted during the steam reforming of hydrocarbons, such as natural gas, liquefied petroleum gas, naphtha, and petroleum residues, and is also one of the by-product gases generated during steelmaking and brine electrolysis[5]. However, all the above-mentioned methods have the disadvantages of difficult mass production of H_2 and generation of CO_2 during the manufacturing processes, which defeats the purpose of a low-carbon-emission process. Renewable energy generated by water splitting can, however, produce H_2 in a much more efficient and cleaner way, potentially making the realization of a future carbon-free H_2 society possible.

Water electrolysis is the technology used to electrochemically split water into O_2 and H_2. In a future H_2 society, the power generated from wind, solar, or other renewable energy sources could be connected to electricity grids for daily consumption, while any excess power could be utilized for water electrolysis. The H_2 produced can subsequently be converted to electricity again, by combining it with O_2 when an energy conversion technology, such as fuel cells, is employed[6-8]. By using H_2 as a fuel, polymer electrolyte fuel cells (PEFCs) have in fact been widely investigated in recent years, with one of its successful commercial applications being fuel cell vehicles[9, 10]. Similar H_2 applications in other industrial fields can also be developed.

The establishment of such a sustainable energy strategy cannot, however, be fully realized without the development of efficient water electrolysis and fuel cell techniques. In water electrolysis, the oxygen evolution reaction (OER) occurs at the anode, while the hydrogen evolution reaction (HER) occurs at the cathode[11]. OER is kinetically much slower than HER due to the four electrons involved in the reaction[12]. This rate-limiting step represents the biggest technical challenge to the successful adoption of water electrolysis[13, 14]. In recent years, significant research efforts have been devoted to expanding the fundamental understanding of OER, along with the development of novel OER catalysts in both acidic[15, 16] and alkaline[17, 18] media. However, the extremely complicated OER reaction process, including the formation of unknown adsorbate/ adsorbate intermediates, is yet to be determined[19].

1.2 Evaluation of the OER Reaction Mechanism

1.2.1 Principles of Water Electrolysis

The overall water electrolysis reaction consists of two half reactions, i.e., the OER and HER. The specific mechanisms of these half reactions will depend on the nature of the solutions, as described in the following equations (1)–(6) for acidic, neutral, and alkaline electrolytes[20]:

In acidic solutions (e.g., perchloric acid, sulfuric acid):

Anode: $2H_2O \rightarrow O_2 + 4H^+ + 4e^-$ (1)

Cathode: $4H^+ + 4e^- \rightarrow 2H_2$ (2)

In neutral solutions (e.g., phosphate buffer solution):

Anode: $2H_2O \rightarrow O_2 + 4H^+ + 4e^-$ (3)

Cathode: $4H_2O + 4e^- \rightarrow 2H_2 + 4OH^-$ (4)

In alkaline solutions (e.g., potassium hydroxide):

Anode: $4OH^- \rightarrow O_2 + 2H_2O + 4e^-$ (5)

Cathode: $4H_2O + 4e^- \rightarrow 2H_2 + 4OH^-$ (6)

As stated earlier, the four-electron reaction, OER, has been found to be a more complicated reaction when compared to the HER. Moreover, the water electrolysis reaction is a high-energy process, where the standard-state free energy change ($\Delta G°$) is +237.2 kJ mol^{-1}, i.e., the energy required to convert one mole of water molecules into H_2 and O_2[21]. In addition, the enthalpy change ($\Delta H°$) required for H_2 gas formation is +286 kJ mol^{-1} [22]. Together, this translates into the thermodynamic reversible water electrolysis cell voltage being 1.23 V[22] theoretically, and the application of 1.23 V external potential could therefore be expected to generate H_2 and O_2. However, in practice, additional voltage should typically be applied to achieve significant reaction rates in real water electrolyzers. This difference between the applied voltage and the theoretical value is defined as the overpotential (η) and is a key parameter when evaluating the efficiency of electrocatalysts.

Another essential parameter evaluated during the OER catalyst studies is the Tafel slope, b, in equation (7)[23]. Equation (7) shows the relationship between overpotential η and current density i, and the coefficient constant b indicates the Tafel slope value. It is generally used to investigate the kinetics of the OER, where it varies between 30 and 120 mV dec^{-1} and is also used to identify the rate-determining step[24].

Tafel values and the OER electron-transfer processes will be discussed in detail at a later stage.

$$\eta = a + b \log i \qquad (7)$$

1.2.2 Proposed OER Reaction Mechanism

Two widely accepted OER mechanisms that have been proposed in recent years are the traditional adsorbate evolution mechanism (AEM) and the lattice oxygen mechanism (LOM)[25]. The traditional AEM mechanism is represented in Figure 1. 1[26], where the following reaction mechanisms are proposed for an acidic electrolyte; also as shown in Figure 1.1 (a); where the * mark represents the active sites[27]:

$2H_2O \rightarrow HO^* + H_2O + H^+ + e^-$

$\rightarrow O^* + H_2O + 2H^+ + 2e^-$

$\rightarrow HOO^* + 3H^+ + 3e^-$

$\rightarrow O_2 + 4H^+ + 4e^-$

In addition, the proposed OER mechanism in a basic medium, shown in Figure 1.1 (b), is described as follows[27]:

$4OH^- \rightarrow HO^* + 3OH^- + e^-$

$\rightarrow O^* + H_2O + 2OH^- + 2e^-$

$\rightarrow HOO^* + H_2O + 3OH^- + 3e^-$

$\rightarrow O_2 + 2H_2O + 4e^-$

In these traditional AEMs, the OER processes involve the sequential formation of $M\text{–}OH_{ads}$, $M\text{–}O_{ads}$, and $M\text{–}OOH_{ads}$ adsorption intermediate species, where M represents the active metal sites. Here, the hypothesis is that all O_2 molecules are generated from the O in the water molecules. However, in a benchmarking study by Shao-horn et al., an innovative experimental design employing ^{18}O isotope labeling revealed that the O_2 gas produced also contained O atoms originating from the catalyst lattice oxygen[28]. Further research, employing both the experimental and theoretical approaches, has confirmed that the surface oxygen sites of catalysts could participate in the OER directly[29-32]. LOM was therefore proposed as an appropriate reaction mechanism for both acidic and alkaline electrolytes. As shown in Figure 1.2 (a), LOM in an acidic electrolyte can be described as indicated below, where *, O_L, and V_o represent the metal active site, lattice oxygen, and surface oxygen vacancy, respectively[11]:

$H_2O + * \rightarrow OH^* + H^+ + e^-$

$OH^* \rightarrow O^* + H^+ + e^-$

$O^* + O_L \rightarrow O_2 + V_o$

$V_o + H_2O \rightarrow OH^* + H^+ + e^-$

$H^* \rightarrow * + H^+ + e-$

The LOM in the alkaline electrolyte can be described as follows[25]:

$OH^- + * \rightarrow OH^* + e^-$

$OH^* + OH^- \rightarrow O^* + H_2O + e^-$

$O^* + O_L \rightarrow O_2 + V_o$

$V_o + OH^- \rightarrow H^*$

$H^* + OH^- \rightarrow H_2O$

Here, the lattice oxygen of the catalysts would combine with the adsorbed O* species, produce O_2 gas, and subsequently lead to the formation of O_2 vacancies in the lattice. Because of the diverse proton-electron transfer steps, the catalyst activity is generally dependent on the pH value of the electrolyte, as shown by Shao-Horn, et al.[26] It should however be noted that the catalyst structure instability caused by LOM may also result in the simultaneous occurrence of AEM and LOM[29, 33]. Another recent study further reported that due to the electron transfer rate and intermediate affinity, the pH-dependent OER activity occurred without the lattice oxygen participation[34]. Further research is expected to provide more insight into the OER reaction mechanism.

New reaction mechanisms have also been investigated with the development of novel OER catalysts, including a two-active-site mechanism that was proposed in a recent perovskite catalyst study. According to previous studies on ABO_3 type perovskite catalysts[35], the OER reaction mechanism proceeds at a single, corner-shared MO_6 site, where the B-site metal distance (e.g., Mn-Mn) has an average value of about 3.7–3.9 Å. Such a long M–M bond distance would prevent the formation of a direct O-O bond, which is assumed to enhance the OER activity. Further studies also revealed that a shorter M-M distance could enable direct O–O bond formation[36, 37], which would also lead to enhanced OER activity. Yamada et al. have in fact demonstrated that quadruple perovskite catalysts, owing to the moderate bond distance between adjacent A' sites and B site transition metals, could form O–O bonds directly[38]. These active A'-B bridge sites contribute to the high OER activity of quadruple perovskite catalysts[39, 40].

1.3 OER Electrocatalysts in Acid

Due to their excellent OER activity and long-term stability, noble metal-based OER catalysts, such as Ir- and Ru-based catalysts, are considered the benchmarking catalysts for water electrolysis[41, 42]. Compared to the alkaline water electrolysis, the high proton concentration associated with water splitting when an acidic electrolyte is employed contributes to a faster HER[43]. As such, sulfonic acid side chains have been found to assist in the conduction of hydrogen ions when used with the extensively investigated solid polymer electrolyte (SPE) water electrolyzers and proton-exchange membrane (PEM) water electrolysis[44]. The application of the PEM water electrolyzer will be discussed in detail later. Despite the current development of commercial PEMs, noble metal OER electrocatalysts are still widely applicable because of their high current density, long-term stability, and corrosion resistance in acidic environments. Their scarcity does, however, remain one of the biggest obstacles to further commercialization. The development of OER electrocatalysts for applications in acidic media will now be discussed.

1.3.1 Ir-Based OER Catalysts

The morphology and structure of iridium oxide significantly affect OER activity. Fine iridium oxide crystals, with a particle size <10 nm, have been shown to exhibit superior activity and stability[45]. Here, the decreased particle size associated with the catalyst generally leads to a large, electrochemically active surface area, with a better exposure to highly active sites, thus resulting in an increased OER activity[15, 16, 20]. To take advantage of this fact, various iridium oxide catalysts have been synthesized, employing controllable morphology synthesis methods to produce one-dimensional nanoneedles[46] and nanowires[47-50], two-dimensional ultrathin nanosheets[51-53], and three-dimensional nanostructures with (meso-) porous morphology[54-56]. In another strategy to enhance catalyst performance and reduce the noble metal loading, catalysts can be combined with the supporting materials. Here, the supporting materials are expected to contribute to a good electron conduction, better dispersion of active surfaces, and ensure corrosion resistance in acidic environments. Unfortunately, the carbon-based supporting materials that are most commonly used in oxygen reduction reaction catalysts, can also be easily oxidized at high OER potentials, and are therefore not suitable for use in OER catalysts. Recent studies have therefore focused on antimony-doped tin oxide (ATO) as a potential supporting material for Ir-based catalysts, with ATO being associated with a strong corrosion resistance[57-62]. Oh et al. found that the metal/metal-oxide support interaction effects between oxide supports and IrO_x nanoparticles significantly improved the catalyst activity and corrosion resistance. This effect was not considered earlier and would therefore require further investigation.

Compared to crystallized iridium oxides, which are associated with long-range ordered structures, catalysts with disordered or short-range, ordered amorphous structures generally display a higher OER activity. Although the reaction mechanism of amorphous Ir catalysts remains unclear, it is hypothesized that the superior catalytic performance of these amorphous oxides may be attributed to the extra active sites that result from the defects in the electronic structure[63, 64] and irregular Ir–Ir and/or Ir–O bond interactions[65-70]. In a recent study by Elmaalouf et al., a wide range of Ir-based catalysts were investigated, employing controllable stoichiometry and crystallinity. Here, the results demonstrate that a high OER activity is associated with the amorphous crystalline catalysts with small particles rather than the initial Ir oxidation state, as shown in Figure 1.3[55]. Using a combination of atomic pair distribution function (PDF) analysis and local electronic structure measurements, Willinger et al. were able to show that the high activity of amorphous catalysts is related to the corner- and edge-sharing IrO_6 octahedra[67]. The appearance of hollandite-like structures, as determined by PDF and shown in Figure 1.4, were found to be responsible for the enhanced OER activity, indicating the possibility of designing a catalyst by rational structure arrangement. These special structural properties were also observed in further studies, where orthorhombic and monoclinic symmetry were identified in amorphous iridium oxide[68]. Mixed phases of traditional tetragonal and orthorhombic structures were further shown to exhibit the best OER activity.

In an attempt to identify the reaction mechanism of Ir-based materials, *in situ*/*operando* measurements, such as *operando* O K-edge X-ray absorption spectroscopy (XAS), have been used to determine the changes in reaction intermediates during O_2 evolution. Nong et al. were able to identify two types of O 2p hole character (μ-O and μ-O oxyl) through *operando* O K-edge XAS, as shown in Figure 1.5[71]. By combining pulse voltammetry measurements with density functional theory (DFT) calculations, a linear relationship was observed between the activation free energy and catalytic activity. Pfeifer et al. were also able to capture the intermediate O_2 species by using *in situ* X-ray photoemission (XPS), XAS, and theoretical calculations[72-74]. Their work revealed that electrophilic O^{I-} species increased with active O_2 evolution and disappeared in the absence of the applied potential, suggesting that the O^{I-} species contribute to the OER activity. Despite the various *in situ* techniques that have been developed to determine the intrinsic mechanism of highly active Ir-based materials, a thorough understanding of the morphology, structure, electronic state, and catalytic performance is still required.

Another key parameter in the evaluation of the catalytic performance is stability. This is particularly important when practical applications are considered. To investigate the stability of several Ir-based catalysts, an *in situ* evaluation of the dissolution of Ir during O_2 evolution was conducted by Geiger et al., employing both inductively coupled plasma mass spectrometry and online electrochemical mass spectrometry[75]. Their results, as shown in Figure 1.6, reveal that the leaching of non-noble elements in the catalyst structure results in the formation of isolated IrO_6 octahedra and short-lived vacancies, as well as the amorphization of oxides that would further contribute to Ir dissolution. An

OER reaction mechanism with dissolution pathways was subsequently proposed for Ir-based materials and is shown in Figure 1.7. A stability number (S-number) was also proposed, being defined as the ratio of the amount of evolved O_2 to the amount of dissolved Ir. The applicability of this S-number has since been demonstrated in literature[43, 65]. A similar activity-stability factor has been proposed by Kim et al., where catalytic activity and stability can be estimated from the rate of O_2 production, and the rate of metal dissolution[76]. Current research on the stability of Ir-based catalysts is however incomplete; therefore, further studies are required to provide a more complete understanding of the catalytic behavior and stability.

1.3.2 Ru-based OER Catalysts

Ru-based catalysts are another state-of-the-art type of OER catalysts, for acidic electrolyte applications. One of the main advantages of Ru-based catalysts when compared to Ir-based materials is that the price of Ru is approximately six times lower than that of Ir, making Ru a promising alternative for use in PEM water electrolyzers[77]. The development of Ru-based materials is, however, hampered by the relatively lower acid resistance of the metal when compared to Ir, for instance. Similar to Ir-based catalysts, the morphology and structure of Ru-based catalysts also has a significant impact on the OER performance. The reduced particle size has again been reported to enhance the OER activity[78-80], although extremely small particles of 4-6 nm were found to negatively affect the stability[81]. Various morphologically engineered nanostructures, such as nanorods[82], nanowires[83], ultrathin two-dimensional nanosheets[84-86], and mesoporous structures[87-89], have consequently been studied. Efforts have also been devoted to developing highly active and stable Ru-based catalysts through alloying[90-93], core-shell structure construction[94-96], loading of supporting material[97-99], and other previously reported techniques[100, 101]. Ru-based catalysts not only exhibit excellent OER activity when appropriately modified, but also exhibit active HER catalytic properties[102, 103], making them potential bifunctional catalysts for water electrolysis. However, although several new synthetic methods have been developed for Ru catalysts with superior catalytic activity, research on the stability of the Ru-based materials is still insufficient. Therefore, to ensure the development of practical applications in PEM water electrolyzers, a thorough investigation of the catalyst degradation mechanism is crucial. It is therefore proposed that research employing a combination of advanced techniques, such as *in situ* XAS, transmission electron microscopy (TEM), and Raman spectroscopy, may provide a deeper understanding of Ru-based catalysts.

1.4 OER Electrocatalysts in Alkaline Media

Although Ir- and Ru-based catalysts show superior OER performance, the low abundance and associated high cost of these noble metals inevitably results in an increase in the overall cost of water electrolysis. Alternatively, non-noble, metal-based OER catalysts with comparable activity and durability are therefore necessary. Many recent studies have consequently focused on exploring the potential of transition metal (TM, e.g., Ni, Co, Fe) oxides or transition metal (oxy)hydroxides as active OER catalysts. TM-based catalysts offer important advantages with the metals being abundant having tunable electronic structures and offering a wide selectivity in terms of catalyst design. Being highly dissolvable, this does, however, limit their applications in alkaline electrolytes[17]. Some of the strategies that have been developed to improve both the activity and stability of TM-based catalysts include[18]: (1) element doping through the introduction of other atoms into the parent material to regulate the electronic and/or structural properties (2) alloying of two or more metals to engineer the bond interaction and local ligand environment (3) strain tuning through designed lattice mismatch to modify the absorption energy of reaction intermediates and (4) interface engineering. Through the innovative design of the catalyst structures such as (meso-)porous- and nanostructures, an increased number of active reaction sites can also be exposed, thereby improving the catalytic activity of TM catalysts[18]. TM oxides that have been extensively studied in recent years include spinel-type oxides, perovskite-type oxides, rock-salt-type oxides, hydroxides, and layered double hydroxides, which will be discussed in detail in the following sections.

1.4.1 Spinel-Type OER Catalysts

Spinels are typically described as AB_2O_4. Here, A represents Li, Mn, Zn, Co, Ni, Fe, and other TM metals, and B represents Al, Mn, Fe, Co, Ni, and other TM metals. These spinels consist of a face-centered cubic array of O, with A occupying 1/8 tetrahedral sites and B occupying 1/2 octahedral sites[104]. The structure of a normal spinel is shown in Figure 1.8 (a). Owing to the relatively broad element selectivity for both A- and B-site cations, the structure of the spinels can vary significantly depending on the distribution of cations. Cation distribution can also be affected by the cation radius, with cations having small radii and large radii typically occupying A sites and B sites, respectively. Finally, Coulomb interactions between the cations would also affect the cation distribution. As all these factors could affect cation distribution, spinels also typically exhibit a variety of different structures, including inverse spinel and complex spinel, as shown in Figure 1.8 (b) and (c). The inverse spinel can be described as $B(AB)O_4$, where in the case of $NiFe_2O_4$, half of the Fe^{3+} ions occupy the tetrahedral sites, while the remaining Fe^{3+} and Ni^{2+} ions occupy the octahedral sites. The complex spinels represent a mixed state of normal and inverse structures, where in the case of $CuAl_2O_4$, both Cu^{3+} and Al^{3+} occupy tetrahedral and octahedral sites simultaneously[105]. The coexistence of tetrahedral and octahedral sites in spinels enables the formation of diverse oxides through the accommodation of different TM cations. The structural flexibility of spinels also offers the opportunity to study the catalytic performance through evaluation of site defect effects, including A-site defect, B-site defect, and the oxygen vacancy. This approach has drawn significant attention in recent studies[105].

Several studies have proposed that the octahedral site might be the active site for OER catalytic behavior when spinels are employed. Wei et al. reported Mn in the octahedral site of $MnCo_2O_4$ as the active site[106]. This finding was further applied to a series of eleven spinels, and it was concluded that a strong relationship existed between the OER activity of spinels and the e_g occupancy of the active cation in the octahedral site. Based on this research, a volcano-shaped plot was proposed for the relationship between the OER activity and the e_g occupancy, confirming that the e_g descriptor could not only be applied to perovskite oxides, but also to spinels. Confirmation of the octahedral site as the active site was also obtained in additional studies[34, 107, 108], suggesting that the OER performance of spinels could be improved through an engineering of the octahedral sites. Such engineering solutions could include increasing the octahedral site distortion and enhancing the hybridization between octahedral site cations and O. Another possibility that has also been attracting attention is the preparation of catalysts through delithiation, thereby generating octahedral sites. Robinson et al. [109] found that the $LiMn_2O_4$ spinel became catalytically active with the removal of Li from the tetrahedral sites, while a similar phenomenon was also observed for delithiated

$LiCoO_2$[110]. Another promising spinel is $LiMnNiO_4$, which is already employed as a cathode material for Li-ion batteries. As such, its structure has already been extensively studied[111, 112], with its transformation into active OER catalysts by delithiation appearing to be the obvious next step for future investigations. Co_3O_4, and its related spinels have also shown promising catalytic activity and have also been widely studied. In one such study, Wang et al. independently subtracted the tetrahedral site Co^{2+} and octahedral site Co^{3+} from the inactive cations. The results indicated that at an applied potential, Co^{2+} at the tetrahedral site of Co_3O_4, would release electrons, thereby contributing to the formation of CoOOH at the catalyst surface, significantly increasing the OER activity[113]. Further research indicated that the oxygen vacancy rich surface would further facilitate surface reconstruction prior to the O_2 evolution, explaining the associated high OER activity[114]. This concept was successfully illustrated by Xu et al. through optimization of the surface areas and oxygen vacancies of Co_3O_4 nanosheets to obtain a high OER activity [115]. These studies shed light on catalyst design through defect regulation, to obtain more active sites.

1.4.2 Perovskite-Type OER Catalysts

Perovskite-type materials have also been widely investigated as potential OER catalysts in alkaline media. The simple perovskite generally occurs as ABO_3, where A represents Ca, La, or a wide range of other rare-earth elements as well as transition metals, while B represents transition metals such as Mn, Fe, and Co. As shown in Figure 1.9 (a), B-site cations with relatively small radii occupy the octahedral sites within the structure of BO_6, while the A-site cations are located in the cavities created by BO_6 octahedra. Research on ABO_3-type perovskites revealed that B-site octahedra are the active sites for the OER process. Shao- et al. also proposed that the e_g occupancy of B-site active cations is an important indicator to describe the OER activity[116]. Combining this knowledge with *operando* studies, Fabbri et al. successfully identified the dynamic self-reconstruction behavior of $Ba_{0.5}Sr_{0.5}Co_{0.8}Fe_{0.2}O_{3-\delta}$ perovskite[117]. They proposed that in contrast to the traditional adsorption reaction mechanism, the catalyst can in fact form active oxy(hydroxide) surface layers (called dynamic self-reconstruction) during the OER, which is in turn especially favored by oxygen-vacancy-rich perovskites.

In recent years, quadruple perovskites have been found to exhibit promising OER performance. With the formation of $AA'_3B_4O_{12}$, quadruple perovskites have three quarters of its A-sites (termed as A' site) occupied by elements such as La, Ca, and Cu, as shown in Figure 1.9 (b)[38]. A more complicated structure of quadruple perovskites is also associated with a widespread covalent network, which is expected to enable the formation of more active reaction sites during the OER. Yamada et al. investigated several Mn-based quadruple perovskite oxides and found that the shortened A'-B bond distance improved the direct formation of O–O bonds, thereby enhancing the OER activity[38, 39]. This is different from the single octahedra active site that was proposed in previous research for simple perovskites, where the A' and B' sites worked together to form active sites in quadruple perovskites, thereby generating the concept of a "two-active-site." Although these findings provide insight into the design of novel perovskites, further research is still required to obtain a more complete understanding of these reaction mechanisms.

Double perovskites, with the structure of $LnBaCo_2O_{5+\delta}$ (Ln represent Pr, Sm, Gd, Ho, and Ln), were also studied by Grimaud et al.[118]. The structure of the double perovskite is shown in Figure 1.10. In contrast to the simple ABO_3 perovskite, the large differences in ionic radius and polarizability of Ln and Ba changes the ordering of A-site cations along the *c* direction, while causing the oxygen vacancies to appear in the Ln plane. The resulting regular oxygen vacancies lead to an oxygen-deficient octahedral symmetry, also referred to as a square pyramidal symmetry. Because of the coexistence of octahedral and square pyramidal symmetry, the evaluation of e_g filling has become difficult to determine, and the O *p*-band center was therefore proposed to assess the OER activity. Through DFT calculations, it was found that an optimum O *p*-band center that is neither too close nor too far from the Fermi level can enhance the OER activity. When considering both activity and stability, the double perovskite investigated here performed better than even the most active BSCF reported to date, suggesting their potential for further applications in alkaline electrolytes.

To improve the catalytic performance of perovskites, several strategies have further been proposed either to improve their intrinsic activity, or to increase the number of active sites. These investigations focused on the substitution of cations at the A- and B-sites, or the use of oxygen to modulate the catalyst composition. Here, it is postulated that the substitution of A-site cations could affect the electronic state of B-site ions, enhance the formation of oxygen vacancies, and subsequently increase the number of catalytic active sites[119]. The substitution of B-site cations is typically more complicated, leading to distortion of the octahedra and significant valence changes[119]. Another recent study also showed that partially replacing O with F could optimize the O *p*-band center, and increase the formation of extra oxygen active sites[120]. Morphology engineering has also been widely applied with perovskites to obtain favorable OER catalytic characteristics such as small particle size and a porous structure. To achieve a high specific surface area, special perovskite nanostructures such as nanofibers[121], nanorods[122], and nanowires[123] have therefore been synthesized. All these studies show that the rational design of perovskite structures can lead to better catalytic performance. Oxygen vacancies in perovskite could also significantly affect the intermediate bonding energy, thus affecting the OER activity. Here oxygen-vacancy-rich perovskite oxides are expected to exhibit excellent catalytic performance. This oxygen deficiency can be achieved by lattice strain engineering[119]. Other promising strategies for superior perovskite catalyst design include defect construction, crystal facet control, cation vacancy design, and loading of supporting materials.

1.4.3 Other OER Catalysts for Alkaline Water Electrolysis

Apart from spinels and perovskite oxides, other types of OER catalysts have also been investigated. Ni- and Co-based rock-salt-type oxides are expected to play a key role in alkaline water electrolysis because of their low material cost and easily modifiable structures. The typical structure of rock salt oxides is AO, where the A-site is occupied by alkali or transition metals such as Ni and Co. Ordered rock salt oxides have regular, edge-sharing octahedra, where A-site cations are octahedrally coordinated by O atoms[124]. The OER activity of such rock salt oxides could depend on the synthesis method, where the structural distortion could lead to the creation of more active sites. Trotochaud et al. synthesized NiO_x thin film catalysts with different Co doping contents. The results showed that increasing the Co content had a negative effect on the catalytic activity, which was attributed to the reduced formation of active layered oxyhydroxide[125]. Rock salt oxides also display ternary compositions with potential formulas ABO_2, A_2BO_3, or A_5BO_6, where the element selectivity of A- and B-sites is restricted by electroneutrality[124]. $LiNiO_2$, which has been widely studied as a Li-ion battery cathode material, has recently also drawn attention due to its potential application in alkaline water electrolysis. $LiNiO_2$ has a nominal oxidation state of Ni^{3+} and has been found to exhibit excellent OER activity, when considering the e_g state descriptor. Moreover, because the energy levels of the Ni 3d orbitals of $LiNiO_2$ are close to those of the O 2*p* orbitals, they can strongly hybridize, which can be expected to further enhance the catalytic performance. Furthermore, the dissolution of Li cations might cause a structural mismatch or rearrangement, thereby improving the OER kinetics. However, further research is required in this field.

Due to their superior OER performance, hydroxides and oxyhydroxides, especially Ni- and Fe-based (oxy)hydroxides, $M(OH)_2$, and MOOH (where M represents Ni, Fe, Co, and Mn), have also been intensively investigated in recent years. Hydroxides have a layered structure in which the metal cation is coordinated with six O atoms to form MO_6 octahedra and are then further connected through edge-sharing. Protons are located at the top of this octahedra layer. Dionigi. F concluded that $Ni(OOH)_2$ with a Ni valence of 2^+ would be transformed to NiOOH with a Ni valence of 3^+, while the γ-NiOOH phase resulting from this transformation was proposed to be the active phase[126]. This phase transformation was independently verified by Yan et al.[127], employing *in situ* Raman and *operando* XRD. In addition, it was observed that an intercalation of Ce enhanced the formation of the active γ-NiOOH phase, thereby improving the electrochemical performance. NiFe layered double hydroxide (LDH) has also been widely studied, where Fe^{3+} is incorporated into the Ni host lattice through substitution, producing positively charged layers due to the strong correlation between Ni and Fe. The above-mentioned phase transformation was also observed in NiFe LDHs. In a recent study by Qiu et al. [128], it was found that the NiFe LDH nanosheets undergo dynamic self-optimization to also form the active γ -NiOOH phase. By employing the *in situ* Raman spectro-electrochemistry, they were also able to demonstrate that Fe would form FeOOH and inhibit the Ni self-oxidation. This would not only improve the OER performance, but also improve the reaction rate of H_2 formation during HER. These reported properties of NiFe LDH would make it a promising bifunctional catalyst for water electrolysis applications.

1.4.4 OER Descriptors

Because the intrinsic catalyst active site is difficult to identify, it is important to construct a scaled relationship between the OER catalyst performance and the physical or chemical properties. Such properties, termed as OER descriptors, are important to develop an understanding of the catalytic structure-activity relationships and for the prediction of novel catalyst performance trends[129].

The occupancy of the e_g-symmetry orbital of the transitional metal has been widely used as a descriptor for perovskite OER catalysts[130]. In perovskite oxides, the hybridization of B-site transition metal d orbitals and O *2p* orbitals will split into low-energy t_{2g} and high-energy e_g orbitals[131]. Compared to the t_{2g} orbital, the e_g orbital has a vertical orientation, which would overlap with the O_2 intermediates to a larger extent, thus making the e_g orbital more suitable to describe catalytic behavior. Suntivich et al. proposed a volcano-like plot to indicate the relationship between OER catalytic activity and B-site e_g-symmetry electron occupancy, as shown in Figure 1.11[116]. Based on this, it was predicted that an intermittent e_g number of approximately 1.2 would ensure a high OER activity. This was subsequently verified experimentally through the high activity observed for $Ba_{0.5}Sr_{0.5}Co_{0.8}Fe_{0.2}O_{3-\delta}$. The moderate e_g value at an optimum OER activity is consistent with the Sabatier principle, where the best catalytic performance is predicted to be achieved at moderate adsorption energies[132, 133]. The e_g descriptor was later found to be suitable for transition-metal-based spinels as well[106].

The multiple spin states in Co-based double perovskites make it difficult to estimate the e_g filling number. The O *p*-band center as a bulk-phase property, however, is easier to obtain than the selected catalyst surface information. Grimaud et al. consequently reported the O *p*-band center as a descriptor for OER catalysts through *ab initio* DFT calculations, as shown in Figure 1.12[134]. Their work indicated that a moderate O *p*-band center, relative to the Fermi level, would lead to high OER activity in double perovskites. The strong linear relationship between catalytic activity indicators, such as current density, intermediate binding energy, and the bulk oxygen p-band center, was also supported by the theoretical work of Shao-Horn et al.[135], indicating the promising role of the O *p*-band center in the development of novel catalysts.

Other OER descriptors, such as the *d*-band center[136] and charge transfer energy[35, 137], based on the intermediate reaction energy, have also been studied for various types of catalysts. In addition, structural factors such as M–O bond length[138], M–O–M bond angle[139], and M–M distance[38] have also been proposed in recent research. With these OER descriptors, predicting the catalytic behavior should become straightforward. However, a statistical study of a wide range of descriptors demonstrated that some descriptors are not suitable when employed in isolation, with a combination of several descriptors rather being required to accurately describe catalytic performance[140]. Finding a universal OER descriptor therefore remains a challenge for future catalyst studies. Meanwhile, the established relationships might limit catalytic performance evaluation as well as the search for optimal materials. Therefore, precisely identifying and resolving the existing scaling relationships is crucial for the design of OER catalysts[129, 130].

1.5 Objective

As mentioned above, the design of novel OER catalysts with superior activity and durability depends on a thorough understanding of the reaction mechanism of O_2 evolution. Thus far, current research has not been able to identify all the active sites, intrinsic activity descriptors, and catalytic degradation mechanisms associated with OER. It is therefore essential that further fundamental research be conducted to identify ways in which to further improve the OER catalyst performance. X-ray absorption spectroscopy (XAS), especially when conducted under *operando* conditions coupled with structural evaluation techniques such as X-ray diffraction (XRD) and PDF analyses, provide the ideal set of techniques to effectively evaluate the association between local the electronic and crystal structures and their effect on the catalytic performance. In this study, an *operando* X-ray absorption spectroscopy technique was developed as a new method to measure the structure and electronic structure of catalysts during the reaction process. By combining the developed *operando* technique with various advanced analytical techniques, OER catalysts were thoroughly studied to elucidate the dominant factors of OER activity.

We report the OER activities and stabilities of various transition-metal-based catalysts in alkaline electrolytes, as well as iridium oxides in acidic electrolytes. With the combination of advanced *ex situ* and *operando* XAS techniques, the electronic structure, including transition metal oxidation states and hybridization state of transition metal 3*d* and oxygen 2*p* orbitals were rigorously analyzed. Moreover, the effect of the local structure, such as the bond distance, will be evaluated. The correlation between catalyst properties and catalytic performance was further established to obtain an intrinsic understanding of the reaction mechanism, while providing inspiration for the further design of innovative OER catalysts.

1.6 Outline of the Present Thesis

This thesis consists of nine chapters, wherein the reaction mechanisms of several OER catalysts in both alkaline and acidic electrolytes are reported. The results are based on the investigations using a combination of *ex situ* and *operando* advanced techniques, which provided additional insights required for the further development of OER catalysts.

Chapter 1 provides an overview of water electrolysis, previously proposed OER reaction mechanisms, and the present developments related to OER catalysts. The PEM water electrolyzer will also be introduced.

Chapter 2 investigates the electronic structural changes of nickel at the electrode/electrolyte interface during OER using thin-film Li-doped NiO catalysts. Here, *operando* total reflection florescence-XAS (TRF-XAS) revealed a distinct surface oxidation state change for $Li_{0.59}Ni_{0.41}O$, indicating the formation of high oxidation state Ni sites. The corresponding surface reconstruction resulted in an increased number of active sites on the reaction interface, thereby enhancing the OER activity.

Chapter 3 investigates the electrochemical performance and reaction kinetics of perovskite-type $La_{1-x}Sr_xCoO_{3-\delta}$ thin films as OER catalysts synthesized by the pulsed laser deposition method. Through the innovative combination of *ex situ* XAS and *operando* TRF-XAS, a significant oxidation state change on the surface of $La_{0.6}Sr_{0.4}CoO_{3-\delta}$ was observed. The formation of active surface sites resulting from surface reconstruction at the reaction interface and its effect on the OER activity are discussed.

Chapter 4 discusses the effect of cation mixing in $LiNiO_2$ on OER performance. The *ex situ* XAS revealed a strong hybridization state of Ni 3*d* and O 2*p* orbitals, which is believed to be the origin of the observed differences in catalytic activity behaviors. Moreover, *operando* XAS, combined with inductively coupled plasma optical emission spectrometry was conducted to investigate the Li-ion loss during the OER process. The de-intercalation of Li ions and its effect on the catalytic stability are discussed in detail.

Chapter 5 quantitatively evaluates the activity of low-spin tetravalent Ni ion sites in OER. The Ni valence was changed from divalent to tetravalent through the chemical delithiation of $Li_{0.96}Ni_{0.49}Mn_{1.51}O_4$, and the OER activity was found to increase with decreasing Li content. The high OER activity was attributed to the strong hybridization of the Ni-3*d*–O-2*p* orbital resulting from the downshift of the Ni conduction band, as confirmed through comprehensive XAS analyses.

In Chapter 6, the two-active-site OER mechanisms for quadruple perovskite oxides is discussed in detail. The OER catalytic performance of $CaMn_7O_{12}$ quadruple perovskite oxides with different Mn(A')–Mn(B) distances were carefully examined. Mn(A')–Mn(B) distances were precisely controlled through doping with Sr, Cu, and Al. The crystal structure and state of cations and O was investigated using XRD with Rietveld refinement and XAS. The OER catalytic activity was clearly correlated to the Mn(A')–Mn(B) distance, while the e_g states of both the Mn and O 2p band centers remained unchanged. A shrinkage of the A'–B distance affected the stability of the O–O bond on the A'–B site and accelerated the OER kinetics.

In Chapter 7, the origin of the high OER activity of amorphous iridium oxide is thoroughly investigated. A PDF analysis revealed that the short-range-ordered iridium oxide has two different structure phases. Further *ex situ* and *operando* XAS measurements demonstrated that the mixed phases contributed to an increase in active sites, thus enhancing the OER activity.

Chapter 8 summarizes the conclusions obtained from the present study and discusses the future prospects of water electrolysis.

Reference

1. Götz, M.; Lefebvre, J.; Mörs, F.; McDaniel Koch, A.; Graf, F.; Bajohr, S.; Reimert, R.; Kolb, T., Renewable Power-to-Gas: A technological and economic review. *Renew. Energy* **2016,** *85*, 1371-1390.
2. Anantharaj, S.; Ede, S. R.; Sakthikumar, K.; Karthick, K.; Mishra, S.; Kundu, S., Recent Trends and Perspectives in Electrochemical Water Splitting with an Emphasis on Sulfide, Selenide, and Phosphide Catalysts of Fe, Co, and Ni: A Review. *ACS Catal.* **2016,** *6* (12), 8069-8097.
3. Dincer, I.; Acar, C., Review and evaluation of hydrogen production methods for better sustainability. *Int. J. Hydrogen Energy* **2015,** *40* (34), 11094-11111.
4. Rashid, M. M.; Al Mesfer, M. K.; Naseem, H.; Danish, M., Hydrogen production by water electrolysis: a review of alkaline water electrolysis, PEM water electrolysis and high temperature water electrolysis. *Int. J. Eng. Adv. Technol* **2015,** *4* (3), 2249-8958.
5. Zeng, K.; Zhang, D., Recent progress in alkaline water electrolysis for hydrogen production and applications. *Prog. Energy Combust. Sci.* **2010,** *36* (3), 307-326.
6. Carmo, M.; Fritz, D. L.; Merge, J.; Stolten, D., A comprehensive review on PEM water electrolysis. *Int. J. Hydrogen Energy* **2013,** *38* (12), 4901-4934.
7. Edwards, P. P.; Kuznetsov, V. L.; David, W. I. F.; Brandon, N. P., Hydrogen and fuel cells: Towards a sustainable energy future. *Energy Policy* **2008,** *36* (12), 4356-4362.

8. Laguna-Bercero, M. A., Recent advances in high temperature electrolysis using solid oxide fuel cells: A review. *J. Power Sources* **2012,** *203*, 4-16.
9. Hamada, Y.; Takeda, K.; Goto, R.; Kubota, H. Hybrid utilization of renewable energy and fuel cells for residential energy systems. *Energy Build*. **2011**, 43 (12), 3680-3684
10. Staffell, I.; Scamman, D.; Abad, A. V.; Balcombe, P.; Dodds, P. E.; Ekins, P.; Shah, N.; Ward, K. R. The role of hydrogen and fuel cells in the global energy system. *Energy Environ. Sci*. **2019**, 12 (2), 463-491
11. An, L.; Wei, C.; Lu, M.; Liu, H.; Chen, Y.; Scherer, G. G.; Fisher, A. C.; Xi, P.; Xu, Z. J.; Yan, C.-H., Recent Development of Oxygen Evolution Electrocatalysts in Acidic Environment. *Adv. Mater.* **2021,** *33* (20), 2006328.
12. Wang, J.; Cui, W.; Liu, Q.; Xing, Z.; Asiri, A. M.; Sun, X., Recent Progress in Cobalt-Based Heterogeneous Catalysts for Electrochemical Water Splitting. *Adv. Mater.* **2016,** *28* (2), 215-230.
13. Karmakar, A.; Karthick, K.; Sankar, S. S.; Kumaravel, S.; Madhu, R.; Kundu, S., A vast exploration of improvising synthetic strategies for enhancing the OER kinetics of LDH structures: a review. *J. Mater Chem A* **2021,** *9* (3), 1314-1352.
14. Suen, N. T.; Hung, S. F.; Quan, Q.; Zhang, N.; Xu, Y. J.; Chen, H. M., Electrocatalysis for the oxygen evolution reaction: recent development and future perspectives. *Chem. Soc. Rev.* **2017,** *46* (2), 337-365.
15. Jang, H.; Lee, J., Iridium oxide fabrication and application: A review. *J. Energy Chem.* **2020,** *46*, 152-172.
16. Zhang, Y.; Zhu, X.; Zhang, G.; Shi, P.; Wang, A.-L., Rational catalyst design for oxygen evolution under acidic conditions: strategies toward enhanced electrocatalytic performance. *J. Mater. Chem. A* **2021**.
17. Jamesh, M.-I.; Harb, M., Tuning the electronic structure of the earth-abundant electrocatalysts for oxygen evolution reaction (OER) to achieve efficient alkaline water splitting – A review. *J. Energy Chem.* **2021,** *56*, 299-342.

18. Wang, J.; Gao, Y.; Kong, H.; Kim, J.; Choi, S.; Ciucci, F.; Hao, Y.; Yang, S.; Shao, Z.; Lim, J., Non-precious-metal catalysts for alkaline water electrolysis: operando characterizations, theoretical calculations, and recent advances. *Chem. Soc. Rev.* **2020**.
19. Song, J.; Wei, C.; Huang, Z.-F.; Liu, C.; Zeng, L.; Wang, X.; Xu, Z. J., A review on fundamentals for designing oxygen evolution electrocatalysts. *Chem. Soc. Rev.* **2020,** *49* (7), 2196-2214.
20. Chen, Z.; Duan, X.; Wei, W.; Wang, S.; Ni, B.-J., Iridium-based nanomaterials for electrochemical water splitting. *Nano Energy* **2020,** *78*, 105270.
21. Li, J.; Zheng, G., One-Dimensional Earth-Abundant Nanomaterials for Water-Splitting Electrocatalysts. *Adv. Sci.* **2017,** *4* (3), 1600380.
22. Morales-Guio, C. G.; Stern, L.-A.; Hu, X., Nanostructured hydrotreating catalysts for electrochemical hydrogen evolution. *Chem. Soc. Rev.* **2014,** *43* (18), 6555-6569.
23. Kapałka, A.; Fóti, G.; Comninellis, C., Determination of the Tafel slope for oxygen evolution on boron-doped diamond electrodes. *Electrochem. Commun.* **2008,** *10* (4), 607-610.
24. Doyle, R. L.; Lyons, M. E. G., Kinetics and Mechanistic Aspects of the Oxygen Evolution Reaction at Hydrous Iron Oxide Films in Base. *J. Electrochem. Soc.* **2013,** *160* (2), H142-H154.
25. Kim, B.-J.; Fabbri, E.; Borlaf, M.; Abbott, D. F.; Castelli, I. E.; Nachtegaal, M.; Graule, T.; Schmidt, T. J., Oxygen evolution reaction activity and underlying mechanism of perovskite electrocatalysts at different pH. *Mater. Adv.* **2021,** *2* (1), 345-355.
26. Giordano, L.; Han, B.; Risch, M.; Hong, W. T.; Rao, R. R.; Stoerzinger, K. A.; Shao-Horn, Y., pH dependence of OER activity of oxides: Current and future perspectives. *Catal. Today* **2016,** *262*, 2-10.

27. Rossmeisl, J.; Logadottir, A.; Nørskov, J. K., Electrolysis of water on (oxidized) metal surfaces. *Chem. Phys.* **2005,** *319* (1), 178-184.

28. Grimaud, A.; Diaz-Morales, O.; Han, B.; Hong, W. T.; Lee, Y.-L.; Giordano, L.; Stoerzinger, K. A.; Koper, M. T. M.; Shao-Horn, Y., Activating lattice oxygen redox reactions in metal oxides to catalyse oxygen evolution. *Nat. Chem.* **2017,** *9* (5), 457-465.

29. Yoo, J. S.; Rong, X.; Liu, Y.; Kolpak, A. M., Role of Lattice Oxygen Participation in Understanding Trends in the Oxygen Evolution Reaction on Perovskites. *ACS Catal.* **2018,** *8* (5), 4628-4636.

30. Huang, Z.-F.; Song, J.; Du, Y.; Xi, S.; Dou, S.; Nsanzimana, J. M. V.; Wang, C.; Xu, Z. J.; Wang, X., Chemical and structural origin of lattice oxygen oxidation in Co–Zn oxyhydroxide oxygen evolution electrocatalysts. *Nat. Energy* **2019,** *4* (4), 329-338.

31. Wohlfahrt-Mehrens, M.; Heitbaum, J., Oxygen evolution on Ru and RuO2 electrodes studied using isotope labelling and on-line mass spectrometry. *J. Electroanal. Chem.* **1987,** *237* (2), 251-260.

32. Fierro, S.; Nagel, T.; Baltruschat, H.; Comninellis, C., Investigation of the oxygen evolution reaction on Ti/IrO2 electrodes using isotope labelling and on-line mass spectrometry. *Electrochem. Commun.* **2007,** *9* (8), 1969-1974.

33. Rong, X.; Parolin, J.; Kolpak, A. M., A Fundamental Relationship between Reaction Mechanism and Stability in Metal Oxide Catalysts for Oxygen Evolution. *ACS Catal.* **2016,** *6* (2), 1153-1158.

34. Zhou, Y.; Sun, S.; Song, J.; Xi, S.; Chen, B.; Du, Y.; Fisher, A. C.; Cheng, F.; Wang, X.; Zhang, H.; Xu, Z. J., Enlarged Co□O Covalency in Octahedral Sites Leading to Highly Efficient Spinel Oxides for Oxygen Evolution Reaction. **2018,** *30* (32), 1802912.

35. Hong, W. T.; Stoerzinger, K. A.; Lee, Y. L.; Giordano, L.; Grimaud, A.; Johnson, A. M.; Hwang, J.; Crumlin, E. J.; Yang, W. L.; Shao-Horn, Y., Charge-transfer-energy-dependent oxygen evolution reaction mechanisms for perovskite oxides. *Energy Environ. Sci.* **2017,** *10* (10), 2190-2200.
36. Mattioli, G.; Giannozzi, P.; Amore Bonapasta, A.; Guidoni, L., Reaction Pathways for Oxygen Evolution Promoted by Cobalt Catalyst. *J. Am. Chem. Soc.* **2013,** *135* (41), 15353-15363.
37. Mavros, M. G.; Tsuchimochi, T.; Kowalczyk, T.; McIsaac, A.; Wang, L.-P.; Voorhis, T. V., What Can Density Functional Theory Tell Us about Artificial Catalytic Water Splitting? *Inorg. Chem.* **2014,** *53* (13), 6386-6397.
38. Yamada, I.; Fujii, H.; Takamatsu, A.; Ikeno, H.; Wada, K.; Tsukasaki, H.; Kawaguchi, S.; Mori, S.; Yagi, S., Bifunctional Oxygen Reaction Catalysis of Quadruple Manganese Perovskites. *Adv. Mater.* **2017,** *29* (4), 1603004.
39. Yamada, I., Novel catalytic properties of quadruple perovskites. *Sci. Technol. Adv. Mater.* **2017,** *18* (1), 541-548.
40. Takamatsu, A.; Yamada, I.; Yagi, S.; Ikeno, H., Oxygen Evolution via the Bridging Inequivalent Dual-Site Reaction: First-Principles Study of a Quadruple-Perovskite Oxide Catalyst. *J. Phys. Chem. C* **2017,** *121* (51), 28403-28411.
41. Stoerzinger, K. A.; Diaz-Morales, O.; Kolb, M.; Rao, R. R.; Frydendal, R.; Qiao, L.; Wang, X. R.; Halck, N. B.; Rossmeisl, J.; Hansen, H. A.; Vegge, T.; Stephens, I. E. L.; Koper, M. T. M.; Shao-Horn, Y., Orientation-Dependent Oxygen Evolution on RuO_2 without Lattice Exchange. *ACS Energy Lett.* **2017**, 2 (4), 876-881.
42. Stoerzinger, K. A.; Qiao, L.; Biegalski, M. D.; Shao-Horn, Y., Orientation-Dependent Oxygen Evolution Activities of Rutile IrO2 and RuO2. *J. Phys. Chem. Lett.* **2014**, 5 (10), 1636-1641.

43. Chen, Y.; Li, H.; Wang, J.; Du, Y.; Xi, S.; Sun, Y.; Sherburne, M.; Ager, J. W.; Fisher, A. C.; Xu, Z. J., Exceptionally active iridium evolved from a pseudo-cubic perovskite for oxygen evolution in acid. *Nat. Commun.* **2019,** *10* (1), 572.
44. Wang, C.; Lan, F.; He, Z.; Xie, X.; Zhao, Y.; Hou, H.; Guo, L.; Murugadoss, V.; Liu, H.; Shao, Q.; Gao, Q.; Ding, T.; Wei, R.; Guo, Z., Iridium-Based Catalysts for Solid Polymer Electrolyte Electrocatalytic Water Splitting. *ChemSusChem* **2019,** *12* (8), 1576-1590.
45. Lee, Y.; Suntivich, J.; May, K. J.; Perry, E. E.; Shao-Horn, Y., Synthesis and activities of rutile IrO_2 and RuO_2 nanoparticles for oxygen evolution in acid and alkaline solutions. *J. Phys. Chem. Lett.* **2012,** *3* (3), 399-404.
46. Lim, J.; Park, D.; Jeon, S. S.; Roh, C.-W.; Choi, J.; Yoon, D.; Park, M.; Jung, H.; Lee, H., Ultrathin IrO2 Nanoneedles for Electrochemical Water Oxidation. *Adv. Funct. Mater.* **2018,** *28* (4), 1704796.
47. Alia, S. M.; Shulda, S.; Ngo, C.; Pylypenko, S.; Pivovar, B. S., Iridium-Based Nanowires as Highly Active, Oxygen Evolution Reaction Electrocatalysts. *ACS Catal.* **2018,** *8* (3), 2111-2120.
48. Pawluk, T.; Hirata, Y.; Wang, L., Studies of Iridium Nanoparticles Using Density Functional Theory Calculations. *J. Phys. Chem. B* **2005,** *109* (44), 20817-20823.
49. Fu, L.; Yang, F.; Cheng, G.; Luo, W., Ultrathin Ir nanowires as high-performance electrocatalysts for efficient water splitting in acidic media. *Nanoscale* **2018,** *10* (4), 1892-1897.
50. Gou, W.; Zhang, M.; Zou, Y.; Zhou, X.; Qu, Y., Iridium-Chromium Oxide Nanowires as Highly Performed OER Catalysts in Acidic Media. *ChemCatChem* **2019,** *11* (24), 6008-6014.
51. Wu, G.; Zheng, X. S.; Cui, P. X.; Jiang, H. Y.; Wang, X. Q.; Qu, Y. T.; Chen, W. X.; Lin, Y.; Li, H.; Han, X.; Hu, Y. M.; Liu, P. G.; Zhang, Q. H.; Ge, J.

J.; Yao, Y. C.; Sun, R. B.; Wu, Y.; Gu, L.; Hong, X.; Li, Y. D., A general synthesis approach for amorphous noble metal nanosheets. *Nat. Commun.* **2019,** *10.*

52. Takimoto, D.; Fukuda, K.; Miyasaka, S.; Ishida, T.; Ayato, Y.; Mochizuki, D.; Shimizu, W.; Sugimoto, W., Synthesis and Oxygen Electrocatalysis of Iridium Oxide Nanosheets. *Electrocatalysis* **2017,** *8* (2), 144-150.
53. Takimoto, D.; Ayato, Y.; Mochizuki, D.; Sugimoto, W., Lateral Size Effects of Two-dimensional IrO2 Nanosheets towards the Oxygen Evolution Reaction Activity. *Electrochemistry* **2017,** *85* (12), 779-783.
54. Ahmed, J.; Mao, Y., Ultrafine Iridium Oxide Nanorods Synthesized by Molten Salt Method toward Electrocatalytic Oxygen and Hydrogen Evolution Reactions. *Electrochim. Acta* **2016,** *212*, 686-693.
55. Elmaalouf, M.; Odziomek, M.; Duran, S.; Gayrard, M.; Bahri, M.; Tard, C.; Zitolo, A.; Lassalle-Kaiser, B.; Piquemal, J.-Y.; Ersen, O.; Boissière, C.; Sanchez, C.; Giraud, M.; Faustini, M.; Peron, J., The origin of the high electrochemical activity of pseudo-amorphous iridium oxides. *Nat. Commun.* **2021,** *12* (1), 3935.
56. Faustini, M.; Giraud, M.; Jones, D.; Rozière, J.; Dupont, M.; Porter, T. R.; Nowak, S.; Bahri, M.; Ersen, O.; Sanchez, C.; Boissière, C.; Tard, C.; Peron, J., Hierarchically Structured Ultraporous Iridium-Based Materials: A Novel Catalyst Architecture for Proton Exchange Membrane Water Electrolyzers. *Adv. Energy Mater.* **2019,** *9* (4), 1802136.
57. Bohm, D.; Beetz, M.; Schuster, M.; Peters, K.; Hufnagel, A. G.; Doblinger, M.; Boller, B.; Bein, T.; Fattakhova-Rohlfing, D., Efficient OER Catalyst with Low Ir Volume Density Obtained by Homogeneous Deposition of Iridium Oxide Nanoparticles on Macroporous Antimony-Doped Tin Oxide Support. *Adv. Funct. Mater.* **2020,** *30* (1).

58. da Silva, G. C.; Venturini, S. I.; Zhang, S.; Löffler, M.; Scheu, C.; Mayrhofer, K. J. J.; Ticianelli, E. A.; Cherevko, S., Oxygen Evolution Reaction on Tin Oxides Supported Iridium Catalysts: Do We Need Dopants? *ChemElectroChem* **2020,** *7* (10), 2330-2339.

59. Han, S.-B.; Mo, Y.-H.; Lee, Y.-S.; Lee, S.-G.; Park, D.-H.; Park, K.-W., Mesoporous iridium oxide/Sb-doped SnO2 nanostructured electrodes for polymer electrolyte membrane water electrolysis. *Int. J. Hydrogen Energy* **2020,** *45* (3), 1409-1416.

60. Hartig-Weiss, A.; Miller, M.; Beyer, H.; Schmitt, A.; Siebel, A.; Freiberg, A. T. S.; Gasteiger, H. A.; El-Sayed, H. A., Iridium Oxide Catalyst Supported on Antimony-Doped Tin Oxide for High Oxygen Evolution Reaction Activity in Acidic Media. *ACS Appl. Nano Mater.* **2020,** *3* (3), 2185-2196.

61. Oh, H.-S.; Nong, H. N.; Reier, T.; Bergmann, A.; Gliech, M.; Ferreira de Araújo, J.; Willinger, E.; Schlögl, R.; Teschner, D.; Strasser, P., Electrochemical Catalyst–Support Effects and Their Stabilizing Role for IrOx Nanoparticle Catalysts during the Oxygen Evolution Reaction. *J. Am. Chem. Soc.* **2016,** *138* (38), 12552-12563.

62. Oh, H.-S.; Nong, H. N.; Reier, T.; Gliech, M.; Strasser, P., Oxide-supported Ir nanodendrites with high activity and durability for the oxygen evolution reaction in acid PEM water electrolyzers. *Chem. Sci.* **2015,** *6* (6), 3321-3328.

63. Pfeifer, V.; Jones, T. E.; Velasco Vélez, J. J.; Massué, C.; Arrigo, R.; Teschner, D.; Girgsdies, F.; Scherzer, M.; Greiner, M. T.; Allan, J.; Hashagen, M.; Weinberg, G.; Piccinin, S.; Hävecker, M.; Knop-Gericke, A.; Schlögl, R., The electronic structure of iridium and its oxides. *Surf. Interface Anal.* **2016,** *48* (5), 261-273.

64. Pfeifer, V.; Jones, T. E.; Velasco Vélez, J. J.; Massué, C.; Greiner, M. T.; Arrigo, R.; Teschner, D.; Girgsdies, F.; Scherzer, M.; Allan, J.; Hashagen,

M.; Weinberg, G.; Piccinin, S.; Hävecker, M.; Knop-Gericke, A.; Schlögl, R., The electronic structure of iridium oxide electrodes active in water splitting. *PCCP* **2016,** *18* (4), 2292-2296.

65. Czioska, S.; Boubnov, A.; Escalera-López, D.; Geppert, J.; Zagalskaya, A.; Röse, P.; Saraçi, E.; Alexandrov, V.; Krewer, U.; Cherevko, S.; Grunwaldt, J.-D., Increased Ir–Ir Interaction in Iridium Oxide during the Oxygen Evolution Reaction at High Potentials Probed by Operando Spectroscopy. *ACS Catal.* **2021,** *11* (15), 10043-10057.

66. Kwon, G.; Chang, S. H.; Heo, J. E.; Lee, K. J.; Kim, J.-K.; Cho, B.-G.; Koo, T. Y.; Kim, B. J.; Kim, C.; Lee, J. H.; Bak, S.-M.; Beyer, K. A.; Zhong, H.; Koch, R. J.; Hwang, S.; Utschig, L. M.; Huang, X.; Hu, G.; Brudvig, G. W.; Tiede, D. M.; Kim, J., Experimental Verification of Ir 5d Orbital States and Atomic Structures in Highly Active Amorphous Iridium Oxide Catalysts. *ACS Catal.* **2021,** *11* (15), 10084-10094.

67. Willinger, E.; Massué, C.; Schlögl, R.; Willinger, M. G., Identifying Key Structural Features of IrOx Water Splitting Catalysts. *J. Am. Chem. Soc.* **2017,** *139* (34), 12093-12101.

68. Sharma, R.; Karlsen, M. A.; Morgen, P.; Chamier, J.; Ravnsbæk, D. B.; Andersen, S. M., Crystalline Disorder, Surface Chemistry, and Their Effects on the Oxygen Evolution Reaction (OER) Activity of Mass-Produced Nanostructured Iridium Oxides. *ACS Appl. Energy Mater.* **2021,** *4* (3), 2552-2562.

69. Nong, H. N.; Reier, T.; Oh, H.-S.; Gliech, M.; Paciok, P.; Vu, T. H. T.; Teschner, D.; Heggen, M.; Petkov, V.; Schlögl, R.; Jones, T.; Strasser, P., A unique oxygen ligand environment facilitates water oxidation in hole-doped IrNiOx core–shell electrocatalysts. *Nat. Catal.* **2018,** *1* (11), 841-851.

70. Du, P.; Kokhan, O.; Chapman, K. W.; Chupas, P. J.; Tiede, D. M., Elucidating the Domain Structure of the Cobalt Oxide Water Splitting Catalyst by X-ray Pair Distribution Function Analysis. *J. Am. Chem. Soc.* **2012,** *134* (27), 11096-11099.

71. Nong, H. N.; Falling, L. J.; Bergmann, A.; Klingenhof, M.; Tran, H. P.; Spöri, C.; Mom, R.; Timoshenko, J.; Zichittella, G.; Knop-Gericke, A.; Piccinin, S.; Pérez-Ramírez, J.; Cuenya, B. R.; Schlögl, R.; Strasser, P.; Teschner, D.; Jones, T. E., Key role of chemistry versus bias in electrocatalytic oxygen evolution. *Nature* **2020,** *587* (7834), 408-413.

72. Pfeifer, V.; Jones, T. E.; Wrabetz, S.; Massué, C.; Velasco Vélez, J. J.; Arrigo, R.; Scherzer, M.; Piccinin, S.; Hävecker, M.; Knop-Gericke, A.; Schlögl, R., Reactive oxygen species in iridium-based OER catalysts. *Chem. Sci.* **2016,** *7* (11), 6791-6795.

73. Pfeifer, V.; Jones, T. E.; Velasco Vélez, J. J.; Arrigo, R.; Piccinin, S.; Hävecker, M.; Knop-Gericke, A.; Schlögl, R., In situ observation of reactive oxygen species forming on oxygen-evolving iridium surfaces. *Chem. Sci.* **2017,** *8* (3), 2143-2149.

74. Saveleva, V. A.; Wang, L.; Teschner, D.; Jones, T.; Gago, A. S.; Friedrich, K. A.; Zafeiratos, S.; Schlögl, R.; Savinova, E. R., Operando Evidence for a Universal Oxygen Evolution Mechanism on Thermal and Electrochemical Iridium Oxides. *J. Phys. Chem. Lett.* **2018,** *9* (11), 3154-3160.

75. Geiger, S.; Kasian, O.; Ledendecker, M.; Pizzutilo, E.; Mingers, A. M.; Fu, W. T.; Diaz-Morales, O.; Li, Z.; Oellers, T.; Fruchter, L.; Ludwig, A.; Mayrhofer, K. J. J.; Koper, M. T. M.; Cherevko, S., The stability number as a metric for electrocatalyst stability benchmarking. *Nat. Catal.* **2018,** *1* (7), 508-515.

76. Kim, Y.-T.; Lopes, P. P.; Park, S.-A.; Lee, A. Y.; Lim, J.; Lee, H.; Back, S.; Jung, Y.; Danilovic, N.; Stamenkovic, V.; Erlebacher, J.; Snyder, J.; Markovic,

N. M., Balancing activity, stability and conductivity of nanoporous core-shell iridium/iridium oxide oxygen evolution catalysts. *Nat. Commun.* **2017,** *8* (1), 1449.

77. Creus, J.; De Tovar, J.; Romero, N.; García-Antón, J.; Philippot, K.; Bofill, R.; Sala, X., Ruthenium Nanoparticles for Catalytic Water Splitting. *ChemSusChem* **2019,** *12* (12), 2493-2514.
78. Ma, H.; Liu, C.; Liao, J.; Su, Y.; Xue, X.; Xing, W., Study of ruthenium oxide catalyst for electrocatalytic performance in oxygen evolution. *J. Mol. Catal. A: Chem.* **2006,** *247* (1), 7-13.
79. Nguyen, T. D.; Scherer, G. G.; Xu, Z. J., A Facile Synthesis of Size-Controllable IrO2 and RuO2 Nanoparticles for the Oxygen Evolution Reaction. *Electrocatalysis* **2016,** *7* (5), 420-427.
80. Paoli, E. A.; Masini, F.; Frydendal, R.; Deiana, D.; Schlaup, C.; Malizia, M.; Hansen, T. W.; Horch, S.; Stephens, I. E. L.; Chorkendorff, I., Oxygen evolution on well-characterized mass-selected Ru and RuO_2 nanoparticles. *Chem. Sci.* **2015,** *6* (1), 190-196.
81. Reier, T.; Oezaslan, M.; Strasser, P., Electrocatalytic Oxygen Evolution Reaction (OER) on Ru, Ir, and Pt Catalysts: A Comparative Study of Nanoparticles and Bulk Materials. *ACS Catal.* **2012,** *2* (8), 1765-1772.
82. Wang, J.; Han, L.; Huang, B.; Shao, Q.; Xin, H. L.; Huang, X., Amorphization activated ruthenium-tellurium nanorods for efficient water splitting. *Nat. Commun.* **2019,** *10* (1), 5692.
83. Wang, J.; Ji, Y.; Yin, R.; Li, Y.; Shao, Q.; Huang, X., Transition metal-doped ultrathin RuO2 networked nanowires for efficient overall water splitting across a broad pH range. *J. Mater. Chem. A* **2019,** *7* (11), 6411-6416.
84. Zhao, Z. L.; Wang, Q.; Huang, X.; Feng, Q.; Gu, S.; Zhang, Z.; Xu, H.; Zeng, L.; Gu, M.; Li, H., Boosting the oxygen evolution reaction using defect-rich

ultra-thin ruthenium oxide nanosheets in acidic media. *Energy & Environmental Science* **2020**.

85. Laha, S.; Lee, Y.; Podjaski, F.; Weber, D.; Duppel, V.; Schoop, L. M.; Pielnhofer, F.; Scheurer, C.; Müller, K.; Starke, U.; Reuter, K.; Lotsch, B. V., Ruthenium Oxide Nanosheets for Enhanced Oxygen Evolution Catalysis in Acidic Medium. *Adv. Energy Mater.* **2019,** *9* (15), 1803795.
86. Fukuda, K.; Saida, T.; Sato, J.; Yonezawa, M.; Takasu, Y.; Sugimoto, W., Synthesis of Nanosheet Crystallites of Ruthenate with an α-NaFeO2-Related Structure and Its Electrochemical Supercapacitor Property. *Inorg. Chem.* **2010,** *49* (10), 4391-4393.
87. Kibsgaard, J.; Hellstern, T. R.; Choi, S.-J.; Reinecke, B. N.; Jaramillo, T. F., Mesoporous Ruthenium/Ruthenium Oxide Thin Films: Active Electrocatalysts for the Oxygen Evolution Reaction. **2017,** *4* (10), 2480-2485.
88. Lee, S. W.; Baik, C.; Pak, C., Ordered mesoporous ruthenium oxide with balanced catalytic activity and stability toward oxygen evolution reaction. *Catal. Today* **2020,** *358*, 203-209.
89. Wei, T.-C.; Hillhouse, H. W., Mass Transport and Electrode Accessibility Through Periodic Self-Assembled Nanoporous Silica Thin Films. *Langmuir* **2007,** *23* (10), 5689-5699.
90. Joo, J.; Jin, H.; Oh, A.; Kim, B.; Lee, J.; Baik, H.; Joo, S. H.; Lee, K., An IrRu alloy nanocactus on Cu2−xS@IrSy as a highly efficient bifunctional electrocatalyst toward overall water splitting in acidic electrolytes. *J. Mater. Chem. A* **2018,** *6* (33), 16130-16138.
91. Neyerlin, K. C.; Bugosh, G.; Forgie, R.; Liu, Z.; Strasser, P., Combinatorial Study of High-Surface-Area Binary and Ternary Electrocatalysts for the Oxygen Evolution Reaction. *J. Electrochem. Soc.* **2009,** *156* (3), B363.

92. Yao, Y.; Hu, S.; Chen, W.; Huang, Z.-Q.; Wei, W.; Yao, T.; Liu, R.; Zang, K.; Wang, X.; Wu, G.; Yuan, W.; Yuan, T.; Zhu, B.; Liu, W.; Li, Z.; He, D.; Xue, Z.; Wang, Y.; Zheng, X.; Dong, J.; Chang, C.-R.; Chen, Y.; Hong, X.; Luo, J.; Wei, S.; Li, W.-X.; Strasser, P.; Wu, Y.; Li, Y., Engineering the electronic structure of single atom Ru sites via compressive strain boosts acidic water oxidation electrocatalysis. *Nat. Catal.* **2019,** *2* (4), 304-313.

93. Shan, J.; Ling, T.; Davey, K.; Zheng, Y.; Qiao, S.-Z., Transition-Metal-Doped RuIr Bifunctional Nanocrystals for Overall Water Splitting in Acidic Environments. **2019,** *31* (17), 1900510.

94. Chen, G.; Desinan, S.; Nechache, R.; Rosei, R.; Rosei, F.; Ma, D., Bifunctional catalytic/magnetic Ni@Ru core–shell nanoparticles. *Chem. Commun.* **2011,** *47* (22), 6308-6310.

95. Hwang, H.; Kwon, T.; Kim, H. Y.; Park, J.; Oh, A.; Kim, B.; Baik, H.; Joo, S. H.; Lee, K., Ni@Ru and NiCo@Ru Core–Shell Hexagonal Nanosandwiches with a Compositionally Tunable Core and a Regioselectively Grown Shell. **2018,** *14* (3), 1702353.

96. Jiang, R.; Tran, D. T.; Li, J.; Chu, D., Ru@RuO2 Core-Shell Nanorods: A Highly Active and Stable Bifunctional Catalyst for Oxygen Evolution and Hydrogen Evolution Reactions. **2019,** *2* (3), 201-208.

97. Zhang, Y.; Ren, T., Silica supported ruthenium oxide nanoparticulates as efficient catalysts for water oxidation. *Chem. Commun.* **2012,** *48* (89), 11005-11007.

98. Roca-Ayats, M.; Herreros, E.; García, G.; Peña, M. A.; Martínez-Huerta, M. V., Promotion of oxygen reduction and water oxidation at Pt-based electrocatalysts by titanium carbonitride. *Appl. Catal. B: Environ.* **2016,** *183*, 53-60.

99. Chen, D.; Pu, Z.; Lu, R.; Ji, P.; Wang, P.; Zhu, J.; Lin, C.; Li, H.-W.; Zhou, X.; Hu, Z.; Xia, F.; Wu, J.; Mu, S., Ultralow Ru Loading Transition Metal

Phosphides as High-Efficient Bifunctional Electrocatalyst for a Solar-to-Hydrogen Generation System. **2020,** *10* (28), 2000814.

100. Zhou, F.; Zhang, L.; Li, J.; Wang, Q.; Chen, Y.; Chen, H.; Lu, G.; Chen, G.; Jin, H.; Wang, S.; Wang, J., Novel engineering of ruthenium-based electrocatalysts for acidic water oxidation: A mini review. *Engineering Reports* **2021,** *3* (8), e12437.
101. Yu, J.; He, Q.; Yang, G.; Zhou, W.; Shao, Z.; Ni, M., Recent Advances and Prospective in Ruthenium-Based Materials for Electrochemical Water Splitting. *ACS Catal.* **2019,** *9* (11), 9973-10011.
102. Cherevko, S.; Geiger, S.; Kasian, O.; Kulyk, N.; Grote, J.-P.; Savan, A.; Shrestha, B. R.; Merzlikin, S.; Breitbach, B.; Ludwig, A.; Mayrhofer, K. J. J., Oxygen and hydrogen evolution reactions on Ru, RuO_2, Ir, and IrO_2 thin film electrodes in acidic and alkaline electrolytes: A comparative study on activity and stability. *Catal. Today* **2016,** *262*, 170-180.
103. Sun, X.; Gao, X.; Chen, J.; Wang, X.; Chang, H.; Li, B.; Song, D.; Li, J.; Li, H.; Wang, N., Ultrasmall Ru Nanoparticles Highly Dispersed on Sulfur-Doped Graphene for HER with High Electrocatalytic Performance. *ACS Appl. Mater. Interfaces* **2020,** *12* (43), 48591-48597.
104. Gao, L.; Cui, X.; Sewell, C. D.; Li, J.; Lin, Z., Recent advances in activating surface reconstruction for the high-efficiency oxygen evolution reaction. *Chem. Soc. Rev.* **2021,** *50* (15), 8428-8469.
105. Zhao, Q.; Yan, Z. H.; Chen, C. C.; Chen, J., Spinels: Controlled Preparation, Oxygen Reduction/Evolution Reaction Application, and Beyond. *Chem. Rev.* **2017,** *117* (15), 10121-10211.
106. Wei, C.; Feng, Z.; Scherer, G. G.; Barber, J.; Shao-Horn, Y.; Xu, Z. J., Cations in Octahedral Sites: A Descriptor for Oxygen Electrocatalysis on Transition-Metal Spinels. *Adv. Mater.* **2017,** *29* (23), 1606800.

107. Zhou, Y.; Sun, S. N.; Wei, C.; Sun, Y. M.; Xi, P. X.; Feng, Z. X.; Xu, Z. C. J., Significance of Engineering the Octahedral Units to Promote the Oxygen Evolution Reaction of Spinel Oxides. *Adv. Mater.* **2019,** *31* (41).

108. Sun, S. N.; Sun, Y. M.; Zhou, Y.; Xi, S. B.; Ren, X.; Huang, B. C.; Liao, H. B.; Wang, L. Y. P.; Du, Y. H.; Xu, Z. C., Shifting Oxygen Charge Towards Octahedral Metal: A Way to Promote Water Oxidation on Cobalt Spinel Oxides. *Angew. Chem. Int. Ed.* **2019,** *58* (18), 6042-6047.

109. Robinson, D. M.; Go, Y. B.; Greenblatt, M.; Dismukes, G. C., Water Oxidation by λ-MnO2: Catalysis by the Cubical Mn4O4 Subcluster Obtained by Delithiation of Spinel LiMn2O4. *J. Am. Chem. Soc.* **2010,** *132* (33), 11467-11469.

110. Maiyalagan, T.; Jarvis, K. A.; Therese, S.; Ferreira, P. J.; Manthiram, A., Spinel-type lithium cobalt oxide as a bifunctional electrocatalyst for the oxygen evolution and oxygen reduction reactions. *Nat. Commun.* **2014,** *5* (1), 3949.

111. Saravanan, K.; Jarry, A.; Kostecki, R.; Chen, G., A study of room-temperature LixMn1.5Ni0.5O4 solid solutions. *Sci. Rep.* **2015,** *5* (1), 8027.

112. Xue, Y.; Wang, Z.; Zheng, L.; Yu, F.; Liu, B.; Zhang, Y.; Ke, K., Investigation on preparation and performance of spinel LiNi0.5Mn1.5O4 with different microstructures for lithium-ion batteries. *Sci. Rep.* **2015,** *5* (1), 13299.

113. Wang, H.-Y.; Hung, S.-F.; Chen, H.-Y.; Chan, T.-S.; Chen, H. M.; Liu, B., In Operando Identification of Geometrical-Site-Dependent Water Oxidation Activity of Spinel Co3O4. *J. Am. Chem. Soc.* **2016,** *138* (1), 36-39.

114. Xiao, Z.; Huang, Y.-C.; Dong, C.-L.; Xie, C.; Liu, Z.; Du, S.; Chen, W.; Yan, D.; Tao, L.; Shu, Z.; Zhang, G.; Duan, H.; Wang, Y.; Zou, Y.; Chen, R.; Wang, S., Operando Identification of the Dynamic Behavior of Oxygen Vacancy-Rich Co_3O_4 for Oxygen Evolution Reaction. *J. Am. Chem. Soc.* **2020,** *142* (28), 12087-12095.

115. Xu, L.; Jiang, Q.; Xiao, Z.; Li, X.; Huo, J.; Wang, S.; Dai, L., Plasma-Engraved Co3O4 Nanosheets with Oxygen Vacancies and High Surface Area for the Oxygen Evolution Reaction. **2016,** *55* (17), 5277-5281.

116. Suntivich, J.; May, K. J.; Gasteiger, H. A.; Goodenough, J. B.; Shao-Horn, Y., A Perovskite Oxide Optimized for Oxygen Evolution Catalysis from Molecular Orbital Principles. *Science* **2011,** *334* (6061), 1383-1385.

117. Fabbri, E.; Nachtegaal, M.; Binninger, T.; Cheng, X.; Kim, B. J.; Durst, J.; Bozza, F.; Graule, T.; Schäublin, R.; Wiles, L.; Pertoso, M.; Danilovic, N.; Ayers, K. E.; Schmidt, T. J., Dynamic surface self-reconstruction is the key of highly active perovskite nano-electrocatalysts for water splitting. *Nat. Mater.* **2017,** *16* (9), 925-931.

118. Grimaud, A.; May, K. J.; Carlton, C. E.; Lee, Y.-L.; Risch, M.; Hong, W. T.; Zhou, J.; Shao-Horn, Y., Double perovskites as a family of highly active catalysts for oxygen evolution in alkaline solution. *Nat. Commun.* **2013,** *4* (1), 2439.

119. Liu, D.; Zhou, P.; Bai, H.; Ai, H.; Du, X.; Chen, M.; Liu, D.; Ip, W. F.; Lo, K. H.; Kwok, C. T.; Chen, S.; Wang, S.; Xing, G.; Wang, X.; Pan, H., Development of Perovskite Oxide-Based Electrocatalysts for Oxygen Evolution Reaction. *Small n/a* (n/a), 2101605.

120. Wang, W.; Yang, Y.; Huan, D.; Wang, L.; Shi, N.; Xie, Y.; Xia, C.; Peng, R.; Lu, Y., An excellent OER electrocatalyst of cubic $SrCoO_{3-\delta}$ prepared by a simple F-doping strategy. *J. Mater. Chem. A* **2019,** *7* (20), 12538-12546.

121. Liu, Q.; Jia, C.; Zhou, M.; He, Z.; Gong, Z.; Ling, Y.; Wang, X.; Yashiro, K.; Chen, Y., Modulating Reaction Pathways on Perovskite Cobaltite Nanofibers through Excessive Surface Oxygen Defects for Efficient Water Oxidation. *Energy & Fuels* **2021,** *35* (17), 13967-13974.

122. Liu, Y.; Quiñonero, J.; Yao, L.; Da Costa, X.; Mensi, M.; Gómez, R.; Sivula, K.; Guijarro, N., Defect engineered nanostructured LaFeO3 photoanodes for

improved activity in solar water oxidation. *J. Mater. Chem.y A* **2021,** *9* (5), 2888-2898.

123. Li, C.; Cheng, J.; Jiang, Y.; Xiao, W.; Yan, X., Electronic structure regulation and electrocatalytic mechanism of one-dimensional mesoporous La0.8Sr0.2Mn1-xCoxO3 with bifunctional electrocatalysts towards Zn-air batteries. *J. Power Sources* **2021,** *498*, 229940.
124. Mather, G. C.; Dussarrat, C.; Etourneau, J.; West, A. R., A review of cation-ordered rock salt superstructure oxides. *J. Mater. Chem.* **2000,** *10* (10), 2219-2230.
125. Trotochaud, L.; Ranney, J. K.; Williams, K. N.; Boettcher, S. W., Solution-Cast Metal Oxide Thin Film Electrocatalysts for Oxygen Evolution. *J. Am. Chem. Soc.* **2012,** *134* (41), 17253-17261.
126. Dionigi, F.; Strasser, P., NiFe-Based (Oxy)hydroxide Catalysts for Oxygen Evolution Reaction in Non-Acidic Electrolytes. **2016,** *6* (23), 1600621.
127. Yan, Z.; Sun, H.; Chen, X.; Liu, H.; Zhao, Y.; Li, H.; Xie, W.; Cheng, F.; Chen, J., Anion insertion enhanced electrodeposition of robust metal hydroxide/oxide electrodes for oxygen evolution. *Nat. Commun.* **2018,** *9* (1), 2373.
128. Qiu, Z.; Tai, C.-W.; Niklasson, G. A.; Edvinsson, T., Direct observation of active catalyst surface phases and the effect of dynamic self-optimization in NiFe-layered double hydroxides for alkaline water splitting. *Energy Environ. Sci.* **2019,** *12* (2), 572-581.
129. Zhao, Z.-J.; Liu, S.; Zha, S.; Cheng, D.; Studt, F.; Henkelman, G.; Gong, J., Theory-guided design of catalytic materials using scaling relationships and reactivity descriptors. *Nat. Rev. Mater.* **2019,** *4* (12), 792-804.
130. Liu, J.; Liu, H.; Chen, H.; Du, X.; Zhang, B.; Hong, Z.; Sun, S.; Wang, W., Progress and Challenges Toward the Rational Design of Oxygen Electrocatalysts Based on a Descriptor Approach. **2020,** *7* (1), 1901614.

131. Hwang, J.; Rao, R. R.; Giordano, L.; Katayama, Y.; Yu, Y.; Shao-Horn, Y., Perovskites in catalysis and electrocatalysis. *Science* **2017,** *358* (6364), 751-756.

132. Medford, A. J.; Vojvodic, A.; Hummelshøj, J. S.; Voss, J.; Abild-Pedersen, F.; Studt, F.; Bligaard, T.; Nilsson, A.; Nørskov, J. K., From the Sabatier principle to a predictive theory of transition-metal heterogeneous catalysis. *J. Catal.* **2015,** *328*, 36-42.

133. Laursen, A. B.; Varela, A. S.; Dionigi, F.; Fanchiu, H.; Miller, C.; Trinhammer, O. L.; Rossmeisl, J.; Dahl, S., Electrochemical Hydrogen Evolution: Sabatier's Principle and the Volcano Plot. *J. Chem. Educ.* **2012,** *89* (12), 1595-1599.

134. Grimaud, A.; May, K. J.; Carlton, C. E.; Lee, Y. L.; Risch, M.; Hong, W. T.; Zhou, J. G.; Shao-Horn, Y., Double perovskites as a family of highly active catalysts for oxygen evolution in alkaline solution. *Nat. Commun.* **2013,** *4*.

135. Jacobs, R.; Hwang, J.; Shao-Horn, Y.; Morgan, D., Assessing Correlations of Perovskite Catalytic Performance with Electronic Structure Descriptors. *Chem. Mater.* **2019,** *31* (3), 785-797.

136. Nørskov, J. K.; Bligaard, T.; Rossmeisl, J.; Christensen, C. H., Towards the computational design of solid catalysts. *Nat. Chem.* **2009,** *1*, 37.

137. Yamada, I.; Takamatsu, A.; Asai, K.; Shirakawa, T.; Ohzuku, H.; Seno, A.; Uchimura, T.; Fujii, H.; Kawaguchi, S.; Wada, K.; Ikeno, H.; Yagi, S., Systematic Study of Descriptors for Oxygen Evolution Reaction Catalysis in Perovskite Oxides. *J. Phys. Chem. C* **2018,** *122* (49), 27885-27892.

138. Zhou, W.; Sunarso, J., Enhancing Bi-functional Electrocatalytic Activity of Perovskite by Temperature Shock: A Case Study of $LaNiO_{3-\delta}$. *J. Phys. Chem. Lett.* **2013,** *4* (17), 2982-2988.

139. Choi, M.-J.; Kim, T. L.; Kim, J. K.; Lee, T. H.; Lee, S. A.; Kim, C.; Hong, K.; Bark, C. W.; Ko, K.-T.; Jang, H. W., Enhanced Oxygen Evolution

Electrocatalysis in Strained A-Site Cation Deficient $LaNiO_3$ Perovskite Thin Films. *Nano Lett.* **2020,** *20* (11), 8040-8045.

140. Hong, W. T.; Welsch, R. E.; Shao-Horn, Y., Descriptors of Oxygen-Evolution Activity for Oxides: A Statistical Evaluation. *J. Phys. Chem. C* **2016,** *120* (1), 78-86.
141. Millet, P.; Mbemba, N.; Grigoriev, S. A.; Fateev, V. N.; Aukauloo, A.; Etiévant, C., Electrochemical performances of PEM water electrolysis cells and perspectives. *Int. J. Hydrogen Energy* **2011,** *36* (6), 4134-4142.
142. Browne, M. P.; Dodwell, J.; Novotny, F.; Jaśkaniec, S.; Shearing, P. R.; Nicolosi, V.; Brett, D. J. L.; Pumera, M., Oxygen evolution catalysts under proton exchange membrane conditions in a conventional three electrode cell vs. electrolyser device: a comparison study and a 3D-printed electrolyser for academic labs. *J. Mater. Chem. A* **2021**.

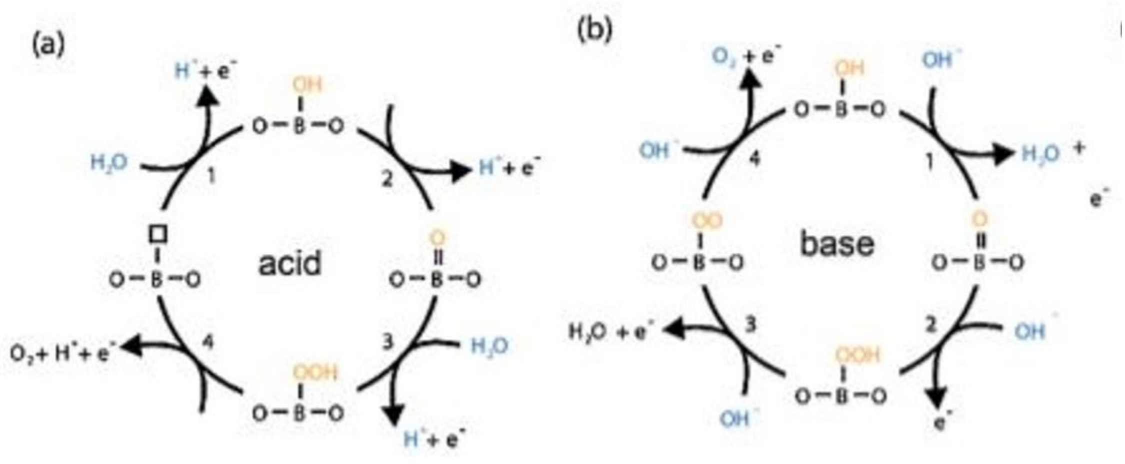

Figure 1.1. Proposed OER mechanism in (a) acid and (b) base[26].

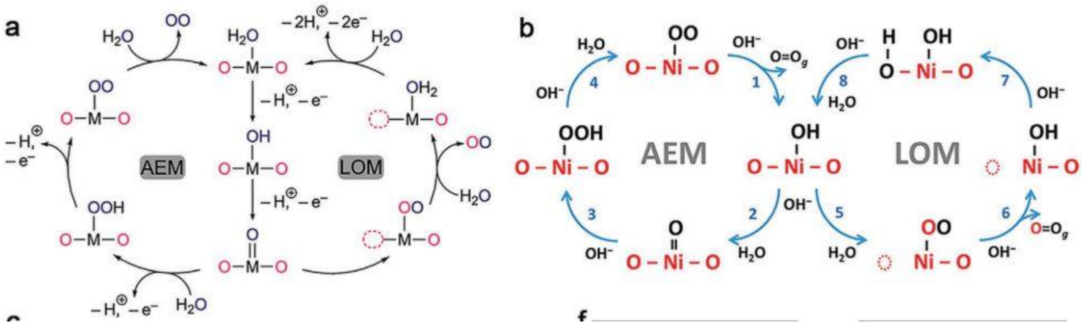

Figure 1.2. Proposed mechanisms for OER in acid (a) and (b) base. The proposed AEM and LOM are displayed[11].

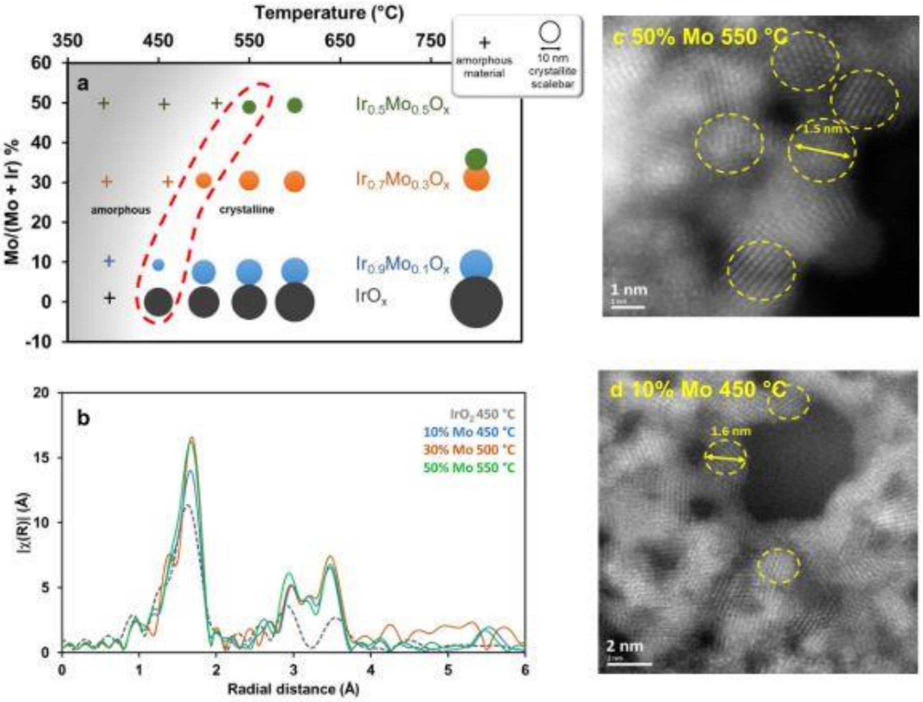

Figure 1.3. Most active materials present similar structural features. (a) Graph summarizing XRD analyses with chemical compositions determined by EDXRF. Amorphous samples are labeled with crosses (+), crystalline samples are marked with plain circles (•), and the circle diameter is proportional to the crystallite size determined by Rietveld analysis. The position of each symbol on the Y-axis corresponds to the Mo content determined by EDXRF analysis. The red-dotted line highlights the most electroactive material for each composition. (b) The superposition of the FT-EXAFS spectra recorded for the most electrochemically active materials for each Mo content, i.e., pure IrO_2 calcined at 450 °C, $Ir_{0.9}Mo_{0.1}O_x$ calcined at 450 °C, $Ir_{0.7}Mo_{0.3}O_x$ calcined at 500 °C and $Ir_{0.5}Mo_{0.5}O_x$ at 550 °C. STEM-HAADF images of the samples prepared with (c) 50% Mo calcined at 550 °C and (d) 10% Mo calcined at 450 °C[55].

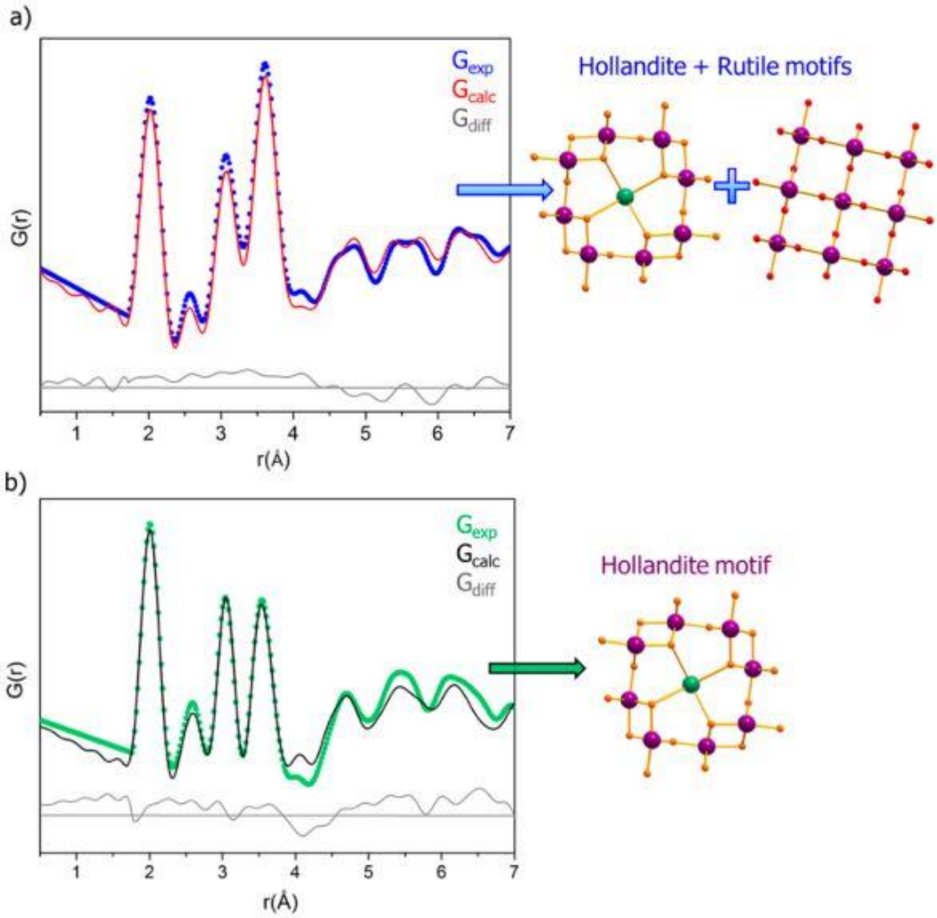

Figure 1.4. ePDF refinement. (a) comparison between the experimental G(r) of IrOx-commercial (blue line) and the calculated G(r) (red line) and (b) comparison between the experimental G(r) of IrO$_x$-FHI (green line) and the calculated G(r) (black line). The differences between G(r) values are shown as a dark grey line[67].

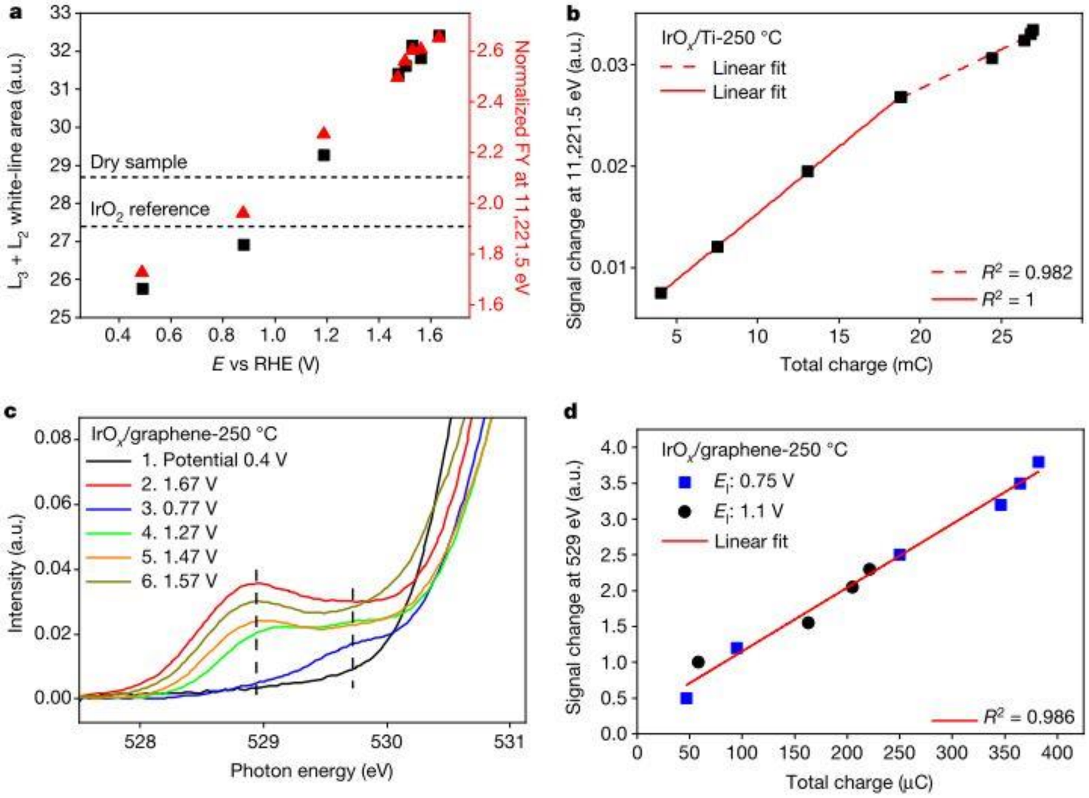

Figure 1.5. Charge storage under steady-state and potentiodynamic conditions. (a) L_3 + L_2 IWL (left) and the normalized fluorescence yield (FY) signal at 11,221.5 eV (right) of steady-state *operando* Ir L-edge XAS of IrO_x/Ti-250 °C versus the potential, together with the dry sample and the reference IrO_2, (b) correlation of the signal change of the Ir L3 edge at 11,221.5 eV versus the total charge for the sample IrO_x/Ti-250 °C, (c) the steady-state *operando* O K-edge XAS of IrO_x/graphene-250 °C at (non-iR-corrected) potentials applied in the order indicated. Dashed lines show the peak position of μ_2-O (528.9 eV) and μ_1-OH (529.7 eV), and (d) the signal change at 529 eV versus the total charge. A reduced catalyst loading resulted in a smaller level of charge than in b[71].

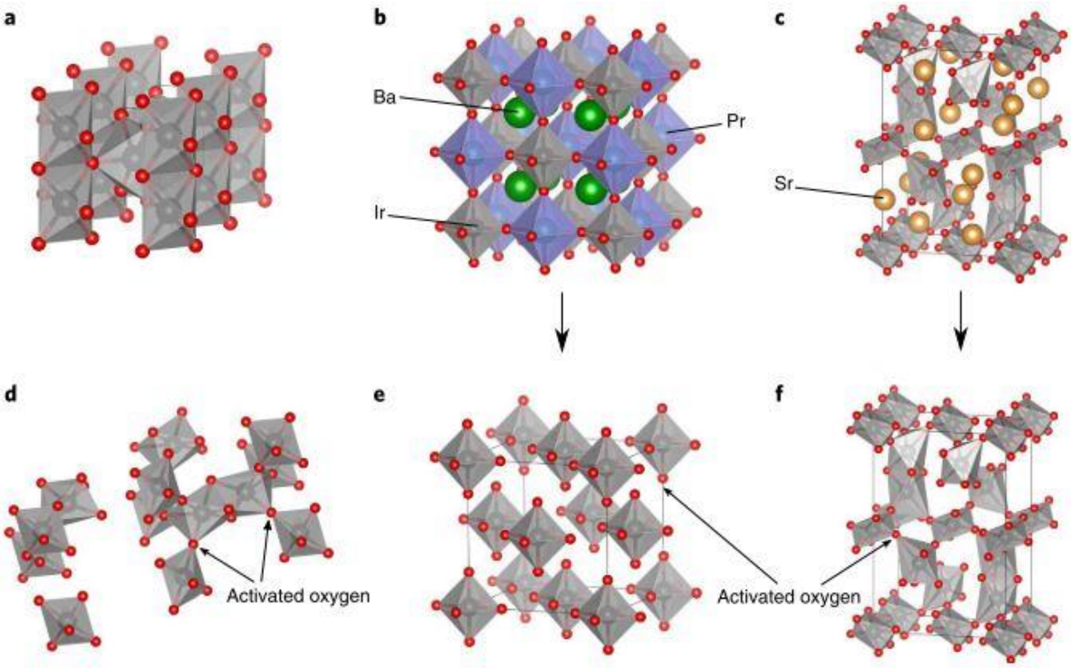

Figure 1.6. Crystal structures of the investigated materials. (a) rutile IrO_2, (b) an example of a B-site-ordered double perovskite (Ba_2PrIrO_6), (c) a single perovskite with alternating cubic and hexagonal layers ($SrIrO_3$), (d) an assumed structure of amorphous iridium oxide, where gaps are filled with intercalated water molecules (not shown), (e) a leached, double perovskite showing isolated IrO_6, which will collapse into an amorphous structure, and (f) leached $SrIrO_3$, resulting in an anatase-like iridium oxide structure[75].

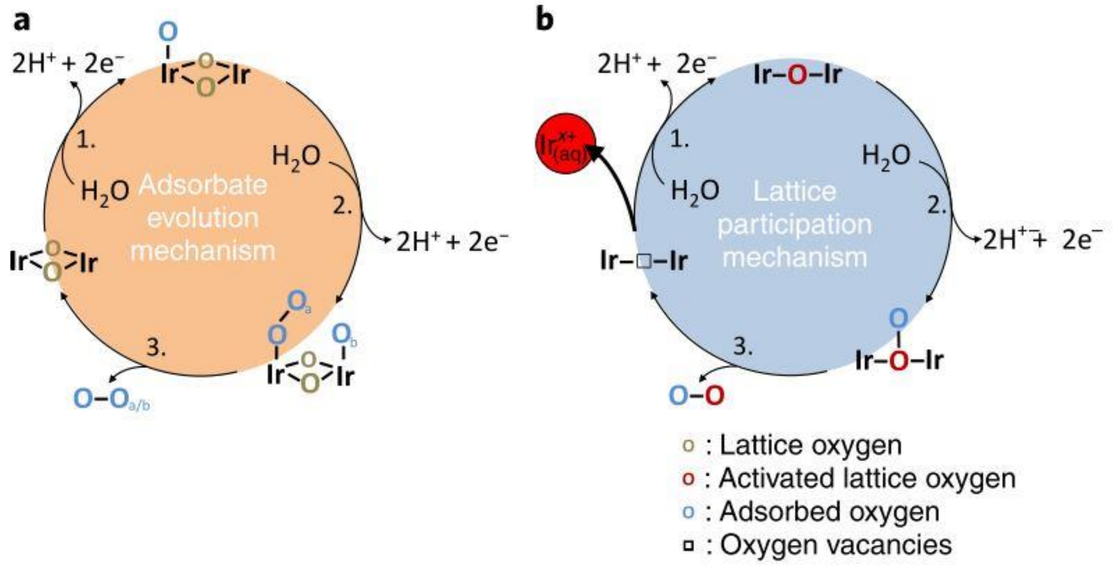

Figure 1.7. Sketch of the simplified OER reaction mechanism with dissolution pathways. (a) classical mechanism for the crystalline IrO_2 without the participation of lattice oxygen. Two possible pathways are presented, single site and double site. (b) the mechanism suggested for amorphous iridium oxide and leached perovskites with the participation of activated oxygen in the reaction forming oxygen vacancies. Weakening the binding of Ir in the structure is considered the main reason for the enhanced dissolution. To complete the cycle, vacancies can be filled again by adsorption of water. The octahedral configuration of Ir is not presented completely, and the nucleophilic attack of water and proton removal are merged into one step for simplicity[75].

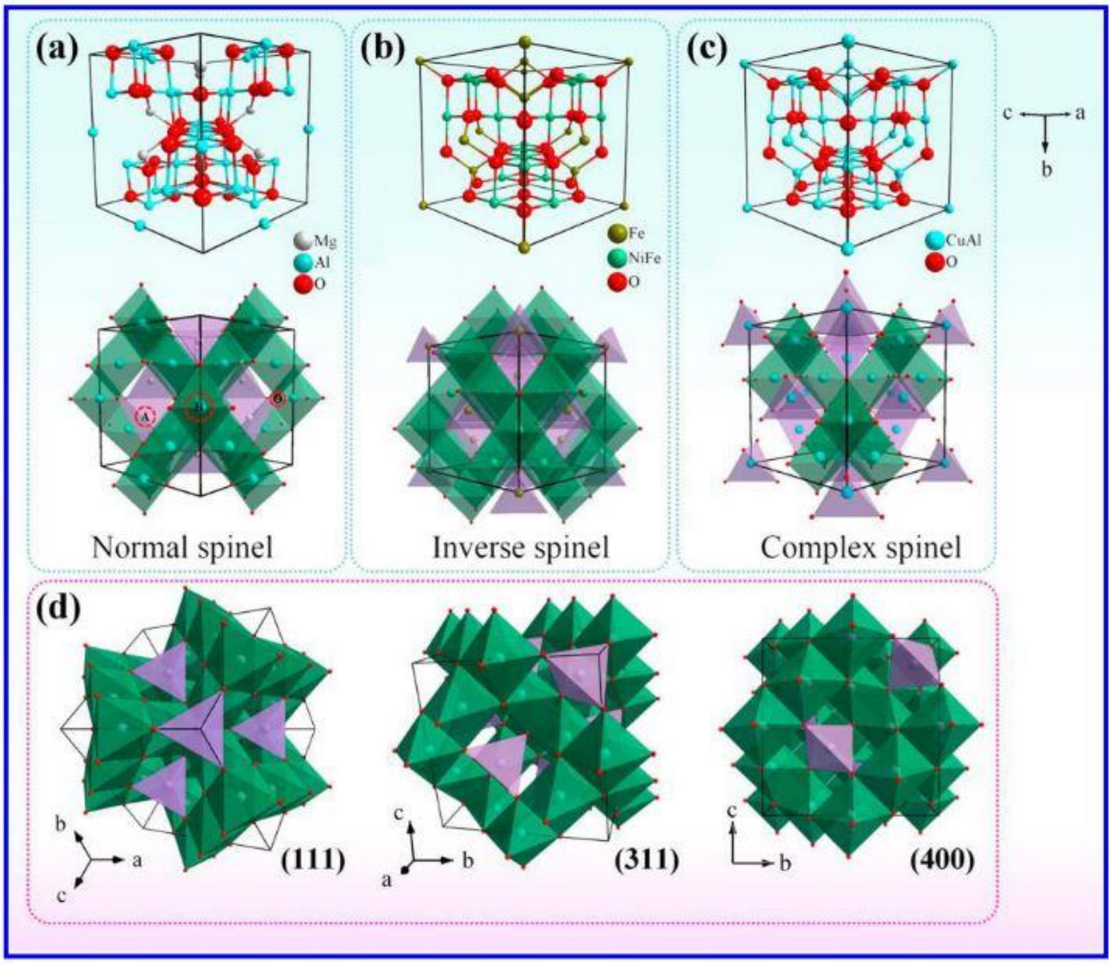

Figure 1.8. Representative structures of (a) a normal spinel ($MgAl_2O_4$), (b) an inverse spinel ($NiFe_2O_4$), and (c) a complex spinel ($CuAl_2O_4$), with different styles and views. The green and purple polyhedra correspond to octahedral and tetrahedral metal occupation sites, respectively. Representative A, B, and O defect sites in spinel AB_2O_4 have been illustrated in panel a; (d) Normal spinel ($MgAl_2O_4$) with (111), (311), and (400) view directions[38].

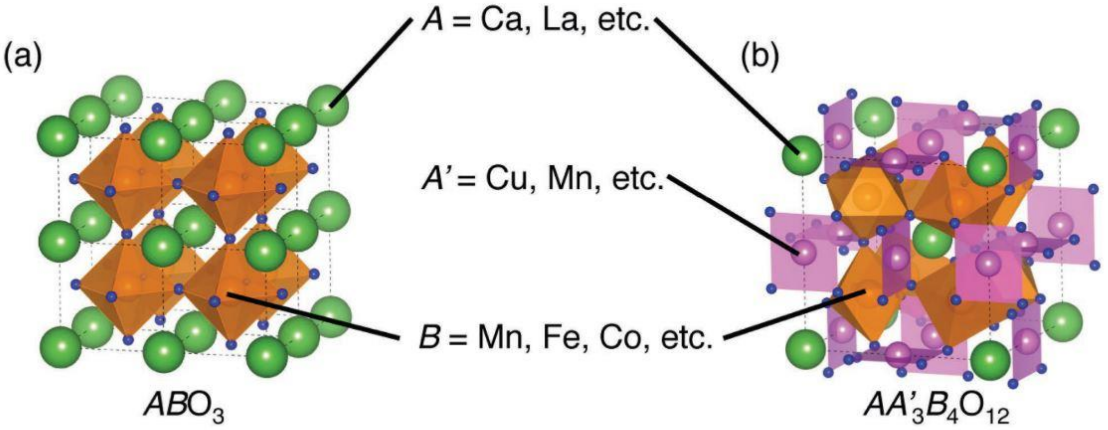

Figure 1.9. Schematics of the crystal structures of (a) simple ABO_3 and (b) quadruple $AA'_3B_4O_{12}$ perovskites. Green, purple, orange, and blue spheres represent A, A', B, and O atoms, respectively. Both perovskites are drawn as cubic structures for simplicity[38].

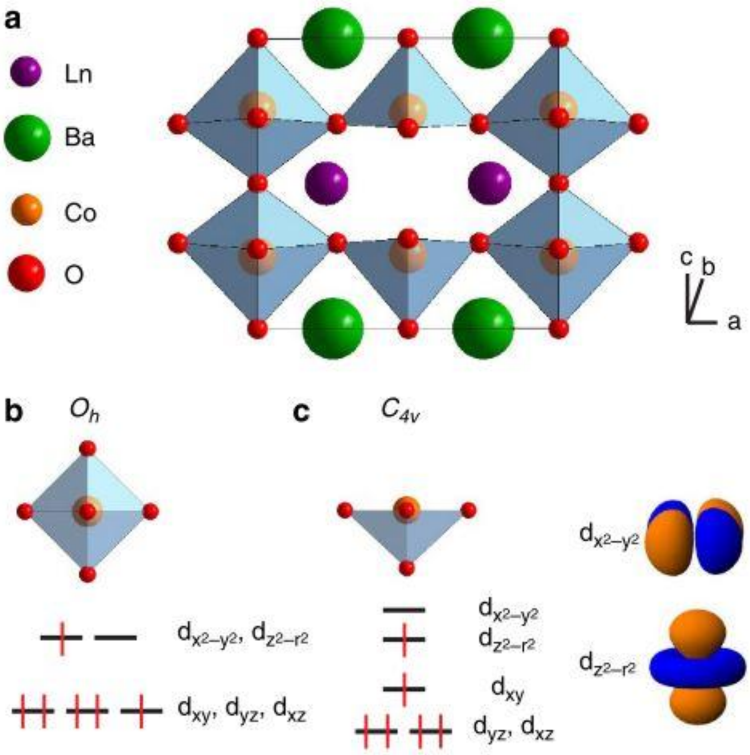

Figure 1.10. Double perovskite crystal structure and cobalt crystal field. (a) a schematic representation of (Ln$_{0.5}$Ba0$_{.5}$)CoO$_{3-\delta}$ double perovskites (LnBaCo$_2$O$_{5+\delta'}$ with $\delta' = 1 - 2\delta$) showing the ordering of Ln and Ba cations and the formation of oxygen deficiency in the LnO$_{1-\delta}$ planes. This ordering is reflected by the doubling of the *c* parameter compared with ideal cubic perovskites, resulting in ap × ap × ap lattice parameters (ap being the lattice parameter of the cubic perovskite indexed in the Pm-3m space group). The structure has (b) octahedral (O$_h$) and (c) square pyramidal (C$_{4v}$) symmetry for Co ions, with distinct crystal-field splitting of d-electron states for the different coordination symmetries[118].

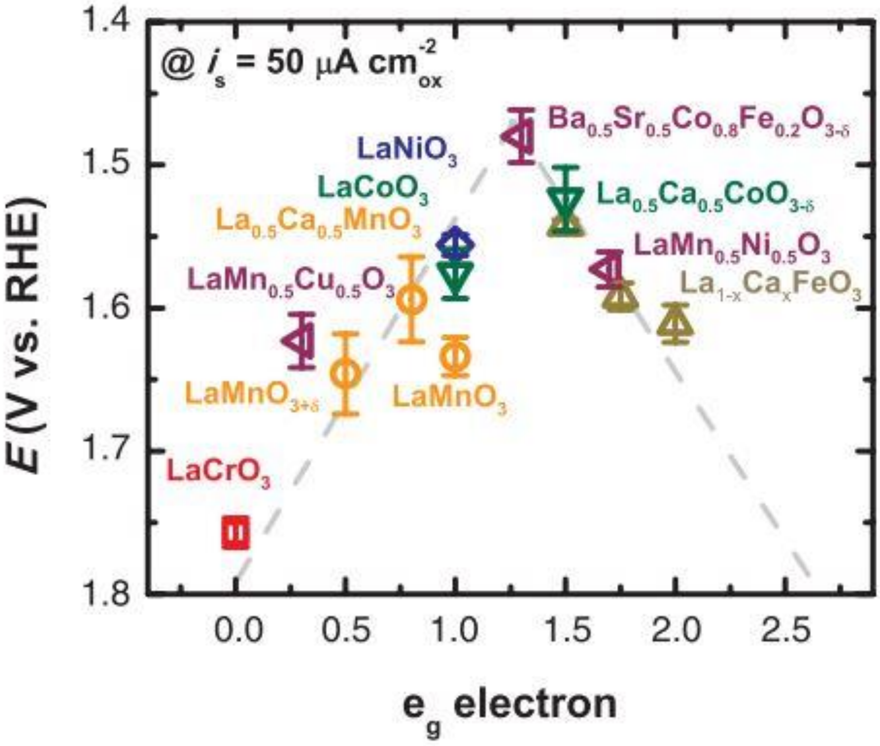

Figure 1.11. The relationship between the OER catalytic activity; defined by the overpotentials at 50 $\mathrm{mAcm}^{-2}{}_{\mathrm{ox}}$ of OER current; and the occupancy of the e_g-symmetry electron of the transition metal (B in ABO_3). Symbols vary with type of B ions (Cr, red; Mn, orange; Fe, beige; Co, green; Ni, blue; mixed compounds, purple), with x = 0, 0.25, and 0.5 for Fe. Error bars represent the standard deviation (SD) of at least three independent measurements. The dashed volcano lines are shown for information purposes only[116].

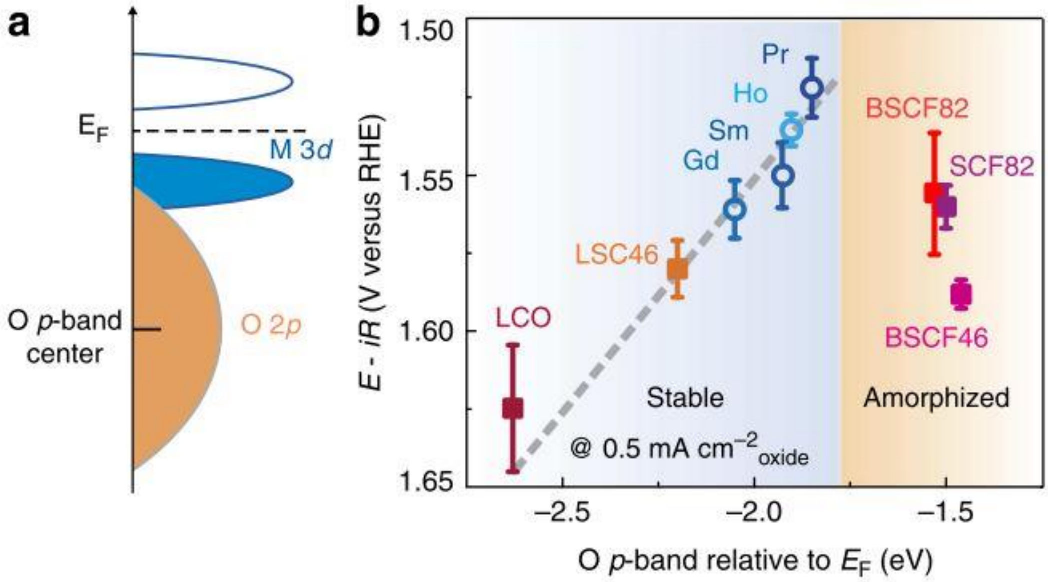

Figure 1.12. Computed oxygen p-band center for oxygen evolution. (a) a schematic representation of the O p-band for transition metal oxides and (b) an evolution of the *iR*-corrected potential at 0.5 mA $cm^{-2}{}_{oxide}$ versus the O p-band center relative to E_F (eV) of $(Ln_{0.5}Ba_{0.5})CoO_{3-\delta}$ with Ln = Pr, Sm, Gd, and Ho, for $LaCoO_3$ (LCO), $La_{0.4}Sr_{0.6}CoO_{3-\delta}$ (LSC46), $Ba_{0.5}Sr_{0.5}Co_{0.8}Fe_{0.2}O_{3-\delta}$ (BSCF82), $Ba_{0.5}Sr_{0.5}Co_{0.4}Fe_{0.6}O_{3-\delta}$ (BSCF46), and $SrCo_{0.8}Fe_{0.2}O_{3-\delta}$ (SCF82), respectively. The O *p*-band center relative to the Fermi level was computed by DFT for the fully oxidized and relaxed structure using the method described in the Methods section. Error bars represent the SD from at least four independent measurements[117].

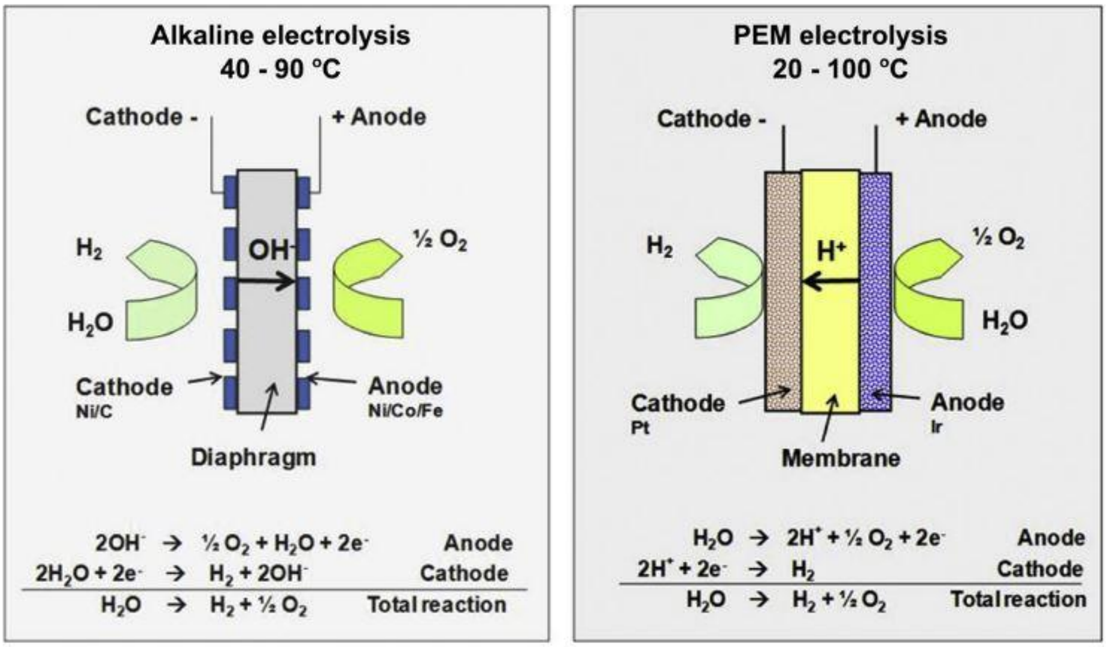

Figure 1.13. Schematic of the operating principle of an alkaline and PEM water electrolysis cell[6].

Chapter 2. Total-reflection Fluorescence X-ray Absorption Spectroscopic Study of the State of the Active Site in Li-doped NiO during Oxygen Evolution Reaction

Understanding the interfacial electronic structure of electrocatalysts is important for elucidating the intrinsic mechanism of the oxygen evolution reaction (OER). In this study, the electronic structural changes of nickel at the electrode/electrolyte interface during the OER of a typical nickel-based electrocatalyst in alkaline water electrolysis was investigated. The flat $Li_xNi_{1-x}O$ thin film catalysts were synthesized by the pulsed laser deposition (PLD) method, and their OER performances and reaction kinetics were measured by electrochemical tests. We innovatively applied *operando* total-reflection fluorescence X-ray absorption spectroscopy (TRF-XAS) to investigate the state of the active site changes during the OER under the applied OER potentials. *Operando* TRF-XAS revealed that a distinct surface oxidation state change of $Li_{0.59}Ni_{0.41}O$, which outperformed NiO in the OER activity, was observed, indicating that high oxidation state of Ni sites was forming. This surface reconstruction resulted in greater number of active sites on the reaction interface, thereby enhancing the OER activity. This study provides a new insight into the surface state changes occurring during the OER and can enhance the design of novel alkaline OER catalysts.

2.1 Introduction

Splitting water to produce hydrogen is generally considered a promising solution to overcome the severe energy crisis. However, it is impeded by the sluggish kinetics of the oxygen evolution reaction (OER)[1-3]. Various types of water electrolysis have been studied till date, among which alkaline water electrolysis is inexpensive and expected to be commercialized on a large scale[4]. Benchmarking catalysts such as Ir- and Ru-based materials have been widely reported for their superior ability to enhance the OER performance[5-8]. Considering the high cost and scarcity of such noble metal catalysts, designing cheaper materials with compatible OER performance is essential. Transition metal (TM = Fe, Co, Ni) oxides are now being widely studied as potential OER catalysts[9] owing to their regulable crystal structure and earth abundance. Some TM oxides have been even reported to outperform noble metal-based catalysts when artfully designed. Among all the TM oxides, Ni-based materials have been found to significantly boost the OER kinetics especially when doped with other metal elements such as Fe[10, 11] and Li[12]. Recently, we have shown that $Li_xNi_{1-x}O$ oxides, in which lithium and nickel ions are cation-mixed, have high oxygen evolution activity and durability[13].The introduction of metal doping has been proposed to modify the active reaction sites or reconstruct the reaction surface areas, thereby improving the catalytic behavior toward OER[10, 14]. However, the mechanism of the activity and durability of the catalyst remains not fully understood. This is because of a lack of information on the electrode/electrolyte interface, which is the active site during the OER reaction.

The active site where the electrochemical reaction occurs in water electrolysis, is the electrode/electrolyte interface, and understanding the interfacial structure of the electrocatalyst is important for obtaining the guidelines for catalyst development. The electronic structure of the electrode at the electrode/electrolyte interface is different when the potential is applied during the OER than when it is not applied. Various *operando* measurement techniques, such as, *operando* X-ray absorption spectroscopy (XAS)[15, 16], *operando* Raman investigation[17], and *operando* X-ray photoelectron spectroscopy (XPS)[18], have been developed to obtain information on the interfacial structure during water electrolysis.

Among all these techniques, XAS has been widely applied to reveal the electronic and local structures of the target materials. Reliable information about several OER catalysts have been provided by *ex situ* and *in situ* XAS analysis[3]. Although normal XAS measurements only investigate the bulk state of the material, the surface state information can be obtained by conducting geometry setups. We applied the XAS-based analysis method to obtain information on the electrode interfaces for various electrochemical devices[19-23]. Total-reflection fluorescence XAS (TRF-XAS)[20, 21] and depth-resolved XAS[22] measurements have been reported on lithium-ion batteries and solid oxide fuel cells to provide surface-sensitive spectra. Especially, TRF-XAS, which integrates the fluorescence yield obtained under total reflection, is a method that can obtain information only near the interface[20].

In this study, we innovatively applied *operando* TRF-XAS to $Li_xNi_{1-x}O$ oxides in alkaline water electrolysis to observe the catalyst surface variations occurring during the OER process and, therefore, to help elucidate the reaction mechanism. $Li_xNi_{1-x}O$ thin films as OER catalysts were synthesized by pulsed laser deposition (PLD) technique to investigate the changes in the active during the OER. Electrochemical tests were conducted to investigate the OER activity. The combination of various techniques used in this study provides direct evidence of the surface state changes occurring during the OER process.

2.2 Experimental

2.2.1 Material Preparation

$Li_xNi_{1-x}O$ (x=0, 0.13, 0.26, 0.51) thin film samples were prepared by the PLD method. Different Li doping levels correspond to the respective $Li_xNi_{1-x}O$ (x= 0, 0.1, 0.3, 0.5) targets used in PLD. The NiO target was synthesized through a series of steps: NiO powder (99.9%, Kojundo Chemical Laboratory Co., LTD.) was first pelletized and pressed by cold isostatic pressing (CIP) followed by calcination at 1000 °C to obtain a dense target pellet with a diameter of 20 mm. The other targets were purchased from Toshima Manufacturing Co., Ltd. (Saitama, Japan) and used directly without further treatment. The substates used in this study for sample characterization, electrochemical tests and X-ray measurements were SiO_2, Au plate and Nb-doped $SrTiO_3$ (Nb-doped STO) respectively. The substrate and target were firstly loaded into the PLD chamber and heated to 600 °C. The atmospheric pressure was then adjusted to 10^{-2} oxygen partial pressure. The distance between the substate and target was maintained at 35 mm. Laser ablation was performed for 1 h after a preliminary 5 min target surface cleaning, at a repetition rate of 10 Hz and laser power of 200 mW. After deposition, the thin film samples were cooled naturally to 25 °C without changing the chamber atmosphere.

2.2.2 Characterization

X-ray diffraction (XRD) of the thin films was performed using an Ultima IV X-ray diffractometer (Rigaku Co., Inc., Tokyo, Japan) with a Cu Kα X-ray source. The thickness of the as-synthesized thin films was measured by optical profilometer (Dektak150, BRUKER). The surface morphology was measured by atomic force microscope (AFM). AFM images were captured using a Dimension ICON AFM system equipped with a Nano Scope V controller (Bruker Co., Inc., Madison, U.S.) in tapping mode. Inductively coupled plasma optical emission spectroscopy (ICP-OES) was conducted at the Industrial Research Center of Shiga Prefecture, Japan, to determine the actual Li concentration in the as-synthesized thin film samples.

2.2.3 Electrochmical Tests

The OER activity tests were performed in a typical three-electrode cell. Each thin film sample was fixed onto a rotating disk electrode (RDE) and used as the working electrode, with Pt wire and a reversible hydrogen electrode (RHE) serving as the counter and reference electrodes, respectively. The cyclic voltammograms (CV) were measured in the range of 1.1 V–1.6 V (vs. RHE) at 5 mV s^{-1} in a N_2 gas-purged 0.1 M KOH solution after the catalyst surface was preliminarily activated by scanning from 1.1 V to 1.6 V at 200 mV s^{-1}. The 0.1 M KOH solution was prepared from deionized water (Milli-Q® ,18 Ohm, Millipore A/S) and high purity KOH (guaranteed reagent, Kanto Chemical Co., Inc) and used without any further purification to avoid the contamination like Fe incorporation.

2.2.4 *Ex situ* and operando Measurement

Ni L-edge and O K-edge XANES were measured at BL-11 at Ritsumeikan SR center, Japan. *Operando* Ni K-edge XAS was measured using TRF-XAS. The thin films were deposited onto the Nb-doped STO substrates and used as the working electrodes. A Kapton film was used to prepare the X-ray window. CV scans were recorded from 0.5 V to 1.6 V (vs. RHE) for 100 cycles to activate the catalyst surface in N_2-saturated 0.1 M KOH solution. Thereafter, the potential was maintained at 0.8, 1.2, 1.4 and 1.5 V (vs. RHE), representing the open circuit potential (OCP), pre-oxidation and active oxygen evolution state, respectively. The *operando* measurements were conducted to investigate the intermediate reaction changes occurring during the OER at different incident angles representing the bulk and surface states. The details of *operando* TR-XAS measurements are explained further in the discussion section. The XAS profiles were analyzed using the Athena software package[25].

To investigate the bulk and surface oxidation states during the OER process, the total reflection *operando* Ni K-edge XANES was measured in the fluorescence mode. Figure 2.1 shows the incident angle dependence of the Ni fluorescence and the calculated critical angle of total reflection(θ_{TR}) was around 0.27º. This critical incident angle was directly observed at approximately 0.25º by using the electrochemical cell with thin film using as the working electrode, Pt wire and RHE serving as the counter and reference electrode (Figure 2.1b). The good agreement between the calculation result and the experimental result indicates that the catalyst surface and bulk modifications during OER process can be captured by using the TR-XAS measurements. Thereby, the X-ray incident angles were set at 1° and 0.25° representing the bulk and surface states, respectively.

2.3 Results and Discussion

2.3.1 Material Characterization

The actual components of the as-synthesized thin films were analyzed by ICP-OES. As shown in Table 2.1 in the Supporting Information, the actual composition of each thin film sample was similar to that of the original target, which confirms that the conditions of PLD were propriate. The samples in this study are hereafter referred according to the ICP results. The XRD patterns of the as-synthesized $Li_xNi_{1-x}O$ thin film materials are shown in Figure 2.2a. The broad hump was attributed to the SiO_2 substrate. The rock salt structure of NiO for all the samples was confirmed by the distinct (111),

(200) and (220) reflection peaks, which is in good agreement with a previously published study[24]. The corresponding lattice constant of each sample as shown in Figure 2.2b was calculated from the XRD results. A linear decrease with increasing Li content was observed, which is consistent with Vegard's law. This lattice constant decrease is attributed to the introduction of Ni^{3+} ions having a smaller ionic radius and the corresponding Ni-O bond shrinkage due to Li doping[25]. Moreover, the surface roughness of the thin film samples was measured using AFM as shown in Figure 2.3. The relatively flat surfaces indicate a uniform distribution of Li-doped NiO onto the substrate surfaces. Table 2.2 shows the film thickness of each sample, varying from 80 nm to 200 nm, conforming the feasibility of the detecting surface and bulk reactions using *operando* TRF-XAS.

2.3.2 Electronic Structure

To reveal the intrinsic electronic structure of the Li-doped NiO, XAS measurements were performed for $Li_{0.51}Ni_{0.49}O$ and NiO. According to the Ni K-edge XANES (Figure 2.4), a shift to high-energy side of $Li_{0.51}Ni_{0.49}O$ was observed, indicating a higher Ni oxidation state as compared to that in the case of NiO. This is further evidenced by the Ni L-edge XANES (Figure 2.5a). The NiO sample displayed typical peaks at 853 eV and 871 eV, indicating Ni L_3 ($2p_{3/2}$) and Ni L_2 ($2p_{1/2}$) edges, respectively[26]. In contrast, the spectra of $Li_{0.51}Ni_{0.49}O$ showed distinct shift toward the high-energy side, suggesting a higher valence state of Ni. Moreover, a satellite peak at approximately 855 eV appeared for $Li_{0.51}Ni_{0.49}O$, which is attributed to the formation of a ligand hole caused by the strong covalency between the Ni 3d and O 2p orbitals[27]. The O K-edge XANES spectra also explains the strong hybridization state between Ni 3d and O 2p orbitals, as shown in Figure 2.5b. The feature at 531 eV for NiO is assigned to the unoccupied Ni 3d e_g hybridized with the O 2p orbitals as reported by several previous studies[28, 29], while a new feature at 527 eV was observed for $Li_{0.51}Ni_{0.49}O$ due to the hole state caused by Li introduction[12].

2.3.3 Catalyst Performance

The *IR*-corrected OER polarization curves are shown in Figure 2.6a. A decrease in the onset potential can be observed with increasing amounts of Li doping, indicating enhanced OER activity. The Tafel slopes were estimated to directly show the kinetics of the OER. As shown in Figure 2.6b, the pure NiO sample showed the Tafel value of 50 mV dec^{-1}, which is consistent with previous research[30]. Meanwhile, the Li-doped samples showed the Tafel values varied from 44 mV dec^{-1} to 48 mV dec^{-1}. The decreasing Tafel slope indicates that the OER reaction kinetics was improved with the Li-doping, thus enhancing the OER performance[31].

2.3.4 Total-reflection *Operando* XANES

Figure 2.7 shows the Ni oxidation state of NiO at different OER potentials. The spectra of catalyst bulk state in Figure 2.7a display no distinct change even at a relatively high potential of 1.5 V (vs. RHE), whereas, the surface state spectra show a slight shift to the high-energy side on increasing the applied potential in Figure 2.7b, indicating that Ni is oxidized to a higher valency at the catalyst surface. The Ni K-edge XANES spectra of $Li_{0.59}Ni_{0.41}O$ are shown in Figure 2.8. The spectra of the bulk state in Figure 2.8a show a negligible shift when the applied potential is increased from 0.8 V (vs. RHE) to 1.5 V (vs. RHE), whereas the spectra display a significant shift to the higher energy side on increasing the applied potential, as shown in Figure 2.8b. The different Ni valence change behavior of these two catalysts correspond well to the catalyst polarization curves as shown in Figure 2.6a, suggesting that $Li_{0.59}Ni_{0.41}O$ outperformed NiO in the OER activity owing to its high oxidation state of surface Ni. As reported by several previous studies, OER catalysts might undergo noticeable surface reconstruction to activate the reaction sites when potential is applied during the OER process[32, 33]. For Ni-based catalysts, a previous study revealed that the electronic structures of the catalyst changed drastically owing to the formation of hydrous structures such as NiOOH and superoxo/peroxo species (e.g., NiOO*) on the catalyst surface[34, 35]. This proposal is also considerably supported by the results obtained in this work. Compared to the bulk state, the significant oxidation state change on the surface of $Li_{0.59}Ni_{0.41}O$ indicated that active surface areas were forming on the Ni sites on applying OER potential. This surface reconstruction resulted in greater number of active sites on the surface and thereby enhancing the OER activity.

2.4 Conclusion

In this study, the electrochemical performance and reaction kinetics of $Li_xNi_{1-x}O$ thin films as OER catalysts synthesized by the PLD method was discussed. To investigate the state of the active site changes occurring during the OER, *operando* TRF-XAS was innovatively measured under the applied OER potentials. According to the results, the significant oxidation state change on the surface of $Li_{0.59}Ni_{0.41}O$ indicated that active surface areas were forming on the Ni sites on applying the OER potential. This surface reconstruction resulted in a great number of active sites on the reaction interface, thereby enhancing the OER activity. The combination of various techniques including *operando* TRF-XAS used in this study provides direct evidence of the surface state modifications occurring during the OER process and can help optimize the design of active OER catalysts by reasonable surface modulation.

Reference

1. Zhang, Y.; Zhu, X.; Zhang, G.; Shi, P.; Wang, A.-L., Rational catalyst design for oxygen evolution under acidic conditions: strategies toward enhanced electrocatalytic performance. *J. Mater. Chem. A* **2021**.
2. Karmakar, A.; Karthick, K.; Sankar, S. S.; Kumaravel, S.; Madhu, R.; Kundu, S., A vast exploration of improvising synthetic strategies for enhancing the OER kinetics of LDH structures: a review. *J. Mater. Chem. A* **2021**, 9 (3), 1314-1352.
3. Jamesh, M.-I.; Harb, M., Tuning the electronic structure of the earth-abundant electrocatalysts for oxygen evolution reaction (OER) to achieve efficient alkaline water splitting – A review. *J. Energy Chem*. **2021**, 56, 299-342.
4. Zhang, N.; Feng, X.; Rao, D.; Deng, X.; Cai, L.; Qiu, B.; Long, R.; Xiong, Y.; Lu, Y.; Chai, Y., Lattice oxygen activation enabled by high-valence metal sites for enhanced water oxidation. *Nat. Commun*. **2020**, 11 (1), 4066.
5. Zhao, Z. L.; Wang, Q.; Huang, X.; Feng, Q.; Gu, S.; Zhang, Z.; Xu, H.; Zeng, L.; Gu, M.; Li, H., Boosting the oxygen evolution reaction using defect-rich ultra-thin ruthenium oxide nanosheets in acidic media. *Ener.g Environ. Sci*. **2020**.
6. Lee, Y.; Suntivich, J.; May, K. J.; Perry, E. E.; Shao-Horn, Y., Synthesis and activities of rutile IrO2 and RuO2 nanoparticles for oxygen evolution in acid and alkaline solutions. *J. Phys. Chem. Lett*. **2012**, 3 (3), 399-404.
7. Jang, H.; Lee, J., Iridium oxide fabrication and application: A review. *J. Energy Chem*. **2020**, 46, 152-172.
8. Willinger, E.; Massué, C.; Schlögl, R.; Willinger, M. G., Identifying key structural features of IrOx water splitting catalysts. *J. Am. Chem. Soc*. **2017**, 139 (34), 12093-12101.

9. Zhang, H.; Maijenburg, A. W.; Li, X.; Schweizer, S. L.; Wehrspohn, R. B., Bifunctional heterostructured transition metal phosphides for efficient electrochemical water splitting. *Adv. Funct. Mater.* **2020**, 30 (34), 2003261.
10. Anantharaj, S.; Kundu, S.; Noda, S., "The Fe Effect": A review unveiling the critical roles of Fe in enhancing OER activity of Ni and Co based catalysts. *Nano. Energy* **2021**, 80, 105514.
11. Mahala, C.; Devi Sharma, M.; Basu, M., Fe-Doped nickel hydroxide/nickel oxyhydroxide function as an efficient catalyst for the oxygen evolution reaction. *ChemElectroChem* **2019**, 6 (13), 3488-3498.
12. Fu, G. L.; Wen, X. J.; Xi, S. B.; Chen, Z. L.; Li, W. W.; Zhang, J. Y.; Tadich, A.; Wu, R. B.; Qi, D. C.; Du, Y. H.; Cheng, J.; Zhang, K. H. L., Tuning the electronic structure of NiO via Li doping for the fast oxygen evolution reaction. *Chem. Mater.* **2019**, 31 (2), 419-428.
13. Ren, Y.; Yamaguchi, R.; Uchiyama, T.; Orikasa, Y.; Watanabe, T.; Yamamoto, K.; Matsunaga, T.; Nishiki, Y.; Mitsushima, S.; Uchimoto, Y., The effect of cation mixing in $LiNiO_2$ toward the oxygen evolution eeaction. *ChemElectroChem* **2021**, 8 (1), 70-76.
14. Peng, Y.; Hajiyani, H.; Pentcheva, R., Influence of Fe and Ni doping on the OER performance at the Co_3O_4(001) surface: insights from DFT+U calculations. *ACS Catal.* **2021**, 11 (9), 5601-5613.
15. Xiao, Z.; Huang, Y.-C.; Dong, C.-L.; Xie, C.; Liu, Z.; Du, S.; Chen, W.; Yan, D.; Tao, L.; Shu, Z.; Zhang, G.; Duan, H.; Wang, Y.; Zou, Y.; Chen, R.; Wang, S., Operando identification of the dDynamic behavior of oxygen vacancy-rich Co3O4 for oxygen evolution reaction. *J. Am. Chem. Soc.* **2020**, 142 (28), 12087-12095.

16. Fabbri, E.; Abbott, D. F.; Nachtegaal, M.; Schmidt, T. J., Operando X-ray absorption spectroscopy: A powerful tool toward water splitting catalyst development. *Curr. Opin. Electrochem.* **2017**, 5 (1), 20-26.
17. Qiu, Z.; Ma, Y.; Edvinsson, T., In operando Raman investigation of Fe doping influence on catalytic NiO intermediates for enhanced overall water splitting. *Nano. Energ*y **2019**, 66, 104118.
18. Favaro, M.; Yang, J.; Nappini, S.; Magnano, E.; Toma, F. M.; Crumlin, E. J.; Yano, J.; Sharp, I. D., Understanding the oxygen evolution reaction mechanism on CoOx using operando ambient-pressure X-ray photoelectron spectroscopy. *J. Am. Chem. Soc*. **2017**, 139 (26), 8960-8970.
19. Gao, X.; Yamamoto, K.; Hirai, T.; Uchiyama, T.; Ohta, N.; Takao, N.; Matsumoto, M.; Imai, H.; Sugawara, S.; Shinohara, K.; Uchimoto, Y., Morphology changes in perfluorosulfonated ionomer from thickness and thermal treatment conditions. *Langmuir* **2020**, 36 (14), 3871-3878.
20. Tsuji, Y.; Sako, S.; Nitta, K.; Yamamoto, K.; Shao-horn, Y.; Uchimoto, Y.; Orikasa, Y., Surface analysis of lanthanum strontium cobalt oxides under cathodic polarization at high temperature through operando total-reflection X-ray absorption and X-ray fluorescence spectroscopy. *Solid State Ionics* **2020**, 357, 115502.
21. Orikasa, Y.; Ina, T.; Yamamoto, K.; Nakao, T.; Mineshige, A.; Amezawa, K.; Kawada, T.; Tanida, H.; Uruga, T.; Uchimoto, Y., Direct bbservation of rate determining step for Nd[2]NiO[4+δ] SOFC cathode reaction by operando electrochemical XAS. *Electrochemistry* **2014**, 82 (10), 897-900.
22. Okumura, T.; Nakatsutsumi, T.; Ina, T.; Orikasa, Y.; Arai, H.; Fukutsuka, T.; Iriyama, Y.; Uruga, T.; Tanida, H.; Uchimoto, Y.; Ogumi, Z., Depth-resolved X-ray absorption spectroscopic study on nanoscale observation of the electrode–solid electrolyte interface for all solid state lithium ion batteries. *J. Mater. Chem.2011*, 21 (27), 10051-10060.

23. Takamatsu, D.; Koyama, Y.; Orikasa, Y.; Mori, S.; Nakatsutsumi, T.; Hirano, T.; Tanida, H.; Arai, H.; Uchimoto, Y.; Ogumi, Z., First in situ observation of the LiCoO2 electrode/electrolyte interface by total-reflection X-ray absorption spectroscopy. *Angew. Chem. Int. Ed.* **2012**, 51 (46), 11597-11601.
24. Zhang, J. Y.; Li, W. W.; Hoye, R. L. Z.; MacManus-Driscoll, J. L.; Budde, M.; Bierwagen, O.; Wang, L.; Du, Y.; Wahila, M. J.; Piper, L. F. J.; Lee, T. L.; Edwards, H. J.; Dhanak, V. R.; Zhang, K. H. L., Electronic and transport properties of Li-doped NiO epitaxial thin films. *J. Mater. Chem. C* **2018**, 6 (15), 4326-4326.
25. Goodenough, J. B.; Wickham, D. G.; Croft, W. J., Some magnetic and crystallographic properties of the system $Li^{+}_{x}Ni^{++}_{1-2x}ni^{+++}_{x}O$. *J. Phys. Chem. Solids* **1958**, 5 (1), 107-116.
26. van Elp, J.; Searle, B. G.; Sawatzky, G. A.; Sacchi, M., Ligand hole induced symmetry mixing of d8 states in $Li_xNi_{1-x}O$, as observed in Ni 2p x-ray absorption spectroscopy. *Solid State Commun.* **1991**, 80 (1), 67-71.
27. Kuiper, P.; Kruizinga, G.; Ghijsen, J.; Sawatzky, G. A.; Verweij, H., Character of holes in LixNi1-xO and their magnetic behavior. *Phys. Rev. Lett* **1989**, 62 (2), 221-224.
28. Zhang, K. H. L.; Wu, R.; Tang, F.; Li, W.; Oropeza, F. E.; Qiao, L.; Lazarov, V. K.; Du, Y.; Payne, D. J.; MacManus-Driscoll, J. L.; Blamire, M. G., Electronic structure and band alignment at the NiO and $SrTiO_3$ p–n heterojunctions. *ACS Appl. Mater. Interfaces* **2017**, 9 (31), 26549-26555.
29. Uchimoto, Y.; Sawada, H.; Yao, T., Changes in electronic structure by Li ion deintercalation in $LiNiO_2$ from nickel L-edge and O K-edge XANES. *J. Power Sources* **2001**, 97-98, 326-327.
30. Iqbal, M. Z.; Kriek, R. J., Silver/Nickel Oxide (Ag/NiO) Nanocomposites Produced Via a Citrate Sol-Gel Route as Electrocatalyst for the Oxygen Evolution Reaction (OER) in Alkaline Medium. *Electrocatalysis* **201**8, 9 (3), 279-286.

31. Shinagawa, T.; Garcia-Esparza, A. T.; Takanabe, K., Insight on Tafel slopes from a microkinetic analysis of aqueous electrocatalysis for energy conversion. *Sci. Rep.* **2015**, 5 (1), 13801.

32. Steimecke, M.; Seiffarth, G.; Schneemann, C.; Oehler, F.; Förster, S.; Bron, M., Higher-valent nickel oxides with improved oxygen evolution activity and stability in alkaline media prepared by high-temperature treatment of $Ni(OH)_2$. *ACS Catal.* **2020**, 10 (6), 3595-3603.

33. Klaus, S.; Cai, Y.; Louie, M. W.; Trotochaud, L.; Bell, A. T., Effects of Fe electrolyte impurities on $Ni(OH)_2$/NiOOH structure and oxygen evolution activity. *J. Phys. Chem. C* **2015**, 119 (13), 7243-7254.

34. Zhao, X.; Liu, X.; Huang, B.; Wang, P.; Pei, Y., Hydroxyl group modification improves the electrocatalytic ORR and OER activity of graphene supported single and bi-metal atomic catalysts (Ni, Co, and Fe). *J. Mater. Chem. A* **2019**, 7 (42), 24583-24593.

35. Louie, M. W.; Bell, A. T., An investigation of thin-film Ni–Fe oxide catalysts for the electrochemical evolution of oxygen. *J. Am. Chem. Soc.* **2013**, 135 (33), 12329-12337.

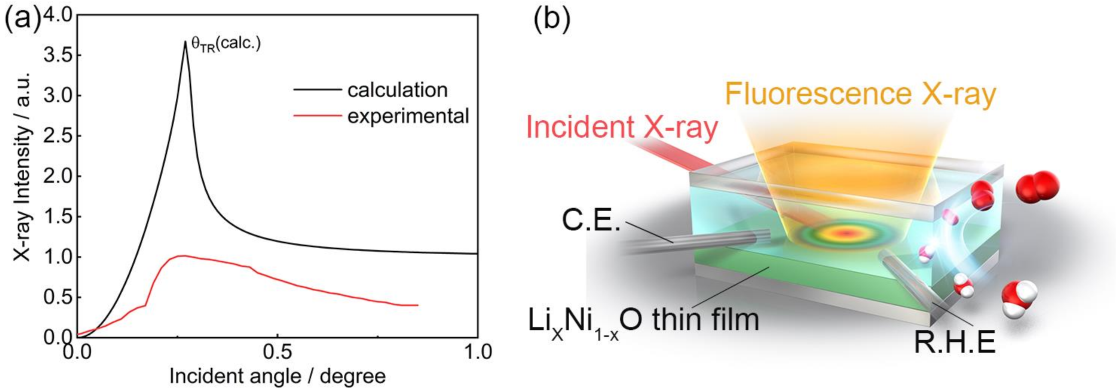

Figure 2.1. (a) Incident X-ray angle dependence of the Ni Fluorescence for the calculation result and experimental result; (b) the electrochemical cell used for operando TR-XAS measurements.

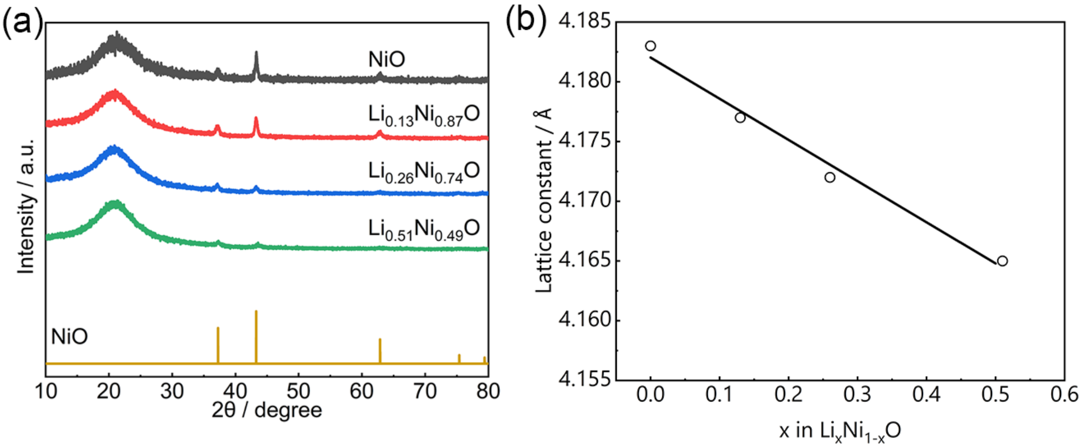

Figure 2.2. (a) XRD patterns of the $Li_xNi_{1-x}O$ thin films and (b) lattice constants of as-synthesized samples

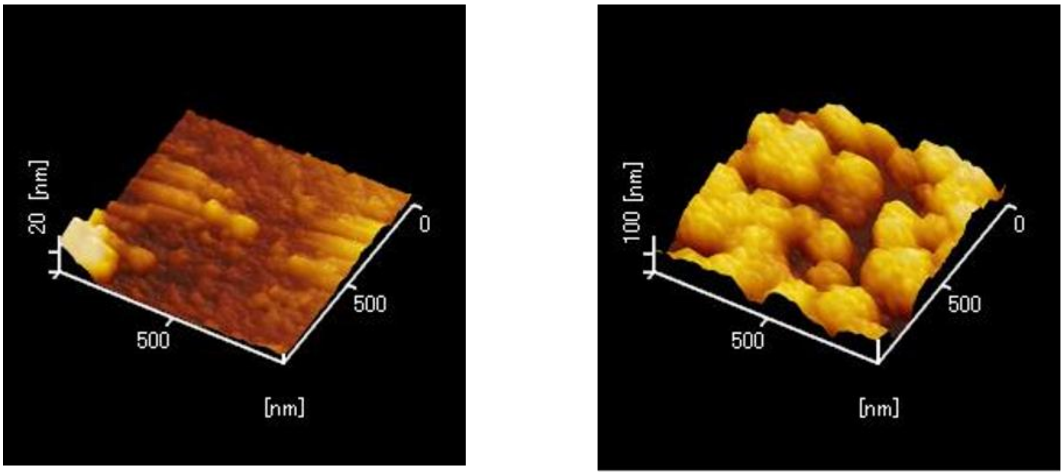

$Li_{0.13}Ni_{0.87}O$ $Li_{0.51}Ni_{0.49}O$

Figure 2.3. AFM image of (a) $Li_{0.13}Ni_{0.87}O$ and (b) $Li_{0.51}Ni_{0.49}O$ films. AFM measurements revealed surface RMS roughness of ~10 nm and ~50 nm, respectively.

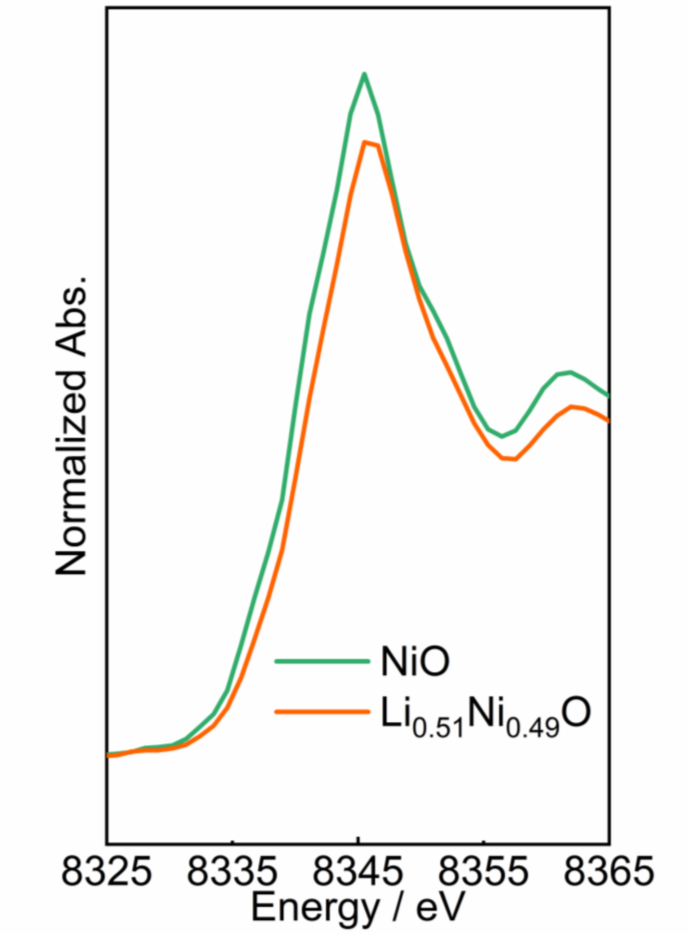

Figure 2.4. *Ex situ* Ni K-edge XANES of bulk NiO and $Li_{0.51}Ni_{0.49}O$

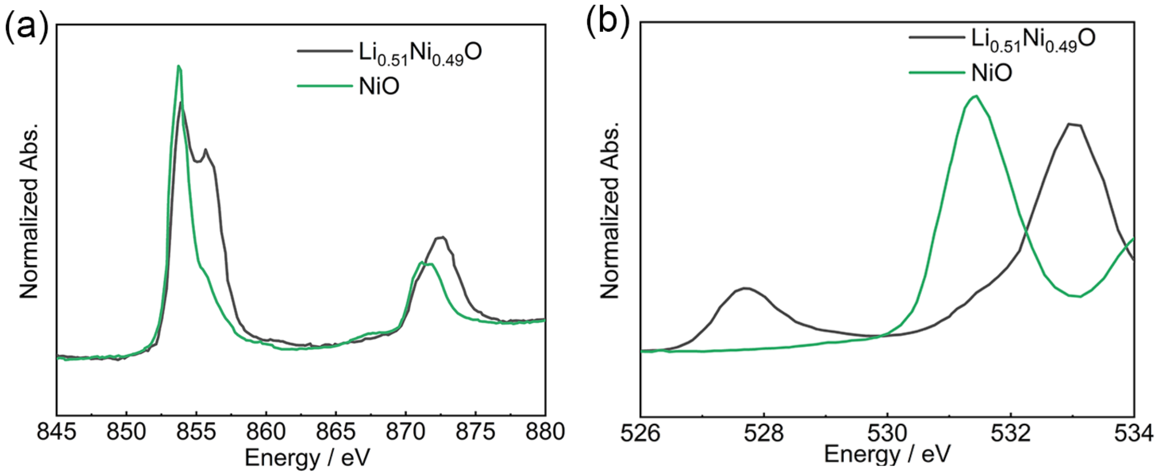

Figure 2.5. Electronic structures of NiO and $Li_{0.51}Ni_{0.49}O$: (a) Ni L-edge XANES and (b) O K-edge XANES

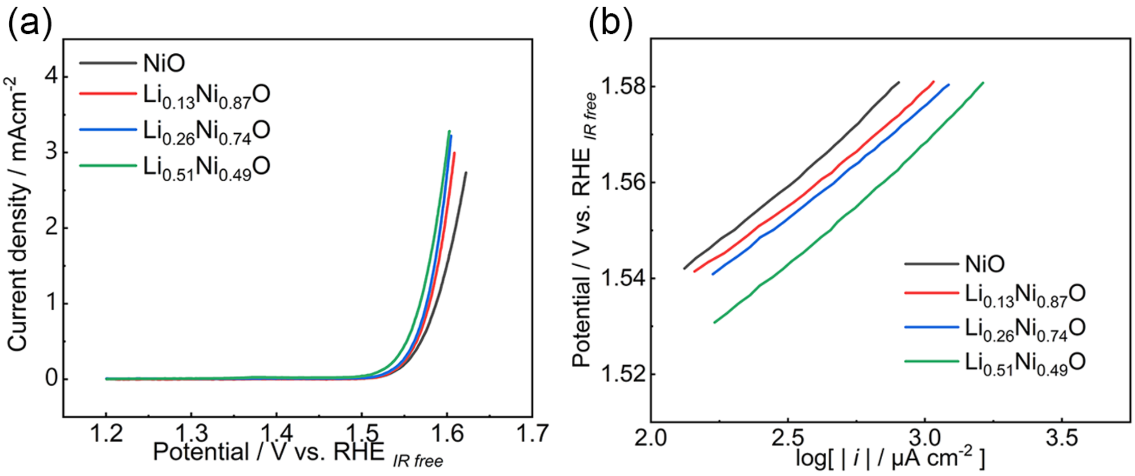

Figure 2.6. (a) IR-corrected linear sweep voltammetry curves of $Li_xNi_{1-x}O$ in 0.1 M KOH and (b) Tafel plots

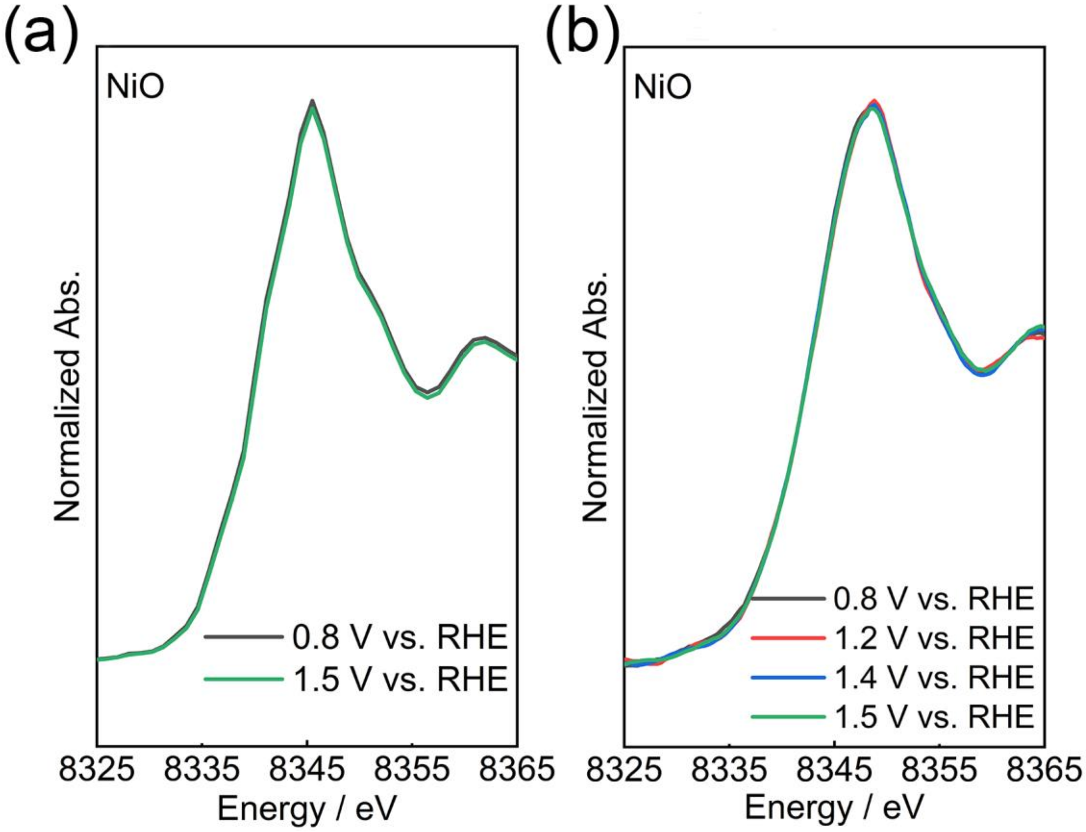

Figure 2.7. *Operando* Ni K-edge XANES of NiO (a) bulk and (b) surface states

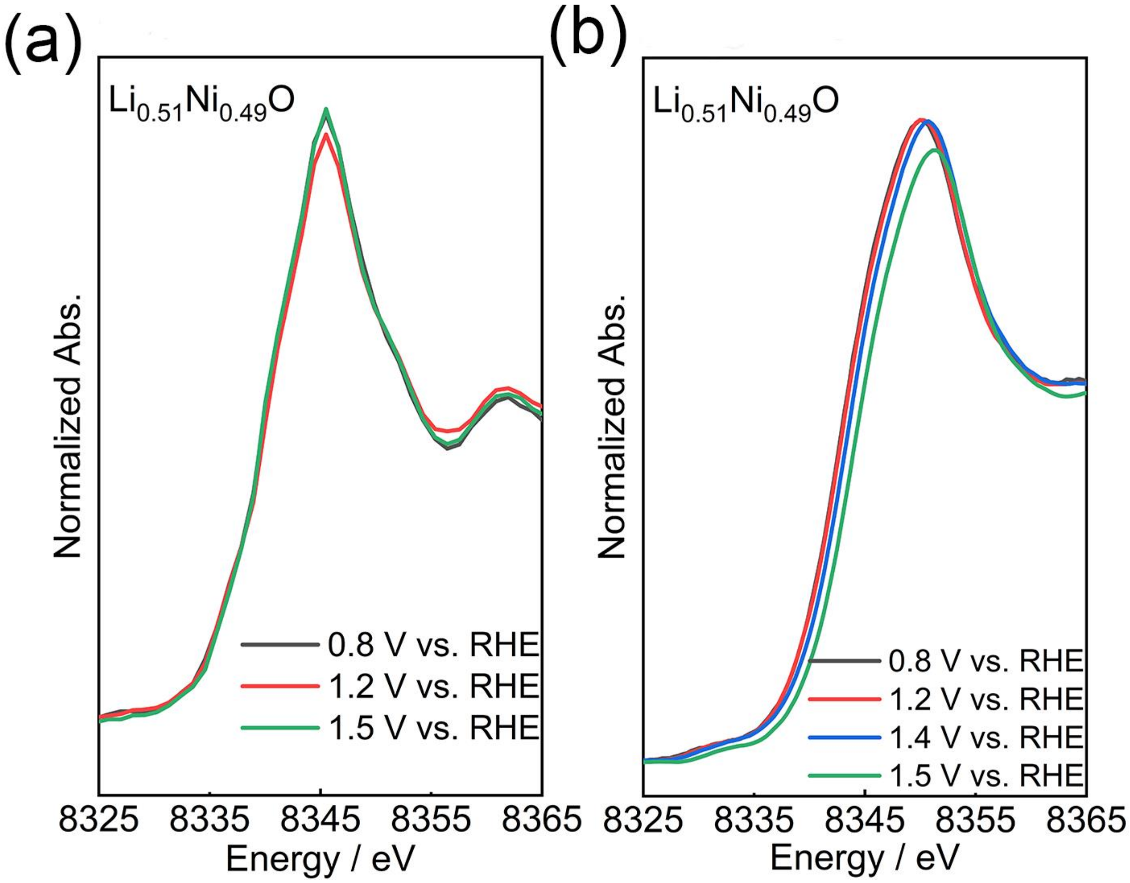

Figure 2.8. Operando Ni K-edge XANES of $Li_{0.59}Ni_{0.41}O$(a) bulk and (b) surface states

Table 2.1. The target composition and the concentration analysis result of the as-synthesized thin films from ICP-OES

Target composition	ICP-OES composition
NiO	NiO
$Li_{0.10}Ni_{0.90}O$	$Li_{0.13}Ni_{0.87}O$
$Li_{0.30}Ni_{0.70}O$	$Li_{0.26}Ni_{0.74}O$
$Li_{0.50}Ni_{0.50}O$	$Li_{0.51}Ni_{0.49}O$

Table 2.2. The film thickness of the as-synthesized thin film samples

Target composition	Thin film thickness / nm
NiO	80
$Li_{0.13}Ni_{0.87}O$	100
$Li_{0.26}Ni_{0.74}O$	120
$Li_{0.51}Ni_{0.49}O$	130

Chapter 3. The State of the Active Site in $La_{1-x}Sr_xCoO_{3-\delta}$ under Oxygen Evolution Reaction Investigated by Total-reflection Fluorescence X-ray Absorption Spectroscopy

Recent developments in hydrogen energy devices have furthered the research on sustainable hydrogen production methods. Among those, the water splitting process has been considered a promising hydrogen production method, particularly, in alkaline media. The lack of information on the reaction active sites under the conditions of the oxygen evolution reaction (OER) hinders establishing guidelines for catalyst development. In the case of powder catalysts, many *operando* techniques also measure bulk information, therefore, extracting information on the reaction active sites is challenging. Accordingly, film electrodes were used in this study and the electrochemical performance and reaction kinetics of perovskite-type $La_{1-x}Sr_xCoO_{3-\delta}$ films as OER catalysts synthesized by pulsed laser deposition were investigated. By combining *ex situ* X-ray absorption spectroscopy (XAS) and *operando* total-reflection fluorescence X-ray absorption spectroscopy (TRF-XAS), we succeeded in observing a significant oxidation state change on the surface of $La_{0.6}Sr_{0.4}CoO_{3-\delta}$, which indicated that the active surface sites were formed upon applying the OER potential. This surface reconstruction resulted in numerous active sites on the reaction interface, thereby enhancing the OER activity. This study provides definitive evidence for the surface reconstruction of OER catalysts, which enhance the fundamental understanding of OER catalyst behaviors, and can inspire the design of active OER catalysts by suitable surface modulation.

3.1 Introduction

The development of renewable energy storage technology is envisioned to replace the conventional fossil fuels to impede global warming and to meet the growing demand for energy sources. Among many proposed solutions, renewable source-derived water electrolysis is considered a promising mass production tool for generating O_2 and H_2 for the storage of chemicals as fuels[1-3]. However, the oxygen evolution reaction (OER) requires a high overpotential to promote the reaction because of the complex four-electron transfer[4, 5]. At present, noble metal-based oxides such as IrO_2, RuO_2, and their mixed oxides are reported to have high catalytic activities toward OER[6-9]; however, their least abundance on the earth, high cost, and stability issues during operation[10, 11] prevent water electrolysis from further development. Therefore, it is important to develop efficient OER electrocatalysts comprising earth-abundant elements to circumvent the issues related to energy resources.

Utilizing alkaline electrolytes is a feasible solution to use earth-abundant 3*d* transition metal oxides as electrocatalysts because of their structural and chemical stability. As catalysts for alkaline water electrolysis, perovskite-type oxides such as $La_{1-x}Sr_xCoO_{3-\delta}$[12, 13] have been reported to show high OER activity. Recently, it has been reported that Fe-doped Ni and Co oxides exhibit superior electrochemical performance under rational design[14-17]. However, the electrode/electrolyte interface reaction mechanism, which is necessary to understand the origin of the excellent catalytic performance, has not been fully clarified. In this study, we focus on the typical $La_{1-x}Sr_xCoO_{3-\delta}$ perovskite oxides. Perovskite-type oxides with alkaline or rare-earth cations at the A site and 3*d* transition metal cations at the B site have attracted attention as efficient electrocatalysts for OER in alkaline media ($4OH^- \rightarrow O_2 + 2H_2O + 4e^-$)[18, 19]. The physicochemical properties can be tuned by partial substitution at the A -and B-sites under structural requirements known as the Goldschmidt tolerance factor t[20]. Extensive studies of perovskite-type oxides have been performed through experimental[21, 22] and computational[23, 24] approaches to discover the OER descriptors to design highly active and robust catalysts. Suntivich et al. observed that the occupancy of e_g electrons of 3d transition metal (B-site) cations is correlated with OER activities and the cation with e_g = 1.2 exhibited the highest OER performance[25]. According to this mechanism, a high OER activity can be obtained by optimizing the binding strength between the reaction intermediates and B-site cations. Recently, there has been increasing research interest on the covalency of B–O bond[26], O 2p band center[18], oxygen vacancies[27, 28] and active sites of lattice oxygen[29, 30]; these studies have considered other descriptors for OER. Therefore, most studies on perovskites for OER have focused on identifying the descriptors of the activity based on bulk electronic and structural properties. Recently, amorphization and dissolution of Ba^{2+} / Sr^{2+} at the A site on the surface of $Ba_{0.5}Sr_{0.5}Co_{0.8}Fe_{0.2}O_{3-\delta}$ during the OER induced a change in the Co ion arrangement from corner sharing to edge sharing octahedra, which could be responsible for its high activity[31]. These results suggest that the OER cannot always be explained by bulk electronic configurations. In addition, the structure of the interface under OER progress is different from that of the bulk structure, in many systems[32-34]. Therefore, investigating the electronic states on the electrode surface under the application of the OER potential is essential for understanding the OER activity.

As the contribution of the catalyst for the OER is restricted to the near-surface region, surface-sensitive *in situ*/*operando* measurements are required to discern the behavior of the catalyst. Recently, the formation of μ-OO peroxide (Co−OO−Co) in

Co_3O_4 was identified on the onset potential for OER by *in situ* Raman spectroscopy[35]. Tung et al. investigated the formation of CoOOH on Co_3O_4-CoO core-shell single-crystal nanocubes by *in situ* grazing-angle X-ray diffraction[36]. The electrochemical transformation of these cobalt oxides to enable OER activity was also investigated by *operando* ambient pressure X-ray photoelectron spectroscopy[37]. Moreover, various advanced techniques were applied in recent catalytic studies, i.e., isotope labeling technique[16, 17], *in situ* inductively coupled plasma–mass spectrometry[38] and so on, to provide direct insights into element dissolution, surface reconstruction and active site tracing, which significantly deepened the understanding towards OER catalysts. In a recent work of Markovic's group, the formation of active Co hydr(oxy)oxide layer driven by A-site dissolution and oxygen vacancy formation was confirmed in Sr-doped $LaCoO_3$[38]. This active CoO_xH_y layer could promote the stability against Co dissolution and significantly improve the activity-stability factor, shedding light on disclosing the reaction mechanism of perovskite catalyst. The information between electrode and electrolyte interface can be obtained by XAS using a film electrode[39-41]. Total-reflection fluorescence XAS (TRF-XAS)[39, 41] and depth-resolved XAS[42] measurements of lithium-ion batteries and solid oxide fuel cells have been recorded to obtain surface-sensitive spectra. In particular, TRF-XAS, which integrates the fluorescence yield obtained under total reflection, investigates near electrode–electrolyte interfaces in *operando* conditions. Our group observed that the valence state of Mn in $La_{0.67}Sr_{0.33}MnO_3$ film surface was lowered under oxygen reduction reaction (ORR) potential using *operando* TRF-XAS[43]. This result suggests that the ORR catalytic activity of $La_{0.67}Sr_{0.33}MnO_3$ was affected by the oxygen vacancies on the surface layer. However, to the best of our knowledge, this *operando* TRF-XAS method is limited to ORR applications[43] and has never been applied to OER catalysts.

Herein, we investigated $La_{1-x}Sr_xCoO_{3-\delta}$films ($x$ = 0.0–0.4) as OER electrocatalysts in alkaline media. Although many studies have investigated the electrochemical performance, electronic structure, and reaction mechanism of the Sr-doped perovskite-type $LaCoO_3$ as an OER catalyst[13, 44, 45], the reported OER activity varies. This might be because the catalytic activity of the OER depends on the morphology, particle size and surface area of the material. In this study, we report the preparation of thin comprising active materials by pulsed laser deposition (PLD) to explore the origin of the catalytic activity. In addition, the reaction mechanism is discussed in conjunction with the results of XAS. Further, with *operando* TRF-XAS, the initial valence and spin states of cobalt and oxygen in $La_{1-x}Sr_xCoO_{3-\delta}$ were investigated by *ex situ* soft XAS coupled with *operando* TRF-XAS. The combination of various techniques used in this study provides direct evidence of changes in the surface-state of Co ions during the OER process.

3.2 Experimental

3.2.1 Material Preparation

$La_{1-x}Sr_xCoO_{3-\delta}$ (x=0.0, 0.2, 0.3, 0.4) film samples were prepared by PLD method. The corresponding targets were synthesized via solid-phase synthesis. La_2O_3 (high purity chemical, 99.99 %), $Sr(NO_3)_2$ (Wako Pure Chemical, 98.0 %), and Co_3O_4 (high purity chemical, 99.9 %) were weighed in stoichiometric proportions and mixed in a mortar. The mixtures were pressed into 20 φ pellets and subsequently calcined at 800 °C for 12 h under atmospheric conditions. The as-obtained pellets were ground, pelletized, and calcined again at 1200 °C for 12 h to obtain dense target pellets. The substate used in this study for film deposition was 0.5 wt.% Nb doped (001) oriented $SrTiO_3$ (Nb-doped STO; NSTO) single crystal with a resistivity of approximately 3×10^{-3} Ω cm (Shinkosha, 99.98 %). The films were deposited at 700 °C under oxygen partial pressure of 1.0 Pa. The distance between the substrate and the target was maintained at 40 mm. The deposition time was maintained for 15 min at a repetition rate of 10 Hz and a laser power of 200 mW. After deposition, the film samples were cooled naturally to 25 °C without changing the chamber atmosphere.

3.2.2 Characterization

X-ray diffraction (XRD) analysis of the films was performed using an Ultima IV X-ray diffractometer (Rigaku Co., Inc., Tokyo, Japan) with a Cu Kα X-ray source. The thicknesses of the as-synthesized films were measured using a surface profilometer (Dektak150, BRUKER). Surface morphology was measured by atomic force microscopy (AFM). The AFM images were captured using a Dimension ICON AFM system equipped with a Nano Scope V controller (Bruker Co., Inc., Madison, USA) in tapping mode. To characterize the thickness and morphology of the film, transmission electron microscopy (TEM) measurements were performed at 200 keV (JEM-2200FS, JEOL Ltd.).

3.2.3 Electrochmical Tests

OER activity tests were performed using a typical three-electrode cell. Each film sample was fixed onto a gold rotating disk electrode (RDE, Hokudo Denko) and used as the working electrode (Figure 3.1), with a Pt mesh and a reversible hydrogen electrode (RHE) as counter and reference electrodes, respectively. The same electrolyte solution was used in the reference compartment and 5 % H_2/N_2 balance was supplied continually to the reference electrode compartment during all electrochemical tests. A potential compensation of 38.4 mV was applied according the Nernst equation considering the H_2 partial pressure[46]. The cyclic voltammograms (CV) were measured in the range of 1.1–1.6 V (vs. RHE) at 10 mV s^{-1} in O_2 gas-purged 0.1 M KOH solution after the catalyst surface was preliminarily activated by scanning in the range of 1.1–1.6 V at 200 mV s^{-1}. The 0.1 M KOH solution was prepared from deionized water (Milli-Q®,18 Ohm, Millipore A/S) and KOH (guaranteed reagent, Kanto Chemical Co., Inc.) and was used without further purification. The current density to evaluate the catalytic performance was normalized based on the geometric surface areas of films (0.385 cm^2). To compensate the ohmic impedance, the electrochemical impedance spectroscopy (EIS) was measured for each sample at open circuit voltage and the as obtained values were used to correct the OER activities.

3.2.4 *Ex situ* and *operando* Measurement

Operando Co K-edge XAS was measured at beamline 37XU at SPring-8, Japan. The schematic of the cell used for the XAS measurements is shown in Figure 3.2(a). Figure 3.1(b) shows the incident angle dependence of Co fluorescence, and the calculated critical angle of total reflection (θ_{TR}) was approximately 0.395°. The agreement between the calculation and experimental results indicates that the catalyst surface and bulk modifications during the OER process can be captured by the TRF-XAS measurements. Therefore, the X-ray incident angles were set at 0.26° and 2.26°, representing the bulk and surface states, respectively.

An Au rod, an RHE, and O_2 saturated 0.1 M KOH were used as the counter electrode, the reference electrode, the electrolyte, respectively. The $La_{1-x}Sr_xCoO_{3-\delta}$film electrode was attached to a Ti base with carbon tape as the working electrode. To investigate the structural changes during OER, XAS measurements were carried out with potentials at 0.8, 1.0 and 1.4 V (vs. RHE) at different incident angles. During the XAS measurement, the sample was placed in close proximity to the Kapton film X-ray window to eliminate the scattering of the solution. All the measurements were carried out at room temperature. The k-value (Å-1) was recorded to 14 for *ex situ* and *operando* samples.

Ex situ O K-edge X-ray absorption near edge structure (XANES) spectra were collected at the Ritsumeikan SR center (BL11). XAS profiles were analyzed using the Athena software package[47]. For O K-edge XAS spectra, pre-edge background subtraction and post-edge normalization were performed using average intensities of three subsequent data points closest to 523 eV and 570 eV for pre- and posted region, respectively.

3.3 Results and Discussion

3.3.1 Material Characterization

The XRD patterns of the films, fabricated by PLD are shown in Figure 3.3(a). Diffraction peaks from $La_{1-x}Sr_xCoO_{3-\delta}$ were observed at a higher angle than those of the Nb-doped $SrTiO_3$ substrate (NSTO). No peaks could be regarded as impurities. The difference in the lattice constant between the substrate and the generated film and the large half-width of the diffraction peak of the film suggest that the film is not an epitaxial but a polycrystalline film with a distorted structure. TEM images in Figure 3.3(b) indicated the film had a thickness of approximately 100 nm, which is suitable for further characterization of the surface and bulk states. Further, Co K-edge XANES and extended X-ray absorption fine structure (EXAFS) results suggested the successful synthesis of $La_{1-x}Sr_xCoO_3$ perovskite-type oxides. The AFM results of $La_{1-x}Sr_xCoO_{3-\delta}$films with $x =$

0.0, 0.2, and 0.4 are shown in Figures 3.3(c) and Figure 3.4. The root mean square roughness of the surfaces was measured to be 0.46, 1.01, and 2.02 nm, respectively, confirming the fabrication of films with high nanoscale smoothness, which is appropriate for the measurement of TRF-XAS. Moreover, to investigate the atomic composition concentration of the as-synthesized samples, XPS survey scan were conducted. As shown in Figure 3.5 (a) and Table 3.1, La, Co, Sr and O were identified and the metal contents determined from XPS were in good agreement with the stoichiometric values.

3.3.2 Electronic Structure

XPS measurements were conducted to investigate the surface state of the as-synthesized films. As shown in Figure 3.5, with the increasing of Sr doping level, the Sr 3d peak intensity correspondingly increased. the binding energies of O 1s and Sr 3d shifted to lower energy values (Figure 3.5(c) and (d)), which was attributed to the transition from semiconducting to metallic character due to Sr doping[12]. Meanwhile, the Co $2p_{3/2}$ peak shifted to higher binding energy values (Figure 3.5(b)), indicating the higher oxidation state of Co. Figure 3.6(a) and 3.6(b) show the XANES spectra and EXAFS spectra of the $La_{1-x}Sr_xCoO_{3-\delta}$films. The XANES pre-edge features appearing at approximately 7710 eV are attributed to the Co 3*d*–O 2*p* hybridization states (e_g and t_{2g} states)[48]. The intensity of this pre-edge increases with the Sr doping level, suggesting the formation of a hole in the Co 3*d*-O 2*p* hybridized orbital[48]. Simultaneously, a shift in the main edge of XANES to higher energy along owing to Sr doping was observed. The Co oxidation states were determined using the known metal Co oxidation vs. edge position relationship of reference compounds. As shown in Figure 3.7, the oxidation state of Co increased with the Sr doping level, in good agreement of XPS Co 2p core level results

(Figure 3.5). The EXAFS oscillation and its Fourier-transformed spectra (Figure 3.6(c)), were similar to those reported previously for perovskite oxides[49]. The peak observed at approximately 1.5 Å corresponds to Co-O bonds in perovskite oxides. The change in intensity of the peaks at approximately 3–4 Å originates from the contributions of Co–Co, Co–La, and Co–Sr bonds. These Co K-edge XANES pre-edge, main-edge, and EXAFS features are typical features of perovskite structure[50]. Therefore, the $La_{1-x}Sr_xCoO_{3-\delta}$ perovskite-type oxides were successfully synthesized. Further, as the EXAFS spectra contain structural information, such as the near-neighbor atomic distance and the coordination number, they were further analyzed through FEFF fitting. As mentioned, the second EXAFS peak contains many scattering paths that are too complicated to identify. However, the first peak corresponds only to the Co–O bond; therefore, reliable information can be obtained through first-shell fitting. As shown in Figure 3.8 and Table 3.2, the Co–O bond distance was in a similar range for all samples, indicating a similar state of cobalt valence[49]. To compensate for the charge deficit introduced by Sr^{2+} substitution, the Sr-doped samples probably have different degrees of oxygen vacancies[19,51]. This was further verified by the fitting results where the average value of the coordination number decreased with an increase in Sr doping (Table 3.2).

To discern the effect of Sr doping on the number of e_g electrons, Co L-edge XAS and O K-edge XAS were investigated and the results are shown in Figure 3.9. In the Co L_{III}-edge, a shoulder peak appeared when Sr was doped. Abbate investigated the L-edge XAS of $LaCoO_{3-\delta}$ and reported that shoulder peaks were observed when Co was in a high spin state[52]. Therefore, in this study, the Co L_{III}-edge spectra indicated that the spin state of Co changed from a low-spin state to a high-spin state owing to Sr doping. Figure 3.6(d) shows the O K-edge XAS spectra of Sr-doped $LaCoO_{3-\delta}$. According to the literature[53, 54], the features in the energy range of 526–533 eV were predominantly attributed to transitions of the O 1*s* to Co 3*d*–O 2*p* hybridized orbital. The contributions from La 5d and Sr 4*d* appeared at approximately 535 eV; in addition, the O 1*s* to Co 4*s*, and 4*p* states are also involved in the O K-edge spectra above 540 eV. In the region of 526–533 eV, only one peak at approximately 528.8 eV was observed for x = 0.0 sample, while a new peak at ca. 527.6 eV appeared for Sr-doped $LaCoO_{3-\delta}$ samples and its peak intensity increased with Sr-doping level, which is in good agreement with recent work of Shen et. al.[12]. As demonstrated through Co K-edge XAS and Co L-edge XAS measurements, Co oxidation states increased with the Sr doping level, leading to the Co spin state changing from low spin state in $LaCoO_{3-\delta}$ ($e_g^0\, t_{2g}^6$) to high-spin configuration ($e_g^2\, t_{2g}^4$)[55] due to the additional transition being allowed to partially empty the t_{2g} states. Therefore, the new peak in O K-edge XAS of Sr-doped samples was attributed to the hole state in the t_{2g} orbitals. According to the research of Shen et. al., this hole state enhanced the orbital overlap and resulted in the stronger Co 3d-O 2p hybridization., thus enhancing the OER through promoting the deprotonation step during the OER process[12].

3.3.3 Catalyst Performance

The results of the evaluation of OER activity are shown in Figure 3.10(a). The substrate NSTO showed inert activity toward OER, making it suitable as the substrate for OER evaluation of the film deposited samples. The OER activities of all samples were corrected through ohmic resistance measured by EIS (Figure 3.11 (a), Table 3.3), and the catalytic performance with and without iR-compensation was displayed in Figure S3.11(b). The onset current for the OER shifted to a lower potential by an increase in the Sr doping level. This indicates that the OER activity was enhanced by increasing the Sr doping. These results are in good agreement with those reported by other studies[56, 13]. Figure 3.10(b) and Table 3.4 show the Tafel plots and the corresponding Tafel slopes. The Tafel slopes for $La_{1-x}Sr_xCoO_{3-\delta}$ samples were ~ 60 mV/dec, suggesting that Sr doping did not change the rate determining step. In the study by Bockris and Matsumoto, the Tafel slope for $La_{1-x}Sr_xCoO_{3-\delta}$ was also 60 mV/dec[57, 58]. From this result, Bockris stated that the following equation is the rate-limiting step.

$$\text{Co-OH} + \text{OH}^- \rightarrow \text{Co}\bullet\bullet\bullet\text{H}_2\text{O}_2 + \text{e}^- \qquad (1)$$

Bockris also stated that the binding energy of the B-site cation to the hydroxide ion is weak and that the e_g electrons of the $3d$ transition metal have a large effect on the binding energy of the hydroxide ion[44]. With the *OH adsorption being the rate determining step, the OER activity promoted by Sr doping might be attributed to the enhanced adsorption of *OH.

Catalytic stability measurements were conducted by 30 cycles of CV from 1.0 V to 1.7 V vs. RHE at 10 mV / s in 0.1 M KOH electrolyte, according to previous Shen et. al.'s research[12]. As shown in Figure 3.12 (a)–(c), the CV shapes of all the samples showed obvious changes at the first 5 cycles, especially for x = 0.4 sample, which might indicate the surface reconstruction to form active sites. Moreover, the current at 1.63 V vs. RHE was extracted at the anodic scan of CV cycles, as shown in Figure 3.12 (d). All the samples showed slight activity decay after 30 CV cycles. It is worth noticing that for x = 0.4 sample, the OER current significantly increased at the first 5 cycles and showed negligible changes at the subsequent cycles. To investigate the surface state before and after electrolysis, focused ion beam (FIB) was used to cut the thin film for TEM observation. The cross-section area for x = 0.4 thin film was observed, as shown in Figure 3.13. Compared with the pristine sample, the post-electrolysis sample displayed an amorphous layer, indicating the surface constructions after electrolysis.

To further examine the component dissolution and electronic structures after electrolysis, XPS measurements were performed for pristine and post-electrolysis samples. As shown in Figure 3.14, compared with the pristine samples, the Sr 3d peak intensity decreased obviously, indicating the Sr dissolution after electrolysis (Table 3.5), as also mentioned in several previous research[38, 59, 60]. For post-catalysis samples, Co 2p XPS showed negligible changes, which might be due to the identical Co 2p peaks of Co hydr(oxy)oxides formed during electrolysis, as confirmed by the recent work of Markovic's group[38]. The decrease of peak intensity of Sr 3d spectra could be attributed to the Sr depletion after electrolysis. Moreover, for x = 0.4 sample, the O 1s core level XPS spectra displayed significant differences (Figure 3.14(c)). The intensity of the peak at approximately 528.2 eV, which is generally attributed to lattice oxygen, decreased significantly relative to the surface OH peak at ca. 531.2 eV. Lopes et. al. demonstrated in their previous research that the participation of lattice oxygen resulted in the formation of oxygen vacancies, thus promoting the A-site Sr dissolution and the active Co hydr(oxy)oxides formation, finally enhancing the OER activities[38]. Combining our characterization of pristine and post-electrolysis samples, it is safe to conclude that our results also provide evidence of the Sr leaching and active amorphous layer formation.

3.3.4 Total-reflection *Operando* XANES

TRF-XAS was measured to directly observe the catalytic behaviors during OER for $La_{1-x}Sr_xCoO_{3-\delta}$ samples for x = 0.0 and x = 0.4. The comparison of Co K-edge XANES spectra of the bulk and surface states (electrode/electrolyte interface) of both catalysts under open circuit potential (OCP) are shown in Figure 3.15. The enlarged figure shows that the absorption edge energy (E_0) of $La_{1-x}Sr_xCoO_{3-\delta}$ samples in the bulk state shifts to the lower energy side for the sample in the surface state, indicating the reduction of Co. Furthermore, this energy change was significant for the x = 0.4 sample. This reduction of Co at the interface between electrode and electrolyte was due to the charge compensation at the defected surface as observed in a previous study by our group[40]. The results of the Co K-edge XAS of the surface and the bulk states of $LaCoO_{3-\delta}$ under applied potential are shown in Figure 3.16(a). The E_0 value of $LaCoO_{3-\delta}$ did not change with the increasing potential, indicating that the oxidation state of Co did not change. Figure 3.16(b) shows the surface and bulk Co K-edge XAS results for $La_{0.6}Sr_{0.4}CoO_{3-\delta}$. At 1.4 V, where the OER started to occur on the surface, the E_0 value shifted to the high-energy side, suggesting the higher oxidation of Co. Furthermore, the *operando* EXAFS and the corresponding FEFF fitting results are shown in Figure 3.17–3.19 and Table 3.6 and 3.7. The average coordination number of $LaCoO_{3-\delta}$ marginally decreased at 1.4 V vs. RHE. Contrarily, the average coordination number of $La_{0.6}Sr_{0.4}CoO_{3-\delta}$ showed significant changes in the surface state compared to the bulk state. This indicates that the valence of Co in $La_{0.6}Sr_{0.4}CoO_{3-\delta}$ increased under OER conditions, the concentration of oxygen vacancies formed by Sr doping decreased accordingly, and the surface of $La_{0.6}Sr_{0.4}CoO_{3-\delta}$ underwent more noticeable reaction activities than the bulk.

The E_0 values of $LaCoO_{3-\delta}$ and $La_{0.6}Sr_{0.4}CoO_{3-\delta}$ are plotted against the applied potential in Figure 3.20. Considering $LaCoO_{3-\delta}$, there is almost no change with the potential; however, in $La_{0.6}Sr_{0.4}CoO_{3-\delta}$, E_0 shifts to the higher energy side from 0.8 to 1.4 V vs. RHE, particularly, on the surface. For perovskite catalysts, a previous study revealed that the electronic structures of the catalyst changed drastically owing to surface reconstruction[61] because the catalytic activity for the OER correlated with the oxygen vacancy concentration[13]. Our *operando* XAS results indicated that in $La_{0.6}Sr_{0.4}CoO_{3-\delta}$, the non-stoichiometric oxygen content of the surface layer reaches the stoichiometric composition as the potential increases. A previously reported analysis of the reaction pathway using the density functional theory on [001] BO_2 terminated surfaces showed that under the operating electrode potential of the OER, OH^- tends to electrochemically fill the O vacancies on the surface of Sr-doped $LaCoO_{3-\delta}$, and the stoichiometry of the surface layer is similar to that of the bulk stoichiometric ABO_3[13]. This proposition is also supported by the results obtained in this study. Compared to the bulk state of $La_{0.6}Sr_{0.4}CoO_{3-\delta}$, significant changes in the oxidation state on the surface of $La_{0.6}Sr_{0.4}CoO_{3-\delta}$ indicated that active surface sites formed when the OER potential was applied. This surface reconstruction resulted in a large number of active sites on the surface, thereby enhancing the OER activity.

3.3.5 Discussions of Reaction Mechanism

Combining the data obtained in this work, the reaction mechanism of $La_{1-x}Sr_xCoO_{3-\delta}$ is further discussed. In the work of Stevens et. al., an electrolyte permeable film was electrochemically deposited and the different incorporation states of Fe site were discussed[14]. They identified Fe incorporation at the edge/defect sites and concluded that the exceptional activity of Ni-Fe activity is more related to the local active-site environment, i.e., coordinatively unsaturated corner and edge sites, than the “bulk” electronic environments. In the recent work of Strasser’s group, the lattice OER mechanism, where lattice oxygen atoms at the catalyst surface were involved in the O-O bond formation, was verified through the advanced application of isotope labelling-enhanced mass spectrometric[62]. Moysiadou et. al. proposed that the OER mechanism of

CoOOH involves the combination of two lattice oxygen atoms to form the CoO_2 intermediate, and the release of dioxygen from the CoO_2 intermediate is the rate-determining step[63]. However, an early work of Roy et. al. found that no lattice oxygen was involved in the oxygen evolution in $NiFeO_xH_y$ through isotope labelling and operando mass spectrometry studies[15]. They concluded that the active sites were attributed to the ~3 atomic layer redox-active near-surface region of the nanoparticles. The recent results described above have made a significant contribution to the understanding of the OER mechanism, providing important insights into the structure changes of the OER reaction field at the electrode/electrolyte interface. However, the OER mechanism is still under controversial arguments, and it is hoped that further elucidation of the OER reaction mechanism can be achieved by adding information on the reaction field at the *operando* to the studies described above. In this study, we clarified that the *OH adsorption was the rate-determining step, which was further evidenced by the enhanced *OH peak in the post-electrolysis XPS and surface reconstruction detected by *operando* TRF-XAS. The *operando* TRF-XAS method used in this study could detect the differences of electronic structure changes, therefore would inspire the development of advanced techniques in the future OER catalyst research. However, it should be noted that although the *operando* TRF-XAS method we used is surface sensitive, it also contains bulk information due to its relatively deep detection depth. We clarify that the surface state detected in this study represented not all the active sites, but the outer shell of nanoparticles, since the out shell of the nanoparticles was consisted of both coordinatively saturated and unsaturated sites as widely proved by above-mentioned previous works.

3.4 Conclusion

The electrochemical performance and the reaction kinetics of perovskite-type $La_{1-x}Sr_xCoO_{3-\delta}$ thin films as OER catalysts synthesized by the PLD method are discussed in this study. The combination of *ex situ* XAS and *operando* TRF-XAS was applied to investigate the active sites during the OER process. Based on the obtained results, $La_{0.6}Sr_{0.4}CoO_{3-\delta}$ showed a significant oxidation state change on the surface, indicating that active surface sites were formed upon applying the OER potential. This surface reconstruction resulted in numerous active sites on the reaction interface, thereby enhancing the OER activity. The direct observation of intermediates occurring during OER process is challenging; however, this study provided definitive evidence for the surface reconstruction of the catalysts by combining various techniques including *operando* TRF-XAS. The methodology and conclusions of this study can provide a new platform for optimizing the design of active OER catalysts by appropriate surface modulation, i.e., introducing OER active element (i.e., Fe) into the lattice to form the active surface incorporation environment.

Reference

1. Dincer, I.; Acar, C., Review and evaluation of hydrogen production methods for better sustainability. *Int. J.Hydrog. Energy* **2015,** *40* (34), 11094-11111.
2. Rashid, M. M.; Al Mesfer, M. K.; Naseem, H.; Danish, M., Hydrogen production by water electrolysis: a review of alkaline water electrolysis, PEM water electrolysis and high temperature water electrolysis. *Int. J. Eng. Adv. Technol.* **2015,** *4* (3), 2249-8958.
3. Carmo, M.; Fritz, D. L.; Merge, J.; Stolten, D., A comprehensive review on PEM water electrolysis. *Int. J.Hydrog. Energy* **2013,** *38* (12), 4901-4934.

4. Song, J.; Wei, C.; Huang, Z.-F.; Liu, C.; Zeng, L.; Wang, X.; Xu, Z. J., A review on fundamentals for designing oxygen evolution electrocatalysts. *Chem. Soc. Rev.* **2020,** *49* (7), 2196-2214.
5. Karmakar, A.; Karthick, K.; Sankar, S. S.; Kumaravel, S.; Madhu, R.; Kundu, S., A vast exploration of improvising synthetic strategies for enhancing the OER kinetics of LDH structures: a review. *J. Mater. Chem. A* **2021,** *9* (3), 1314-1352.
6. Yu, H.; Danilovic, N.; Wang, Y.; Willis, W.; Poozhikunnath, A.; Bonville, L.; Capuano, C.; Ayers, K.; Maric, R., Nano-size IrOx catalyst of high activity and stability in PEM water electrolyzer with ultra-low iridium loading. *Appl. Catal. B: Environ.* **2018,** *239*, 133-146.
7. Elmaalouf, M.; Odziomek, M.; Duran, S.; Gayrard, M.; Bahri, M.; Tard, C.; Zitolo, A.; Lassalle-Kaiser, B.; Piquemal, J.-Y.; Ersen, O.; Boissière, C.; Sanchez, C.; Giraud, M.; Faustini, M.; Peron, J., The origin of the high electrochemical activity of pseudo-amorphous iridium oxides. *Nat. Commun.* **2021,** 12 (1), 1-10.
8. Cherevko, S.; Geiger, S.; Kasian, O.; Kulyk, N.; Grote, J. P.; Savan, A.; Shrestha, B. R.; Merzlikin, S.; Breitbach, B.; Ludwig, A.; Mayrhofer, K. J. J., Oxygen and hydrogen evolution reactions on Ru, RuO_2, Ir, and IrO_2 thin film electrodes in acidic and alkaline electrolytes: A comparative study on activity and stability. *Catal. Today* **2016,** *262*, 170-180.
9. Zhao, Z. L.; Wang, Q.; Huang, X.; Feng, Q.; Gu, S.; Zhang, Z.; Xu, H.; Zeng, L.; Gu, M.; Li, H., Boosting the oxygen evolution reaction using defect-rich ultra-thin ruthenium oxide nanosheets in acidic media. *Energ. Environ. Sci.* **2020**. 13, 5143-5151

10. Carmo, M.; Fritz, D. L.; Mergel, J.; Stolten, D., A comprehensive review on PEM water electrolysis. *Int. J.Hydrog. Energy* **2013,** *38* (12), 4901-4934.
11. Jang, H.; Lee, J., Iridium oxide fabrication and application: A review. *J. Energy Chem.* **2020,** *46*, 152-172.
12. Shen, Z.; Qu, M.; Shi, J.; Oropeza, F. E.; de la Peña O'Shea, V. A.; Gorni, G.; Tian, C. M.; Hofmann, J. P.; Cheng, J.; Li, J.; Zhang, K. H. L., Correlating the electronic structure of perovskite $La_{1-x}Sr_xCoO_3$ with activity for the oxygen evolution reaction: The critical role of Co 3d hole state. *J. Energy Chem*. **2022**, 65, 637-645.
13. Mefford, J. T.; Rong, X.; Abakumov, A. M.; Hardin, W. G.; Dai, S.; Kolpak, A. M.; Johnston, K. P.; Stevenson, K. J., Water electrolysis on $La_{1-x}Sr_xCoO_{3-\delta}$ perovskite electrocatalysts. *Nat. Commun.* **2016,** 7 (1), 1-11.
14. Stevens, M. B.; Trang, C. D. M.; Enman, L. J.; Deng, J.; Boettcher, S. W., Reactive Fe-Sites in Ni/Fe (Oxy)hydroxide Are Responsible for Exceptional Oxygen Electrocatalysis Activity. *J. Am. Chem. Soc.* 2**017**, 139 (33), 11361-11364.
15. Roy, C.; Sebok, B.; Scott, S. B.; Fiordaliso, E. M.; Sørensen, J. E.; Bodin, A.; Trimarco, D. B.; Damsgaard, C. D.; Vesborg, P. C. K.; Hansen, O.; Stephens, I. E. L.; Kibsgaard, J.; Chorkendorff, I., Impact of nanoparticle size and lattice oxygen on water oxidation on NiFeOxHy. *Nat. Catal.* **2018**, 1 (11), 820-829.
16. Friebel, D.; Louie, M. W.; Bajdich, M.; Sanwald, K. E.; Cai, Y.; Wise, A. M.; Cheng, M.-J.; Sokaras, D.; Weng, T.-C.; Alonso-Mori, R.; Davis, R. C.; Bargar, J. R.; Nørskov, J. K.; Nilsson, A.; Bell, A. T., Identification of Highly Active Fe Sites in (Ni,Fe)OOH for Electrocatalytic Water Splitting. *J. Am. Chem. Soc.* **2015**, 137 (3), 1305-1313.

17. Liu, S.; Cao, E.; Chen, Z.; Wu, H.; Liu, B.; Yang, J.; Du, S.; Ren, Z., Promoting Electrocatalytic Oxygen Evolution of Ultrasmall NiFe (Hydr)oxide Nanoparticles by Graphene-Support Effects. *ChemSusChem* **2021**, 14 (24), 5508-5516.

18. Grimaud, A.; May, K. J.; Carlton, C. E.; Lee, Y. L.; Risch, M.; Hong, W. T.; Zhou, J. G.; Shao-Horn, Y., Double perovskites as a family of highly active catalysts for oxygen evolution in alkaline solution. *Nat. Commun.* **2013,** 4(1), 1-7.

19. Manabe, A.; Kashiwase, M.; Hashimoto, T.; Hayashida, T.; Kato, A.; Hirao, K.; Shimomura, I.; Nagashima, I., Basic study of alkaline water electrolysis. *Electrochim Acta* **2013,** *100*, 249-256.

20. Fu, Y.; Hautzinger, M. P.; Luo, Z.; Wang, F.; Pan, D.; Aristov, M. M.; Guzei, I. A.; Pan, A.; Zhu, X.; Jin, S., Incorporating Large A Cations into Lead Iodide Perovskite Cages: Relaxed Goldschmidt Tolerance Factor and Impact on Exciton–Phonon Interaction. *ACS Cent. Sci.* **2019,** *5* (8), 1377-1386.

21. Petrie, J. R.; Jeen, H.; Barron, S. C.; Meyer, T. L.; Lee, H. N., Enhancing Perovskite Electrocatalysis through Strain Tuning of the Oxygen Deficiency. *J. Am. Chem. Soc.* **2016,** *138* (23), 7252-7255.

22. Sun, H. N.; Xu, X. M.; Hu, Z. W.; Tjeng, L. H.; Zhao, J.; Zhang, Q.; Lin, H. J.; Chen, C. T.; Chan, T. S.; Zhou, W.; Shao, Z. P., Boosting the oxygen evolution reaction activity of a perovskite through introducing multi-element synergy and building an ordered structure. *J. Mater. Chem. A* **2019,** *7* (16), 9924-9932.

23. Wang, J.; Gao, Y.; Kong, H.; Kim, J.; Choi, S.; Ciucci, F.; Hao, Y.; Yang, S.; Shao, Z.; Lim, J., Non-precious-metal catalysts for alkaline water electrolysis: operando characterizations, theoretical calculations, and recent advances. *Chem. Soc. Rev.* **2020**,49, 9154-9196

24. Hong, W. T.; Stoerzinger, K. A.; Lee, Y.-L.; Giordano, L.; Grimaud, A.; Johnson, A. M.; Hwang, J.; Crumlin, E. J.; Yang, W.; Shao-Horn, Y., Charge-transfer-energy-dependent oxygen evolution reaction mechanisms for perovskite oxides. *Energ. Environ. Sci.* **2017,** *10* (10), 2190-2200.

25. Suntivich, J.; May, K. J.; Gasteiger, H. A.; Goodenough, J. B.; Shao-Horn, Y., A Perovskite Oxide Optimized for Oxygen Evolution Catalysis from Molecular Orbital Principles. *Science* **2011,** *334* (6061), 1383-1385.

26. Yagi, S.; Yamada, I.; Tsukasaki, H.; Seno, A.; Murakami, M.; Fujii, H.; Chen, H.; Umezawa, N.; Abe, H.; Nishiyama, N.; Mori, S., Covalency-reinforced oxygen evolution reaction catalyst. *Nat. Commun.* **2015,** 6 (1), 1-6.

27. Marelli, E.; Gazquez, J.; Poghosyan, E.; Müller, E.; Gawryluk, D. J.; Pomjakushina, E.; Sheptyakov, D.; Piamonteze, C.; Aegerter, D.; Schmidt, T. J.; Medarde, M.; Fabbri, E., Correlation between Oxygen Vacancies and Oxygen Evolution Reaction Activity for a Model Electrode: PrBaCo2$O_{5+\delta}$. **2021,** *60* (26), 14609-14619.

28. Miao, X.; Wu, L.; Lin, Y.; Yuan, X.; Zhao, J.; Yan, W.; Zhou, S.; Shi, L., The role of oxygen vacancies in water oxidation for perovskite cobalt oxide electrocatalysts: are more better? *Chem. Commun.* **2019,** *55* (10), 1442-1445.

29. Grimaud, A.; Diaz-Morales, O.; Han, B.; Hong, W. T.; Lee, Y. L.; Giordano, L.; Stoerzinger, K. A.; Koper, M. T. M.; Shao-Horn, Y., Activate lattice oxygen redox reactions in metal oxides to catalyse oxygen evolution. *Nat. Chem.* **2017,** 9 (5), 457-465.

30. Pan, Y.; Xu, X.; Zhong, Y.; Ge, L.; Chen, Y.; Veder, J.-P. M.; Guan, D.; O'Hayre, R.; Li, M.; Wang, G.; Wang, H.; Zhou, W.; Shao, Z., Direct evidence

of boosted oxygen evolution over perovskite by enhanced lattice oxygen participation. *Nat. Commun.* **2020,** *11* (1), 1-10.

31. Risch, M.; Grimaud, A.; May, K. J.; Stoerzinger, K. A.; Chen, T. J.; Mansour, A. N.; Shao-Horn, Y., Structural Changes of Cobalt-Based Perovskites upon Water Oxidation Investigated by EXAFS. *J. Phys. Chem. C* **2013,** *117* (17), 8628-8635.
32. Shen, T.-H.; Spillane, L.; Vavra, J.; Pham, T. H. M.; Peng, J.; Shao-Horn, Y.; Tileli, V., Oxygen Evolution Reaction in $Ba_{0.5}Sr_{0.5}Co_{0.8}Fe_{0.2}O_{3-\delta}$ Aided by Intrinsic Co/Fe Spinel-Like Surface. *J. Am. Chem. Soc.* 2020, 142 (37), 15876-15883.
33. Li, H.; Chen, Y.; Ge, J.; Liu, X.; Fisher, A. C.; Sherburne, M. P.; Ager, J. W.; Xu, Z. J., Active Phase on $SrCo_{1-x}F_{ex}O_{3-\delta}$ ($0 \leq x \leq 0.5$) Perovskite for Water Oxidation: Reconstructed Surface versus Remaining Bulk. *JACS Au* **2021**, 1 (1), 108-115.
34. Zhao, C.; Li, N.; Zhang, R.; Zhu, Z.; Lin, J.; Zhang, K.; Zhao, C., Surface Reconstruction of $La_{0.8}Sr_{0.2}Co_{0.8}Fe_{0.2}O_{3-\delta}$ for Superimposed OER Performance. *ACS Appl. Mater. Interfaces* **2019**, 11 (51), 47858-47867.
35. Wang, H.-Y.; Hung, S.-F.; Hsu, Y.-Y.; Zhang, L.; Miao, J.; Chan, T.-S.; Xiong, Q.; Liu, B., In Situ Spectroscopic Identification of μ-OO Bridging on Spinel Co3O4 Water Oxidation Electrocatalyst. *J. Phys. Chem. Lett.* **2016,** *7* (23), 4847-4853.
36. Tung, C.-W.; Hsu, Y.-Y.; Shen, Y.-P.; Zheng, Y.; Chan, T.-S.; Sheu, H.-S.; Cheng, Y.-C.; Chen, H. M., Reversible adapting layer produces robust single-crystal electrocatalyst for oxygen evolution. *Nat. Commun.* **2015,** *6* (1), 1-9.
37. Favaro, M.; Yang, J.; Nappini, S.; Magnano, E.; Toma, F. M.; Crumlin, E. J.; Yano, J.; Sharp, I. D., Understanding the Oxygen Evolution Reaction Mechanism on

CoOx using Operando Ambient-Pressure X-ray Photoelectron Spectroscopy. *J. Am. Chem. Soc.* **2017,** *139* (26), 8960-8970.

38. Lopes, P. P.; Chung, D. Y.; Rui, X.; Zheng, H.; He, H.; Farinazzo Bergamo Dias Martins, P.; Strmcnik, D.; Stamenkovic, V. R.; Zapol, P.; Mitchell, J. F.; Klie, R. F.; Markovic, N. M., Dynamically Stable Active Sites from Surface Evolution of Perovskite Materials during the Oxygen Evolution Reaction. *J. Am. Chem. Soc.* **2021**, 143 (7), 2741-2750.
39. Orikasa, Y.; Ina, T.; Yamamoto, K.; Nakao, T.; Mineshige, A.; Amezawa, K.; Kawada, T.; Tanida, H.; Uruga, T.; Uchimoto, Y., Direct Observation of Rate Determining Step for Nd[2]NiO[4+δ] SOFC Cathode Reaction by *operando* Electrochemical XAS. *Electrochemistry* **2014,** *82* (10), 897-900.
40. Takamatsu, D.; Koyama, Y.; Orikasa, Y.; Mori, S.; Nakatsutsumi, T.; Hirano, T.; Tanida, H.; Arai, H.; Uchimoto, Y.; Ogumi, Z., First In Situ Observation of the $LiCoO_2$ Electrode/Electrolyte Interface by Total-Reflection X-ray Absorption Spectroscopy. *Angew. Chem. Int. Ed.* **2012,** *51* (46), 11597-11601.
41. Tsuji, Y.; Sako, S.; Nitta, K.; Yamamoto, K.; Shao-horn, Y.; Uchimoto, Y.; Orikasa, Y., Surface analysis of lanthanum strontium cobalt oxides under cathodic polarization at high temperature through operando total-reflection X-ray absorption and X-ray fluorescence spectroscopy. *Solid State Ionics* **2020,** *357*, 115502.
42. Okumura, T.; Nakatsutsumi, T.; Ina, T.; Orikasa, Y.; Arai, H.; Fukutsuka, T.; Iriyama, Y.; Uruga, T.; Tanida, H.; Uchimoto, Y.; Ogumi, Z., Depth-resolved X-ray absorption spectroscopic study on nanoscale observation of the electrode–solid electrolyte interface for all solid state lithium ion batteries. *J. Mater. Chem.* **2011,** *21* (27), 10051-10060.

43. Kan, D.; Orikasa, Y.; Nitta, K.; Tanida, H.; Kurosaki, R.; Nishimura, T.; Sasaki, T.; Guo, H.; Ozaki, Y.; Uchimoto, Y.; Shimakawa, Y., Overpotential-Induced Introduction of Oxygen Vacancy in $La_{0.67}Sr_{0.33}MnO_3$ Surface and Its Impact on Oxygen Reduction Reaction Catalytic Activity in Alkaline Solution. *J. Phys. Chem. C* **2016,** *120* (11), 6006-6010.

44. Bockris, J. O. M., The Electrocatalysis of Oxygen Evolution on Perovskites. *J. Electrochem. Soc.* **1984,** *131* (2), 290-302.

45. Cheng, X.; Fabbri, E.; Nachtegaal, M.; Castelli, I. E.; El Kazzi, M.; Haumont, R.; Marzari, N.; Schmidt, T. J., Oxygen Evolution Reaction on $La_{1-x}Sr_xCoO_3$ Perovskites: A Combined Experimental and Theoretical Study of Their Structural, Electronic, and Electrochemical Properties. *Chem. Mater.* **2015,** *27* (22), 7662-7672.

46. Jerkiewicz, G., Standard and Reversible Hydrogen Electrodes: Theory, Design, Operation, and Applications. *ACS Catal.* **2020**, 10 (15), 8409-8417.

47. Ravel, B.; Newville, M., ATHENA, ARTEMIS, HEPHAESTUS: data analysis for X-ray absorption spectroscopy using IFEFFIT. *J. Synchrotron Radiat.* **2005,** *12* (4), 537-541.

48. Bergmann, A.; Jones, T. E.; Martinez Moreno, E.; Teschner, D.; Chernev, P.; Gliech, M.; Reier, T.; Dau, H.; Strasser, P., Unified structural motifs of the catalytically active state of Co(oxyhydr)oxides during the electrochemical oxygen evolution reaction. *Nat. Catal.* **2018,** *1* (9), 711-719.

49. Haas, O.; Ludwig, C.; Bergmann, U.; Singh, R. N.; Braun, A.; Graule, T., X-ray absorption investigation of the valence state and electronic structure of $La_{1-x}Ca_xCoO_{3-\delta}$ in comparison with $La_{1-x}Sr_xCoO_{3-\delta}$ and $La_{1-x}Sr_xFeO_{3-\delta}$. *J. Solid State Chem.* **2011,** *184* (12), 3163-3171.

50. Hueso, J. L.; Holgado, J. P.; Pereñíguez, R.; Gonzalez-DelaCruz, V. M.; Caballero, A., Structural and chemical reactivity modifications of a cobalt perovskite induced by Sr-substitution. An in situ XAS study. *Mater. Chem. Phys.* **2015,** *151*, 29-33.

51. Mizusaki, J.; Mima, Y.; Yamauchi, S.; Fueki, K.; Tagawa, H., Nonstoichiometry of the perovskite-type oxides $La_{1-x}Sr_xCoO_{3-\delta}$. *J. Solid State Chem.* **1989**, 80 (1), 102-111.

52. Abbate, M.; Fuggle, J. C.; Fujimori, A.; Tjeng, L. H.; Chen, C. T.; Potze, R.; Sawatzky, G. A.; Eisaki, H.; Uchida, S., Electronic structure and spin-state transition of $LaCoO_3$. *Phys. Rev. B* **1993,** *47* (24), 16124-16130.

53. Toulemonde, O.; N'Guyen, N.; Studer, F.; Traverse, A., Spin State Transition in $LaCoO_3$ with Temperature or Strontium Doping as Seen by XAS. *J. Solid Statie Chem.* **2001,** *158* (2), 208-217.

54. Moodenbaugh, A. R.; Nielsen, B.; Sambasivan, S.; Fischer, D. A.; Friessnegg, T.; Aggarwal, S.; Ramesh, R.; Pfeffer, R. L., Hole-state density of $La_{1-x}Sr_xCoO_{3-\delta}$< ~x ~0.5) across the insulator/metal phase boundary. *Phys. Rev. B* **2000,** *61* (8), 5666-5671.

55. Suntivich, J.; Hong, W. T.; Lee, Y.-L.; Rondinelli, J. M.; Yang, W.; Goodenough, J. B.; Dabrowski, B.; Freeland, J. W.; Shao-Horn, Y., Estimating Hybridization of Transition Metal and Oxygen States in Perovskites from O K-edge X-ray Absorption Spectroscopy. *J. Phys. Chem. C* **2014,** *118* (4), 1856-1863.

56. Lu, Y.; Ma, A.; Yu, Y.; Tan, R.; Liu, C.; Zhang, P.; Liu, D.; Gui, J., Engineering Oxygen Vacancies into $LaCoO_3$ Perovskite for Efficient Electrocatalytic Oxygen Evolution. *ACS Sustain. Chem. Eng.* **2019,** *7* (3), 2906-2910.

57. Bockris, J. O. M.; Otagawa, T., Mechanism of oxygen evolution on perovskites. *J. Phys.Chem.* **1983,** *87* (15), 2960-2971.
58. Matsumoto, Y.; Sato, E., Electrocatalytic properties of transition metal oxides for oxygen evolution reaction. *Mater. Chem. Phys.* **1986,** *14* (5), 397-426.
59. Fabbri, E.; Nachtegaal, M.; Binninger, T.; Cheng, X.; Kim, B. J.; Durst, J.; Bozza, F.; Graule, T.; Schäublin, R.; Wiles, L.; Pertoso, M.; Danilovic, N.; Ayers, K. E.; Schmidt, T. J., Dynamic surface self-reconstruction is the key of highly active perovskite nano-electrocatalysts for water splitting. *Nat. Mater.* **2017**, 16 (9), 925-931.
60. Koo, B.; Kim, K.; Kim, J. K.; Kwon, H.; Han, J. W.; Jung, W., Sr Segregation in Perovskite Oxides: Why It Happens and How It Exists. *Joule* **2018**, 2 (8), 1476-1499.
61. Kim, B.-J.; Fabbri, E.; Borlaf, M.; Abbott, D. F.; Castelli, I. E.; Nachtegaal, M.; Graule, T.; Schmidt, T. J., Oxygen evolution reaction activity and underlying mechanism of perovskite electrocatalysts at different pH. *Mater.Adv.* **2021,** *2* (1), 345-355.
62. Ferreira de Araújo, J.; Dionigi, F.; Merzdorf, T.; Oh, H.-S.; Strasser, P., Evidence of Mars-Van-Krevelen Mechanism in the Electrochemical Oxygen Evolution on Ni-Based Catalysts. *Angew. Chem. Int. Ed.* **2021**, 60 (27), 14981-14988.
63. Moysiadou, A.; Lee, S.; Hsu, C.-S.; Chen, H. M.; Hu, X., Mechanism of Oxygen Evolution Catalyzed by Cobalt Oxyhydroxide: Cobalt Superoxide Species as a Key Intermediate and Dioxygen Release as a Rate-Determining Step. *J. Am. Chem. Soc.* **2020**, 142 (27), 11901-11914.

Figure 3.1. A schematic illustration of the working electrode

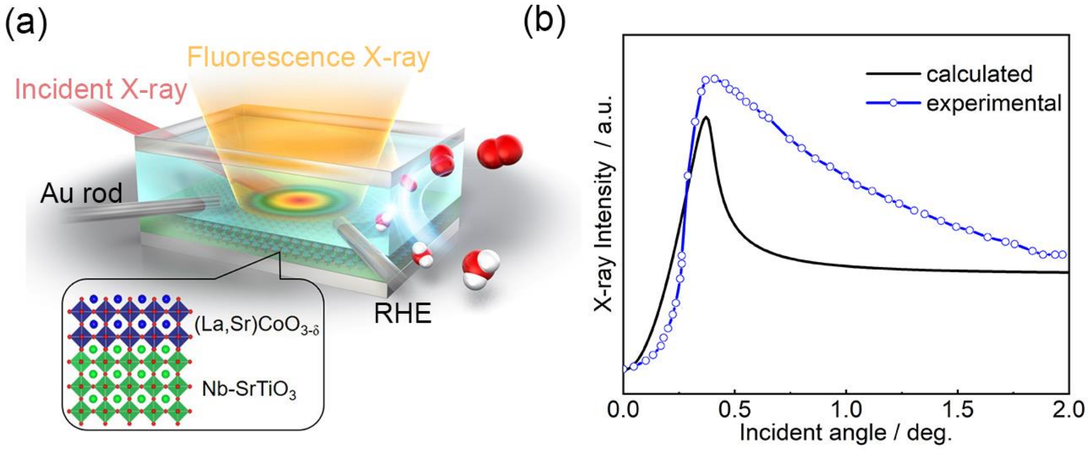

Figure 3.2. (a) Schematic of electrochemical cell used for *operando* TR-XAS measurements; (b) the incident X-ray angle dependence of the Co fluorescence for the calculated and experimental results.

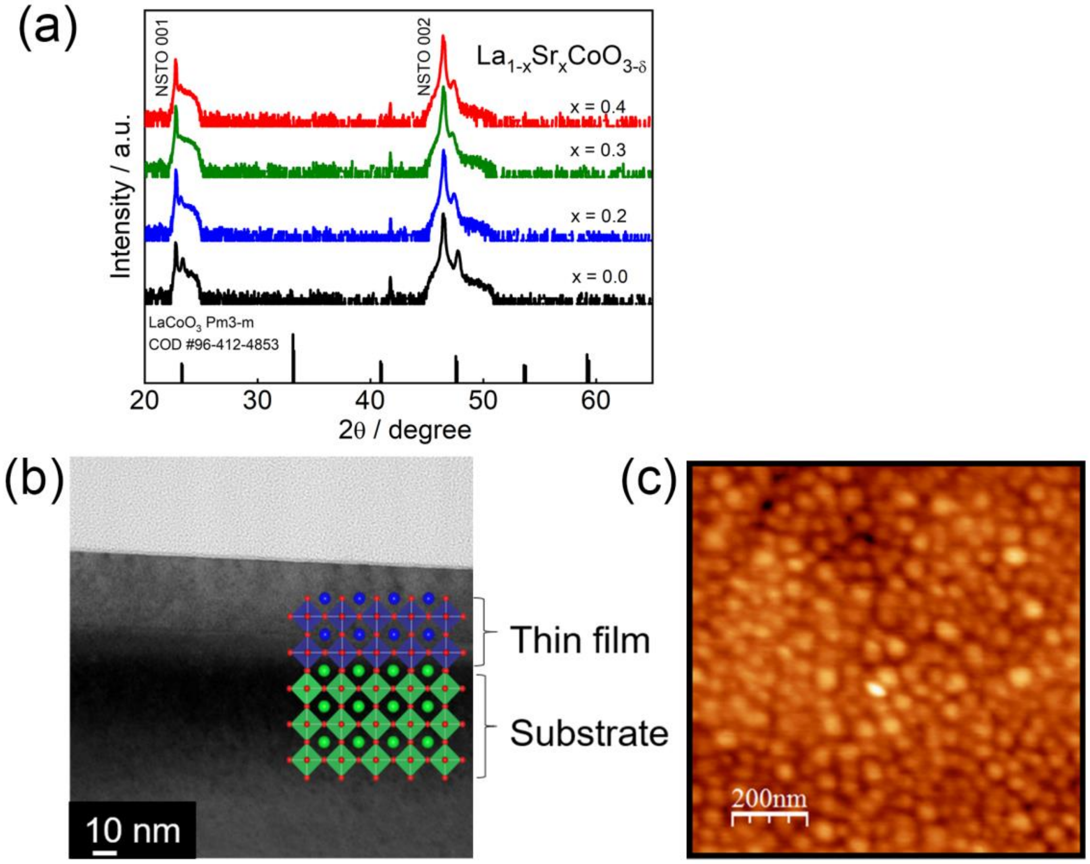

Figure 3.3. (a) XRD results of as-prepared thin film samples with different Sr content, NSTO 001 and NSTO 002 indicate the lattice planes of the Nb-doped $SrTiO_3$ substrate (NSTO); (b) TEM image of as prepared $LaCoO_{3-\delta}$ thin film sample, the insert crystal model, presented in the inset indicates the identical crystal orientation between the thin film and substrate; (c) AFM image of $LaCoO_3$.

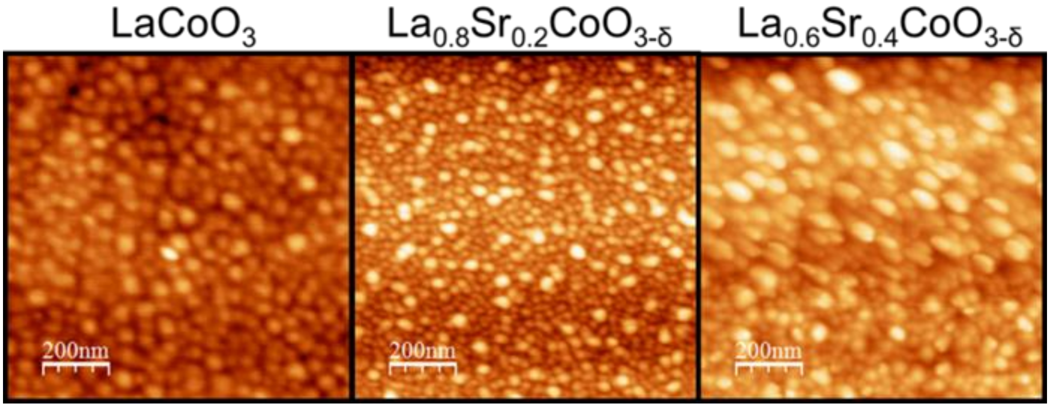

Figure 3.4. AFM images of $La_{1-x}Sr_xCoO_{3-\delta}$($x$ = 0.0, 0.2 and 0.4).

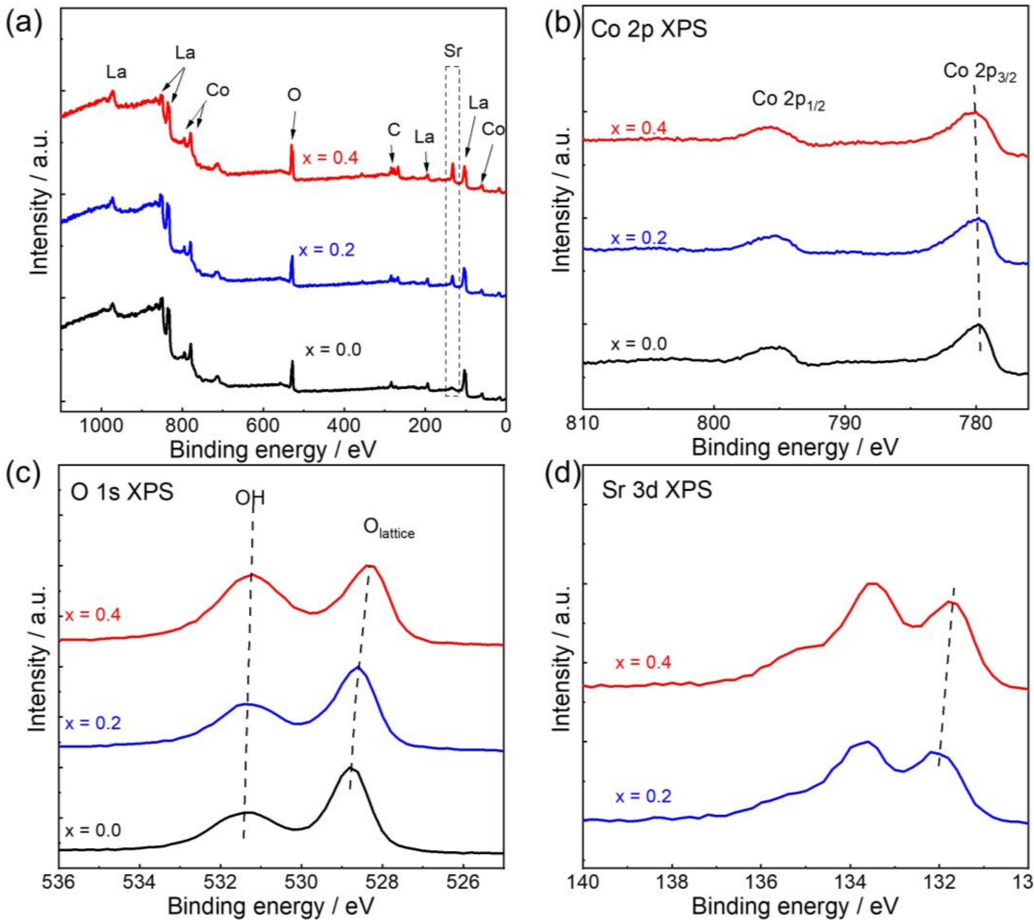

Figure 3.5. (a) XPS survey scan; (b) Co 2p; (c) O 1s and (d) Sr 3d core level XPS spectra of pristine $La_{1-x}Sr_xCoO_{3-\delta}$ (x = 0.0, 0.2, and 0.4)

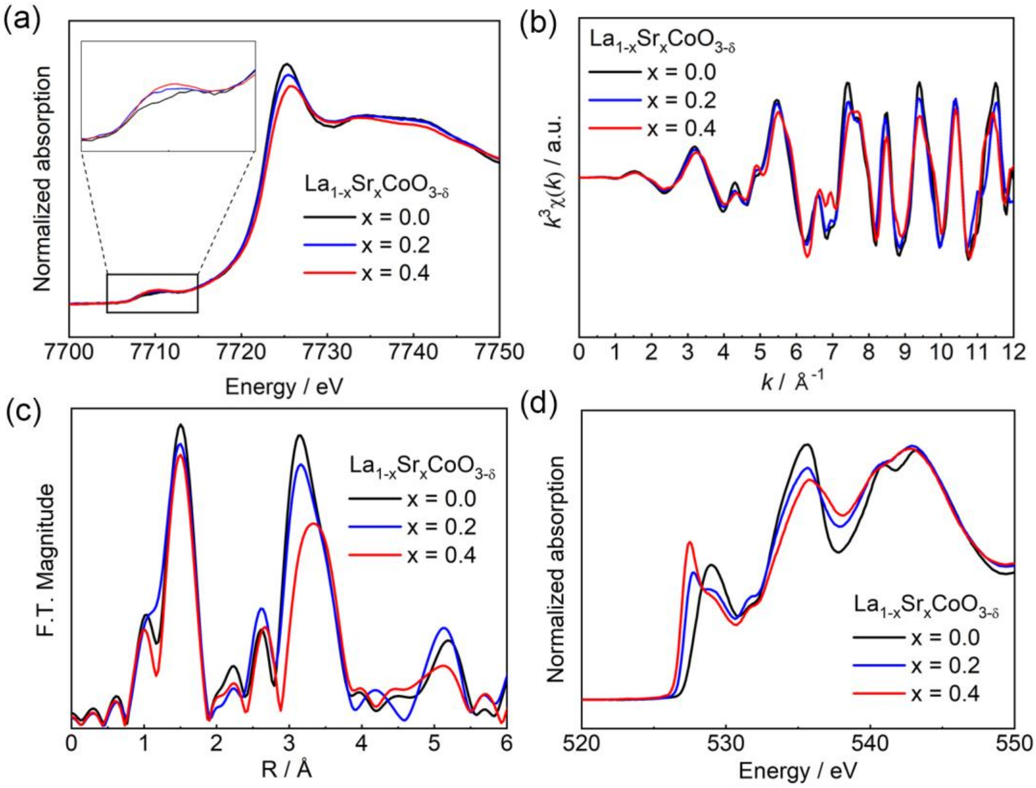

Figure 3.6. Electronic structures of $La_{1-x}Sr_xCoO_{3-\delta}$ ($x = 0$, 0.2 and 0.4) (a) Co K-edge XANES; (b) EXAFS oscillation and (c) Fourier-transformed spectra; (d) O K-edge XAS.

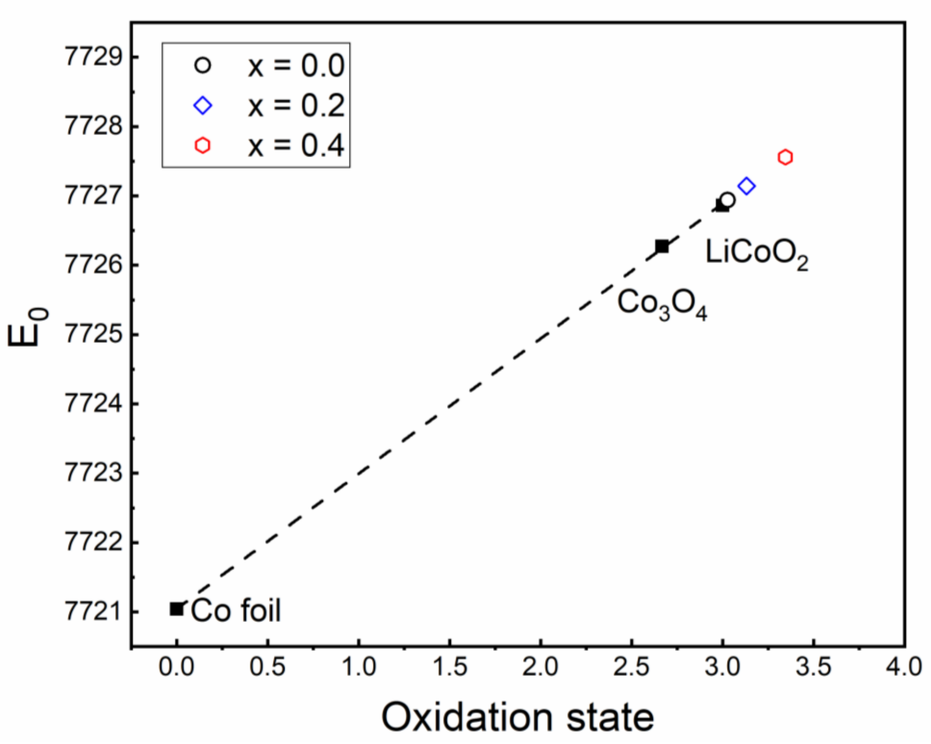

Figure 3.7. The relationship between the edge position (E_0, defined to be the energy at the highest first derivative of the absorbance) of as synthesized samples and the oxidation state. The dash line indicates the relationship between E_0 and oxidation states of standard samples.

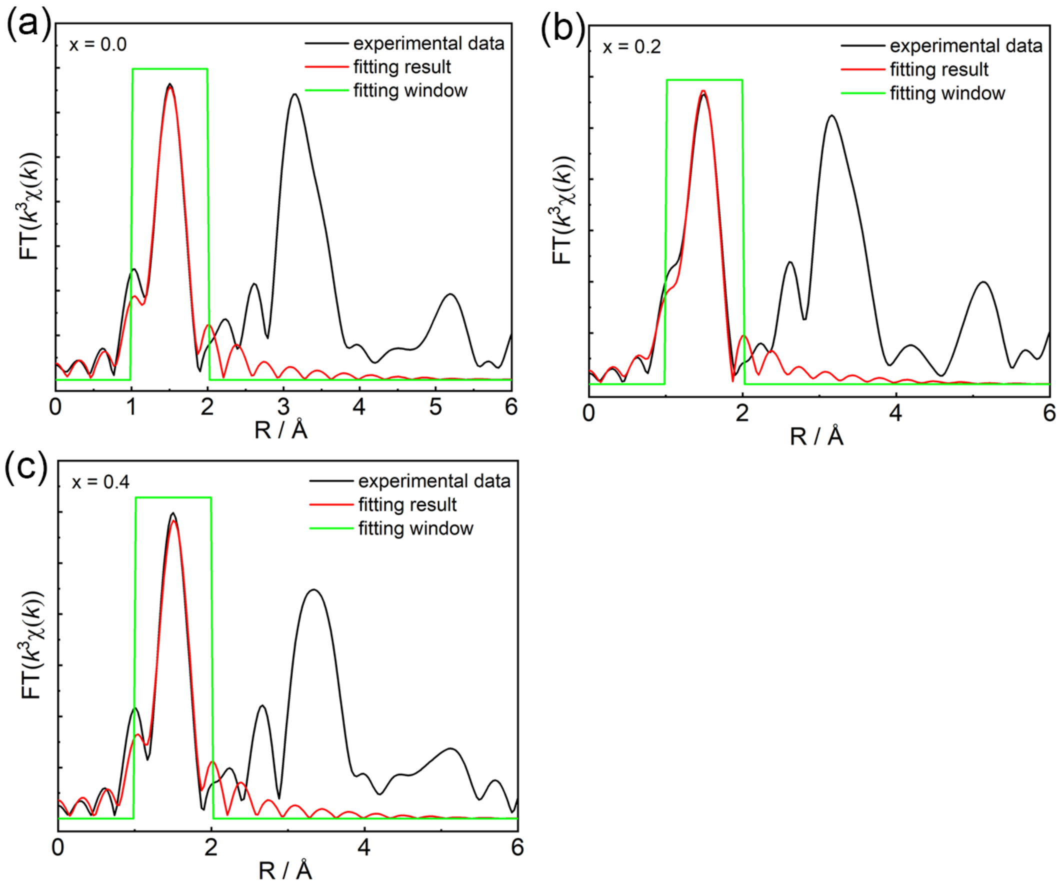

Figure 3.8. *Ex situ* EXAFS fitting results of (a) $LaCoO_{3-\delta}$, (b) $La_{0.8}Sr_{0.2}CoO_{3-\delta}$ and (c) $La_{0.6}Sr_{0.4}CoO_{3-\delta}$

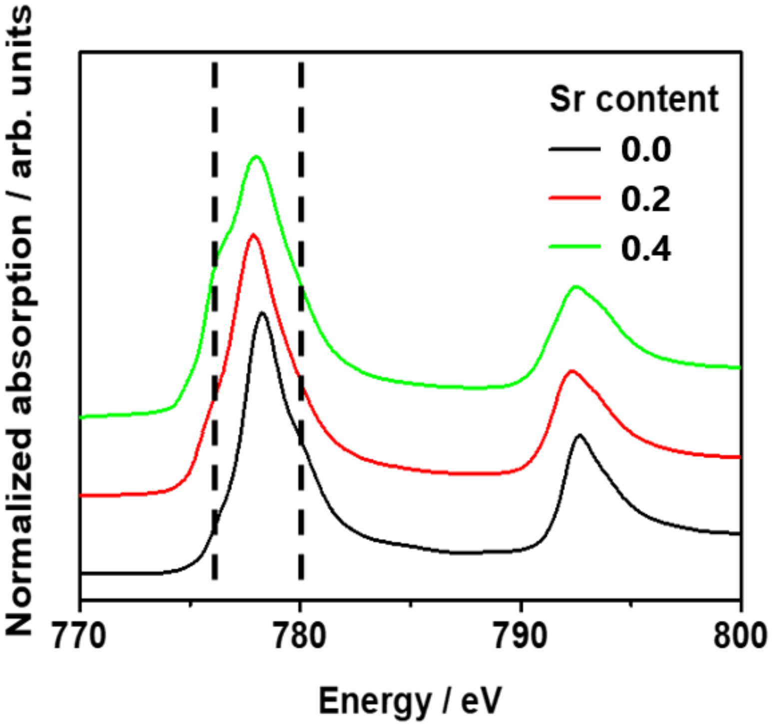

Figure 3.9. Co L-edge XAS spectra of $La_{1-x}Sr_xCoO_{3-\delta}$ ($x = 0.0$, 0.2 and 0.4).

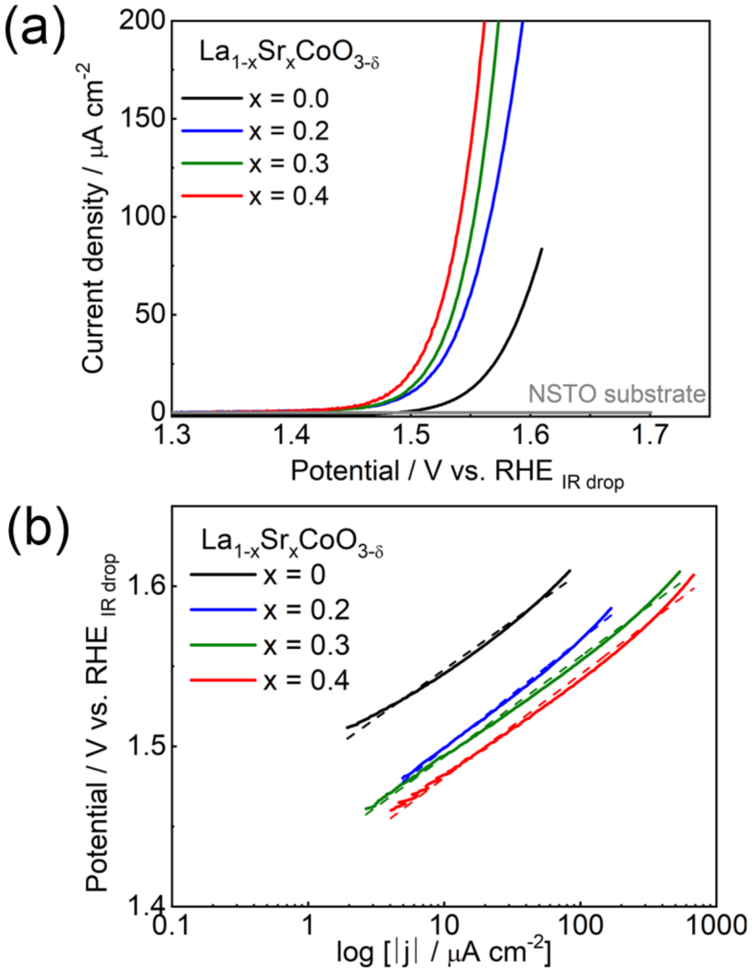

Figure 3.10. (a) OER activities of as-prepared $La_{1-x}Sr_xCoO_{3-\delta}$ (x = 0.0, 0.2, 0.3, and 0.4) samples and (b) Tafel plots, dashed lines indicate the fitting results.

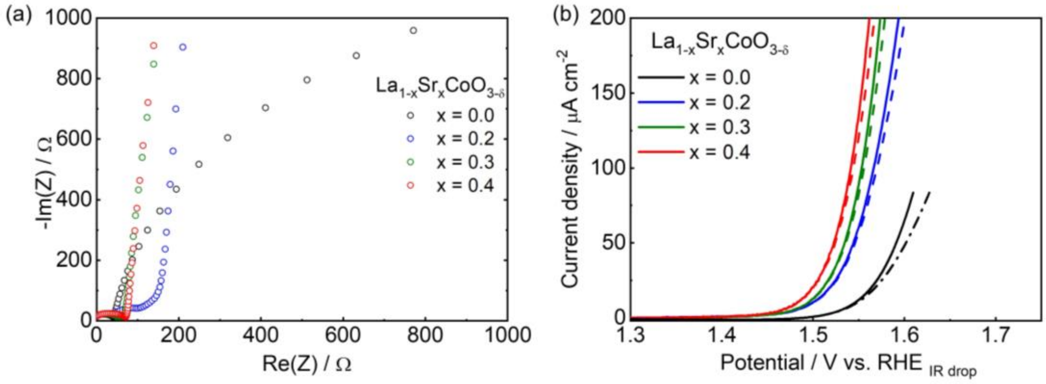

Figure 3.11. (a) Nyquist plot at OCV; (b) OER activities with and without iR-compensation. the solid lines represent results after iR-compensation, while the dash lines represent results without iR-compensation.

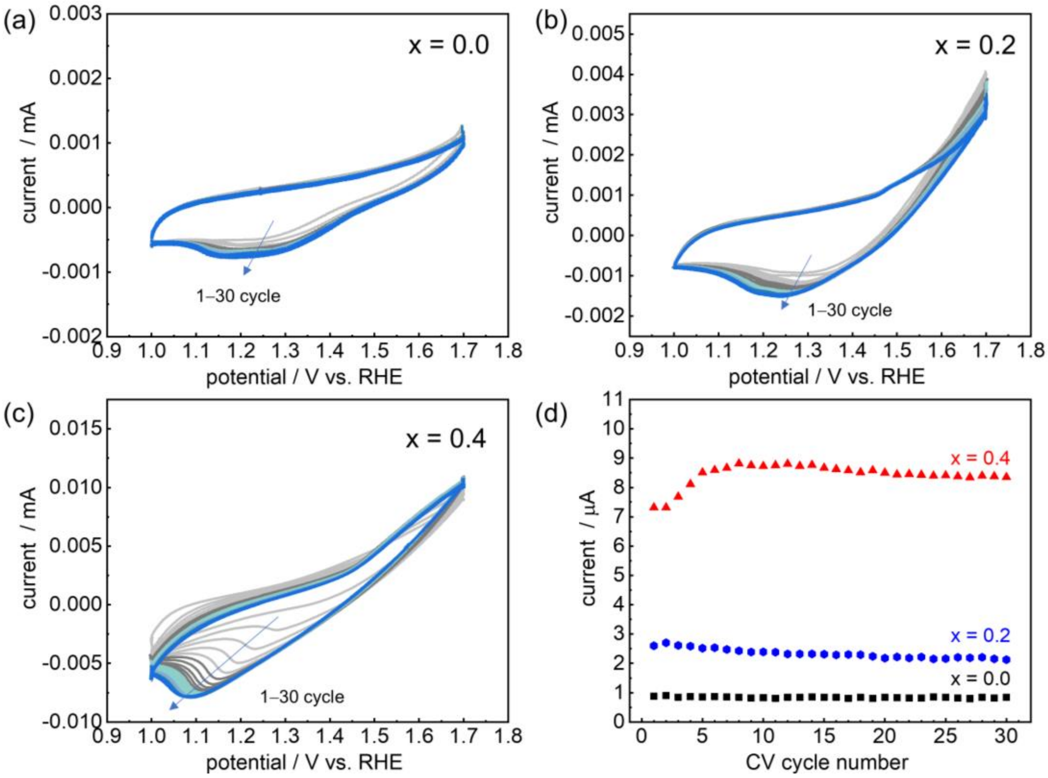

Figure 3.12. 30 cycles of CV measurements of (a) x = 0.0; (b) x = 0.2; and (c) x = 0.4. (d) the recorded current at 1.63 V vs. RHE for each CV cycle.

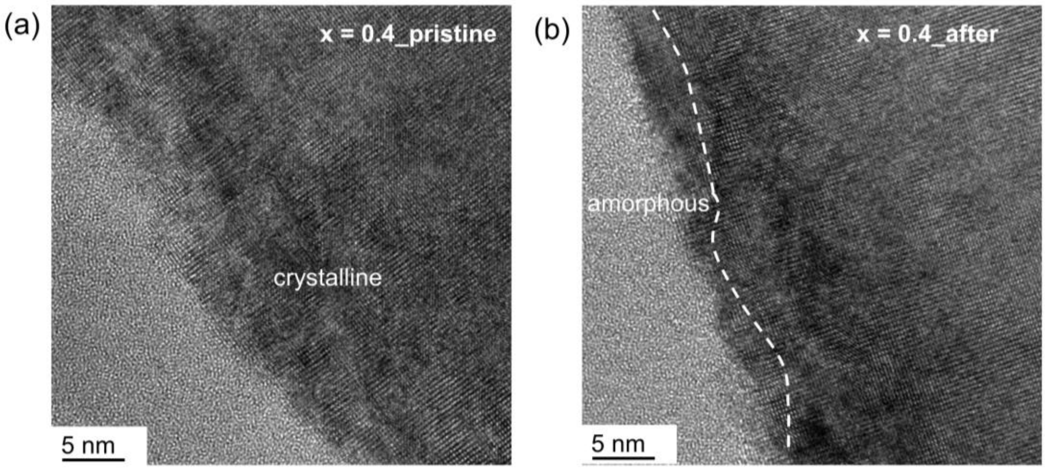

Figure 3.13. High resolution TEM images of x = 0.4 sample (a) pristine and (b) after 30 cycles of CV measurements.

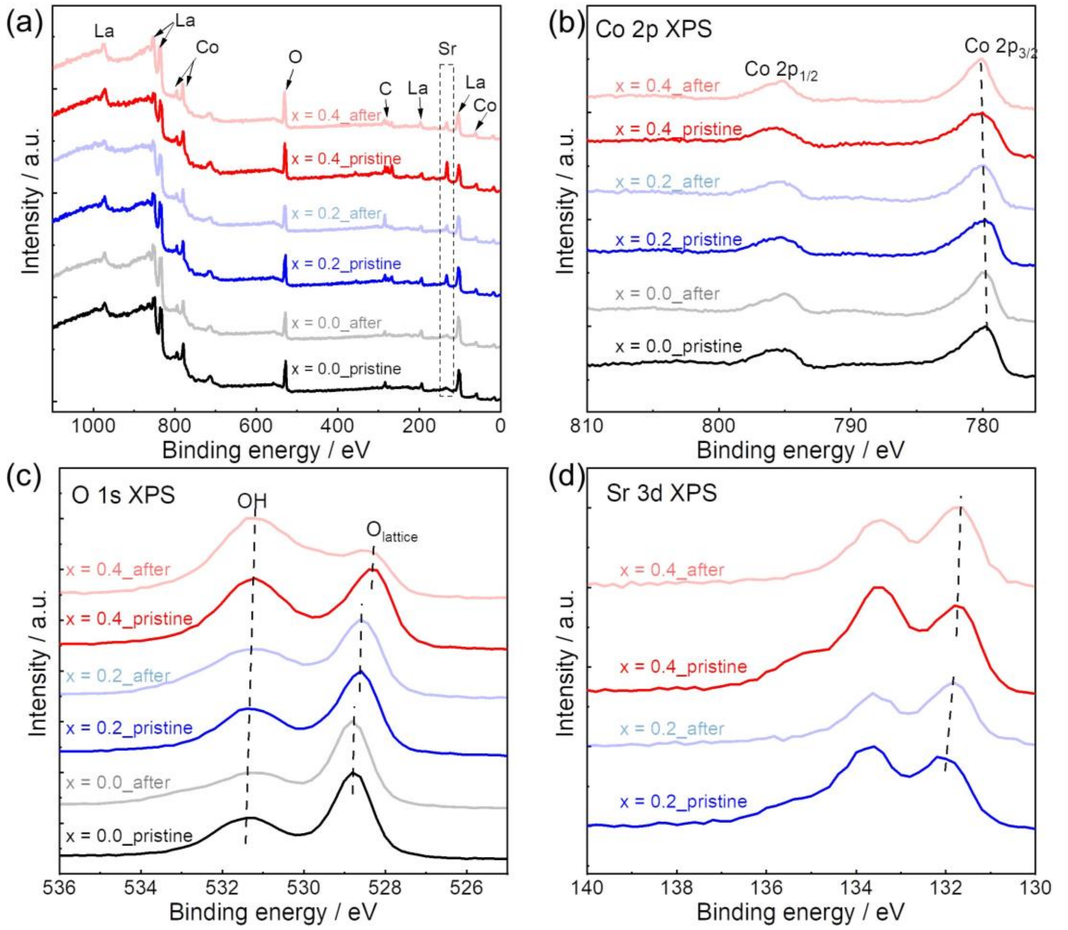

Figure 3.14. (a) XPS survey scan; (b) Co 2p; (c) O 1s and (d) Sr 3d core level XPS spectra of pristine samples and samples after 30 cycles CV measurements.

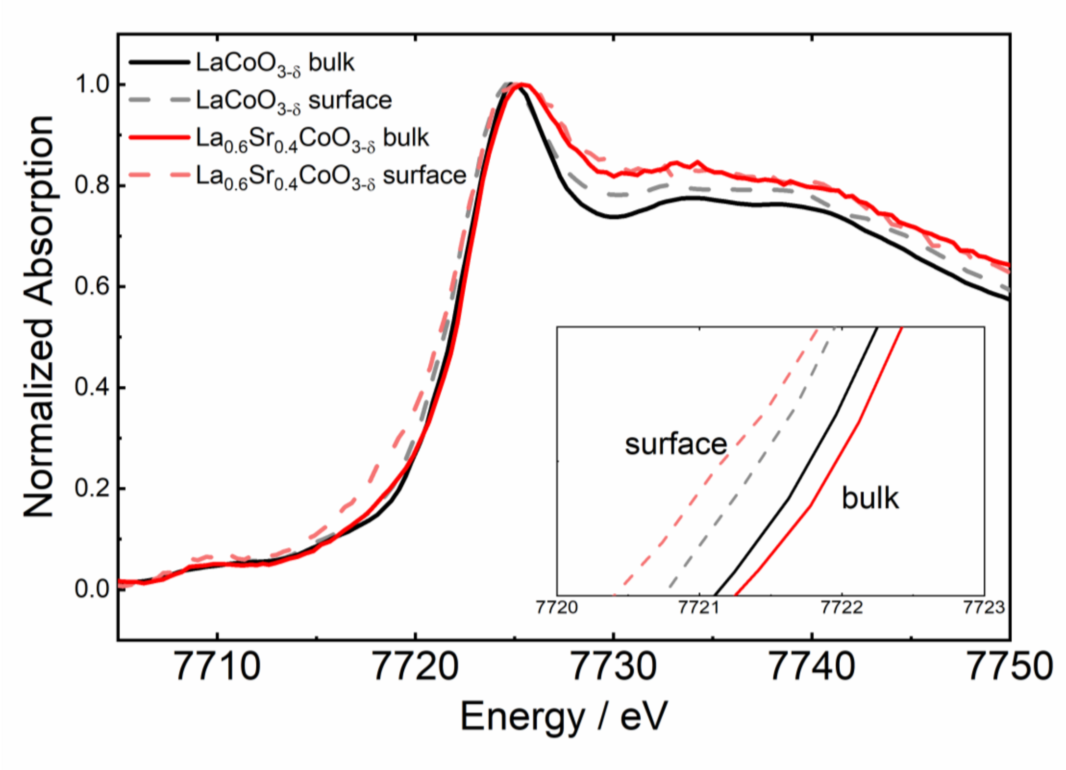

Figure 3.15. Comparison of the surface changes of $LaCoO_{3-\delta}$ and $La_{0.6}Sr_{0.4}CoO_{3-\delta}$ in liquid electrolyte under OCP (0.8 V vs. RHE)

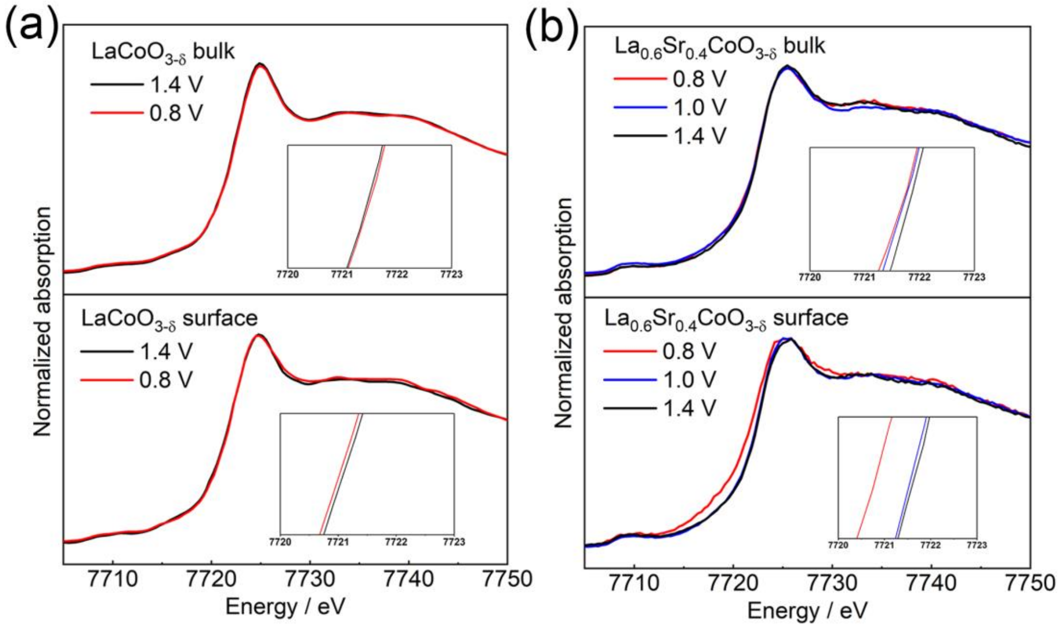

Figure 3.16. *Operando* Co K-edge XANES of of bulk and surface states of (a) $LaCoO_{3-\delta}$ and (b) $La_{0.6}Sr_{0.4}CoO_{3-\delta}$. All applied potentials are vs. RHE.

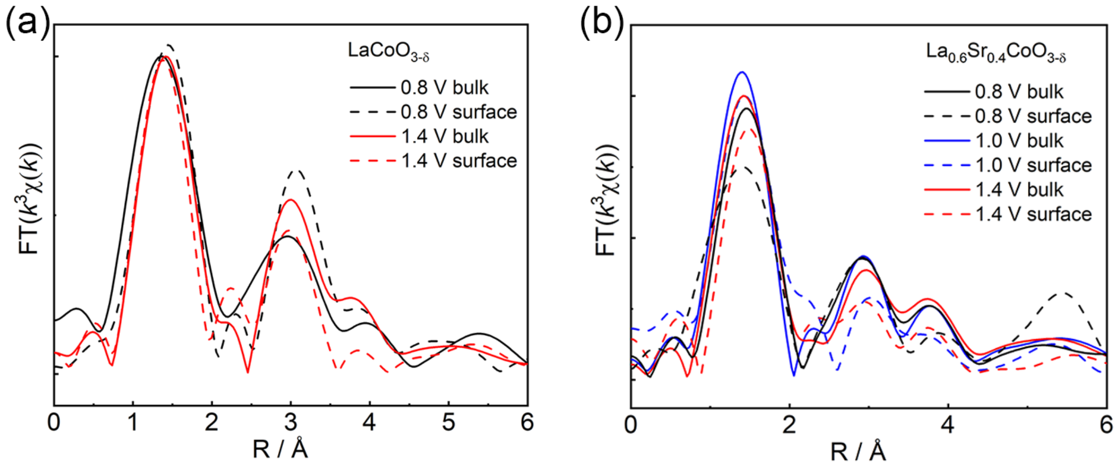

Figure 3.17. *Operando* EXAFS of (a) $LaCoO_{3-\delta}$ and (b) $La_{0.6}Sr_{0.4}CoO_{3-\delta}$

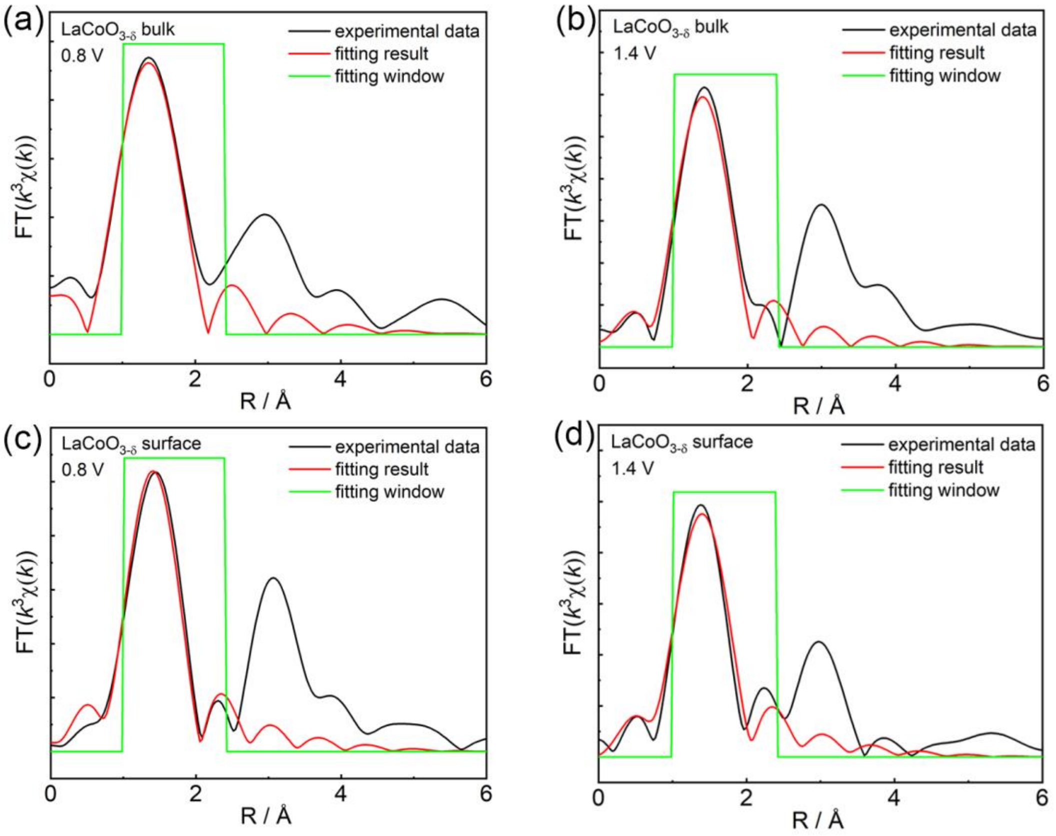

Figure 3.18. *Operando* EXAFS fitting results of $LaCoO_{3-\delta}$. (a)bulk and (c) surface state at 0.8 V vs. RHE; (b) bulk and (c) surface state at 1.4 V vs. RHE.

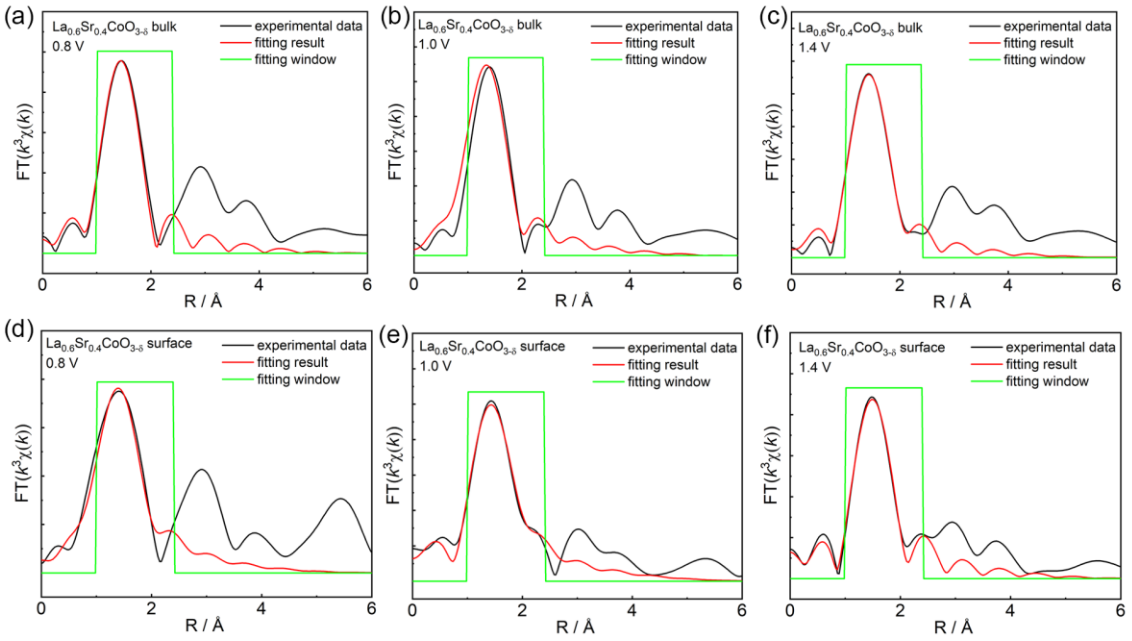

Figure 3.19. *Operando* EXAFS fitting results of $La_{0.6}Sr_{0.4}CoO_{3-\delta}$. (a) bulk and (d) surface state at 0.8 V vs. RHE; (b) bulk and (e) surface state at 1.0 V vs. RHE; (c) bulk and (f) surface state at 1.0 V vs. RHE

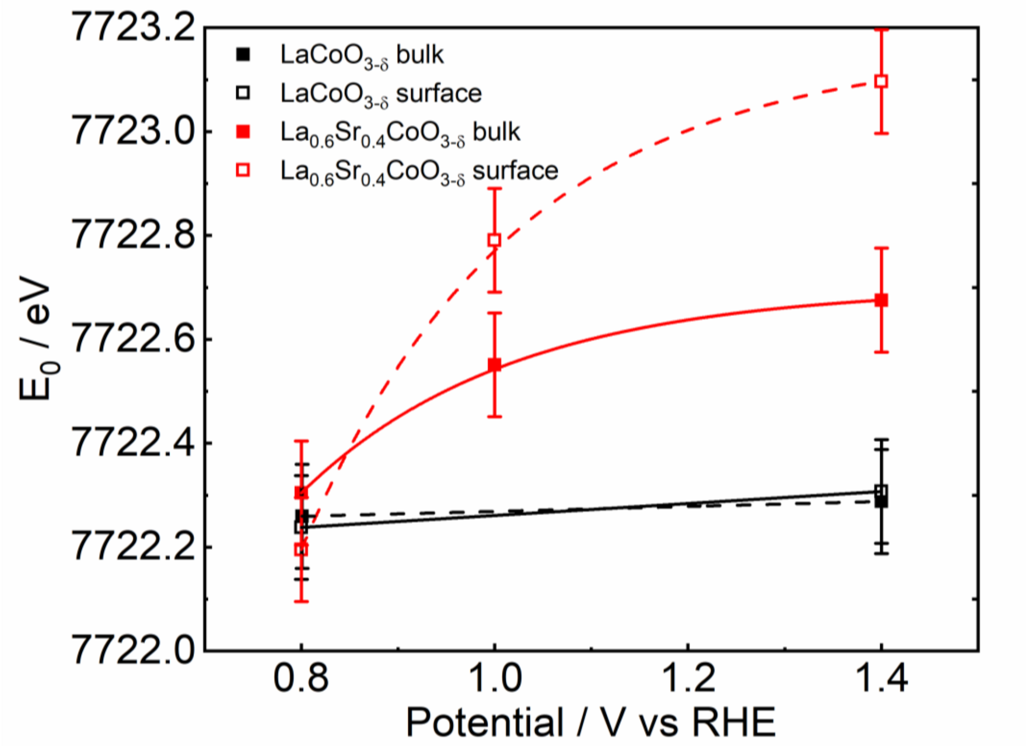

Figure 3.20. XANES absorption edge energy against oxygen potential of $LaCoO_{3-\delta}$ and $La_{0.6}Sr_{0.4}CoO_{3-\delta}$

Table 3.1. XPS-derived atomic concentration data for $La_{1-x}Sr_xCoO_{3-\delta}$ (x = 0.0, 0.2, and 0.4), taking La 3d% + Sr 3d % + Co 2p% = 100%

	x = 0.0	x = 0.2	x = 0.4
La 3d	47% ± 3%	36% ± 4%	25% ± 5%
Sr 3d	---	22% ± 3%	36% ± 3%
Co 2p	53% ± 2%	42% ± 2%	39% ± 3%

Table 3.2. *Ex situ* EXAFS fitting results of Co-O bond for $La_{1-x}Sr_xCoO_{3-\delta}$.

Entry	Path	N a)	R b) / Å	σ^2 c) / Å^2	R_f d) / %
x=0.0	Co-O	6.0*	1.922	0.0035*	1.0
x=0.2	Co-O	5.9	1.921	0.0035*	0.2
x=0.4	Co-O	5.6	1.917	0.0035*	0.2

* fixed value

a) Coordination Number

b) Bond distance

c) Debye-Waller factor

d) Residual factor

$$R_f = \frac{\int \left| k^3 \chi^{obs}(k) - k^3 \chi^{calc}(k) \right|^2 dk}{\int \left| k^3 \chi^{obs}(k) \right|^2 dk} \times 100$$

Table 3.3. Ohmic resistance determined by EIS

Sr content	R / Ω
0	550
0.1	513
0.2	91
0.3	66
0.4	72

Table 3.4. Tafel slopes as-prepared $La_{1-x}Sr_xCoO_{3-\delta}$ (x = 0, 0.1, 0.2, 0.3 and 0.4) samples

samples	$x = 0.0$	$x = 0.1$	$x = 0.2$	$x = 0.3$	$x = 0.4$
Tafel slope	60.6	77.0	74.2	62.6	64.4

Table 3.5. XPS-derived atomic concentration data for $La_{1-x}Sr_xCoO_{3-\delta}$ (x = 0.0, 0.2, and 0.4), taking La 3d% + Sr 3d% + Co 2p% = 100%

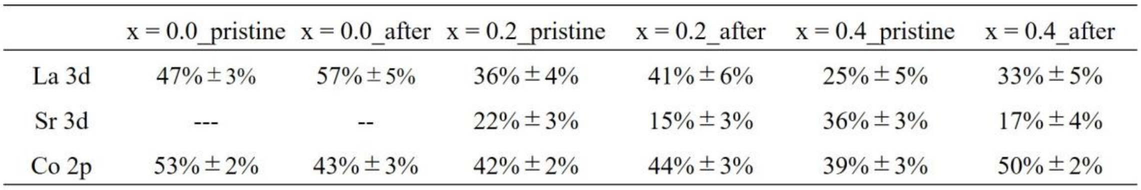

	x = 0.0_pristine	x = 0.0_after	x = 0.2_pristine	x = 0.2_after	x = 0.4_pristine	x = 0.4_after
La 3d	47% ± 3%	57% ± 5%	36% ± 4%	41% ± 6%	25% ± 5%	33% ± 5%
Sr 3d	---	--	22% ± 3%	15% ± 3%	36% ± 3%	17% ± 4%
Co 2p	53% ± 2%	43% ± 3%	42% ± 2%	44% ± 3%	39% ± 3%	50% ± 2%

Table 3.6. *Operando* EXAFS fitting results of Co-O bond for $LaCoO_{3-\delta}$.

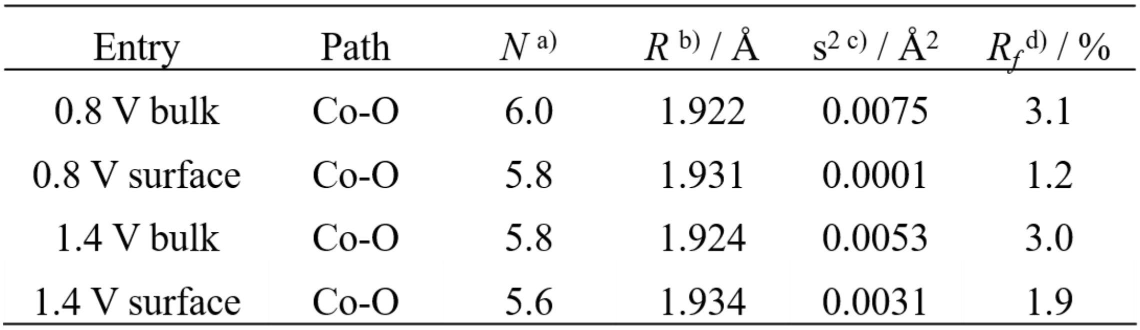

Entry	Path	N a)	R b) / Å	s^2 c) / Å^2	R_f d) / %
0.8 V bulk	Co-O	6.0	1.922	0.0075	3.1
0.8 V surface	Co-O	5.8	1.931	0.0001	1.2
1.4 V bulk	Co-O	5.8	1.924	0.0053	3.0
1.4 V surface	Co-O	5.6	1.934	0.0031	1.9

a) Coordination Number
b) Bond distance
c) Debye-Waller factor
d) Residual factor

$$R_f = \frac{\int \left| k^3 \chi^{obs}(k) - k^3 \chi^{calc}(k) \right|^2 dk}{\int \left| k^3 \chi^{obs}(k) \right|^2 dk} \times 100$$

Table 3.7. *Operando* EXAFS fitting results of Co-O bond for $La_{0.6}Sr_{0.4}CoO_{3-\delta}$.

Entry	Path	N [a]	R [b] / Å	σ^2 [c] / $Å^2$	R_f [d] / %
0.8 V bulk	Co-O	5.6	1.948	0.0060	0.4
0.8 V surface	Co-O	5.5	1.933	0.0147	2.7
1.0 V bulk	Co-O	5.6	1.955	0.0062	1.6
1.0 V surface	Co-O	5.4	1.950	0.0077	0.2
1.4 V bulk	Co-O	5.4	1.958	0.0047	0.5
1.4 V surface	Co-O	5.2	1.969	0.0105	1.5

a) Coordination Number

b) Bond distance

c) Debye-Waller factor

d) Residual factor

$$R_f = \frac{\int \left| k^3 \chi^{obs}(k) - k^3 \chi^{calc}(k) \right|^2 dk}{\int \left| k^3 \chi^{obs}(k) \right|^2 dk} \times 100$$

Chapter 4. The Effect of Cation Mixing in $LiNiO_2$ toward the Oxygen Evolution Reaction

Nickel-based oxide catalysts are widely used for the oxygen evolution reaction (OER) in alkaline water electrolysis because of their low cost and high activity. In particular, the $LiNiO_2$ catalyst shows high activity. Therefore, to elucidate the fundamental relationship between the local structure, catalyst activity, and stability of $LiNiO_2$, we investigated the cation mixing effect by mixing sites of lithium and nickel ions in the $LiNiO_2$-based catalysts. Lower degrees of cation mixing lead to higher intrinsic OER activity but lower long-term stability. The X-ray absorption spectra (XAS) displayed a strong hybridization state of the Ni 3*d* and O 2*p* orbitals, which is the origin of the different catalytic activity behaviors. Meanwhile, operando XAS studies combined with potentiostatic stability tests and inductively coupled plasma optical emission spectrometry (ICP-OES) demonstrated the Li ion loss during the OER process. Thus, the instability of $LiNiO_2$ originates from de-intercalation of Li ions and this irreversible structure change deteriorates the performance. Hindering the lithium diffusion path by cation mixing is a useful strategy for maintaining performance. This strategy could provide a novel design principle for compatible high activity and long-lasting catalysts by reasonable structure mediation.

4.1 Introduction

With increasing global environmental problems, hydrogen, produced by renewable energies, has been considered a sustainable and clean fuel for next-generation energy sources[1]. Among the many proposed methods to produce hydrogen, the most renewable method is water electrolysis. However, the four electrons/protons needed for the oxygen evolution reaction (OER) in water electrolysis result in sluggish kinetics and low efficiency, representing the biggest obstacle for widespread applications[2-5]. Polymer electrolysis membrane (PEM) electrolysis is expected to be commercialized due to its high current density, compact system, and high gas purity[6-8]. Nevertheless, catalyst corrosion in acidic environments and high maintenance costs limit their general application[9-11]. In contrast, alkaline water electrolysis (AWE) has been considered an alternative method for hydrogen production because earth-abundant transition-metal oxides (TM<C=>Fe, Co, and Ni) can be used as catalysts, and certain states of TM cations accelerate the OER[12-16].

To date, many researchers have reported the fundamental mechanism for OER in terms of crystal structures[17-19], electronic structures[20-21] and oxygen vacancy analysis[22]. Earlier studies showed that catalyst performance is related to the binding strength of adsorption intermediates. Suntivich et. al. first demonstrated the relationship between transition metal e_g occupancy and OER activity[23]. More recently, Shao-Horn’s group studied the critical role of metal-oxygen bonds in triggering lattice-oxygen oxidation[24] and the local environment of active site[25]. Further studies showed a strong correlation between OER activity and oxygen p-band center relative to the Fermi level through theoretical calculations[26]. Other parameters, including cations in octahedral sites and transition metal $3d$ - O $2p$ hybridization, have been widely studied by metal doping or partial element substitution[27-30]. Surface reconstruction mediated by transition metals has been reported to form active reaction sites, such as oxyhydroxide sites on the catalyst interface[31,32]. The speed and degree of this active surface reconstruction significantly influences the subsequent deprotonation step, which directly affects OER performance.

While many studies have been devoted to investigating the fundamental kinetics during OER, few have focused on the catalytic degradation process. An early study on the $IrO_x/SrIrO_3$ catalyst revealed that Sr leaching affected the surface rearrangements and contributed to increased stability[33]. Xu et. al. have recently reported that the leaching of Al in Fe-doped $CoAl_2O_4$ resulted in the self-termination of active surface reconstruction, yielding stable active sites for long-term OER[31]. Therefore, since the degradation mechanism depends on the nature of the material, investigating catalyst stability is necessary for designing superior OER catalysts.

Previous studies have focused on Ni-based oxides, including $Ni(OH)_2$ and doped NiOOH, due to their low material cost, easily mediated structure, and high OER activity originating from various dopants, making them promising catalysts to replace noble metal oxides[34-38]. Compared to Co-containing perovskite-type oxides[22,39], relatively few studies correlating the electronic states of Ni-based oxides with their OER activities have been reported. Recent studies on nickel oxides have elaborated the doping effect of lithium on catalyst activity[40,41], such as in $LiNiO_2$ where lithium doping changed the local electronic structure of nickel, improving OER activity. $LiNiO_2$ has a nominal oxidation state of Ni^{3+} and exhibits excellent OER activity considering the e_g state descriptor. Moreover, because the energy levels of the Ni 3*d* orbitals of $LiNiO_2$ are close to those of the O 2*p* orbitals, they can strongly hybridize[42]. Therefore, $LiNiO_2$ offers a suitable model to study the relationship between electronic structure and OER activity. However, for practical catalysts, the durability is also important and the deterioration mechanism of the $LiNiO_2$ catalyst has not yet been clarified. $LiNiO_2$, having an ordered rock salt structure, is a well-known cathode material for lithium-ion batteries, and exhibits extremely high lithium-ion mobility[43,44]. Thus, catalyst degradation may be caused by de-intercalation of lithium ions during anodic polarization. In the Li-ion battery field, many studies have shown that the electrochemical properties of $LiNiO_2$ cathodes are extremely dependent on the degree of cation mixing, primarily due to the presence of Ni^{2+} at Li^+ and Ni^{3+} sites because of the similarity in their ionic radii[45,46]. Cation mixing is a disadvantage for cathode materials because the presence of Ni^{2+} at Li^+ sites hinders Li^+ diffusion. Inspired by this, hindrance of the lithium diffusion path by cation mixing of Li and Ni is expected to be an effective solution when $LiNiO_2$ is applied as an OER catalyst to improve stability.

Herein, the cation mixing effect on OER activity and stability was studied using $Li_xNi_{2-x}O_2$. A combination of transmission electron microscopy (TEM), X-ray absorption near-edge structure (XANES), and extended X-ray absorption fine structure (EXAFS) investigations were conducted to probe the electronic structure of the materials. The valence changes of Ni during OER were further examined by *operando* X-ray absorption spectroscopy (XAS) using a home-made flow-type cell. The degradation process was also investigated in detail using *operando* XAS.

4.2 Experimental

4.2.1 Material synthesis

$Li_xNi_{2-x}O_2$ (x=0.69, 0.76, 0.9, 1.0) were synthesized using the citrate complex method. The molar ratios of x:(2−x):3 for $LiNO_3$ (FUJIFILM Wako Pure Chemical Corporation), $Ni(NO_3)_2 \cdot 6H_2O$ (FUJIFILM Wako Pure Chemical Corporation), and citric acid (anhydrous, FUJIFILM Wako Pure Chemical Corporation), respectively, were dissolved in deionized water. The mixed solution was dried to a powder on a hotplate at 350 °C for 2 h. The precursor powder was subsequently ground, pelletized, and calcined under different conditions to obtain different samples: 2 times at 800 °C for 5 h in air; at 800 °C for 10 h in air; at 550 °C for 5 h followed by 700 °C calcination for 20 h; 3 times at 800 °C for 5 h under an oxygen flow (5 mL min^{-1}).

4.2.2 Characterization

Synchrotron X-ray diffraction (XRD) was performed at beamline BL02B2 in SPring-8, Japan (Proposals No. 2019 A1796, 2019 A1812) and BL5S2 of Aichi Synchrotron Radiation

Center, Aichi Science & Technology Foundation, Aichi, Japan (Proposal No. 202002005). The wavelength was set at 0.61972 Å calibrated using CeO_2. The particle morphology of the samples was observed by TEM (JEM-2200FS, JEOL Ltd.) and scanning electron microscopy (SEM; S-3400 N, Hitachi High-Tech Corporation). Inductively coupled plasma optical emission spectroscopy (ICP-OES) was conducted to analyze the Li concentration in the $Li_xNi_{2-x}O_2$ samples before and after electrolysis (ICPS-8100CL, Shimadzu) at industrial research center of Shiga prefecture, Japan.

4.2.3 Electrochemical measurement

First, 5 mg of the as-prepared catalysts and 45 mL of 5 wt.% Nafion® solution (Sigma-Aldrich) were dispersed in 2 mL of ethanol (FUJIFILM Wako Pure Chemical Corporation) to prepare the catalyst ink. Subsequently, 24 µL of the ink was dropped on a glassy carbon rotating disk electrode (GC RDE, HOKUTO DENKO, area=0.196 cm^2) to support 0.3 mg cm^{-2} of the catalyst. The ink on the RDE was dried at 25 °C while rotating at 700 rpm. 0.1 M KOH electrolyte used for the electrochemical measurement was prepared from ultrapure water with electrical resistivity of 18.2 MΩ.cm or more (Milli-Q®, Millipore A/S) and KOH with an iron impurity content of 1 ppm or less (guaranteed reagent, Kanto Chemical Co., Inc) without any further purification.

The activity test of the OER was performed using a typical three-electrode cell with Pt wire as the counter electrode and a reversible hydrogen electrode (RHE) as the reference electrode. The catalyst loaded RDE was used as the working electrode. Cyclic voltammograms (CV) were preliminarily scanned for 100 cycles from 0.5 to 1.6 V (vs. RHE) at 100 mV s^{-1} in a N_2-saturated 0.1 M KOH aqueous solution to activate the catalyst surface. The OER activities were subsequently obtained by scanning from 1.1 to 1.7 V (vs. RHE) at 5 mV s^{-1} and a rotation speed of 1600 rpm. The durability tests were performed via potentiostatic electrolysis at 1.8 V (vs. RHE) and 3000 rpm for 60 min. The double layer capacitance was estimated from the CV plots obtained at 20, 40, 80, 100, and 200 mV s^{-1} from 0.95 to 1.05 V (vs. RHE).

4.2.4 X-ray absorption spectroscope

XANES and EXAFS at the Ni K-edge were measured at beamline BL01B1 and BL14B2 in SPring 8, Japan (Proposals No. 2017B1451, 2017B1555, 2017B1918, 2017B1919, 2018 A1592) and BL11S2 of Aichi Synchrotron Radiation Center, Aichi Science & Technology Foundation, Aichi, Japan (Proposal No. 202002006). XAS spectra were acquired in transmission and florescence modes at 25 °C using a Si (111) double-crystal monochromator. A 19-element Ge detector was used for fluorescence mode and a pair of Rh-coated mirrors was used to eliminate the higher harmonics. The Ni L-edge and O K-edge XANES spectra were collected in florescence mode at the Ritsumeikan SR center at BL10. The XAS spectra were analyzed using the Athena software package[47] *Operando* Ni K-edge XAS were collected using a home-made flow-type cell. The catalyst ink was loaded onto an Au (50 nm) sputtered polyetherimide film (Mitsubishi Chemical Corporation) to prepare both the X-ray window and working electrode. Cyclic voltammograms (CV) were preliminarily scanned for 100 cycles from 0.5 to 1.6 V (vs. RHE) at 100 mV s^{-1} in N_2-saturated 0.1 M KOH aqueous solution to activate the catalyst surface. The flow rate of the solution was controlled at 0.5 L min^{-1} using a non-pulsation pump. The durability tests were performed via potentiostatic electrolysis at 1.8 V (vs. RHE) for 60 min.

4.3 Results and discussion

4.3.1 Crystal Structure

The XRD patterns of the $Li_xNi_{2-x}O_2$ catalysts are provided in Figure 4.1a and all peaks were indexed to the layered rock salt structure of the rhombohedral phase of space group $R\bar{3}m$ according to the Rietveld refinement in Figure 4.2 and Table 4.1, in agreement with previous reports[40--41,48]. When the Li content changed from $LiNiO_2$ to $Li_{0.69}Ni_{1.31}O_2$, the 003 peak around 7.5° decreased, indicating cation mixing of the Li 3*a* site with the Ni 3*b* site. As shown in Figure 4.1b and Table 4.2, the lattice constants increased and the 3*a* site occupancy of Ni increased, verifying the increased degree of cation mixing. This is in accordance with the change of the intensities of the 003 peak at approximately 7.5° and the 111 peak at approximately 18° in the XRD pattern. This systematic change of structural parameters was in agreement with a previous study by Goodenough et. al[49]. In Figure 4.1b, the lattice constants decreased linearly with Li doping, following Vegard's law. This decrease in lattice constants was ascribed to the formation of Ni^{3+} induced by Li doping and shrinkage of the Ni-O bond. Moreover, to confirm the actual elemental contents, ICP-OES measurements were conducted and the results are shown in Table 4.3. Each composition was similar to the charged amount and the estimated values from the Rietveld refinement. In addition, the well-crystallized layered rock-salt structure of all samples was observed by TEM images and their fast Fourier transform (FFT) pattern is provided in Figure 4.1c. Two dominant crystal structures were observed in the pattern: $Fm\bar{3}m$ and $R\bar{3}m$. The rock-salt phase, $Fm\bar{3}m$, was found in NiO, while the FFT patterns of the Li-doped NiO provided evidence of conversion to a layered rock-salt phase, $R\bar{3}m$. The particle size of all samples was approximately 1 µm, as estimated from the SEM images in Figure 4.3.

4.3.2 Electrochemical Performance of the Catalysts

Figure 4.4 shows the CVs for all samples in 0.1 M N_2-saturated KOH solution. The electric double layer capacity from the CV measurements were subsequently measured following previously reported methods[50]. The scan results are shown in Figure 4.5 and the relative parameters are listed in Table 4.4. According to Figure 4.4a, $LiNiO_2$ shows the lowest onset potential for the OER current, indicating that it exhibits the best OER activity, in a good agreement with a previous study[40]. In addition, a decreasing tendency toward OER activity corresponds to increasing cation mixing. An obvious difference in redox behavior was observed at approximately 1.25 and 1.40 V (vs. RHE). This redox pair is directly related to the degree of cation mixing, as shown in Figure 4.6, and the lower cation mixing sample showed higher and sharper anodic/cathodic peaks. Moreover, the anodic/cathodic peak shifted positively/negatively with increasing Li content, which correlated with the observed OER activity trends. For $LiNiO_2$, one anodic (A1) and two cathodic peaks (C1, C2) were observed in the cyclic voltammetry in Figure 4.4a. These features were consistent with previously reported papers[51,52]. The oxidation peak of A1 and reduction peak of C1, C2 were considered the electrochemical delithiation and intercalation of proton, respectively[52], although their origin of structural changes have not yet revealed. Fu et. al. proposed that the redox peak of NiO is associated with a nominal Ni^{2+}/Ni^{3+} couple and the increased amount of Ni^{3+} induced by Li doping results in a positive shift of redox peaks associated with the nominal Ni^{3+}/Ni^{4+} redox couple[40]. These studies suggest that the behavior of the CVs presented herein corresponds to the de-intercalation of Li^+ and intercalation of H^+ in the $LiNiO_2$ host matrix, owing to the Ni^{3+}/Ni^{4+} redox. To directly compare the oxygen evolution kinetics, the Tafel slopes were estimated, as shown in Figure 4.4b. In this study, the Tafel slopes were estimated in the potential range from 1.5 to 1.6 V (vs. RHE) excluding 1.30-1.50 V (vs. RHE) as reported by Fu et. al.[40] because the redox peaks appeared. The slope for NiO was 80 mV dec^{-1}. and decreased to 64--70 mV dec^{-1} for $Li_xNi_{2-x}O_2$, consistent with the literature[40]. This reduction in the Tafel slope is related to the favorable adsorption of OH intermediates resulting from the Ni^{3+} oxidization state induced by Li doping[53].

To demonstrate the effect of cation mixing on catalyst stability, the potential was kept at 1.8 V (vs. RHE) for 3600 seconds. As shown in Figure 4.4c, $LiNiO_2$ with the best activity also showed the highest initial current density. However, the current density of $LiNiO_2$ suddenly decreased after approximately 10 seconds and showed the lowest current value after approximately 40 seconds. In contrast, $Li_{0.69}Ni_{1.31}O_2$ showed the best stability. As $LiNiO_2$ is a widely reported cathode material for lithium-ion batteries, de-intercalation of lithium ions likely occurs more easily during anodic polarization. Conversely, the cation mixing by Ni cations occupying Li sites results in a higher activation energy barrier for Li diffusion, while this structural instability deteriorates the charge/discharge performance[54,55]. Here, it was assumed that lithium de-intercalation leads to stability decay when $LiNiO_2$ is used as an OER catalyst. To confirm this assumption, ICP-OES measurements were conducted to investigate the catalyst composition after electrolysis. $LiNiO_2$ and $Li_{0.69}Ni_{1.31}O_2$ powders were collected from the GC electrode surfaces after the durability tests. As shown in Figure 4.4d, the Li content decreased to 85 % after the durability test, while the lithium in $Li_{0.69}Ni_{1.31}O_2$ maintained the same content before and after electrolysis. Therefore, it is clear that lithium deficiency is the reason behind the poor stability of $LiNiO_2$. Considering the structural change during the cation mixing, by replacing some Li 3*a* sites, Ni on the 3*a* site presents an obstacle for Li breaking away. Moreover, the TEM images shown in Figure 4.7 reveal that after electrolysis, the surface of $LiNiO_2$ became vague, while that of $Li_{0.69}Ni_{1.31}O_2$ remained nearly unchanged. Our results in Figure 4.7b indicate the surface layer with a thickness of about 5 nm formed after delithiation from the ordered $LiNiO_2$. Ren and co-workers have also reported that NiOOH layer with a thickness of 5--10 nm was formed on ordered $LiNiO_2$ after the electrolysis[56]. However, in the case of $Li_{0.69}Ni_{1.31}O_2$ (Figure 4.7a), the formation of the thick surface layer was not observed, which might be the reason of high durability of the catalyst.

4.3.3 Electronic Structure

XAS measurements were performed to determine the catalyst electronic structure and further explain the observed electrochemical behaviors. Figure 4.8 shows the Ni K-edge XANES spectra of $Li_xNi_{2-x}O_2$. With decreasing cation mixing, obvious trends toward the high energy side were observed, indicating the presence of a higher valence of Ni^{3+}, which was also verified in EXAFS. Figure 4.8b shows the Fourier transforms at the Ni K-edge oscillations, and the refined structural parameters are listed in Table 4.5. With increasing Li content, decreased cation mixing resulted in Ni-O and

Ni-Ni bond shrinkage. For example, the Ni-O and Ni-Ni bond lengths changed to 1.933 and 2.871 Å for $LiNiO_2$, while those of $Li_{0.69}Ni_{1.31}O_2$ were 1.955 Å and 2.914 Å, respectively. Further information regarding the state of Ni and O was probed by Ni L-edge and O K-edge XAS. The hybridized states of the Ni 3d and O 2p orbitals were investigated by O K-edge XAS, as shown in Figure 4.8c. The main characteristic peak of NiO at approximately 532 eV, which is assigned to the unoccupied Ni $3d\ e_g$ hybridized with O $2p$ orbitals, was not observed for other Li-containing materials. Instead, an additional feature appeared at approximately 528 eV, consistent with the literature[57--58]. This remarkable change was ascribed to the formation of an unoccupied hole state induced by Li doping, as suggested by the Ni L-edge XAS in Figure 4.8d. An additional peak at 857 eV was observed in Figure 4.8d, indicating that the formation of $3d^7$ and $3d^8\underline{L}$ configurations[59] (where $\underline{L}$ denotes a ligand hole) due to the strong covalent bond formed between the Ni 3d and O 2p orbitals[60].

4.3.4 Operando XAS Measurement

Figure 4.9 indicates the current-time response of $Li_{0.69}Ni_{1.31}O_2$ and $LiNiO_2$ in home-made flow cell for operando X-ray absorption spectroscopy. At 0.8 V, no current was observed. At 1.5 V, the higher current of $LiNiO_2$ than $Li_{0.69}Ni_{1.31}O_2$ was observed due to the high activity of $LiNiO_2$. However, the current was suddenly decreased when 1.8 V was applied for $LiNiO_2$ while $Li_{0.69}Ni_{1.31}O_2$ showed the stable current. Their behavior has a good agreement with Figure 4.4a, c. *operando* Ni K-edge XANES was performed to examine the dynamic valence state of Ni during the anodic CV sweep. As shown in Figure 4.10a and 4.10b, the spectra were recorded at 0.8, 1.5, and 1.8 V (vs. RHE) for $Li_{0.69}Ni_{1.31}O_2$ and $LiNiO_2$. For both catalysts, a shift toward the high-energy side was observed with increasing applied potential, indicating the emergence of the high oxidation state of Ni during the OER. Considering the CV plots in Figure 4.4a, this energy shift responds well to the different pseudocapacitive behaviors of $Li_{0.69}Ni_{1.31}O_2$ and

$LiNiO_2$. The more significant spectrum shift for $LiNiO_2$ was also correlated to a stronger redox peak than the others before OER. This *operando* XAS study showed that the pseudocapacitive redox behavior before OER indicates oxidation of Ni^{3+} to Ni^{4+} by de-intercalation of Li^+. Moreover, as shown in Figure 4.6, the larger charge of oxidation, the higher XANES shift was observed. Therefore, the presence of high valence state of Ni^{4+} on the surface promotes the OER activity[40]. The high valence state of Ni^{4+} was also found on $LiNiO_2$ after the electrochemical delithiation combining with XAS and XRD by Ren et. al.[56]. In this study, the oxidation state change of Ni^{3+} into Ni^{4+} due to the delithiation was confirmed by *operando* XAS measurements in Figure 4.10b. This result corresponds to Ren at al.[56], which is the strong evidence of the existence of Ni^{4+} under the electrolysis.

operando Ni K-edge XANES during the durability test was also performed to investigate the mechanism underlying the different OER performances. The results at the first minute and at the end of 60 min are shown in Figures 4.11a and 4.11b. $Li_{0.69}Ni_{1.31}O_2$ was unchanged after 60 min of electrolysis. In contrast, the XANES spectra of $LiNiO_2$ shifted to a higher energy in the first minute, which was further enhanced at the end of electrolysis, while the peak showed a lower intensity with a constant anodic potential. These behaviors were consistent with typical *operando* XAS of $LiNiO_2$ battery cathode materials during charging[61,62]. Therefore, it can be concluded that the instability of $LiNiO_2$ originated from the loss of Li ions in the bulk, and this irreversible structural change decreased performance because $LiNiO_2$ exhibits low electro-chemical stability[63,64]. Therefore, hindering the lithium diffusion path by cation mixing can improve the stability of $LiNiO_2$ by preventing the loss of Li ions from the host matrix. This is a useful guideline for designing future $LiNiO_2$-based OER catalysts.

4.4 Conclusions

This study focused on the cation mixing effects on OER activity and stability when $LiNiO_2$-based oxides are used as water oxidation electrocatalysts. Samples with different degrees of cation mixing were synthesized via the citrate complex method. The electrochemical tests showed that a lower degree of cation mixing results in improved OER activity, while the stability performance showed the opposite trend. XAS measurements revealed the formation of a hole state in the lower cation mixing material, indicating strong hybridization of the Ni 3d and O 2p orbitals and different pseudocapacitive behaviors towards the OER. The *operando* XAS study further revealed the shift toward a high oxidation of Ni during the OER. The local structure change during the stability test was studied by *operando* XANES, where $LiNiO_2$ showed significant spectral changes compared to $Li_{069}Ni_{1.31}O_2$. The instability of $LiNiO_2$ originated from de-intercalation of Li ions and the irreversible structure change decreased performance. The intercalation/de-intercalation of ions also occurs during the OER process, similar to lithium-ion batteries. It was demonstrated that hindering the lithium diffusion path by cation mixing is useful for maintaining performance. While abundant research has focused on facilitating catalyst active sites to improve OER activity, the fundamental degradation mechanism has attracted little attention. This study provides a novel design principle for compatible high activity and long-lasting catalysts by reasonable structure mediation induced by cation mixing.

Reference

1. Suen, N. T.; Hung, S. F.; Quan, Q.; Zhang, N.; Xu, Y. J.; Chen, H. M., Electrocatalysis for the oxygen evolution reaction: recent development and future perspectives., *Chem. Soc. Rev.* **2017**, 46, (2), 337–365.
2. Ouyang, T.; Ye, Y. Q.; Wu, C. Y.; Xiao, K.; Liu, Z. Q., Heterostructures Composed of N-Doped Carbon Nanotubes Encapsulating Cobalt and β-Mo(2) C Nanoparticles as Bifunctional Electrodes for Water Splitting. *Angew. Chem. Int. Ed.* **2019**, 58, (15) 4923–4928.

3. Feng, J.-X.; Ye, S.-H.; Xu, H.; Tong, Y.-X.; Li, G.-R., Design and Synthesis of FeOOH/CeO2 Heterolayered Nanotube Electrocatalysts for the Oxygen Evolution Reaction. *Adv. Mater.* **2016**, 28, (23) 4698–4703.
4. Cao, J.; Lei, C.; Yang, J.; Cheng, X.; Li, Z.; Yang, B.; Zhang, X.; Lei, L.; Hou, Y.; Ostrikov, K., An ultrathin cobalt-based zeolitic imidazolate framework nanosheet array with a strong synergistic effect towards the efficient oxygen evolution reaction. *J. Mater. Chem. A* **2018**, 6, (39) 18877–18883.
5. Lu, X. F.; Gu, L. F.; Wang, J. W.; Wu, J. X.; Liao, P. Q.; Li, G. R., Bimetal-Organic Framework Derived $CoFe_2O_4$ /C Porous Hybrid Nanorod Arrays as High-Performance Electrocatalysts for Oxygen Evolution Reaction. *Adv. Mater.* **2017**, 29, (3) 1604437.
6. Carmo, M.; Fritz, D. L.; Merge, J.; Stolten, D., A comprehensive review on PEM water electrolysis. *Int. J. Hydrogen Energy* **2013**, 38, (12) 4901–4934.
7. Puthiyapura, V. K.; Mamlouk, M.; Pasupathi, S.; Pollet, B. G.; Scott, K., Physical and electrochemical evaluation of ATO supported IrO_2 catalyst for proton exchange membrane water electrolyser. *J. Power Sources* **2014**, 269, 451–460.
8. Siracusano, S.; Van Dijk, N.; Payne-Johnson, E.; Baglio, V.; Arico, A. S., Nanosized IrO_x and $IrRuO_x$ electrocatalysts for the O_2 evolution reaction in PEM water electrolysers. *Appl. Catal. B* **2015**, 164, 488–495.
9. Rashid, M. M.; Al Mesfer, M. K.; Naseem, H.; Danish, M., Hydrogen production by water electrolysis: a review of alkaline water electrolysis, PEM water electrolysis and high temperature water electrolysis. *Int. J. Eng.* **2015**, 4, (3) 2249–8958.

10. Millet, P.; Mbemba, N.; Grigoriev, S. A.; Fateev, V. N.; Aukauloo, A.; Etiévant, C., Electrochemical performances of PEM water electrolysis cells and perspectives. *Int. J. Hydrogen Energy* **2011**, 36, (6) 4134–4142.

11. Marshall, A. T.; Sunde, S.; Tsypkin, M.; Tunold, R., Performance of a PEM water electrolysis cell using $Ir_xRu_yTa_zO_2$ electrocatalysts for the oxygen evolution electrode. *Int. J. Hydrogen Energy* **2007**, 32, (13) 2320–2324.

12. Hwang, J.; Rao, R. R.; Giordano, L.; Katayama, Y.; Yu, Y.; Shao-Horn, Y., Perovskites in catalysis and electrocatalysis. *Science* **2017**, 358, (6364) 751–756.

13. Li, X.; Wang, H.; Cui, Z. M.; Li, Y. T.; Xin, S.; Zhou, J. S.; Long, Y. W.; Jin, C. Q.; Goodenough, J. B., Exceptional oxygen evolution reactivities on $CaCoO_3$ and $SrCoO_3$. *Sci. Adv.* **2019**, 5, (8) No. eaav6262.

14. Sun, S. N.; Sun, Y. M.; Zhou, Y.; Xi, S. B.; Ren, X.; Huang, B. C.; Liao, H. B.; Wang, L. Y. P.; Du, Y. H.; Xu, Z. C., Shifting Oxygen Charge Towards Octahedral Metal: A Way to Promote Water Oxidation on Cobalt Spinel Oxides. *Angew. Chem. Int. Ed.* **2019**, 58, (18) 6042–6047.

15. Hong, W. T.; Stoerzinger, K. A.; Lee, Y. L.; Giordano, L.; Grimaud, A.; Johnson, A. M.; Hwang, J.; Crumlin, E. J.; Yang, W. L.; Shao-Horn, Y., Charge-transfer-energy-dependent oxygen evolution reaction mechanisms for perovskite oxides. *Energy Environ. Sci.* **2017**, 10, 2190–2200.

16. Yang, F.; Sliozberg, K.; Sinev, I.; Antoni, H.; Bähr, A.; Ollegott, K.; Xia, W.; Masa, J.; Grünert, W.; Cuenya, B. R.; Schuhmann, W.; Muhler, M., Synergistic Effect of Cobalt and Iron in Layered Double Hydroxide Catalysts for the Oxygen Evolution Reaction. *ChemSusChem*. **2017**, 10, 156–165.

17. Li, H.; Chen, Y.; Xi, S.; Wang, J.; Sun, S.; Sun, Y.; Du, Y.; Xu, Z. J., Degree of Geometric Tilting Determines the Activity of FeO_6 Octahedra for Water Oxidation. *Chem. Mater.* **2018**, 30, (13) 4313–4320.
18. Fabbri, E.; Nachtegaal, M.; Binninger, T.; Cheng, X.; Kim, B. J.; Durst, J.; Bozza, F.; Graule, T.; Schäublin, R.; Wiles, L.; Pertoso, M.; Danilovic, N.; Ayers, K. E.; Schmidt, T. J., Dynamic surface self-reconstruction is the key of highly active perovskite nano-electrocatalysts for water splitting. *Nat. Mater.* **2017**, 16, (9), 925-931.
19. Bergmann, A.; Martinez-Moreno, E.; Teschner, D.; Chernev, P.; Gliech, M.; de Araújo, J. F.; Reier, T.; Dau, H.; Strasser, P., Reversible amorphization and the catalytically active state of crystalline Co_3O_4 during oxygen evolution. *Nat. Commun.* **2015**, 6, (1), 8625.
20. Suntivich, J.; Hong, W. T.; Lee, Y.-L.; Rondinelli, J. M.; Yang, W.; Goodenough, J. B.; Dabrowski, B.; Freeland, J. W.; Shao-Horn, Y., Estimating Hybridization of Transition Metal and Oxygen States in Perovskites from O K-edge X-ray Absorption Spectroscopy. *J. Phys. Chem. C* **2014**, 118, (4),1856–1863.
21. Cheng, J.; Liu, X.; Kattirtzi, J. A.; VandeVondele, J.; Sprik, M., Aligning Electronic and Protonic Energy Levels of Proton-Coupled Electron Transfer in Water Oxidation on Aqueous TiO2. *Angew. Chem. Int. Ed.* **2014**, 53, 12046–12050; *Angew. Chem.* **2014**, 126, 12242–12246.
22. Mefford, J. T.; Rong, X.; Abakumov, A. M.; Hardin, W. G.; Dai, S.; Kolpak, A. M.; Johnston, K. P.; Stevenson, K. J., Water electrolysis on $La_{1-x}Sr_xCoO_{3-\delta}$ perovskite electrocatalysts. *Nat. Commun.* **2016**, 7, (1), 11053.

23. Suntivich, J.; May, K. J.; Gasteiger, H. A.; Goodenough, J. B.; Shao-Horn, Y., A Perovskite Oxide Optimized for Oxygen Evolution Catalysis from Molecular Orbital Principles. *Science* **2011**, 334, (6061), 1383-1385.
24. Grimaud, A.; Diaz-Morales, O.; Han, B.; Hong, W. T.; Lee, Y. L.; Giordano, L.; Stoerzinger, K. A.; Koper, M. T. M.; Shao-Horn, Y., Activate lattice oxygen redox reactions in metal oxides to catalyse oxygen evolution. *Nat. Chem.* **2017**, 9, 457–465.
25. Rao, R. R.; Kolb, M. J.; Giordano, L.; Pedersen, A. F.; Katayama, Y.; Hwang, J.; Mehta, A.; You, H.; Lunger, J. R.; Zhou, H.; Halck, N. B.; Vegge, T.; Chorkendorff, I.; Stephens, I. E. L.; Shao-Horn, Y., *Operando* identification of site-dependent water oxidation activity on ruthenium dioxide single-crystal surfaces. *Nat. Catal.* **2020**, 3 (6), 516-525.
26. Jacobs, R.; Hwang, J.; Shao-Horn, Y.; Morgan, D., Assessing Correlations of Perovskite Catalytic Performance with Electronic Structure Descriptors. *Chem. Mater.* **2019**, 31, (3), 785-797.
27. Wei, C.; Feng, Z. X.; Scherer, G. G.; Barber, J.; Shao-Horn, Y.; Xu, Z. C. J., Cations in Octahedral Sites: A Descriptor for Oxygen Electrocatalysis on Transition-Metal Spinels. *Adv. Mater.* **2017,** 29, (23), 1606800.
28. Wang, H. Y.; Hung, S. F.; Chen, H. Y.; Chan, T. S.; Chen, H. M.; Liu, B., In *Operando* Identification of Geometrical-Site-Dependent Water Oxidation Activity of Spinel Co_3O_4. *J. Am. Chem. Soc.* **2016**, 138, (1), 36-39.
29. Yamada, I.; Takamatsu, A.; Asai, K.; Shirakawa, T.; Ohzuku, H.; Seno, A.; Uchimura, T.; Fujii, H.; Kawaguchi, S.; Wada, K.; Ikeno, H.; Yagi, S., Systematic Study of

Descriptors for Oxygen Evolution Reaction Catalysis in Perovskite Oxides. *J. Phys. Chem. C.* **2018**, 122, (49), 27885-27892.

30. Li, H. Y.; Sun, S. N.; Xi, S. B.; Chen, Y. B.; Wang, T.; Du, Y. H.; Sherburne, M.; Ager, J. W.; Fisher, A. C.; Xu, Z. C. J., Metal-Oxygen Hybridization Determined Activity in Spinel-Based Oxygen Evolution Catalysts: A Case Study of $ZnFe_{2-x}Cr_xO4$. *Chem. Mater.* **2018**, 30, (19), 6839-6848.
31. Wu, T.; Sun, S.; Song, J.; Xi, S.; Du, Y.; Chen, B.; Sasangka, W. A.; Liao, H.; Gan, C. L.; Scherer, G. G.; Zeng, L.; Wang, H.; Li, H.; Grimaud, A.; Xu, Z. J., Iron-facilitated dynamic active-site generation on spinel $CoAl_2O_4$ with self-termination of surface reconstruction for water oxidation. *Nat. Catal.* **2019**, 2, (9), 763-772.
32. Song, J.; Wei, C.; Huang, Z.-F.; Liu, C.; Zeng, L.; Wang, X.; Xu, Z. J., A review on fundamentals for designing oxygen evolution electrocatalysts. *Chem. Soc. Rev.* **2020**, 49, (7), 2196-2214.
33. Seitz, L. C.; Dickens, C. F.; Nishio, K.; Hikita, Y.; Montoya, J.; Doyle, A.; Kirk, C.; Vojvodic, A.; Hwang, H. Y.; Norskov, J. K.; Jaramillo, T. F., A highly active and stable $IrO_x/SrIrO_3$ catalyst for the oxygen evolution reaction. *Science* **2016**, 353, (6303), 1011-1014.
34. Shin, H.; Xiao, H.; Goddard, W. A., In Silico Discovery of New Dopants for Fe-Doped Ni Oxyhydroxide ($Ni_{1-x}Fe_xOOH$) Catalysts for Oxygen Evolution Reaction. *J. Am. Chem. Soc.* **2018**, 140, (22), 6745–6748.
35. Martirez, J. M. P.; Carter, E. A., Noninnocent Influence of Host β-NiOOH Redox Activity on Transition-Metal Dopants' Efficacy as Active Sites in Electrocatalytic Water Oxidation. ACS Catal. 2020, 10, (4), 2720–2734.

36. Zhao, G.; Li, P.; Cheng, N.; Dou, S. X.; Sun, W., An Ir/Ni(OH)$_2$ Heterostructured Electrocatalyst for the Oxygen Evolution Reaction: Breaking the Scaling Relation, Stabilizing Iridium(V), and Beyond. *Adv. Mater.* **2020**, 32, 2000872.

37. Saha, S.; Ganguli, A. K., FeCoNi Alloy as Noble Metal-Free Electrocatalyst for Oxygen Evolution Reaction (OER). *ChemistrySelect* **2017**, 2 (4), 1630-1636.

38. Mahala, C.; Devi Sharma, M.; Basu, M., Fe-Doped Nickel Hydroxide/Nickel Oxyhydroxide Function as an Efficient Catalyst for the Oxygen Evolution Reaction. *ChemElectroChem* **2019**, 6 (13), 3488-3498.

39. Rincón, R. A.; Ventosa, E.; Tietz, F.; Masa, J.; Seisel, S.; Kuznetsov, V.; Schuhmann, W., Evaluation of Perovskites as Electrocatalysts for the Oxygen Evolution Reaction. *ChemPhysChem* **2014**, 15 (13), 2810-2816.

40. Fu, G. L.; Wen, X. J.; Xi, S. B.; Chen, Z. L.; Li, W. W.; Zhang, J. Y.; Tadich, A.; Wu, R. B.; Qi, D. C.; Du, Y. H.; Cheng, J.; Zhang, K. H. L., Tuning the Electronic Structure of NiO via Li Doping for the Fast Oxygen Evolution Reaction. *Chem. Mater.* **2019**, 31, (2), 419-428.

41. Zhang, J. Y.; Li, W. W.; Hoye, R. L. Z.; MacManus-Driscoll, J. L.; Budde, M.; Bierwagen, O.; Wang, L.; Du, Y.; Wahila, M. J.; Piper, L. F. J.; Lee, T. L.; Edwards, H. J.; Dhanak, V. R.; Zhang, K. H. L., Electronic and transport properties of Li-doped NiO epitaxial thin films. *J. Mater. Chem. C* **2018**, 6, 2275– 2282.

42. Kalyani, P.; Kalaiselvi, N., Various aspects of LiNiO$_2$ chemistry: A review. *Sci. Technol. Adv. Mater.* **2005**, 6, (6), 689-703.

43. Grimaud, A.; Hong, W. T.; Shao-Horn, Y.; Tarascon, J. M., Anionic redox processes for electrochemical devices. *Nat. Mater.* **2016**, 15, (2) 121–126.

44. Ohzuku, T.; Ueda, A.; Nagayama, M., Electrochemistry and structural chemistry of LiNiO2 (R3m) for 4 volt secondary lithium cells. *J. Electrochem. Soc.* **1993**, 140, (7), 1862.

45. Choi, Y.-M.; Pyun, S.-I.; Bae, J.-S.; Moon, S.-I., Effects of lithium content on the electrochemical lithium intercalation reaction into $LiNiO_2$ and $LiCoO_2$ electrodes. *J. Power Sources* **1995**, 56, (1) 25– 30.

46. Muto, S.; Sasano, Y.; Tatsumi, K.; Sasaki, T.; Horibuchi, K.; Takeuchi, Y.; Ukyo, Y., Capacity-fading mechanisms of $LiNiO_2$-based lithium-ion batteries II. Diagnostic analysis by electron microscopy and spectroscopy. *J. Electrochem. Soc*. **2009**, 156, (5), A371–A377.

47. Ravel, B.; Newville, M., ATHENA, ARTEMIS, HEPHAESTUS: data analysis for X-ray absorption spectroscopy using IFEFFIT. *J. Synchrotron Radiat.* **2005**, 12, (4), 537–541.

48. Gupta, A.; Chemelewski, W. D.; Buddie Mullins, C.; Goodenough, J. B., High-Rate Oxygen Evolution Reaction on Al-Doped $LiNiO_2$. *Adv. Mater.* **2015**, 27, (39), 6063-6067.

49. Goodenough, J. B.; Wickham, D. G.; Croft, W. J., Some magnetic and crystallographic properties of the system $Li^{+}_{x}Ni^{++}_{1-2x}Ni^{+++}_{x}O$. *J. Phys. Chem. Solids* **1958**, 5, (1), 107–116.

50. Kornienko, N., Enhancing Catalysis through Substitute-Driven Redox Tuning. *Joule* **2018**, 2, (2), 207-209.

51. Mohan Rao, M.; Jayalakshmi, M.; Schäf, O.; Guth, U.; Wulff, H.; Scholz, F., Electrochemical behaviour of solid lithium nickelate ($LiNiO_2$) in an aqueous electrolyte system. *J. Solid State Electrochem.* **1999**, 4, (1), 17–23.

52. Augustyn, V.; Therese, S.; Turner, T. C.; Manthiram, A., Nickel-rich layered $LiNi_{1-x}M_xO_2$ (M = Mn, Fe, and Co) electrocatalysts with high oxygen evolution reaction activity. *J. Mater. Chem. A*, **2015**, 3, (32), 16604-16612.

53. Bockris, J. O. M., The Electrocatalysis of Oxygen Evolution on Perovskites. *J. Electrochem. Soc.* **1984**, 131, (2), 290.

54. Zou, Y.; Yang, X.; Lv, C.; Liu, T.; Xia, Y.; Shang, L.; Waterhouse, G. I.; Yang, D.; Zhang, T., Multishelled Ni-Rich Li $(Ni_xCo_yMn_z)$ O_2 Hollow Fibers with Low Cation Mixing as High-Performance Cathode Materials for Li-Ion Batteries. *Adv. Sci.* **2017**, 4, (1), 1600262.

55. Zhang, X.; Jiang, W.; Mauger, A.; Gendron, F.; Julien, C., Minimization of the cation mixing in $Li_{1+x}(NMC)_{1-x}O_2$ as cathode material. *J. Power Sources* **2010**, 195, (5), 1292–1301.

56. Ren, X.; Wei, C.; Sun, Y.; Liu, X.; Meng, F.; Meng, X.; Sun, S.; Xi, S.; Du, Y.; Bi, Z.; Shang, G.; Fisher, A. C.; Gu, L.; Xu, Z. J., Constructing an Adaptive Heterojunction as a Highly Active Catalyst for the Oxygen Evolution Reaction. *Adv. Mater.* **2020**, 32 (30), 2001292.

57. Zhang, K. H. L.; Wu, R.; Tang, F.; Li, W.; Oropeza, F. E.; Qiao, L.; Lazarov, V. K.; Du, Y.; Payne, D. J.; MacManus-Driscoll, J. L.; Blamire, M. G., Electronic Structure and Band Alignment at the NiO and $SrTiO_3$ p–n Heterojunctions. *ACS Appl. Mater. Interfaces* **2017**, 9, (31), 26549–26555.

58. Uchimoto, Y.; Sawada, H.; Yao, T., Changes in electronic structure by Li ion deintercalation in $LiNiO_2$ from nickel L-edge and O K-edge XANES. *J. Power Sources* **2001**, 97-98, 326-327.

59. van Elp, J.; Searle, B. G.; Sawatzky, G. A.; Sacchi, M., Ligand hole induced symmetry mixing of d8 states in $Li_xNi_{1-x}O$, as observed in Ni 2*p* x-ray absorption spectroscopy. *Solid State Commun.* **1991**, 80, (1), 67–71

60. Kuiper, P.; Kruizinga, G.; Ghijsen, J.; Sawatzky, G. A.; Verweij, H., Character of holes in $Li_xNi_{1-x}O$ and their magnetic behavior. *Phys. Rev. Lett.* **1989**, 62, (2), 221–224.

61. Nowack, L.; Grolimund, D.; Samson, V.; Marone, F.; Wood, V., Rapid Mapping of Lithiation Dynamics in Transition Metal Oxide Particles with Operando X-ray Absorption Spectroscopy. *Sci. Rep.* **2016**, 6, (1), 21479.

62. Nishimura, Y. F.; Kondo, Y.; Oka, H., Estimation of the average oxidation number of nickel in a nickel oxide based on local structural information. *Power Sources* **2020**, 446, 227351.

63. Mu, L.; Kan, W. H.; Kuai, C.; Yang, Z.; Li, L.; Sun, C.-J.; Sainio, S.; Avdeev, M.; Nordlund, D.; Lin, F., Structural and Electrochemical Impacts of Mg/Mn Dual Dopants on the $LiNiO_2$ Cathode in Li-Metal Batteries. *ACS Appl. Mater. Interfaces* **2020**, 12, (11), 12874–12882.

64. Cho, E.; Seo, S.-W.; Min, K., Theoretical Prediction of Surface Stability and Morphology of $LiNiO_2$ Cathode for Li Ion Batteries. ACS Appl. Mater. Interfaces 2017, 9, 33257– 33266.

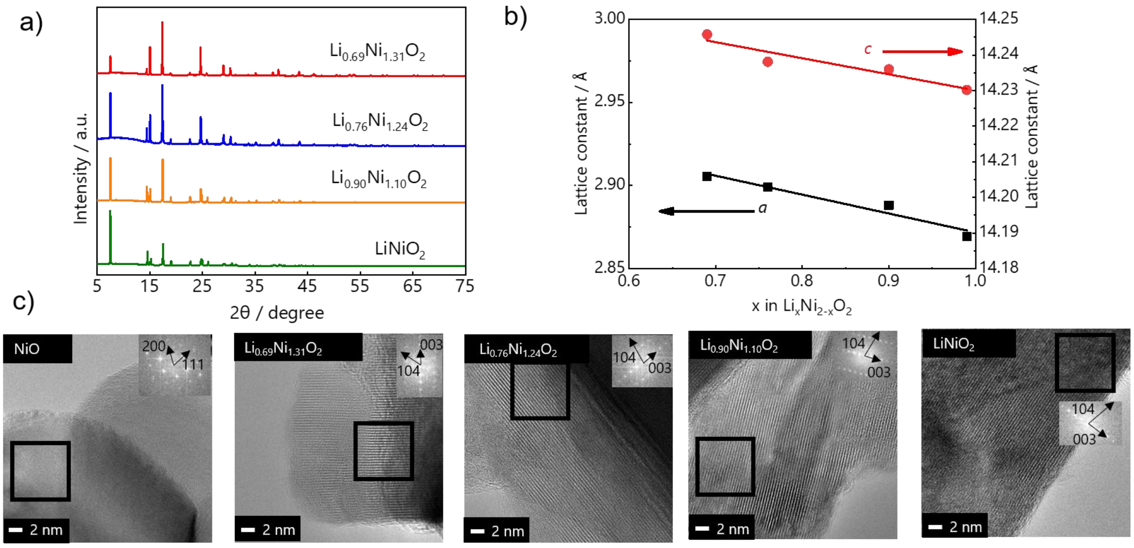

Figure 4.1. Crystal structures for NiO and $Li_xNi_{2-x}O_2$ (x=0.69, 0.76, 0.9, 1.0). a) XRD patterns; b) lattice constant changes extracted from XRD as a function of x; c) TEM images with FFT pattern of the as-synthesized samples.

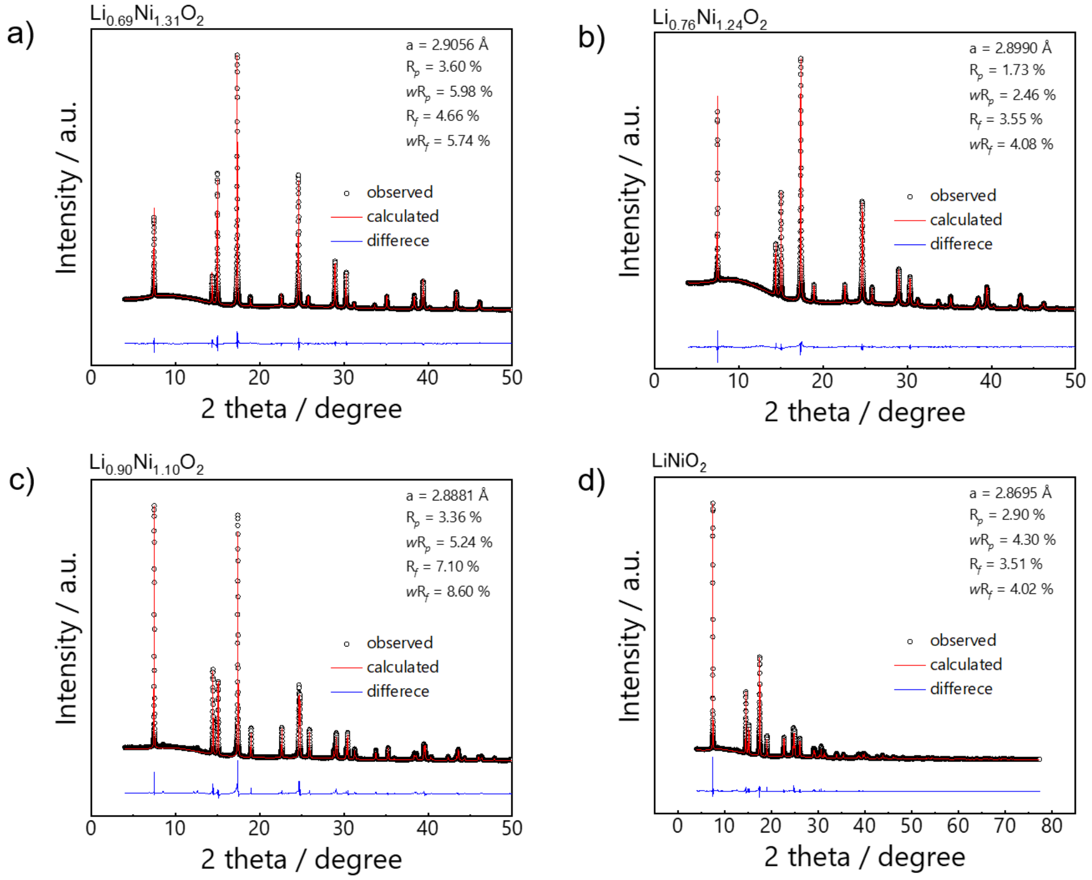

Figure 4.2. XRD Rietveld refinement results of as-synthesized catalysts

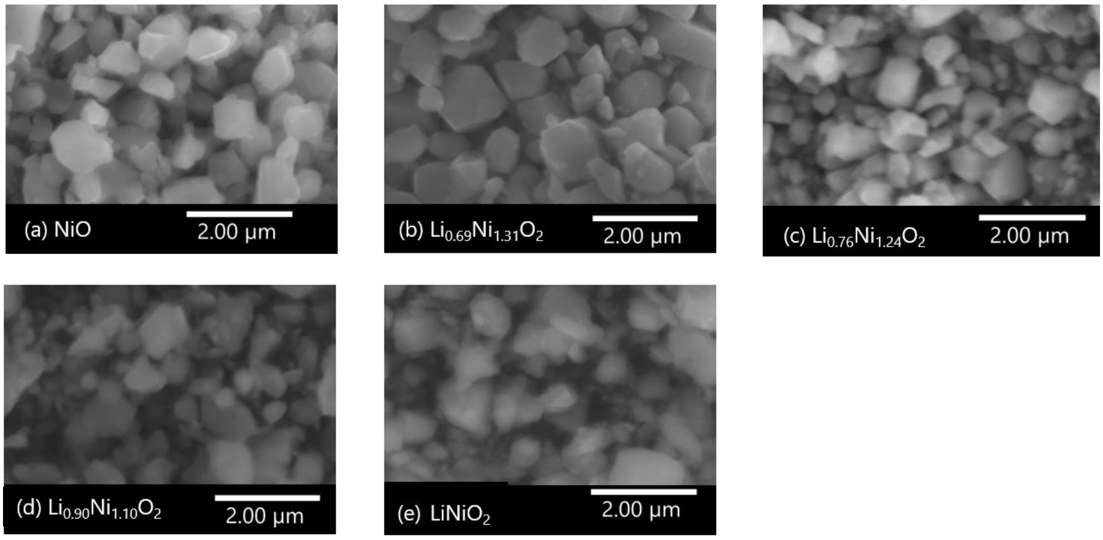

Figure 4.3. SEM images of as-synthesized catalysts

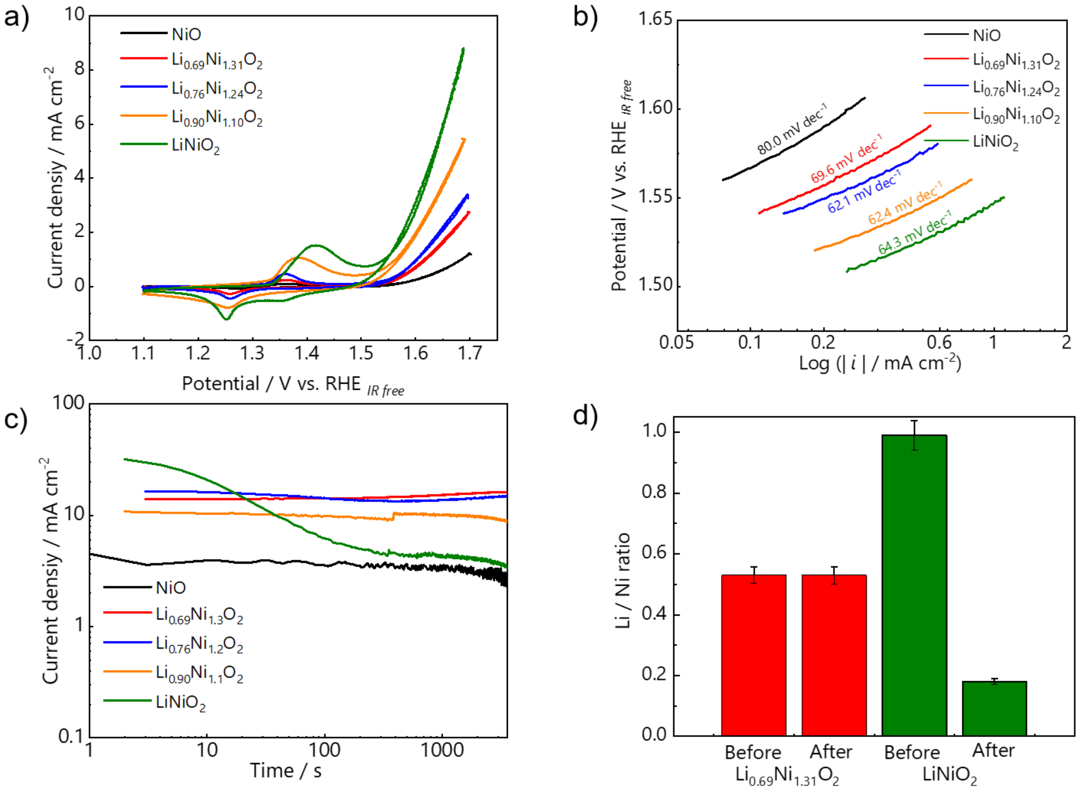

Figure 4.4. a) OER activities of $Li_xNi_{2-x}O_2$; b) Tafel plots; c) durability test at 1.8 V vs. RHE for 60 min; d) ICP analysis after the durability test.

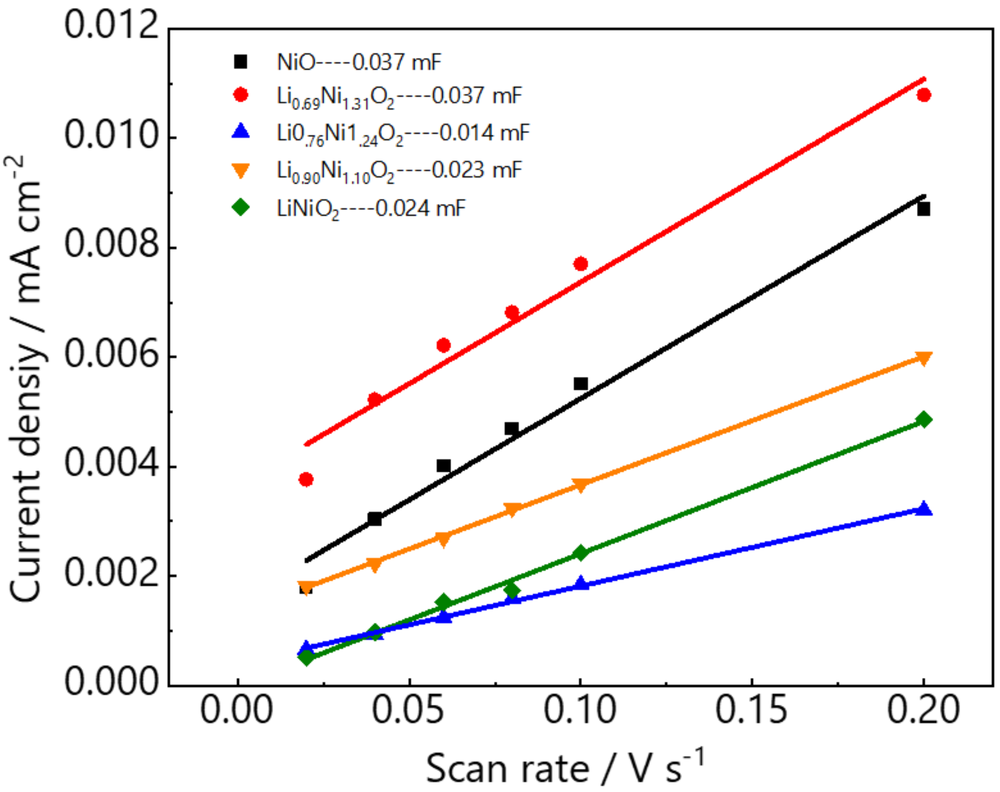

Figure 4.5. Double layer capacity measurement results.

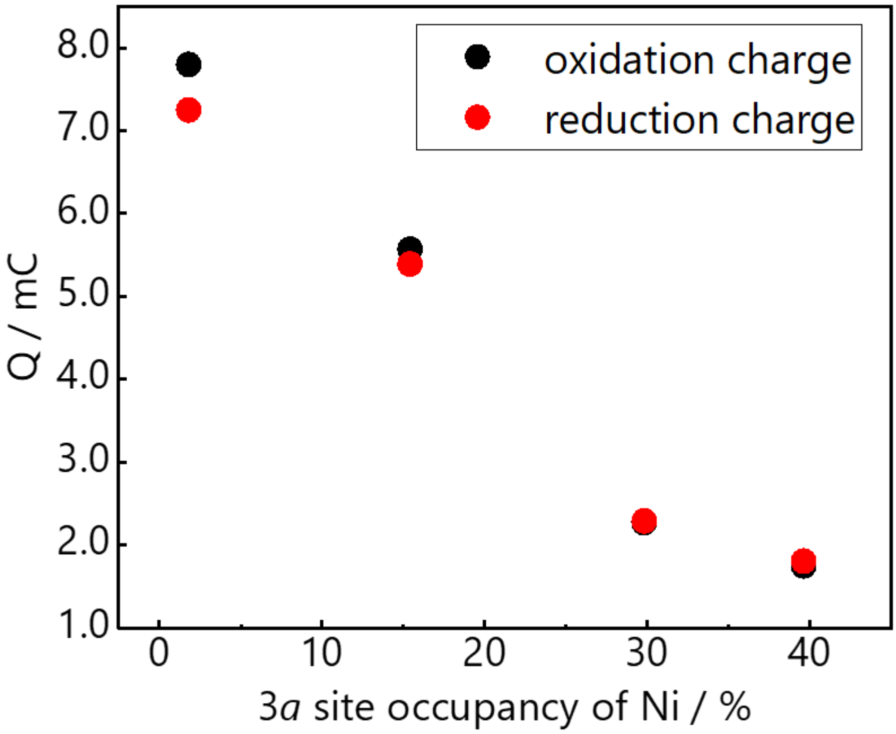

Figure 4.6. Oxidation/reduction charge with different nickel site occupancy in cyclic voltammetry

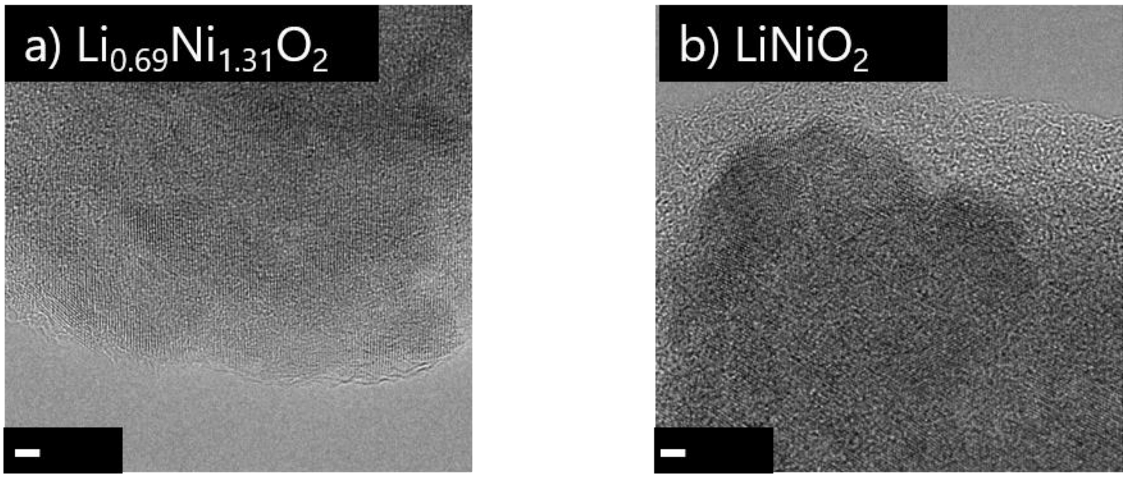

Figure 4.7. TEM images after electrolysis for a) $Li_{0.69}Ni_{1.31}O_2$ and b) $LiNiO_2$

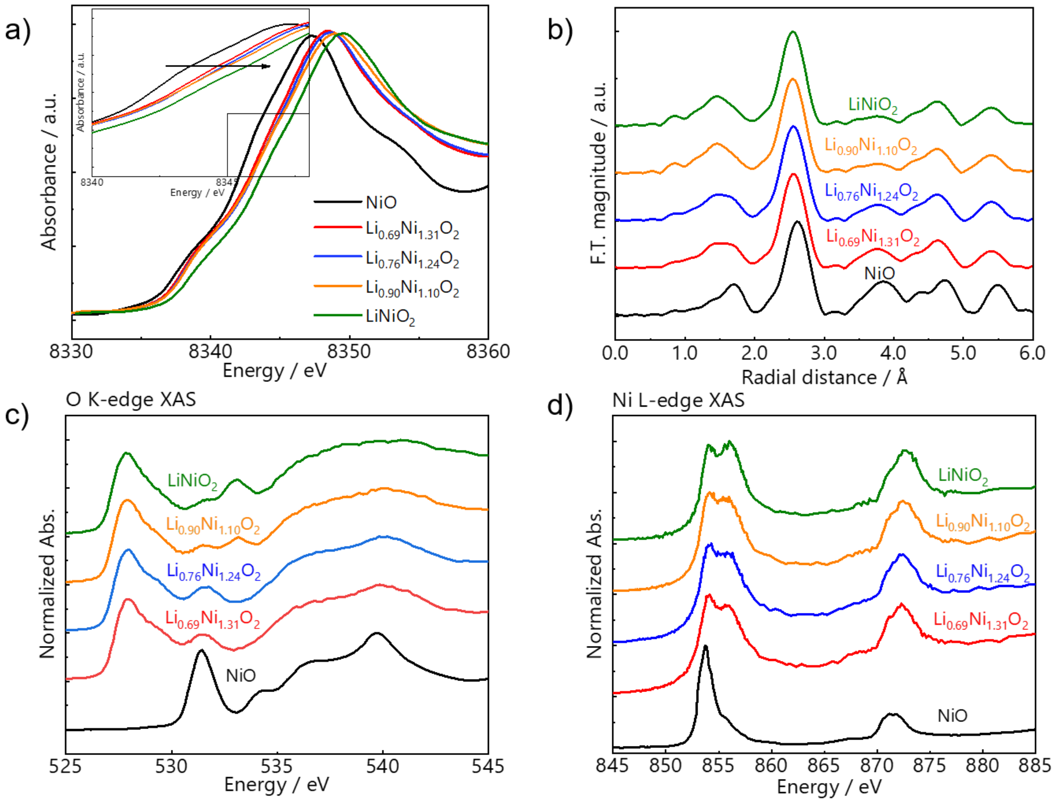

Figure 4.8. Electronic structures of $Li_xNi_{2-x}O_2$(x=0.69, 0.76, 0.9, 1.0). a) Ni Kedge XANES spectra (Inset is the enlarged region at the main adsorption edge). The shift towards the high-energy side with increasing× indicates increasing Ni oxidation states. b) Fourier transform of Ni K-edge EXAFS spectra, c) O K-edge, and d) Ni L-edge XAS.

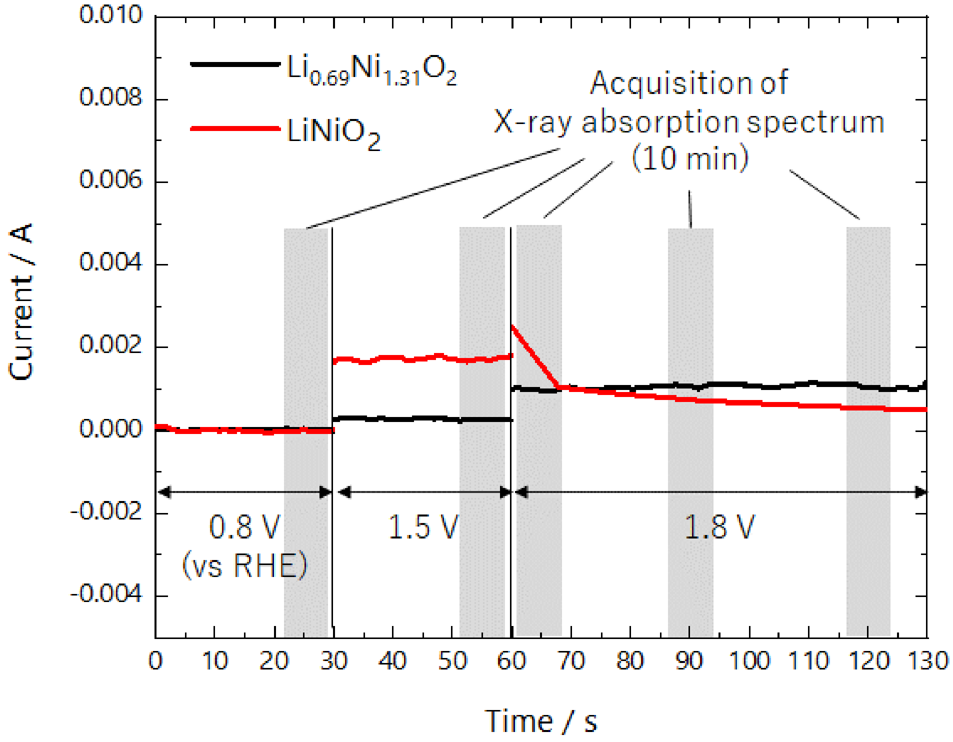

Figure 4.9. Current-time response of $Li_{0.69}Ni_{1.31}O_2$ and $LiNiO_2$ in home-made flow cell for operando X-ray absorption spectroscopy. X-ray absorption spectra was measured at the time shown in gray in the figure.

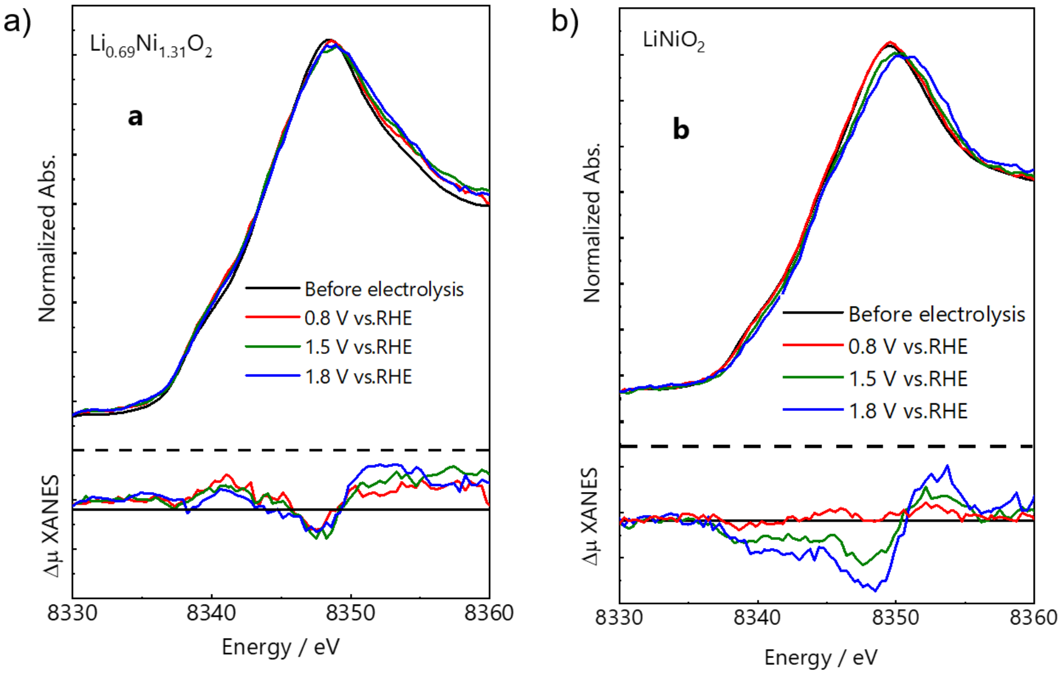

Figure 4.10. *Operando* Ni K-edge XANES spectra and relative difference spectra of a) $Li_{0.69}Ni_{1.31}O_2$ and b) $LiNiO_2$ immediately after applying the potential.

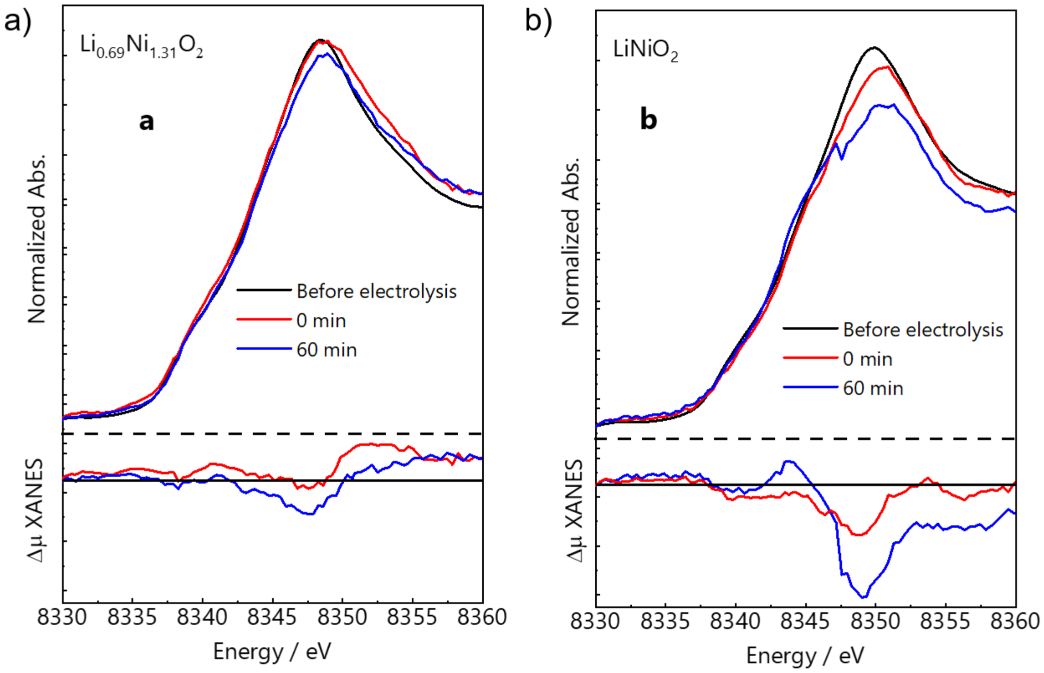

Figure 4.11. operando Ni K-edge XANES spectra and relative difference spectra of a) $Li_{0.69}Ni_{1.31}O_2$ and b) $LiNiO_2$ during the durability test with the potential maintained at 1.8 V vs. RHE

Table 4.1. Rietveld refinement results of $Li_xNi_{1-x}O_2$

sample	Spacegroup	Atom	Wyck	Site	S.O.F	x / a	y / b	z / c	U / Å^2
$Li_{0.69}Ni_{1.31}O_2$	R-3m(166) - trigonal	Li1	3a	-3m	0.604	0	0	0	0.0053
		Ni1	3a	-3m	0.396	0	0	0	0.0053
		Li2	3b	-3m	0.065	0	0	0.5	0.0053
		Ni2	3b	-3m	0.935	0	0	0.5	0.0053
		O1	6c	3m	2	0	0	0.23858	0.0053
$Li_{0.76}Ni_{1.24}O_2$	R-3m(166) - trigonal	Li1	3a	-3m	0.702	0	0	0	0.0040
		Ni1	3a	-3m	0.298	0	0	0	0.0040
		Li2	3b	-3m	0.038	0	0	0.5	0.0040
		Ni2	3b	-3m	0.962	0	0	0.5	0.0040
		O1	6c	3m	2	0	0	0.23858	0.0040
$Li_{0.90}Ni_{1.10}O_2$	R-3m(166) - trigonal	Li1	3a	-3m	0.846	0	0	0	0.0047
		Ni1	3a	-3m	0.154	0	0	0	0.0047
		Li2	3b	-3m	0.010	0	0	0.5	0.0047
		Ni2	3b	-3m	0.990	0	0	0.5	0.0047
		O1	6c	3m	2	0	0	0.23858	0.0047
$LiNiO_2$	R-3m(166) - trigonal	Li1	3a	-3m	0.982	0	0	0	0.0047
		Ni1	3a	-3m	0.018	0	0	0	0.0047
		Li2	3b	-3m	0.000	0	0	0.5	0.0047
		Ni2	3b	-3m	1.000	0	0	0.5	0.0047
		O1	6c	3m	2	0	0	0.23858	0.0047

Table 4.2. Site occupancy of $Li_xNi_{1-x}O_2$

Site	Site occupancy			
	$Li_{0.69}Ni_{1.31}O_2$	$Li_{0.76}Ni_{1.24}O_2$	$Li_{0.90}Ni_{1.10}O_2$	$LiNiO_2$
Li(3*a*)	0.604	0.702	0.846	0.982
Ni(3*a*)	0.396	0.298	0.154	0.018
Li(3*b*)	0.065	0.038	0.010	0.000
Ni(3*b*)	0.935	0.962	0.990	1.000

Table 4.3 The concentration analysis results of as-synthesized materials from ICP-OES and Rietveld refinement

Rietveld composition	ICP-OES composition
$Li_{0.67}Ni_{1.3}O_2$	$Li_{0.69}Ni_{1.31}O_2$
$Li_{0.74}Ni_{1.3}O_2$	$Li_{0.76}Ni_{1.24}O_2$
$Li_{0.86}Ni_{1.1}O_2$	$Li_{0.90}Ni_{1.10}O_2$
$Li_{0.98}Ni_{1.0}O_2$	$Li_{1.0}Ni_{1.0}O_2$

Table 4.4. ECSA parameters

samples	double layer capacitance / mF	ECSA / cm^2
NiO	0.024	0.60
$Li_{0.69}Ni_{1.31}O_2$	0.026	0.65
$Li_{0.76}Ni_{1.24}O_2$	0.024	0.60
$Li_{0.90}Ni_{1.10}O_2$	0.023	0.58
$Li_{0.99}Ni_{1.01}O_2$	0.024	0.60

Table 4.5. EXAFS fitting results with Rietveld refinement-based coordination number. With the increase of Li content, which means less cation mixing condition, the bond length of Ni-O became shorter. This also indicates a tendency from Ni2+ to Ni3+ happened.

Sample	Path	N [c]	R [d] / Å	σ^2 [e] / Å^2	R_f [f] / %
NiO	Ni-O	6*	2.086	0.0043	1.5
	Ni-Ni	12*	2.949	0.0049	
$Li_{0.69}Ni_{1.31}O_2$	Ni-O1 [a]	6*	2.089	0.0065	0.3
	Ni-O2 [b]	6*	1.947	0.0019	
	Ni-Ni	7.8*	2.871	0.0052	
$Li_{0.76}Ni_{1.24}O_2$	Ni-O1	6*	2.089	0.0023	0.3
	Ni-O2	6*	1.947	0.0072	
	Ni-Ni	7.4*	2.871	0.0053	
$Li_{0.90}Ni_{1.10}O_2$	Ni-O1	6*	2.089	0.0019	0.3
	Ni-O2	6*	1.947	0.0087	
	Ni-Ni	6.8*	2.871	0.0055	
$Li_{0.90}Ni_{1.10}O_2$	Ni-O2	6*	1.947	0.0098	0.6
	Ni-Ni	6*	2.871	0.0051	

* Fixed value estimated from XRD

a) Ni-O1; Bond between Ni(3*a*) and O
b) Ni-O2; Bond between Ni(3*b*) and O
c) Average coordination Number estimated from Rietveld refinement
d) Bond distance
e) Debye-Waller factor
f) Residual factor

$$R_f = \frac{\int \left| k^3 \chi^{obs}(k) - k^3 \chi^{calc}(k) \right|^2 dk}{\int \left| k^3 \chi^{obs}(k) \right|^2 dk} \times 100$$

Chapter 5. Quantitative Evaluation of the Activity of Low-Spin Tetravalent Nickel Ion Sites for the Oxygen Evolution Reaction

Oxide catalysts containing tetravalent nickel exhibit high oxygen-active catalytic activity. We investigated the effects of lithium content (x) on the electrocatalytic activity of $LixNi_{0.5}Mn_{1.5}O_4$, a spinel that provides only divalent and tetravalent nickel ions in a KOH aqueous electrolyte for the oxygen evolution reaction (OER). The lithium content was controlled by the chemical delithiation of $Li_{0.96}Ni_{0.49}Mn_{1.51}O_4$ using NO_2BF_4. Upon employing this approach, nickel changed from the divalent to tetravalent state. The OER activity increased with decreasing x, and a higher activity than that of standard LaNiO3 was observed at x = 0.00. Comprehensive Tafel analyses and X-ray spectroscopic investigations revealed a downshift in the Ni conduction band, indicating that high OER activity correlated with strong hybridization of the Ni 3*d* and O 2*p* orbitals. These insights into the role of Ni^{4+} in high OER activity are expected to facilitate the development of other highly active Ni-based electrocatalysts.

5.1 Backgound

Water electrolysis is considered a sustainable method for the production of hydrogen, a clean energy source for fuel cells.[1–5] The oxygen evolution reaction (OER; $4OH^- = 2H_2O + O_2 + 4e^-$ in alkaline solution) involves a multistep transfer of four electrons, which is kinetically sluggish; thus, a reduction in polarization in the OER is required.[6,7] Therefore, there is a need for effective electrocatalysts to promote the OER, thereby improving the energy conversion efficiency. Numerous highly active catalysts have been investigated for the OER[8–12] in which IrO_2- and RuO_2-based materials are the most active.[13,14] However, these precious metals are expensive, which limits their large-scale applications. Therefore, considerable efforts have been devoted to the development of inexpensive and highly active catalysts. In particular, non-noble-metal-based oxides are considered promising candidates because of their extensive availability, high natural abundance, and excellent activity under alkaline conditions.[15,16] Previous studies have shown that OER activity depends on the electronic state of the active cationic sites, as well as the occupancy of the 3*d* eg orbital,[17,18] O *p*-band center,[19] and covalency.[20] According to the Sabatier principle, OER activity is high when interactions between the active site and intermediate species have moderate strength (i.e., neither too strong nor too weak).[21] Metal cations in the octahedral sites form σ-bonds with oxygen ligands via the 3*d* e_g orbital.[22] Therefore, the occupancy state of the metal cation may have a significant effect on the strength of the bond between the metal and the intermediate.[18,23] Suntivich et al. found a volcano-like relationship between the eg occupancy in perovskite oxide and OER activity. High e_g filling tends to result in extremely weak binding of the *OH intermediates, whereas low eg filling results in excessively strong binding. An e_g filling of ~1.2 was found to be the optimum.[17] Nevertheless, some materials do not follow this trend, such as oxides containing a high Ni(4+) valence state. The electronic structure of low-spin Ni^{4+} is $t_{2g}^6e_g^0$, suggesting that OER activity decreases as Ni is further oxidized from the trivalent to tetravalent state.[17] Recent studies indicate that Ni in a high valence state of Ni can accelerate the OER.[24–27] Du and coworker synthesized $La_{1-x}Sr_xNiO_3$ thin films on $LaAlO_3$ substrates using the oxygen-plasma-assisted molecular beam epitaxial method and found that Sr substitution can enhance the OER activity, although the e_g occupancy of Ni ions was far from unity.[24] They argued that the increase in Ni 3*d*–O 2*p* covalency upon Ni oxidation and the increase in orbital overlap between Ni 3*d* and O 2*p* contributed to the high activity of the Sr-substituted $LaNiO_3$ thin film.[24]

To elucidate the effect of high-valence Ni on OER activity, it is necessary to evaluate the OER activity of materials with Ni in a stable high oxidation state (4+). However, in the case of perovskites, the formation of Ni^{4+} requires calcination under high oxygen partial pressures (60–200 bar)[28,29] or reactive oxygen species (e.g., oxygen radicals) under special conditions.[24] Therefore, these materials are not actively studied. In contrast, $LiNi_{0.5}Mn_{1.5}O_4$ (LNMO) with a spinel structure has been widely studied as a cathode for lithium-ion secondary batteries, and importantly, lithium ions are desorbed by oxidation to produce tetravalent nickel ions stoichiometrically.[30] Therefore, using this material as an oxygen-evolving electrode, it is possible to quantitatively evaluate the activity of tetravalent nickel ions.

Herein, we report the OER activity of nickel-manganese spinel in which Ni^{4+} is stable up to the bulk. The material was synthesized by chemical delithiation of LNMO using NO_2BF_4. LNMO is an oxide with a spinel-type structure (AB_2O_4) in which Li^+ occupies the tetrahedral A site and Ni^{2+} and Mn^{4+} occupy the octahedral B site. When Li is desorbed from LNMO, Ni^{2+} is oxidized to Ni^{4+} with Ni providing charge compensation according to eq 1.

$$LiNi_{0.5}Mn_{1.5}O_4 \rightarrow Li_x\, Ni_{0.5}Mn_{1.5}O_4 + (1\text{-}x)\, Li^+ + (1\text{-}x)\, e^- \qquad (1)$$

$Ni_{0.5}Mn_{1.5}O_4$ with extracted Li was reported31 to be stable in air. We investigated the effects of Ni^{4+} on OER activity. Soft Xray absorption spectroscopy (XAS) and Tafel analysis were conducted to elucidate the mechanism corresponding to the high activity in the presence of high-valence Ni. We concluded that the formation of Ni^{4+} in $Ni_{0.5}Mn_{1.5}O_4$ resulted in a downshift of the Ni conduction-band energy, thereby enhancing the OER kinetics. Although the electrochemical delithiation method has already been applied for $LiCoO_2$ toward the OER,[30] the effects of electrolyte-derived decomposition products and binders have not been eliminated. Moreover, our study on chemical delithiation of $Li_{0.96}Ni_{0.49}Mn_{1.51}O_4$ using NO_2BF_4 was better for OER catalyst studies without binders and was applied for the first time in this field. This allowed us to precisely control the electronic structure of the catalyst by delithiated ions and to thoroughly study the catalyst electronic structure and OER activity.

5.2 Experimental

5.2.1 Material Synthesis

$LiNi_{0.5}Mn_{1.5}O_4$ powder was synthesized as follows. Stoichiometric amounts of $LiNO_3$, $Ni(NO_3)_2.6H_2O$, and $Mn(NO_3)_2.6H_2O$ (FUJIFILM Wako Pure Chemical Corporation) were dissolved in ultrapure water. A four- to fivefold molar excess of citric acid (anhydrous, FUJIFILM Wako Pure Chemical Corporation) was added while stirring. This solution was gradually heated to 400 °C using a hot plate to obtain the precursor. During heating, the mixture formed a sticky gel. The temperature was held at 400 °C until the mixture was sufficiently dried to collect the precursor powder. The obtained powder was calcined at 800 °C for 12 h and at 700 °C for 48 h under pure O_2.

Various levels of chemical delithiation were achieved by reacting $LiNi_{0.5}Mn_{1.5}O_4$ with nitronium tetrafluoroborate (NO_2BF_4, SigmaAldrich) in acetonitrile solution (superdehydrated, FUJIFILM Wako Pure Chemical Corporation) for 48 h at 25 °C. Note that the NO_2BF_4 can react with water to form HF; hence, the superdehydrated acetonitrile should be used.[41] The degree of delithiation was controlled by changing the molar ratio of $LiNi_{0.5}Mn_{1.5}O_4$ to NO_2BF_4. The suspension of $LiNi_{0.5}Mn_{1.5}O_4$ and NO_2BF_4 was stirred for 48 h to obtain a uniform particle composition. Subsequently, the suspension was filtered, thoroughly washed with acetonitrile at least three times, and dried overnight in a vacuum oven.

5.2.2 Characterization

The chemical compositions of the materials were determined using inductively coupled plasma optical emission spectrometry (ICP-OES; ICPS-8100CL, Shimadzu, Co. Ltd.). X-ray diffraction (XRD) patterns were collected using BL02B2 at SPring-8, Japan (Proposal No. 2018A1749, 2018A1750, 2018B1616, and 2019A1763) and BL5S2 at Aichi Synchrotron Radiation Center, Aichi Science & Technology Foundation, Aichi, Japan (Proposal No. 202002005). The wavelength, set to 0.61972 Å, was calibrated using CeO_2 for both beamlines at SPring-8 and the Aichi Synchrotron Radiation Center. The lattice parameters and phase ratios were determined by Rietveld refinements using Jana 2006 software. Raman spectra were recorded on a Raman microscope (RAMANtouch, Nanophoton Corp.), in the confocal backscattering configuration, with a 532 nm argon ion laser. XAS was conducted for Mn and Ni Kedges, and the spectra were obtained in the transmission mode using a Si (111) monochromator on BL01B1 and BL14B2 at SPring-8, Japan (Proposal No. 2019A1820, 2019B1855, and 2019B1899) and BL11S2 at Aichi Synchrotron Radiation Center, Aichi Science & Technology Foundation, Aichi, Japan (Proposal No. 202002006). XAS for Mn and Ni L-edges, and O K-edge was conducted in the fluorescence mode on BL-11 at the SR center, Ritsumeikan University, Japan. Scanning electron microscopy (SEM) experiments were conducted at 15 kV (S-3400 N, Hitachi High-Tech Corp.). Transmission electron microscopy (TEM) experiments were conducted at 200 kV (JEM-2200FS, JEOL Ltd.). X-ray photoelectron spectroscopy (XPS) was performed to reveal the catalyst surface valence state using PHI5000 VersaProbe2.

5.2.3 Electrochemical Measurements

Catalyst inks were prepared by mixing 4 mg of the catalyst powder with 998 μL of acetonitrile and 2 μL of 5 wt % Nafion solution (Sigma-Aldrich). The inks were sonicated in an ice bath for 20 min before they were cast on the electrode. A total of 24.5 μL of ink was dropped on a polished glassy carbon (GC) rotating disk electrode (Hokuto denko, 5 mm diameter, 0.196 cm^2). The electrochemical measurements were performed using a standard three-electrode cell connected to an MPG-205-NUC system (Bio-Logic). A Pt mesh was used as the counter electrode, a reversible hydrogen electrode (RHE) was used as the reference electrode, and the catalyst-coated GC was used as the working electrode. The electrochemical activities of the catalysts were investigated using linear sweep voltammetry (LSV) in the range of 1.1 to 1.8 V vs RHE at 5 mV s^{-1} in N_2-saturated 0.1 M KOH. The electrochemically active surface area (ECSA) was estimated using the methods proposed by McCrory et al.32 For comparison, the OER performance of $LaNiO_3$ was evaluated using the same process. The observed current measurements were normalized using the ECSA. The working electrode was rotated at 1600 rpm during the measurement. After the LSV measurements, the samples were collected from the electrodes and examined using TEM. The longterm stability tests were conducted to further evaluate the representative catalyst performance. For the $Li_{0.00}Ni_{0.49}Mn_{1.51}O_4$ sample, the current density was kept at 10 mA/cm^2. For the $Li_{0.96}Ni_{0.49}Mn_{1.51}O_4$ sample, because it was difficult to apply a current of 10 mA/cm^2 because of the low activity, constant current electrolysis was performed at 6 mA/cm^2, making the initial potential the same for both samples before the long-term stability test. After long-term stability tests, the catalysts were collected for TEM and XPS measurements.

5.3 Results and Discussion

5.3.1 Crystal Structure

Table 5.1 shows the chemical composition of the delithiated $LiNi_{0.5}Mn_{1.5}O_4$, which was determined using ICP-OES. The Li (x) content decreased from 0.96 to 0.00 as the NO_2BF_4 content increased, whereas those of Ni and Mn remained almost the same. The samples were labeled $x = 0.96$, 0.80, 0.60, 0.42, 0.14, and 0.00. Figure 5.1 shows the synchrotron XRD patterns ($\lambda = 0.61972$ Å) of the delithiated $LiNi_{0.5}Mn_{1.5}O_4$. For the pristine sample ($x = 0.96$), all the peaks were indexed to the cubic phase, and no impurities were observed. The Raman spectrum (Figure 5.2) of x = 0.96, specifically the additional peaks at 222 and 243 cm^{-1} and a sharp peak at 406 cm^{-1}, indicated the existence of the $P4_332$ space group.[32] The XRD patterns and weight fractions of the phases in the samples were refined using the full-pattern Rietveld method, and their structural parameters are shown in Tables 5.2−7 and Figures 5.3 and 5.4. Delithiation of LNMO resulted in a mixture of three cubic phases, namely, $LiNi_{0.5}Mn_{1.5}O_4$ (phase I), $Li_{0.5}Ni_{0.5}Mn_{1.5}O_4$ (phase II), and $Ni_{0.5}Mn_{1.5}O_4$ (phase III), as reported previously.[30] The lattice parameters in phases I, II, and III were approximately 8.16, 8.09, and 8.00 Å, respectively. The lattice constants of phases II and III were smaller than that of phase I because the ionic radii, affected by the valence state of Ni ions in phases II(Ni^{2+}/ Ni^{4+}) and III(Ni^{4+}), were smaller than that in phase I(Ni^{2+}).[33] TEM images of $x = 0.96$ and $x = 0.00$ samples (Figure 5.5 a,b) indicated that both samples were well crystallized. The average particle size was ~1.5 μm, as observed in the SEM images (Figure 5.6). Therefore, we successfully conducted topochemical delithiation using NO_2BF_4 to obtain spinels with varying Li content, while maintaining the crystal structure.

5.3.2 Bulk Electronic Structure

The electronic structures of Ni and Mn were investigated using XAS to determine the changes in their average valence states. The Ni K-edge X-ray absorption near edge structure (XANES) (Figure 5.7) showed a monotonous edge-shift toward higher energy with a decrease in the Li content in LNMO. The degree of edge-shift (~3.8 eV) was consistent with the average valence state of nickel, changing from Ni^{2+} in $LiNi_{0.5}Mn_{1.5}O_4$ to Ni^{4+} in $Ni_{0.5}Mn_{1.5}O_4$.[33] The XANES spectra showed two isosbestic points at 8353.3 and 8354.9 eV, suggesting that chemical delithiation of LNMO proceeded via two sets of two-phase reactions (i.e., phase I−II and phase II−III), as reported previously.[34] This result agreed with the XRD findings.[35] Figure 5.7b shows the Mn K-edge XANES. In contrast to the results for Ni, the Mn K-edge spectra showed only a slight edge-shift, confirming that the state of Mn remained unchanged at Mn^{4+}, as reported previously.[35,36] The slight change in the Mn K-edge was due to the local structural change of the Mn ion. These results confirmed that we successfully synthesized a catalyst that contains Ni^{4+} via chemical oxidation using NO_2BF_4.

5.3.3 Electrochemical Performance

In this study, OER performance was evaluated using a three-electrode cell. For comparison, the benchmark catalyst $LaNiO_3$ was also evaluated because it is a classic Ni-based OER catalyst and Ni is not hybridized with Fe or other transition metals as in Ni-Fe spinels[18] or Ni LDH.[11] Figure 5.8 shows the results of the double layer capacitance (Cdl) measurement. The ECSA of each sample was calculated using Eq 2:

$$ECSA = \frac{C_{dl}}{C_s} \qquad (2)$$

where Cs (specific capacitance) is equal to 0.04 mF cm^{-2}.

Table 5.8 shows the ECSA values of each sample. All the LNMO samples (x = 0.96, 0.80, 0.60, 0.42, 0.14, and 0.00) had almost the same ECSA value of approximately 1.00 cm^2. All the current measurements were normalized to the ECSA to evaluate the true OER activity, which is independent of the surface area.[31] Figure 5.9a shows the LSV curves at a scan rate of activity of delithiated LNMO needs to be elucidated. Moreover, the XRD pattern and catalyst morphology were investigated for samples x = 0.96 and x = 0.00 after electrolysis. Both samples showed no obvious changes (Figures 5.10 and 5.11), indicating that the structures were stable after electrolysis. The long-term stability tests were conducted to further evaluate the representative catalyst performance. As shown in Figure 5.12, both samples showed the potential increase during the long-term stability tests, suggesting that the state of the catalyst has changed. Even though the stability test of $Li_{0.00}Ni_{0.49}Mn_{1.51}O_4$ was performed at a larger current density value, the percentage increase in potential is almost the same as that of $Li_{0.96}Ni_{0.49}Mn_{1.51}O_4$. The amorphization of the surface was observed for both samples in the TEM images, indicating the collapse of the initial crystalline structure, as shown in Figure 5.13. The surface valence state after stability tests was further investigated by XPS, as shown in Figure 5.14. The main peak of O 1 s spectra at 529.4 eV corresponds to lattice oxygen and the shoulder at a higher energy side can be assigned to surface oxygen species (OH, H_2O) and/or carbonates (C=O),[37–39] as shown in Figure 5.14a. After stability tests, the surface oxygen species increased, which might be due to the surface reconstruction as observed by TEM images. In Figure 5.14b, Ni $2p_{3/2}$ spectra at 854.2 eV corresponding to

Ni^{2+} were observed as the main peak.[37–39] For $x = 0.00$. a shoulder peak at the higher energy side appeared, suggesting the existence of higher valence Ni (Ni^{4+}). For the $x = 0.96$ sample, this shoulder peak appeared after the long-term stability test. This is because Li^{+} was desorbed from the spinel structure over 2 V (vs RHE) during the stability test. Moreover, the $x = 0.00$ sample after the stability test showed a broadened peak at around 854.2 eV, which could be attributed to the surface reconstruction. As shown in Figure 5.14c, Mn $2p_{3/2}$ spectra at 641.9 eV correspond to Mn^{3+} and the shoulder peak at a higher energy side at 642.8 eV can be assigned to Mn^{4+}.[37–39] The Mn $2p_{3/2}$ spectra were almost identical for $x = 0.00$ and $x = 0.96$ before the stability test. However, after that, $x = 0.00$ showed a more broadened peak at around 641.9 eV and a shoulder peak at a lower energy side, which indicates the surface reconstruction after the stability test.

Tafel analysis was performed to predict the rate-determining step (RDS) of the OER. Figure 5.15 and Table 5.9 show the Tafel slopes for each sample. The Tafel slope of $LaNiO_3$ was 73.3 mV dec^{-1}, which was consistent with previously reported values (60–70 mV dec^{-1}).[17,31,40] The Tafel slope for $x = 0.96$ was ~122 mV dec^{-1}, which also agreed with a previous study.[41] The Tafel slope decreased from 98.2 to 66.0 mV dec^{-1} with a decrease in x values from 0.80 to 0.00. According to the Doyle and Lyons mechanism, the Tafel slopes of the RDS were estimated as follows.[42] Doyle and co-workers first proposed this mechanism based on their experimental results. Then they assumed each step to be the RDS and conducted the theoretical analysis guided by earlier work and recent density functional theory calculation developments. When considering each step as the RDS, they combined the net reaction flux calculation, quasi steady-state approximation, and the Butler–Volmer rate equation and then gave the theoretical value for each step. Step 6 is rarely a RDS; therefore, the Tafel slope is undefined.[42]

Step 1 $M + OH^{-} \rightarrow M - OH^{*} + e^{-}$ 120 mV dec^{-1} (3)

Step 2 $\mathrm{M - OH + OH^{-} \rightarrow M - O^{-} + H_2O}$ 60 mV dec^{-1} (4)

Step 3 $\mathrm{M - O^{-} \rightarrow M - O^{*} + e^{-}}$ 120 mV dec^{-1} (5)

Step 4 $\mathrm{M - O^{*} + OH^{-} \rightarrow M - OOH^{*} + e^{-}}$ 40 mV dec^{-1} (6)

Step 5 $\mathrm{M - OOH^{*} + OH^{-} \rightarrow M - O_2 + H_2O + e^{-}}$ 40 mV dec^{-1} (7)

Step 6 $\mathrm{M - O_2 + OH^{-} \rightarrow M - OH^{*} + e^{-}}$ --- mV dec^{-1} (8)

The RDS of $LaNiO_3$ (Tafel slope: 73.3 mV dec^{-1}) was Step 2: proton transfer from OH*.[42] This was consistent with a previous report based on calculations. According to the Tafel slope, the RDS in the case of x = 0.96 (Tafel slope: ~ 122 mV dec^{-1}) should have been Step 1 or Step 3. However, because Ni existed mainly as Ni^{2+}($t_{2g}^{6}e_{g}^{2}$) in $LiNi_{0.49}Mn_{1.51}O_4$, Step 1 was considered the RDS.[42] The RDS when $x = 0.00$ (Tafel slope: 66.0 mV dec^{-1}) was step 2, similar to the case of $LaNiO_3$. Therefore, the adsorption of OH* may increase in the presence of high-valence Ni. In summary, an OER catalyst was successfully synthesized with the same RDS step and superior OER kinetics compared with those of $LaNiO_3$.

5.3.4 Electronic Structure

The electronic states of Mn, Ni, and O were also observed using soft XAS. Figure 5.16a shows the Mn L-edge XANES spectra of the chemically delithiated $LiNi_{0.49}Mn_{1.51}O_4$. The shape was almost the same, and two peaks were observed at 641 and 643 eV. This result clearly showed that the Mn electronic structure remained almost unchanged by delithiation.[43] Figure 5.16b shows the Ni L-edge XANES spectra of the chemically delithiated $LiNi_{0.49}Mn_{1.51}O_4$. The intensity of the peak at 857 eV became stronger at lower values of *x*, indicating the formation of 3d^{8}L̲ configurations (where L̲ denotes a ligand hole)[44] because of the strong hybridization between the Ni 3*d* and O 2*p* orbitals. According to a previous research study,[45] shifts in the Ni L-edge XANES spectra also indicated the low-spin state of Ni^{4+} in $Li_{0.00}Ni_{0.49}Mn_{1.51}O_4$. Figure 5.17a shows the oxygen K-edge XANES measured in the PFY mode. The pre-edge character in the O K-edge XAS at 528 and 532 eV was assigned to the unoccupied state of the O 2p band hybridized with Mn 3d t_{2g} and e_g states.[44,46] In addition, especially for lower values of *x*, there were additional peaks at 526–527 eV assigned to the hybridization of the Ni 3*d* e_g–O 2*p* states.[46] This result indicated that Ni^{4+}-induced hole creation on O 2*p* and the energy of Ni 3*d* e_g decreased because of the highly effective nuclear charge of Ni^{4+}.

Finally, we describe the electronic structure of $Li_{0.96}Ni_{0.49}Mn_{1.51}O_4$ and $Li_{0.00}Ni_{0.49}Mn_{1.51}O_4$ using our previous findings,[47] and we discuss the mechanism of their high activity. From the O K-edge XAS results, the positions of the Mn t_{2g}–O 2*p* and Mn e_g–O 2*p* hybridization orbitals did not change significantly, whereas the Ni e_g–O 2*p* hybridization orbitals were downshifted by the formation of Ni^{4+} at $x = 0.00$. Figure 5.18 shows the electronic structures of $Li_{0.96}Ni_{0.49}Mn_{1.51}O_4$ and $Li_{0.00}Ni_{0.49}Mn_{1.51}O_4$.

The OER proceeds with a charge-transfer process from the adsorbate to the active site at each step.[48] Therefore, a smaller charge-transfer energy (Δ), defined by the energy difference between the occupied O 2*p* orbital and the unoccupied Ni e_g orbital, promotes the charge-transfer process to enhance the OER activity.[48] In the present system, the charge-transfer energy of the sample after Li desorption was lowered (Figure 5.18) owing to the downshift of Ni e_g orbitals, and it was concluded that this factor enhanced the OER activity.

5.4 Conclusion

This study focused on the electrocatalytic activity of $Li_xNi_{0.5}Mn_{1.5}O_4$ spinels with different lithium contents. The lithium (x) content in $Li_xNi_{0.49}Mn_{1.51}O_4$ was controlled by topochemical delithiation using NO_2BF_4 in an acetonitrile solution. Upon applying this approach, nickel changed from the divalent to tetravalent state, while the tetravalent state of manganese was maintained. The OER activity was found to increase with decreasing x. $x = 0.00$ showed the highest OER activity. The Tafel slopes indicated that the RDS changed from OH^- adsorption to proton transfer from OH*; thus, the OER kinetics was enhanced. The XAS spectra of Ni and O indicated that the presence of Ni^{4+} caused a downshift in the unoccupied Ni 3*d* state and decreased the energy barrier of charge transfer from the oxygen intermediate species to the metal active site; hence, the OER activity was enhanced. This study revealed the mechanism underpinning the high OER activity of high valence Ni (4+) and also provided an approach for the development of highly active catalyst materials, namely, topochemical delithiation.

Reference

1. Dincer, I.; Acar, C., Review and Evaluation of Hydrogen Production Methods for Better Sustainability. *Int. J. Hydrogen Energy* **2015,** *40*, 11094-11111.
2. Götz, M.; Lefebvre, J.; Mörs, F.; McDaniel Koch, A.; Graf, F.; Bajohr, S.; Reimert, R.; Kolb, T., Renewable Power-to-gas: A Technological and Economic Review. *Renewable Energy* **2016,** *85*, 1371-1390.
3. Mazloomi, K.; Gomes, C., Hydrogen as An Energy Carrier: Prospects and Challenges. *Renewable Energy* **2012,** *16*, 3024-3033.
4. Turner, J.; Sverdrup, G.; Mann, M. K.; Maness, P.-C.; Kroposki, B.; Ghirardi, M.;

Evans, R. J.; Blake, D., Renewable Hydrogen Production. *International Journal of Energy Research* **2008,** *32*, 379-407.

5. Wee,J.-H., Applications of Proton Exchange Membrane Fuel Cell Systems. *Renewable Sustainable Energy Rev.* **2007,** *11*, 1720-1738.
6. Zeng, K.; Zhang, D., Recent Progress in Alkaline Water Wlectrolysis for Hydrogen Production and Applications. *Prog. Energy Combust. Sci.* **2010,** *36*, 307-326.
7. Suen, N. T.; Hung, S. F.; Quan, Q.; Zhang, N.; Xu, Y. J.; Chen, H. M., Electrocatalysis for the Oxygen Evolution Reaction: Recent Development and Future Perspectives. *Chem. Soc. Rev.* **2017,** *46*, 337-365.
8. Li, X.; Hao, X.; Abudula, A.; Guan, G., Nanostructured Catalysts for Electrochemical Water Splitting: Current State and Prospects. *J. Mater. Chem. A* **2016,** *4*, 11973-12000.
9. Wang, J.; Cui, W.; Liu, Q.; Xing, Z.; Asiri, A. M.; Sun, X., Recent Progress in Cobalt-based Heterogeneous Catalysts for Electrochemical Water Splitting. *Adv. Mater.* **2016,** *28*, 215-230.
10. Laguna-Bercero, M. A., Recent Advances in High Temperature Electrolysis Using Solid Oxide Fuel Cells: A review. *J. Power Sources* **2012,** *203*, 4-16.
11. Gong, M.; Dai, H., A Mini Review of NiFe-based Materials as Highly Active Oxygen Evolution Reaction Electrocatalysts. *Nano Res.* **2015,** *8*, 23-39.
12. Carmo, M.; Fritz, D. L.; Mergel, J.; Stolten, D., A Comprehensive Review on PEM Water Electrolysis. *Int. J. Hydrogen Energy* **2013,** *38*, 4901-4934.
13. Lee, Y.; Suntivich, J.; May, K. J.; Perry, E. E.; Shao-Horn, Y., Synthesis and Activities of Rutile IrO_2 and RuO_2 Nanoparticles for Oxygen Evolution in Acid and Alkaline Solutions. *J. Phys. Chem. Lett.* **2012,** *3*, 399-404.
14. Reier, T.; Oezaslan, M.; Strasser, P., Electrocatalytic Oxygen Evolution Reaction

(OER) on Ru, Ir, and Pt catalysts: A comparative Study of Nanoparticles and Bulk Materials. *ACS Catal.* **2012,** *2*, 1765-1772.

15. Fabbri, E.; Habereder, A.; Waltar, K.; Kötz, R.; Schmidt, T. J., Developments and Perspectives of Oxide-based Catalysts for the Oxygen Evolution Reaction. *Catal. Sci. Technol.* **2014,** *4*, 3800-3821.
16. Anantharaj, S.; Ede, S. R.; Sakthikumar, K.; Karthick, K.; Mishra, S.; Kundu, S., Recent Trends and Perspectives in Electrochemical Water Splitting with An Emphasis on Sulfide, Selenide, and Phosphide Catalysts of Fe, Co, and Ni: A Review. *ACS Catal.* **2016,** *6*, 8069-8097.
17. Suntivich, J.; May, K. J.; Gasteiger, H. A.; Goodenough, J. B.; Shao-Horn, Y., A Perovskite Oxide Optimized for Oxygen Evolution Catalysis from Molecular Orbital Principles. *Science* **2011,** *334*, 1383-1385.
18. Wei, C.; Feng, Z. X.; Scherer, G. G.; Barber, J.; Shao-Horn, Y.; Xu, Z. C. J., Cations in Octahedral Sites: A Descriptor for Oxygen Electrocatalysis on Transition-Metal Spinels. *Adv. Mater.* **2017,** *29* (23), 1601800.
19. Grimaud, A.; May, K. J.; Carlton, C. E.; Lee, Y. L.; Risch, M.; Hong, W. T.; Zhou, J. G.; Shao-Horn, Y., Double Perovskites as A Family of Highly Active Catalysts for Oxygen Evolution in Alkaline Solution. *Nat. Commun.* **2013,** *4*, 2439.
20. Cheng, X.; Fabbri, E.; Nachtegaal, M.; Castelli, I. E.; El Kazzi, M.; Haumont, R.; Marzari, N.; Schmidt, T. J., Oxygen Evolution Reaction on $La_{1-x}Sr_xCoO_3$ Perovskites: A Combined Experimental and Theoretical Study of Their Structural, Electronic, and Electrochemical Properties. *Chem. Mater.* **2015,** *27*, 7662-7672.
21. Medford, A. J.; Vojvodic, A.; Hummelshoj, J. S.; Voss, J.; Abild-Pedersen, F.; Studt, F.; Bligaard, T.; Nilsson, A.; Norskov, J. K., From the Sabatier Principle to A

Predictive Theory of Transition-Metal Heterogeneous Catalysis. *J. Catal.* **2015**, *328*, 36-42.

22. Liu, J. Y.; Liu, H.; Chen, H. J.; Du, X. W.; Zhang, B.; Hong, Z. L.; Sun, S. H.; Wang, W. C., Progress and Challenges Toward the Rational Design of Oxygen Electrocatalysts Based on a Descriptor Approach. *Adv. Sci.* **2020,** *7* (1), 1901614.
23. Matsumoto, Y.; Sato, E., Electrocatalytic Properties of Transition-Metal Oxides for Oxygen Evolution Reacrion. *Mater. Chem. Phys.* **1986**, *14* (5), 397-426.
24. Liu, J. S.; Jia, E. D.; Wang, L.; Stoerzinger, K. A.; Zhou, H.; Tang, C. S.; Yin, X. M.; He, X.; Bousquet, E.; Bowden, M. E.; Wee, A. T. S.; Chambers, S. A.; Du, Y. G., Tuning the Electronic Structure of $LaNiO_3$ through Alloying with Strontium to Enhance Oxygen Evolution Activity. *Adv. Sci.* **2019**, 7, 1901073.
25. Zhang, N.; Feng, X.; Rao, D.; Deng, X.; Cai, L.; Qiu, B.; Long, R.; Xiong, Y.; Lu, Y.; Chai, Y., Lattice Oxygen Activation Enabled by High-valence Metal Sites for Enhanced Water Oxidation. *Nat. Commun.*. 2020, 11 (1), 4066.
26. Steimecke, M.; Seiffarth, G.; Schneemann, C.; Oehler, F.; Förster, S.; Bron, M., Higher-Valent Nickel Oxides with Improved Oxygen Evolution Activity and Stability in Alkaline Media Prepared by High-Temperature Treatment of $Ni(OH)_2$. *ACS Catal.* 2020, 10 (6), 3595-3603.
27. Li, N.; Bediako, D. K.; Hadt, R. G.; Hayes, D.; Kempa, T. J.; von Cube, F.; Bell, D. C.; Chen, L. X.; Nocera, D. G., Influence of Iron Doping on Tetravalent Nickel Content in Catalytic Oxygen Evolving Films. *Proc. Natl. Acad. Sci. U. S. A.* 2017, 114 (7), 1486-1491.
28. Takeda, Y.; Kume, S.; Hashino, T.; Miyamoto, H.; Kanamaru, F.; Koizumi, M., Synthesis of $SrNiO_3$ and Related Compound, $Sr_2Ni_2O_5$. *J. Inorg. Nucl.*

Chem. **1972,** *34* (5), 1599-1601.

29. Takeda, Y.; Kanamura, F.; Shimada M.; Koizumi M., The Crystal Structure of $BaNiO_3$. *Acta Crystallogr.* **1976,** B32, 2464.
30. Lu, Z.; Wang, H.; Kong, D.; Yan, K.; Hsu, P.-C.; Zheng, G.; Yao, H.; Liang, Z.; Sun, X.; Cui, Y., Electrochemical Tuning of Layered Lithium Transition Metal Oxides for Improvement of Oxygen Evolution Reaction. *Nat. Commun.* **2014,** *5*, 4345.
31. Saravanan, K.; Jarry, A.; Kostecki, R.; Chen, G., A Study of Room-Temperature $Li_xMn_{1.5}Ni_{0.5}O_4$ Solid Solutions. *Sci. Rep.* **2015,** *5*, 8027.
32. McCrory, C. C. L.; Jung, S.; Peters, J. C.; Jaramillo, T. F., Benchmarking Heterogeneous Electrocatalysts for the Oxygen Evolution Reaction. *J. Am. Chem. Soc.* **2013,** *135* (45), 16977-16987.
33. Wang, L. P.; Li, H.; Huang, X. J.; Baudrin, E., A Comparative Study of Fd-3m and P4(3)32 "$LiNi_{0.5}Mn_{1.5}O_4$". *Solid State Ionics* **2011,** *193* (1), 32-38.
34. Kuppan, S.; Xu, Y. H.; Liu, Y. J.; Chen, G. Y., Phase Transformation Mechanism in Lithium Manganese Nickel Oxide Revealed by Single-crystal Hard X-ray Microscopy. *Nat. Commun.* **2017,** *8*, 14309.
35. Ariyoshi, K.; Iwakoshi, Y.; Nakayama, N.; Ohzuku, T., Topotactic Two-phase Reactions of $Li[Ni_{1/2}Mn_{3/2}]O_4$ ($P4_332$) in Nonaqueous Lithium Cells. *J. Electrochem. Soc.* **2004,** *151*, A296-A303.
36. Okumura, T.; Yamaguchi, Y.; Kobayashi, H., X-ray Absorption Near-edge Structures of $LiMn_2O_4$ and $LiNi_{0.5}Mn_{1.5}O_4$ Spinet Oxides for Lithium-ion Batteries: the First-Principles Calculation Study. *Phys. Chem. Chem. Phys.* **2016**, 18 (27), 17827-17830.
37. Lahiru Sandaruwan, R. D.; Cong, L.; Ma, L.; Ma, S.; Wang, H., Tackling the interfacial issues of spinel $LiNi_{0.5}Mn_{1.5}O4$ by room-temperature spontaneous

dediazonation reaction. *ACS Appl. Mater. Interfaces* 2021 13 (11), 13264-13272.

38. Xue, Y., Wang, Z., Zheng, L. Yu, F.; Liu, B.; Zhang, Y.; Ke, K. Investigation on preparation and performance of spinel $LiNi_{0.5}Mn_{1.5}O_4$ with different microstructures for lithium-ion batteries. *Sci. Rep.* 2015 5 13299.

39. Yang, T., Zhang, N., Lang, Y. & Sun, K. Enhanced rate performance of carbon-coated LiNi0.5Mn1.5O4 cathode material for lithium ion batteries. *Electrochim. Acta* 2011 56 4058–4064.

40. Matienzo, D. D.; Kutlusoy, T.; Divanis, S.; Di Bari, C.; Instuli, E., Benchmarking Perovskite Electrocatalysts' OER Activity as Candidate Materials for Industrial Alkaline Water Electrolysis. *Catalysts* **2020,** *10* (12), 1387.

41. Maiyalagan, T.; Chemelewski, K. R.; Manthiram, A., Role of the Morphology and Surface Planes on the Catalytic Activity of Spinel $LiMn_{1.5}Ni_{0.5}O_4$ for Oxygen Evolution Reaction. *ACS Catal.* **2014,** *4* (2), 421-425.

42. Doyle, R. L.; Lyons, M. E. G., Kinetics and Mechanistic Aspects of the Oxygen Evolution Reaction at Hydrous Iron Oxide Films in Base. *J. Electrochem. Soc.* **2013,** *160* (2), H142-H154.

43. Qiao, R. M.; Wray, L. A.; Kim, J. H.; Pieczonka, N. P. W.; Harris, S. J.; Yang, W. L., Direct Experimental Probe of the Ni(II)/Ni(III)/Ni(IV) Redox Evolution in $LiNi_{0.5}Mn_{1.5}O_4$ Electrodes. *J. Phys. Chem.C* **2015,** *119* (49), 27228-27233.

44. Drevon, D.; Görlin, M.; Chernev, P.; Xi, L.; Dau, H.; Lange, K. M., Uncovering the Role of Oxygen in Ni-Fe(O_xH_y) Electrocatalysts Using In situ Soft X-ray Absorption Spectroscopy during the Oxygen Evolution Reaction. *Sci. Rep.***2019,** *9*, 1532.

45. Gu, W.; Wang, H.; Wang, K., Nickel L-edge and K-edge X-ray Absorption Spectroscopy of Non-innocent $Ni[S_2C_2(CF_3)_2]_2^n$ series (n = −2, −1, 0): Direct Probe

of Nickel Fractional Oxidation State Changes. *Dalton Trans.* **2014**, 43 (17), 6406-6413.

46. Suntivich, J.; Hong, W. T.; Lee, Y.-L.; Rondinelli, J. M.; Yang, W.; Goodenough, J. B.; Dabrowski, B.; Freeland, J. W.; Shao-Horn, Y., Estimating Hybridization of Transition Metal and Oxygen States in Perovskites from O K-edge X-ray Absorption Spectroscopy. *J. Phys. Chem. C* **2014,** *118*, 1856-1863.
47. Lim, J. M.; Oh, R. G.; Kim, D.; Cho, W.; Cho, K.; Cho, M.; Park, M. S., Design of Surface Doping for Mitigating Transition Metal Dissolution in $LiNi_{0.5}Mn_{1.5}O_4$ Nanoparticles. *ChemSusChem* **2016,** *9* (20), 2967-2973.
48. Hong, W. T.; Stoerzinger, K. A.; Lee, Y. L.; Giordano, L.; Grimaud, A.; Johnson, A. M.; Hwang, J.; Crumlin, E. J.; Yang, W. L.; Shao-Horn, Y., Charge-transfer-energy-dependent Oxygen Evolution Reaction Mechanisms for Perovskite Oxides. *Energy Environ. Sci.* **2017,** *10* (10), 2190-2200.

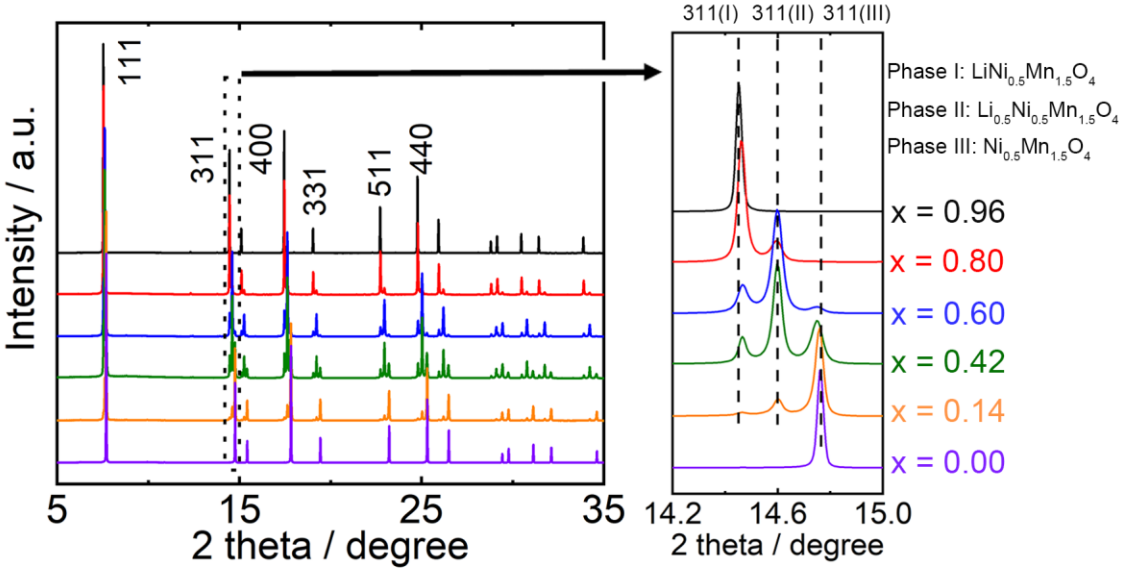

Figure 5.1. XRD patterns of $Li_xNi_{0.5}Mn_{1.5}O_4$. The Miller index indicate that each Phase I, II, III has a $P4_332$ space group of 311 plane.

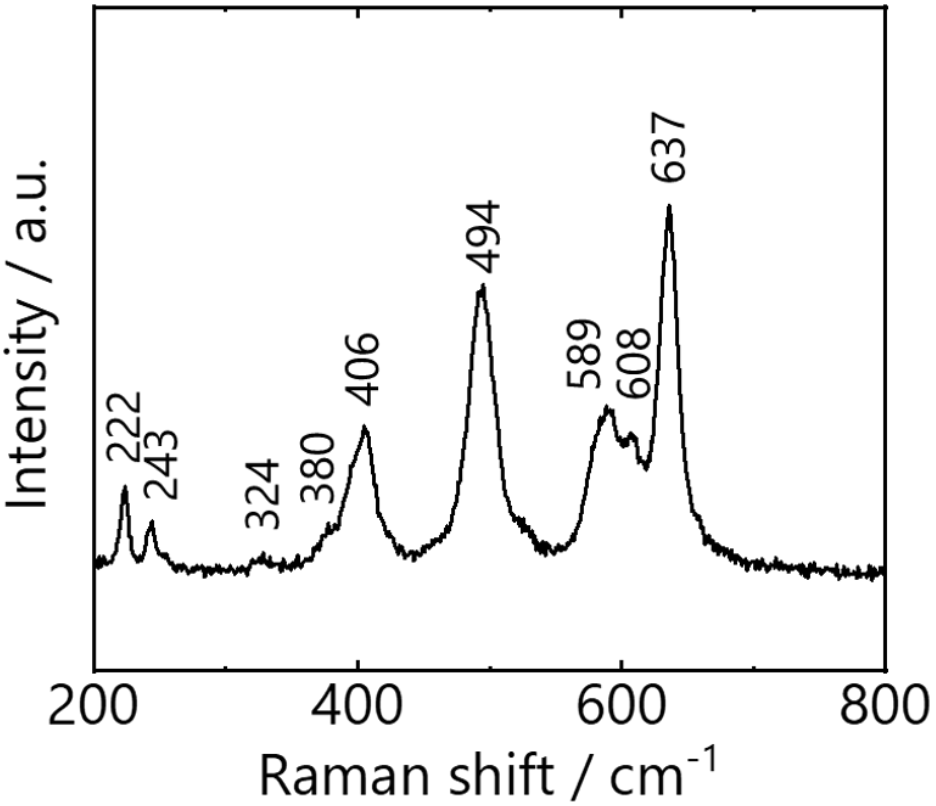

Figure 5.2. Raman spectrum for the pristine $Li_{0.96}Ni_{0.49}Mn_{1.51}O_4$.

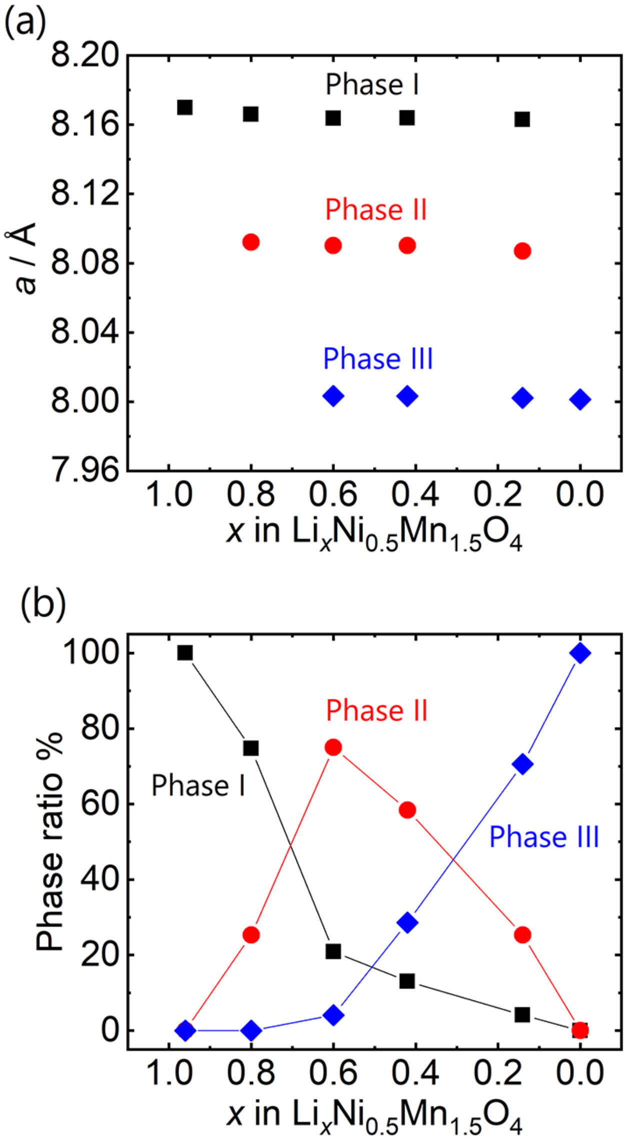

Figure 5.3. (a)Lattice parameters and (b) ratio of Phase I, II, III in $Li_xNi_{0.5}Mn_{1.5}O_4$.

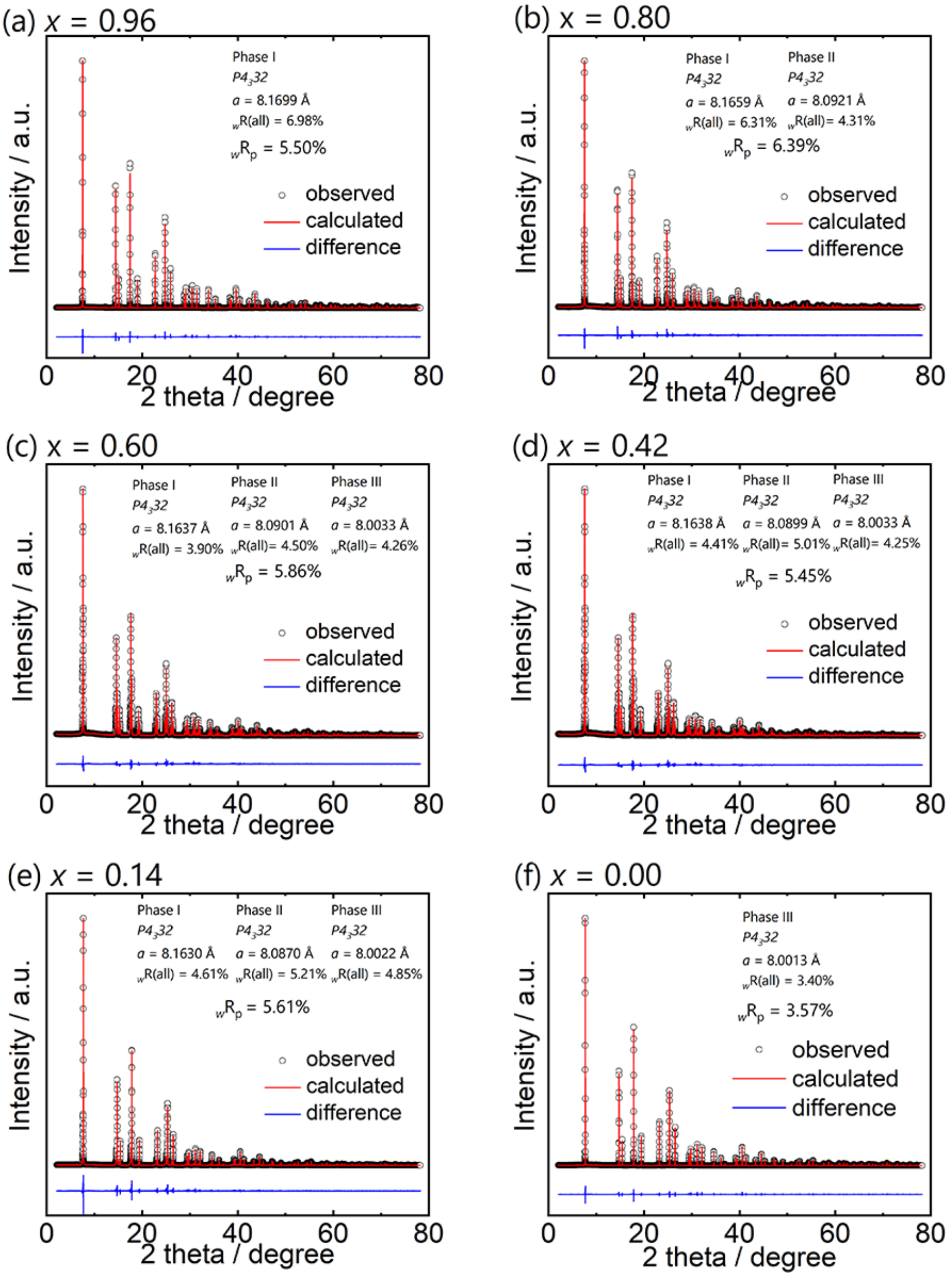

Figure 5.4. Rietveld refinement results for Li$_x$Ni$_{0.5}$Mn$_{1.5}$O$_4$

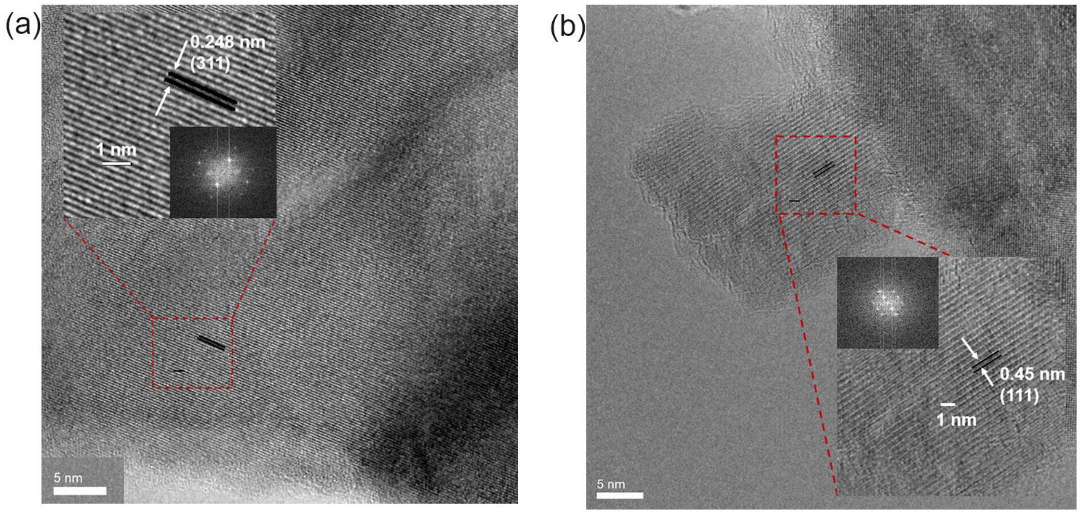

Figure 5.5. TEM images of (a) $x = 0.96$ and (b) $x = 0.00$

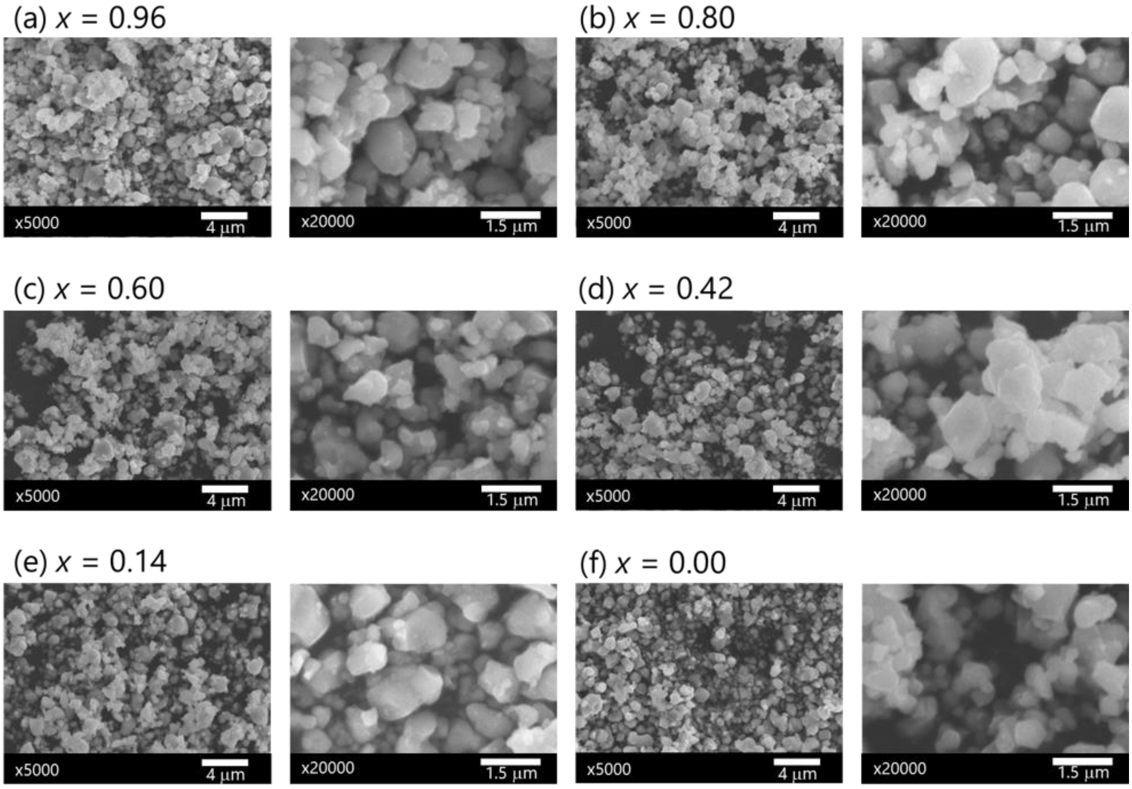

Figure 5.6. SEM images for $Li_xNi_{0.5}Mn_{1.5}O_4$.

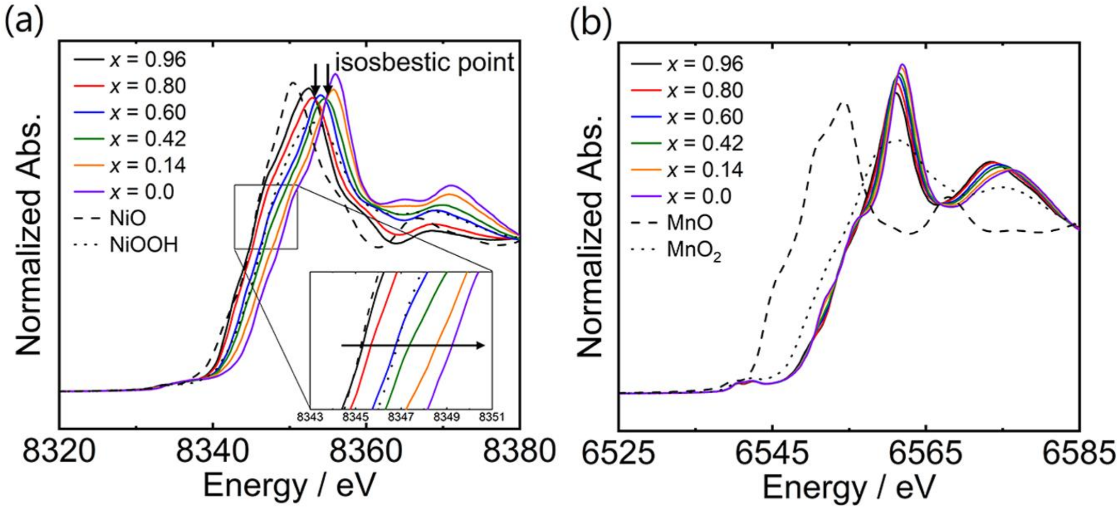

Figure 5.7. XANES spectra of (a) Ni K-edge and (b) Mn K-edge for $Li_xNi_{0.5}Mn_{1.5}O_4$.

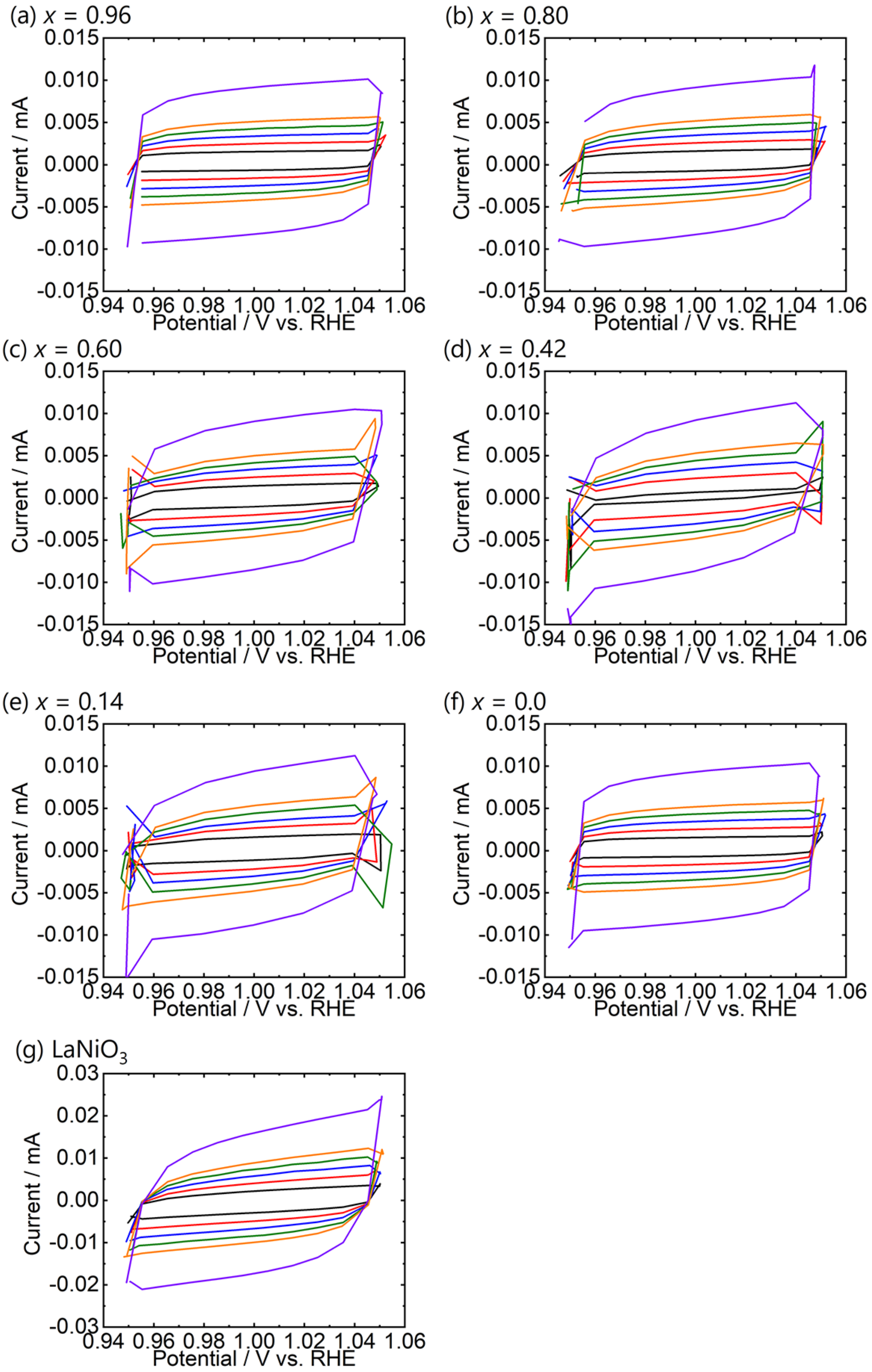

Figure 5.8. Double layer capacity measurement results for $Li_xNi_{0.5}Mn_{1.5}O_4$.

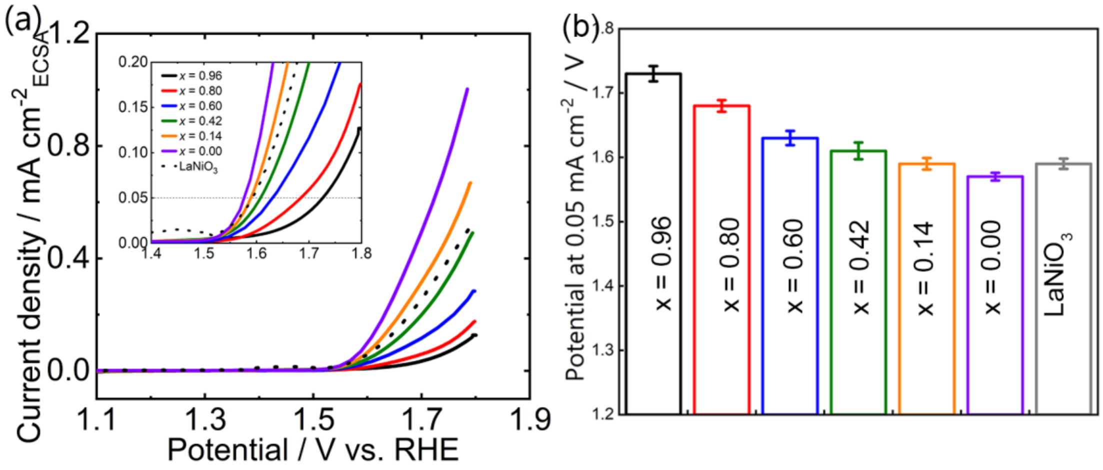

Figure 5.9. (a) LSV curves and (b) potential needed to achieve 0.05 mA cm^{-2}$_{ECSA}$ of Li$_x$Ni$_{0.49}$Mn$_{1.51}$O$_4$.

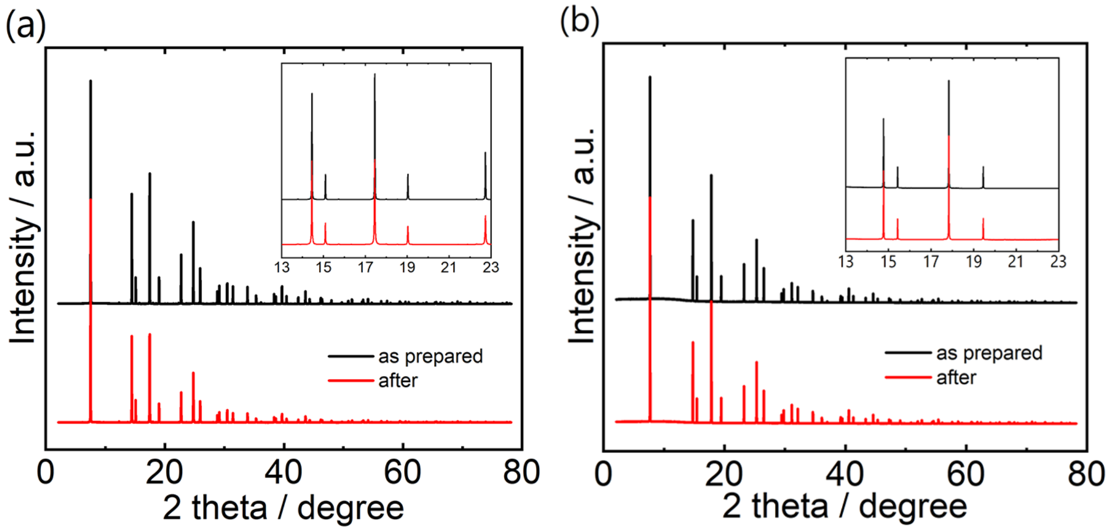

Figure 5.10. XRD of as prepared and after electrolysis samples for (a) x = 0.96 and (b) x = 0.0

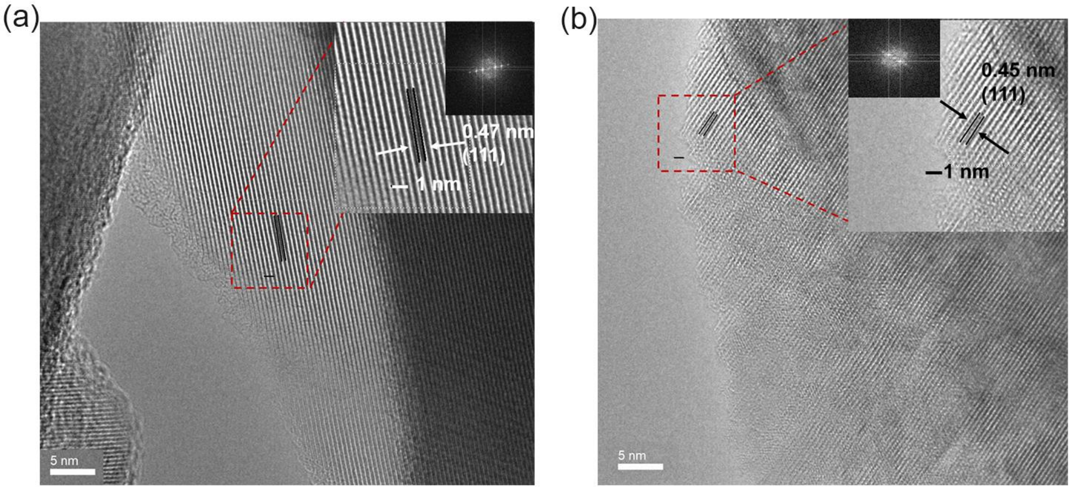

Figure 5.11. TEM after electrolysis for (a) $x = 0.96$ and (b) $x = 0.0$.

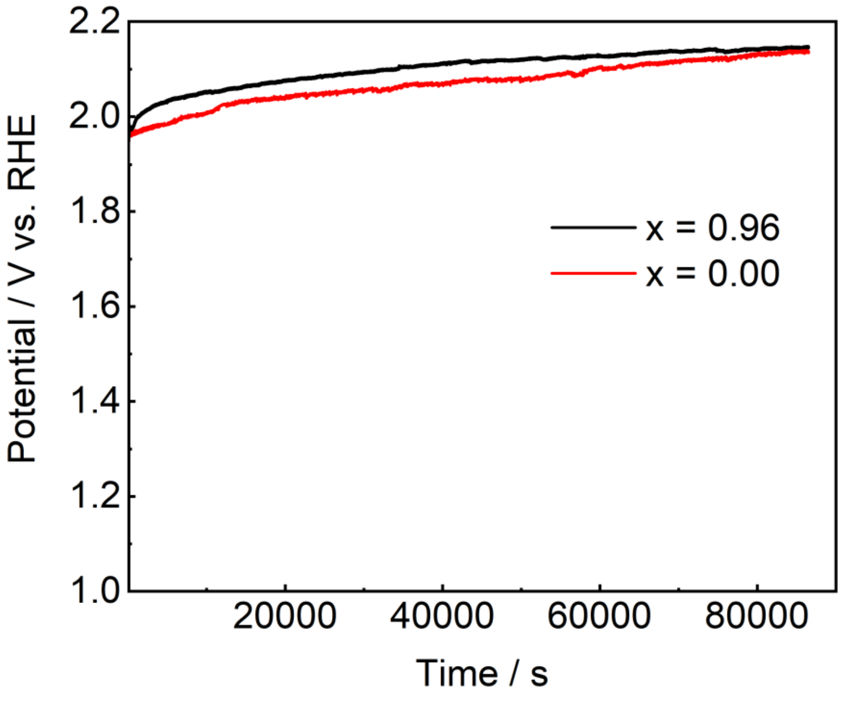

Figure 5.12. Long-term stability tests for $Li_{0.96}Ni_{0.49}Mn_{1.51}O_4$ and $Li_{0.00}Ni_{0.49}Mn_{1.51}O_4$. For $Li_{0.00}Ni_{0.49}Mn_{1.51}O_4$ sample, the current density was kept at 10 mA/cm^2. For $Li_{0.96}Ni_{0.49}Mn_{1.51}O_4$ sample, the current was kept at 6 mA/cm^2, making the initial potential the same for both samples before the long-term stability test.

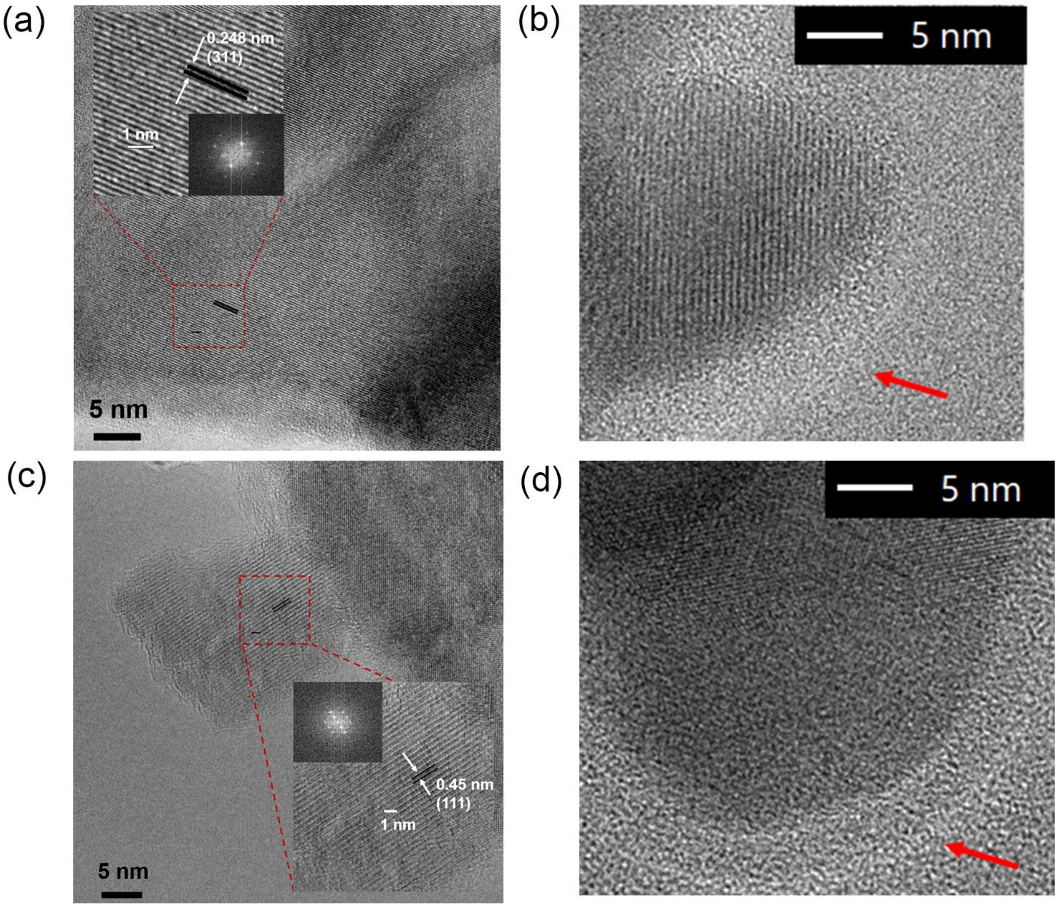

Figure 5.13. TEM images after long-term stability tests for (a) $Li_{0.96}Ni_{0.49}Mn_{1.51}O_4$ and (b) $Li_{0.00}Ni_{0.49}Mn_{1.51}O_4$

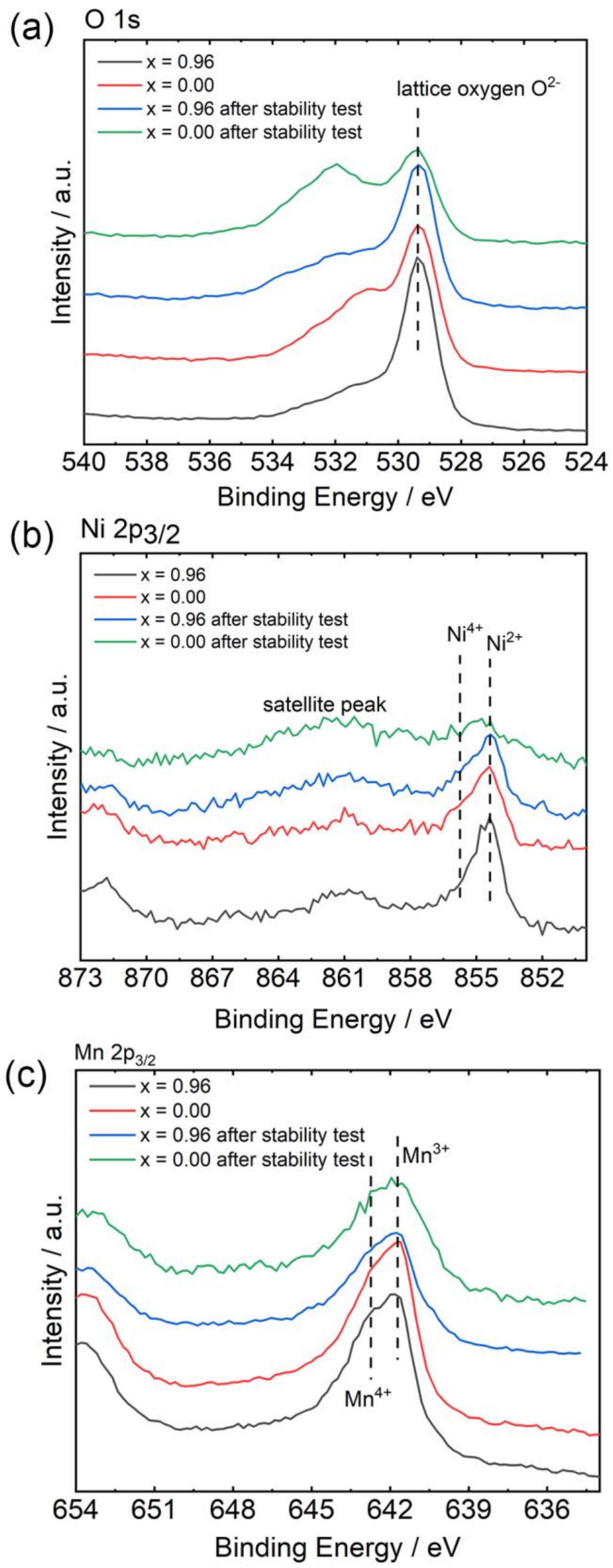

Figure 5.14. XPS spectra of (a) O 1s, (b) Ni 2p 3/2 and (c) Mn 2p 3/2 for *x*=0.00 and *x* = 0.96 before/after stability test.

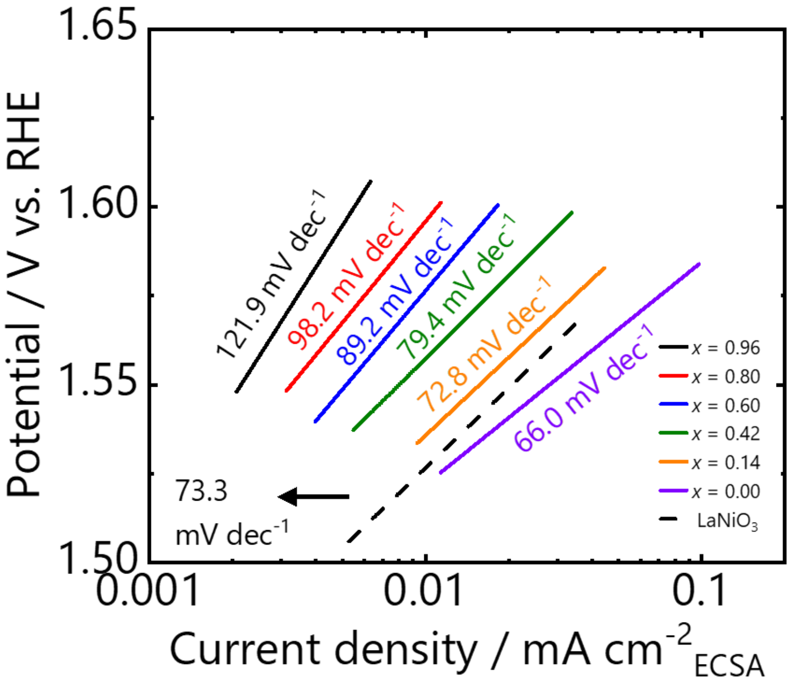

Figure 5.15. Tafel plots of LixNi0.5Mn1.5O4 spinels

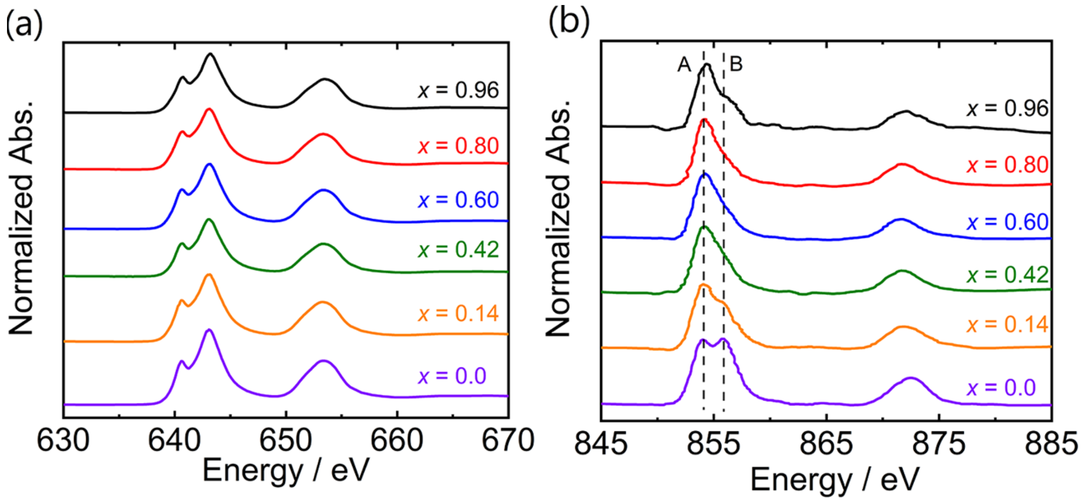

Figure 5.16. (a) Mn L-edge and (b) Ni L-edge XAS measured with the TEY mode of $Li_xNi_{0.49}Mn_{1.51}O_4$.

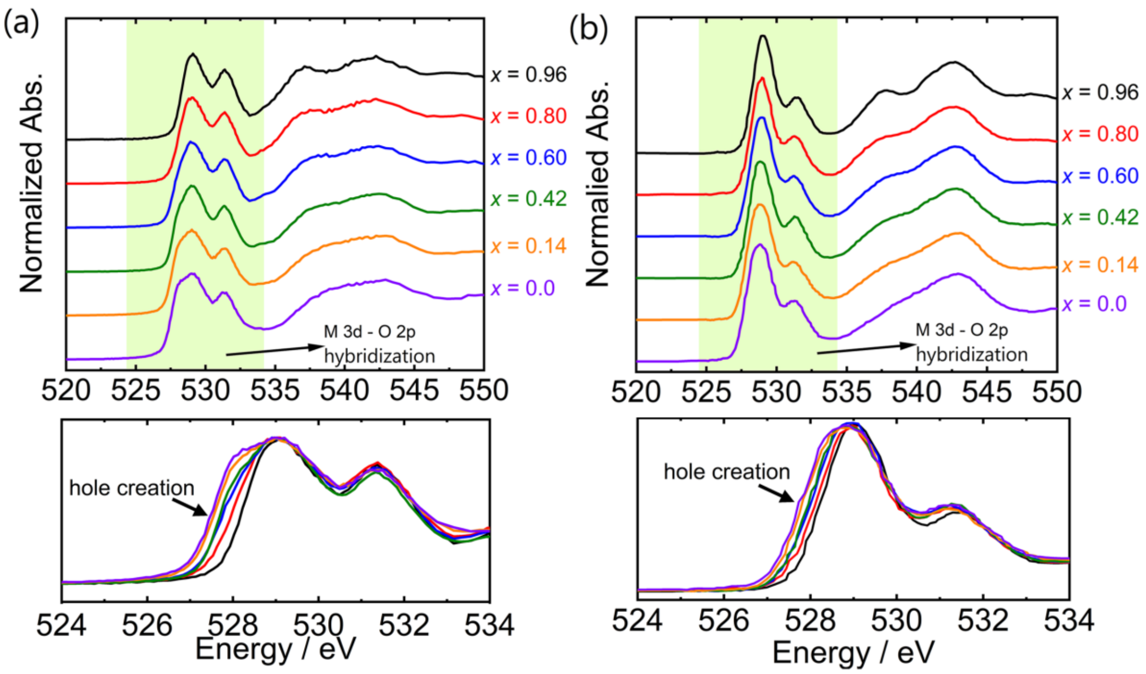

Figure 5.17. O K-edge XAS of $Li_xNi_{0.49}Mn_{1.51}O_4$ measured with (a) PFY mode and (b) TEY mode

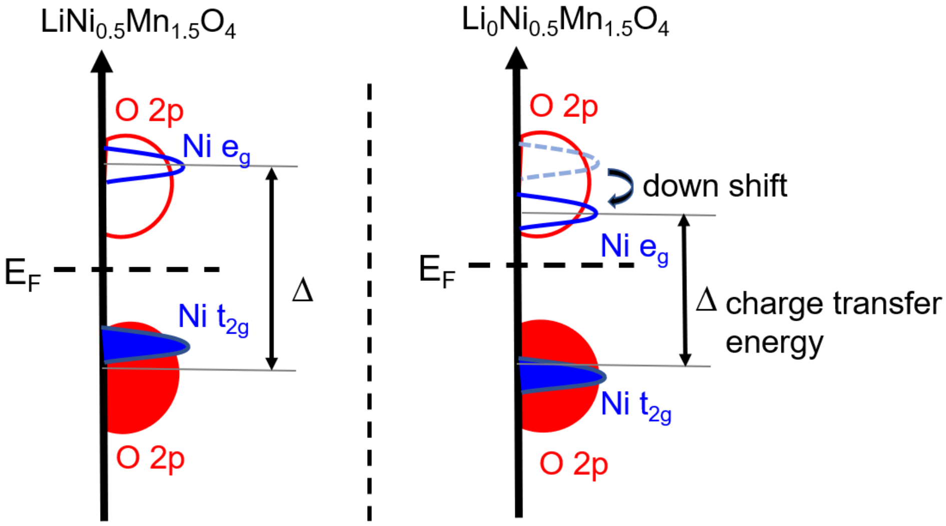

Figure 5.18. Electronic structure of $LiNi_{0.5}Mn_{1.5}O_4$ and $Li_0Ni_{0.5}Mn_{1.5}O_4$ near the Fermi level

Table 5.1. Chemical composition of each sample detected by ICP-OES.

Entry	$LiNi_{0.5}Mn_{1.5}O_4$: NO_2BF_4	Chemical Composition
1	1 : 0.00	$Li_{0.96}Ni_{0.49}Mn_{1.51}O_4$
2	1 : 0.73	$Li_{0.80}Ni_{0.50}Mn_{1.50}O_4$
3	1 : 0.92	$Li_{0.60}Ni_{0.49}Mn_{1.51}O_4$
4	1 : 1.24	$Li_{0.42}Ni_{0.49}Mn_{1.51}O_4$
5	1 : 2.29	$Li_{0.14}Ni_{0.50}Mn_{1.50}O_4$
6	1 : 10.1	$Li_{0.00}Ni_{0.49}Mn_{1.51}O_4$

Table 5.2. Rietveld refinement parameters for $x = 0.96$.

Phase	Space group	Atom	Wyck	S.O.F	*x* / a	*y* / b	*z* / c	*B* / Å^2
I	*P*4$_3$32 - Cubic	Li1	8c	1.000	0.004	0.004	0.004	=Mn1(B)
		Ni1	4a	1.000	0.625	0.625	0.625	=Mn1(B)
		Mn1	12d	1.000	0.125	0.379	-0.129	0.300
		O1	8c	1.000	0.384	0.384	0.384	=O2(B)
		O2	24e	1.000	0.149	-0.142	0.126	0.253

Table 5.3. Rietveld refinement parameters for $x = 0.80$.

Phase	Spacegroup	Atom	Wyck	S.O.F	*x* / a	*y* / b	*z* / c	*B* / Å^2	ratio
I	*P*4$_3$32 - Cubic	Li1	8c	1.000	0.004	0.004	0.004	=Mn1(B)	74.70%
		Ni1	4a	1.000	0.625	0.625	0.625	=Mn1(B)	
		Mn1	12d	1.000	0.125	0.378	-0.128	0.325	
		O1	8c	1.000	0.389	0.389	0.389	=O2(B)	
		O2	24e	1.000	0.140	-0.144	0.121	0.273	
II	*P*4$_3$32 - Cubic	Li1	8c	0.500	0.004	0.004	0.004	=Mn1(B)	25.30%
		Ni1	4a	1.000	0.625	0.625	0.625	=Mn1(B)	
		Mn1	12d	1.000	0.125	0.379	-0.129	0.324	
		O1	8c	1.000	0.384	0.384	0.384	=O2(B)	
		O2	24e	1.000	0.133	-0.142	0.126	0.271	

Table 5.4. Rietveld refinement parameters for x = 0.60.

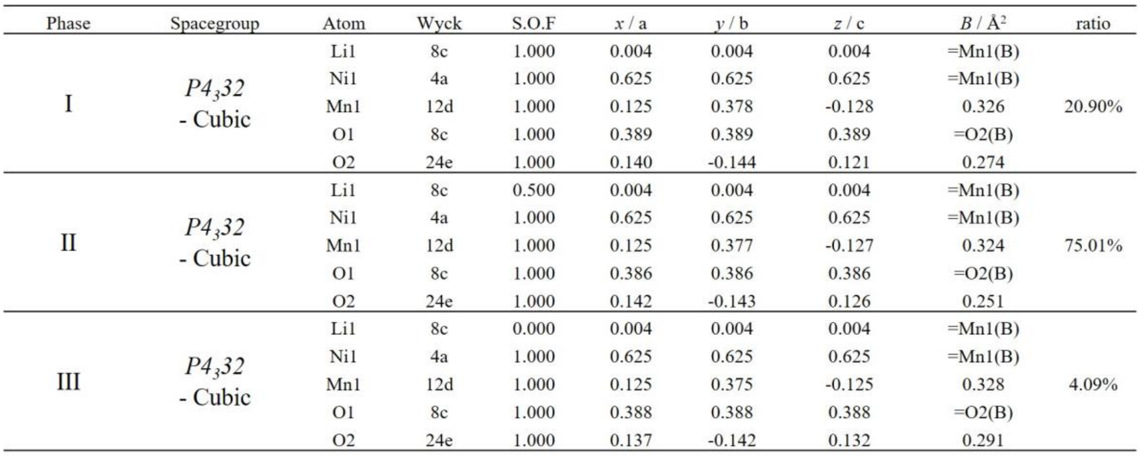

Phase	Spacegroup	Atom	Wyck	S.O.F	x / a	y / b	z / c	B / Å^2	ratio
I	$P4_332$ - Cubic	Li1	8c	1.000	0.004	0.004	0.004	=Mn1(B)	20.90%
		Ni1	4a	1.000	0.625	0.625	0.625	=Mn1(B)	
		Mn1	12d	1.000	0.125	0.378	-0.128	0.326	
		O1	8c	1.000	0.389	0.389	0.389	=O2(B)	
		O2	24e	1.000	0.140	-0.144	0.121	0.274	
II	$P4_332$ - Cubic	Li1	8c	0.500	0.004	0.004	0.004	=Mn1(B)	75.01%
		Ni1	4a	1.000	0.625	0.625	0.625	=Mn1(B)	
		Mn1	12d	1.000	0.125	0.377	-0.127	0.324	
		O1	8c	1.000	0.386	0.386	0.386	=O2(B)	
		O2	24e	1.000	0.142	-0.143	0.126	0.251	
III	$P4_332$ - Cubic	Li1	8c	0.000	0.004	0.004	0.004	=Mn1(B)	4.09%
		Ni1	4a	1.000	0.625	0.625	0.625	=Mn1(B)	
		Mn1	12d	1.000	0.125	0.375	-0.125	0.328	
		O1	8c	1.000	0.388	0.388	0.388	=O2(B)	
		O2	24e	1.000	0.137	-0.142	0.132	0.291	

Table 5.5. Rietveld refinement parameters for x = 0.42.

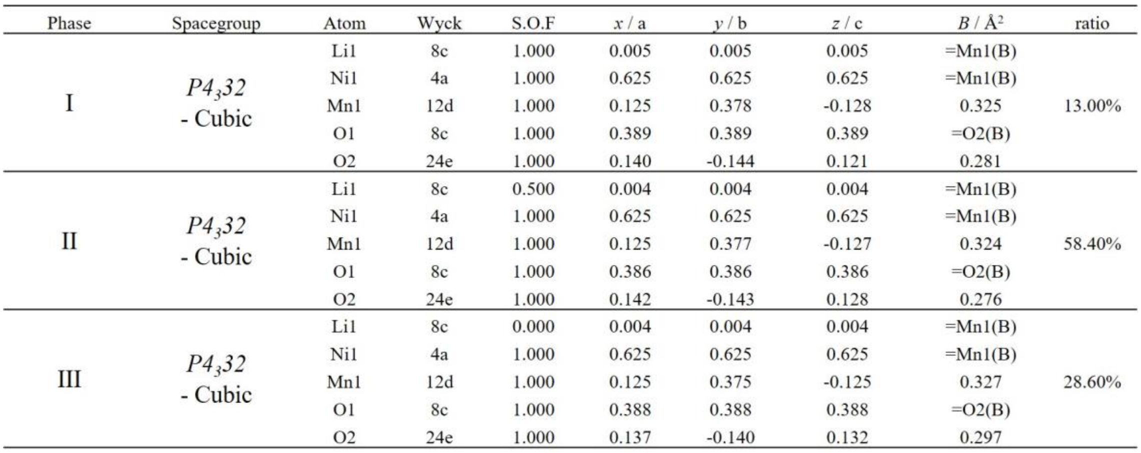

Phase	Spacegroup	Atom	Wyck	S.O.F	x / a	y / b	z / c	B / Å^2	ratio
I	$P4_332$ - Cubic	Li1	8c	1.000	0.005	0.005	0.005	=Mn1(B)	13.00%
		Ni1	4a	1.000	0.625	0.625	0.625	=Mn1(B)	
		Mn1	12d	1.000	0.125	0.378	-0.128	0.325	
		O1	8c	1.000	0.389	0.389	0.389	=O2(B)	
		O2	24e	1.000	0.140	-0.144	0.121	0.281	
II	$P4_332$ - Cubic	Li1	8c	0.500	0.004	0.004	0.004	=Mn1(B)	58.40%
		Ni1	4a	1.000	0.625	0.625	0.625	=Mn1(B)	
		Mn1	12d	1.000	0.125	0.377	-0.127	0.324	
		O1	8c	1.000	0.386	0.386	0.386	=O2(B)	
		O2	24e	1.000	0.142	-0.143	0.128	0.276	
III	$P4_332$ - Cubic	Li1	8c	0.000	0.004	0.004	0.004	=Mn1(B)	28.60%
		Ni1	4a	1.000	0.625	0.625	0.625	=Mn1(B)	
		Mn1	12d	1.000	0.125	0.375	-0.125	0.327	
		O1	8c	1.000	0.388	0.388	0.388	=O2(B)	
		O2	24e	1.000	0.137	-0.140	0.132	0.297	

Table 5.6. Rietveld refinement parameters for x = 0.14.

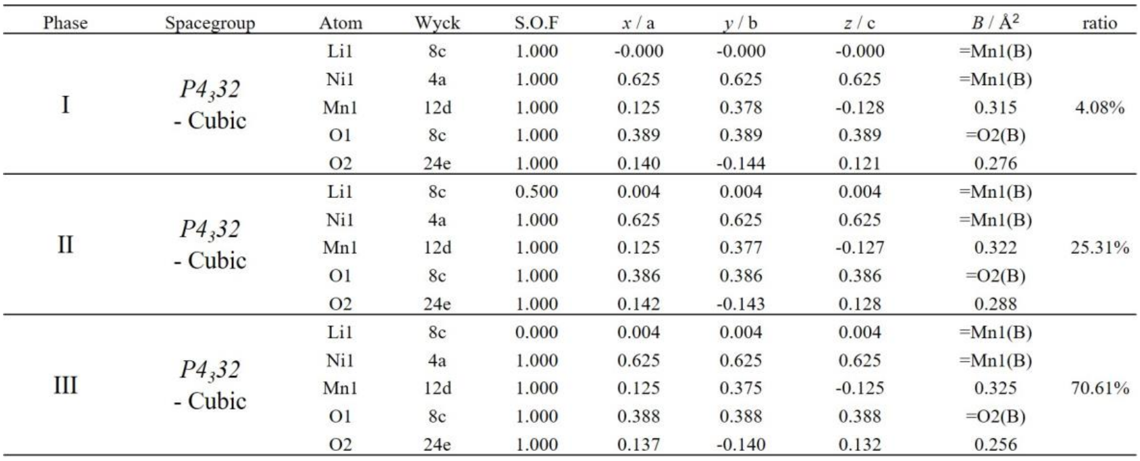

Phase	Spacegroup	Atom	Wyck	S.O.F	x / a	y / b	z / c	B / Å^2	ratio
I	$P4_332$ - Cubic	Li1	8c	1.000	-0.000	-0.000	-0.000	=Mn1(B)	4.08%
		Ni1	4a	1.000	0.625	0.625	0.625	=Mn1(B)	
		Mn1	12d	1.000	0.125	0.378	-0.128	0.315	
		O1	8c	1.000	0.389	0.389	0.389	=O2(B)	
		O2	24e	1.000	0.140	-0.144	0.121	0.276	
II	$P4_332$ - Cubic	Li1	8c	0.500	0.004	0.004	0.004	=Mn1(B)	25.31%
		Ni1	4a	1.000	0.625	0.625	0.625	=Mn1(B)	
		Mn1	12d	1.000	0.125	0.377	-0.127	0.322	
		O1	8c	1.000	0.386	0.386	0.386	=O2(B)	
		O2	24e	1.000	0.142	-0.143	0.128	0.288	
III	$P4_332$ - Cubic	Li1	8c	0.000	0.004	0.004	0.004	=Mn1(B)	70.61%
		Ni1	4a	1.000	0.625	0.625	0.625	=Mn1(B)	
		Mn1	12d	1.000	0.125	0.375	-0.125	0.325	
		O1	8c	1.000	0.388	0.388	0.388	=O2(B)	
		O2	24e	1.000	0.137	-0.140	0.132	0.256	

Table 5.7. Rietveld refinement parameters for x = 0.00.

Phase	Spacegroup	Atom	Wyck	S.O.F	x / a	y / b	z / c	B / Å^2
III	$P4_332$ - Cubic	Li1	8c	0.000	0.004	0.004	0.004	=Mn1(B)
		Ni1	4a	1.000	0.625	0.625	0.625	=Mn1(B)
		Mn1	12d	1.000	0.125	0.375	-0.125	0.312
		O1	8c	1.000	0.391	0.391	0.391	=O2(B)
		O2	24e	1.000	0.135	-0.138	0.137	0.156

Table 5.8. The electrochemical surface area parameters for $Li_xNi_{0.5}Mn_{1.5}O_4$.

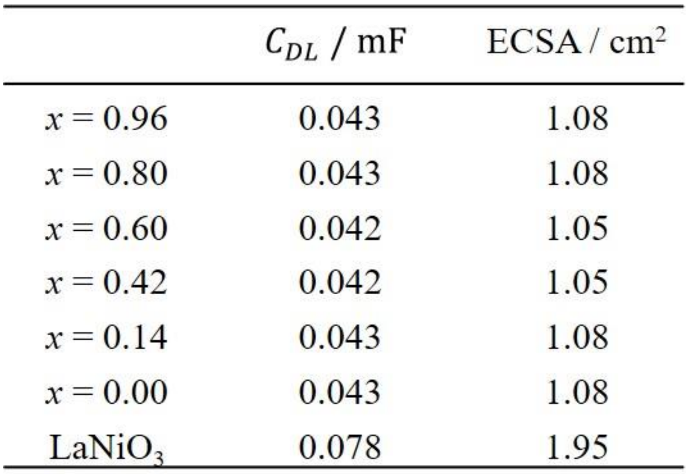

	C_{DL} / mF	ECSA / cm^2
$x = 0.96$	0.043	1.08
$x = 0.80$	0.043	1.08
$x = 0.60$	0.042	1.05
$x = 0.42$	0.042	1.05
$x = 0.14$	0.043	1.08
$x = 0.00$	0.043	1.08
$LaNiO_3$	0.078	1.95

Table 5.9. Tafel slope value of $Li_xNi_{0.5}Mn_{1.5}O_4$ series and $LaNiO_3$.

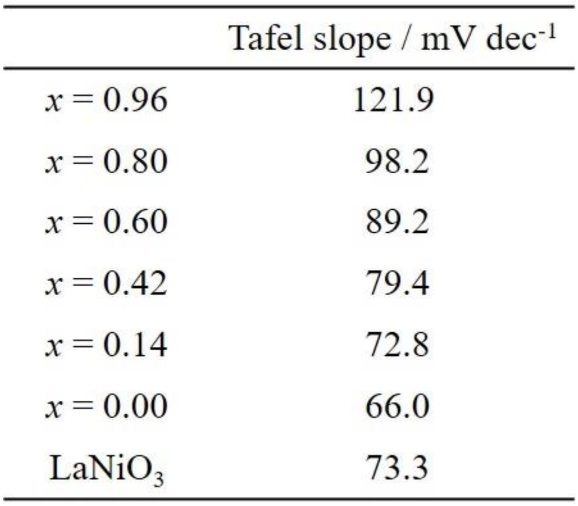

	Tafel slope / mV dec^{-1}
$x = 0.96$	121.9
$x = 0.80$	98.2
$x = 0.60$	89.2
$x = 0.42$	79.4
$x = 0.14$	72.8
$x = 0.00$	66.0
$LaNiO_3$	73.3

Chapter 6. Quadruple Perovskite Oxides $CaMn_7O_{12}$ Proceed by Two-active-site Reaction Mechanism for Oxygen Evolution Reaction

The oxygen evolution reaction (OER) is one of the essential energy conversion reactions for hydrogen production. In quadruple perovskite oxides $AA'_3B_4O_{12}$ (A = Ca, Sr, A' = Cu, Mn and B = 3d metals), the new reaction mechanism of O-O bond formation between adsorbed oxygen species at adjacent A'-B sites has been proposed in recent studies. This idea of multiple transition metals working together to form an active site, rather than a single active site, is appealing, but has not been systematically investigated so far. This study examined OER catalytic performances of $CaMn_7O_{12}$ quadruple perovskite oxides with precisely controlled Mn(A')-Mn(B) distance by doping with Sr, Cu and Al. The crystal structure and the state of cations and O were investigated through XRD with Rietveld refinement and X-ray absorption spectroscopy. The OER catalytic activity is clearly correlated to the distance of Mn(A')-Mn(B) while both e_g state of Mn and O 2*p* band center unchanged. The shrinkage of the A'-B distance affects the stability of O-O bond on A'-B site and accelerates OER kinetics.

6.1 Introduction

Water electrolysis is one of the most important technologies to store the electricity generated from sustainable but intermittent energy sources such as wind and solar power into hydrogen as fuels. However, the sluggish kinetics of oxygen evolution reaction impedes water electrolysis from the wider promotion, even when facilitated by precious metal-based catalysts such as RuO_2 and IrO_2[1-3]. The discovery of efficient electro-catalysts that consists of only earth-abundant elements are highly desired and investigated for a few decades[3-5]. Many efforts have been devoted to understanding the mechanism of OER activity and discovering an activity descriptor[6-11]. With these reports on high OER activity, many studies have been conducted to clarify the relationship between the electronic state of transition metals in perovskites and OER activity[12-18]. Suntivich et al. conducted a systematic investigation of several transition metals contained in perovskite-type oxides and revealed that the number of occupied e_g states of the metal cations could be used as the activity descriptor[12]. That is, the highest OER activity can be attained when the number of eg electrons of the B-site cations is close to 1.2, well-known as volcano plot. Their subsequent experimental and ab initio computational study indicated that the importance of controlling a transition metal in perovskite oxide having the O p-band close to the Fermi level as a promising strategy to design efficient catalysts for OER[13].

Recently, Yamada et al. reported that quadruple perovskite oxides $AA'_3B_4O_{12}$ (A = Ca, Sr, A' = Cu, Mn and B = 3*d* metals) exhibited OER catalytic activity that was higher than that of simple perovskite oxides ABO_3 with the same B-site elements[19-22]. The crystal structures of various perovskites were shown in Figure 6.1. Compared with the simple ABO_3 type perovskite, the quadruple type perovskite has three quarters of A-site (A' site) occupied by transition metal such as Mn and Co, which allows a complicated covalent network between atoms and could accelerate the OER due to additional active sites[20]. For example, $LaMn_7O_{12}$ displayed better OER activity than $LaMnO_3$, even though above-mentioned descriptors of both materials were almost the same. They proposed the two-active-site (A'-B bridge site) reaction mechanism based on density functional theory calculations, where the high catalytic activities of quadruple perovskites were attributed to O-O dimer formation on adjacent A’ and B sites on a (220) surface[22] as a quadruple perovskite has two distinct close crystallographic sites of [$A'O_4$] pseudo-square units and [BO_6] octahedral units. This OER mechanism is significantly different from the conventional single-active-site mechanism as widely accepted in simple perovskites[23]. This pioneering work is of importance in designing a new strategy for OER catalysts because this unique structure of quadruple perovskites can provide an opportunity to study unexplored interactions between the oxides and the adsorbed species. When the specific activities were plotted against the average Mn-Mn distance for manganese oxides (Mn_2O_3, Mn_3O_4, $AMnO_3$, and AMn_7O_{12}), the best OER activity is observed at 3.2 Å (AMn_7O_{12}), which indicates that Mn-Mn distance may be a possible descriptor for OER activity in quadruple perovskites[20]. Since O-O dimer bridged on the top of A’ and B site of 3*d*-metal ions, the stability of O-O bond may be modified and the higher activity can be realized by optimizing 3*d*- metal A’ ion- 3*d*-metal B bond length.

This catalyst design guideline may exhibit higher catalytic activity than that predicted by the volcano plot for conventional catalysts with a single active site for oxygen evolution. However, there is an overwhelming lack of knowledge about the activity dominant factor for catalysts with these two active sites. In this study, Mn(A’)-Mn(B) bond length of $CaMn_7O_{12}$ quadruple perovskite was precisely controlled by element doping with Al, Sr and Cu to validate the descriptor and the origin of the catalytic activity. A systematic investigation of the influence of crystal structure and the electronic state of Mn on OER were presented by X-ray diffraction (XRD), transmission electron microscopy (TEM), X-ray absorption spectroscopy (XAS), X-ray photoelectron spectroscopy (XPS) and the electrochemical measurements. The effect of doping on catalytic activity as well as Mn(A’)-Mn(B) bond length was discussed.

6.2 Experimental

6.2.1 Material Preparation

Sr, Cu and Al doped $CaMn_7O_{12}$ was prepared by citrate complexation method. The stoichiometric mixtures of Sr(NO3)$_2$, $Al(NO_3)_3$ $CaCO_3$ (FUJIFILM Wako Pure Chemical Corporation), $Mn(NO_3)_2 \cdot 6H_2O$(FUJIFILM Wako Pure Chemical Corporation) and $Ni(NO_3)_2 \cdot 6H_2O$ (FUJIFILM Wako Pure Chemical Corporation) were dissolved into nitric acid. Five-fold excess of citric acid and stoichiometric amount of 1,2-ethanediol were added to the solution under stirring. The solution was heated to 300 °C and held at the same temperature to obtain the dried powder. This precursor was calcined in a furnace at 400 °C for 1h and 675 °C for 12 h in air. Then, Sr, Cu and Al doped $CaMn_7O_{12}$ was finally obtained at 900 °C for 12 h in air.

6.2.2 Characterization

Powder X-ray diffraction (XRD) patterns were collected at the BL02B2 beamline of SPring-8 and BL5S2 of Aichi Synchrotron Radiation Center, Japan. The wavelength was determined using CeO_2 as reference (λ = 0.61972 Å). The crystal structure refinement was conducted using a Rietveld refinement program Jana2006. Mn and Ni K-edge hard X-ray absorption fine structures (XAFS) were collected in transmission mode and fluorescence mode using Si (111) monochromator at BL14B2 and BL01B1 beamline of SPring-8 and BL11S2 of Aichi Synchrotron Radiation Center, Japan. Mn and Ni L-edge, O K-edge soft X-ray XAFS were collected at BL-11 beamline of SR center, Ritsumeikan university, Japan.

6.2.3 Electrochmical Tests

The catalyst inks were prepared by mixing 10 mg of catalyst, 2 mg of acetylene black (DENKA Company Ltd.), 40 µL of 5wt% proton-type Nafion® suspension (Sigma-Aldrich), 20 µL of 0.1 M KOH aqueous solution and 1.94 mL of tetrahydrofuran

(FUJIFILM Wako Pure Chemical Corporation). The inks were sonicated for 30 min to obtain uniform suspension. A rotating disk electrode (HOKUTO DENKO, Japan) consisting of a glassy carbon (GC) disk (5 mm in diameter) was used as working electrode. 10 μL of catalyst ink was drop-casted onto the GC-disk and dried for 12 h in vacuum at room temperature. Electrochemical measurements were performed using a rotating disk electrode rotator (HOKUTO DENKO, Japan) in combination with a potentiogalvanostat (MPG-205-NUC, Bio-Logic). Pt wire electrode and reversible hydrogen electrode (RHE) filled with 0.1 M KOH aqueous solution were used as counter and reference electrodes, respectively. The catalyst-coated disk was rotated at 1600 rpm during the measurements. All electrochemical measurements were conducted under N_2 atmosphere at room temperature. In the OER test, the disk potential was controlled between 1.2 V to 1.8 V vs RHE at a scan rate of 5 mV s^{-1}. The *iR*-correction (R ~12 Ω) was carried out for all data after measurement. The electrochemical surface area (ECSA) was estimated using the methods proposed by McCrory et al[36]. The cyclic voltammograms were measured in a non-Faradaic region at the scan rate of 20, 40, 60, 80, 100, 200 mV s^{-1}. The double layer capacitance (C_{dl}) is obtained from the following equation (1), where i_c represents the charge current and the v represents the scan rate:

$$C_{dl} = i_c / v \tag{1}$$

ECSA is calculated using equation (2) as following, whereas the specific capacitance (C_s) is 0.040 mF cm-2 in 0.1 M KOH aqueous solutionR8:

$$ECSA = C_{dl} / C_s \tag{2}$$

In order to discuss the practical catalytic activity of this catalyst in large scale applications, it is necessary to discuss it in terms of overpotential at 10 mA cm^{-2}. However, in this paper, we are doing a modeling study to identify the dominant factors of catalytic activity, which needs to be discussed in terms of specific activity per electrochemically active surface area. Therefore, the specific current density was calculated based on the previous work of Yamada et. al[19, 20]. The specific OER activities were normalized by ECSA of all samples at 1.7 V vs. RHE. The catalysts stability was measured using the galvanostatic method at the mass activity of 10 A g^{-1} for over 2 h. The catalyst-coated RDE was rotated at 3600 rpm during the stability tests.

6.3 Results and Discussion

6.3.1 Crystal Structure

Figure 6.2, Table 6.1, Table 6.2 and Figure 6.3 show the XRD patterns of Sr, Cu and Al doped $CaMn_7O_{12}$. According to the Rietveld refinement results (Table 6.1), all the samples with different amount of doping did not contain or contain very few amounts of oxygen vacancies, which cannot be quantitatively evaluated by Rietveld refinement. The amount of oxygen vacancies may vary depending on the doping, but the Rietveld analysis confirmed that the amount of oxygen vacancies is not large in these catalysts, so the effect of the amount of oxygen vacancies on the catalytic activity is considered to be small. According to Figure 6.2(a), Sr doping content (x) clearly leads to peak shift to lower angle, suggesting expansion of the lattice due to substitution of Ca^{2+} by larger Sr^{2+}. The lattice constants show a systematic increase as a function of x without changing its space group (Table 6.1). The single phase could not be obtained when $x \geq 0.4$. These results had a good agreement with one previous study[25]. On the other hand, the doping of Cu clearly leads to phase transition in the crystal structure. This effect is particularly remarkable in the enlarged view of main diffraction peaks at 2 theta = 13−14° (Figure 2b). The disappearance of some diffraction peaks in Cu doped $CaMn_7O_{12}$ suggested that $y = 0.3$

sample displayed the crystal structural change. According to Rietveld refinement results shown in Table 6.1 and Figure 6.3, the sample with y = 0.0, 0.1, 0.2 displayed a distorted perovskite structure with trigonal symmetry, $R\bar{3}$ space group, while y = 0.3 showed a cubic symmetry, $Im\bar{3}$ space group. We could not obtain the sample with $x \geq 0.4$ due to the presence of impurities. The lattice constants show a systematic increase as a function of y from 0.0 to 0.2. The Mn, Cu and O positional parameters obtained from Rietveld analysis was identical to the previous study[26]. In addition, when Al was doped into the host matrix, the peaks were shifted to higher angle due to the shrinkage of the lattice, indicating that Al was properly incorporated into $CaMn_7O_{12}$ lattice[27]. Therefore, we have succeeded in changing the Mn(A')-Mn(B) bond length in the crystal structure by heterogeneous cation (Sr, Cu, Al) doping.

6.3.2 Electronic Structure

The electronic structure of Mn and O were investigated by XAS. According to Mn K-edge XANES shown in Figure 6.4a, the state of Mn was constant regardless of the doping level. The shoulder peak at 6548 eV is assigned to 1s-4pz transition induced by [MnO_4] pseudo-square-planner coordination in $CaMn_7O_{12}$2[8]. Mn L-edge XAS spectra in Figure 6.5. Figure 6.5 (a), (c) and (e) showed a closer inspection of $CaMn_7O_{12}$ that possess multivalent signature like RMn_2O_5[29,30]. Two spectral features at 641 eV and 644 eV in L_{III}-edge are assigned to t_{2g} and e_g state, respectively. Since there were no significant change in the spectra, the proportion of Mn^{3+}/Mn^{4+} has not changed regardless of doping level as expected from Mn K/L-edge XAS in Sr, Al doped $CaMn_7O_{12}$. Since Ca^{2+} and Mn3^{+} were replaced with cations of the same valence states (Sr^{2+}, Al^{3+}, respectively), the average valence of Mn is not expected to change. In Cu doped $CaMn_7O_{12}$, the valence state of Mn is expected to change because Cu^{2+} substituted Mn^{3+}. However, no change was observed in Mn L-edge spectra. This discrepancy can be attributed to the fact that the doping of Cu is less than 5% at most with respect to Mn, resulting in little change in the Mn K/L-edge spectrum. The features of O 2*p* states and hybridized Ca and Mn are characterized by the O K-edge spectra in Figure 6.6(b) and Figure 6.5 (b), (d), and (f). The pre-edge splitting peaks at 529, 530, and 531 eV indicated the transitions from 1*s* state to hybridized O 2*p* and Mn 3*d* orbitals. Mannella et al. have inferred this splitting as an indication of the degeneracy breaking of e_g state due to a Jahn-teller distorted MnO_6 octahedra[31]. The O K-edge spectra did not change because the addition of Sr, Cu and Al were quite smaller than Mn and the electronic state of Mn did not change.

To provide further information about the Mn oxidation state of the doped samples, we measured the XPS of the typical catalysts (pristine $CaMn_7O_{12}$, x =0.1, y = 0.2, and z = 0.3 samples). XPS is a widely used technique for determining the oxidation states of the constituent elements in the catalysts study. As shown in Figure 6.6 (a), all the samples showed very similar Mn 2*p* peaks. The main peaks at around 642 and 654 eV correspond to Mn 2*p*3/2 and Mn 2*p*1/2, respectively, which is consistent with previous research[32-34]. Such peak splitting was attributed to the spin-orbit coupling, indicating that Mn has the mixed valent state of trivalence and quadrivalence[34]. The identical Mn 2*p* peak positions for all the samples in Figure 6.6 (a) further proved that the Mn electronic structure stated unchanged with the current element doping. Moreover, O 1*s* XPS (Figure 6.6b) showed the main peak at around 529. 6 eV, which was attributed to the lattice oxygen at normal lattice sites in the catalyst crystal structure. The broad energy peaks at higher binding energy (about 532 eV) might be due to the surface adsorbed oxygen or environmental hydroxyl species, which is common in O 1*s* spectrum since XPS is very surface sensitive[33]. The extremely similar peak positions in Figure 6.6(b) also evidence that the lattice oxygen shared the same state for all the samples. Combining the XAS results with the XPS results, we could conclude that the Mn electronic state was not affected with the current element doping.

6.3.3 Electrochemical Performance

OER catalytic performances, normalized by ECSA (Electrochemically active surface area, determined by Figure 6.7, Figure 6.8), of Sr, Cu, and Al doped samples were shown in Figure 6.9. As there were no significant differences in double layer capacitance (Table 6.3), the order of activity and ECSA (Figure 6.6, 6.7) would not change. It was observed that there was a correlation between the OER catalytic activity and the amount of Sr doping. According to Figure 6.9(a), $x = 0.0$ showed the lowest onset potential for OER current, indicating that it has the best OER activity. In addition, a decreasing tendency toward OER activity corresponds to increasing x. When $CaMn_7O_{12}$ was doped with Cu, obvious enhancement of OER activity can be observed, as shown in Figure 6.9(b). The best OER activity was achieved when Cu doping is 0.2. However, when Cu doping further increased to 0.3, a significant current density drop happened. The OER activity of $y = 0.3$ sample was even lower than pristine $CaMn_7O_{12}$. This can be attributed to the structure change from trigonal symmetry to cubic symmetry, resulting in the increase of Mn(A')-Mn(B) bond length as shown in Figure 6.1(b). In case of Al doped samples, the best OER activity was achieved at Al doping amount of 0.1. The current density decreased with further doping of Al ($z = 0.2$ and $z = 0.3$). Similarly, an obvious monotonic bond shrinkage of Mn(A')-Mn(B) was observed with the increasing doping of Al, As revealed by Rietveld refinement results (Figure 6.2c). Therefore, a strong relationship between OER activity and Mn(A')-Mn(B) bond distance existed. The Tafel slopes in Figure 6.10(a) for $CaMn_7O_{12}$ was 94 mV dec^{-1}, which is in consistent with previous research[21]. The activity of Cu doped $CaMn_7O_{12}$ was in the order of $y = 0.3 < CaMn_7O_{12} < y = 0.1 < y = 0.2$ and Tafel slope was not changed. In addition, the activity of Al doped $CaMn_7O_{12}$ was in the order of $CaMn_7O_{12} < z = 0.3 < z = 0.2 < z = 0.1$. Moreover, the Tafel slope for all the doped samples were in the same range between 103 mV dec^{-1} ~ 114.1 mV dec^{-1}, as shown in Figure 6.10, indicating the rate-determining step (RDS) of OER for each sample was the same[32]. The slight differences observed in Tafel values might be due to the difference in the resistance of the catalysts to transfer the charge on the surface of the metal oxide[33]. The catalyst performance of the pristine material, $CaMn_7O_{12}$, $CaMn_7O_{12}$, the best catalyst in this study, $CaMn_{6.9}Al_{0.1}O_{12}$ ($z = 0.1$), and the reported catalysts were listed in Table S4. For all catalysts, the overpotential values at 0.25 mg cm^{-2} catalyst loading and 0.05 mA/cm^{-2} were estimated from literature and compared. The pristine $CaMn_7O_{12}$ showed the overpotential of 0.34 V, which was the same as the value reported by the previous study[20]. Meanwhile, the onset overpotential for $CaMn_{6.9}Al_{0.1}O_{12}$ ($z = 0.1$) was 0.32 V, indicating the catalyst activity was improved after doping. Although the catalyst performance in this study did not exceed the benchmarking ones reported by Suntivich et al. [12] and Yamada et al. [19], the main focus of this study is to demonstrate how the atom bond distance affect the catalyst performance. Therefore, we believe this study can provide intrinsic understanding about perovskite OER catalysts. According to TEM images in Figure 6.10, all the synthesized samples were well-crystallized. In addition, the surface of each sample was stable and did not show any significant changes after OER measurements. Moreover, long-term stability tests were conducted for the reference catalyst $CaMn_7O_{12}$ and the most active catalyst $z =$

0.1. The stability tests were conducted following the benchmarking work of Suntivich, et al[12], whereas the current density was kept at 10 A g^{-1} for over 2 h. As shown in Figure 6.11, $CaMn_7O_{12}$ showed slight degradation after electrolysis for over 2 h, while the most active z = 0.1 sample showed negligible current density drop, indicating its superior performance in both activity and stability.

6.3.4 Discussions about Reaction Mechanism

Based on the above results, we further discuss the reaction mechanism of the quadruple perovskites. In the benchmarking work on perovskite catalysts by Suntivich et al., they proposed the famous volcano relation between the OER catalytic activity and surface cation e_g occupancy, claiming the e_g occupancy is an important indicator to predict the catalyst activity[12]. To examine whether eg occupancy can be used to describe the OER catalytic activities of the quadruple perovskites in this study, the relation of the OER activities against e_g occupancy was displayed in Figure 6.12. The e_g filling values of Mn active sites was estimated from the Mn K-edge XANES (Figure 6.13) studies based on the method from Suntivich et al.[12]. The specific OER activities were normalized by ECSA of all samples at 1.7 V vs. RHE. The relation between activity and e_g occupancy is very vague, indicating e_g descriptor cannot be used to explain the catalyst activity mechanism in this study. Therefore, we investigated the relation between Mn(A')-Mn(B) distance and catalytic activities in Figure 6.14a. The strong correlation indicated that using Mn(A')-Mn(B) distance as the descriptor in this study is reasonable.

According to previous studies about ABO_3 type perovskite catalysts[5], the OER reaction mechanism proceeds on a single corner-shared MO_6 site, where B-site metal distance (e.g., Mn-Mn) has an average value of about 3.7~3.9 Å. Such longer M-M bond distance cannot form direct O-O bond, which was believed to be able to enhance OER activities greatly. In contrast, recent studies revealed that shorter M-M distance can enable direct O-O bond formation[34, 35], leading to the enhanced OER activity. Yamada et al. demonstrated that quadruple perovskite catalysts, due to the moderate bond distance of adjacent A' site and B site transition metal, could form O-O bond directly[20]. Such active A'-B bridge site contribute to the high OER activity of the quadruple perovskite catalysts[21, 22]. The best active catalyst in this study, which consists of corner-shared pseudo-square planes (A' site) and octahedra structure (B site), has the Mn(A')-Mn(B) bond distance of 3.19151 Å (z = 0.1 sample). Such a short bond distance could easily form the O-O bond (Figure 6.15b), therefore, leading to the increase of *-OO intermediates and higher OER activity (* represents the active reaction site). When bond distance is further increasing as shown in the right half volcano part (Figure 6.15a), the O-O bond formation would be impeded, resulting in the decrease of OER activity. Moreover, with the further shrinkage of Mn(A')-Mn(B) bond distance, as shown in the left half volcano part of Figure 6.15(a), the decrease of OER activities were also observed. This can be attributed to the repulsion between adsorbed species, as observed in some Mn_2O_3 and Mn_3O_4 oxides, which have the very short Mn-Mn distance of about 3 Å and relatively low OER activities[21]. To conclude, the optimum bond distance between the two active sites (Mn(A') and Mn(B)), leads to the direct formation of O-O bond, thus enhance the OER activity.

6.4 Conclusion

In summary, this study focused on the effect of Sr, Cu and Al doping on OER catalytic performances of $CaMn_7O_{12}$ quadruple perovskite oxides. The states of Mn and

O were investigated through X-ray absorption spectroscopy. It is revealed that Sr, Cu, and Al was successfully incorporated into the host matrix while the state of Mn and O did not show significant changes. According to electrochemical tests, OER performance was clearly correlated to the distance of Mn(A')-Mn(B) with a volcano-like relationship. This indicates that Mn(A')-Mn(B) bond distance is a possible descriptor for OER activity in $CaMn_7O_{12}$. The too much shrinkage or elongation of the bond decreased the OER activity due to the change of the stability of O-O bond on A'-B site. Therefore, the two active sites mechanism in $CaMn_7O_{12}$ was experimentally proved in this study.

Reference

1. Song, F.; Bai, L.; Moysiadou, A.; Lee, S.; Hu, C.; Liardet, L.; Hu, X., Transition Metal Oxides as Electrocatalysts for the Oxygen Evolution Reaction in Alkaline Solutions: An Application-Inspired Renaissance. *J. Am. Chem. Soc.* **2018**, 140 (25), 7748-7759.
2. Long, X.; Lin, H.; Zhou, D.; An, Y.; Yang, S., Enhancing Full Water-Splitting Performance of Transition Metal Bifunctional Electrocatalysts in Alkaline Solutions by Tailoring CeO2–Transition Metal Oxides–Ni Nanointerfaces. *ACS Energy Lett.* **2018**, 3 (2), 290-296.
3. Doyle, R. L.; Godwin, I. J.; Brandon, M. P.; Lyons, M. E. G., Redox and electrochemical water splitting catalytic properties of hydrated metal oxide modified electrodes. *Phys. Chem. Chem. Phys.* **2013**, 15 (33), 13737-13783.
4. Sun, S. N.; Sun, Y. M.; Zhou, Y.; Xi, S. B.; Ren, X.; Huang, B. C.; Liao, H. B.; Wang, L. Y. P.; Du, Y. H.; Xu, Z. C., Shifting Oxygen Charge Towards Octahedral Metal: A Way to Promote Water Oxidation on Cobalt Spinel Oxides.

Angew. Chem. Int. Edit **2019**, 58 (18), 6042-6047.

5. Hong, W. T.; Stoerzinger, K. A.; Lee, Y. L.; Giordano, L.; Grimaud, A.; Johnson, A. M.; Hwang, J.; Crumlin, E. J.; Yang, W. L.; Shao-Horn, Y., Charge-transfer-energy-dependent oxygen evolution reaction mechanisms for perovskite oxides. *Energ. Environ. Sci.* **2017**, 10, 2190-2200.
6. Fabbri, E.; Nachtegaal, M.; Binninger, T.; Cheng, X.; Kim, B. J.; Durst, J.; Bozza, F.; Graule, T.; Schäublin, R.; Wiles, L.; Pertoso, M.; Danilovic, N.; Ayers, K. E.; Schmidt, T. J., Dynamic surface self-reconstruction is the key of highly active perovskite nano-electrocatalysts for water splitting. *Nat. Mater*. **2017**, 16, 925-931.
7. Bergmann, A.; Martinez-Moreno, E.; Teschner, D.; Chernev, P.; Gliech, M.; de Araújo, J. F.; Reier, T.; Dau, H.; Strasser, P., Reversible amorphization and the catalytically active state of crystalline Co_3O_4 during oxygen evolution. *Nat. Commun.* **2015**, 6 (1), 8625.
8. Rao, R. R.; Kolb, M. J.; Giordano, L.; Pedersen, A. F.; Katayama, Y.; Hwang, J.; Mehta, A.; You, H.; Lunger, J. R.; Zhou, H.; Halck, N. B.; Vegge, T.; Chorkendorff, I.; Stephens, I. E. L.; Shao-Horn, Y., Operando identification of site-dependent water oxidation activity on ruthenium dioxide single-crystal surfaces. *Nat. Catal*. **2020**, 3 (6), 516-525.
9. Cheng, J.; Liu, X.; Kattirtzi, J. A.; VandeVondele, J.; Sprik, M., Aligning Electronic and Protonic Energy Levels of Proton-Coupled Electron Transfer in Water Oxidation on Aqueous TiO_2. *Angew. Chem. Int. Ed.* **2014**, 53 (45), 12046-12050.
10. Mefford, J. T.; Rong, X.; Abakumov, A. M.; Hardin, W. G.; Dai, S.; Kolpak, A. M.; Johnston, K. P.; Stevenson, K. J., Water electrolysis on $La_{1-x}Sr_xCoO_{3-\delta}$ perovskite electrocatalysts. *Nat. Commun*. **2016**, 7, 11053.

11. Grimaud, A.; Diaz-Morales, O.; Han, B.; Hong, W. T.; Lee, Y. L.; Giordano, L.; Stoerzinger, K. A.; Koper, M. T. M.; Shao-Horn, Y., Activate lattice oxygen redox reactions in metal oxides to catalyse oxygen evolution (vol 9, pg 457, 2017). *Nat. Chem*. **2018**, 10 (2).
12. Suntivich, J.; May, K. J.; Gasteiger, H. A.; Goodenough, J. B.; Shao-Horn, Y., A perovskite oxide optimized for oxygen evolution catalysis from molecular orbital principles. *Science* **2011**, 334, 1383-1385.
13. Grimaud, A.; May, K. J.; Carlton, C. E.; Lee, Y.-L.; Risch, M.; Hong, W. T.; Zhou, J.; Shao-Horn, Y., Double perovskites as a family of highly active catalysts for oxygen evolution in alkaline solution. *Nat. Commun*. **2013**, 4, 2439.
14. Yang, F.; Sliozberg, K.; Sinev, I.; Antoni, H.; Bähr, A.; Ollegott, K.; Xia, W.; Masa, J.; Grünert, W.; Cuenya, B. R.; Schuhmann, W.; Muhler, M., Synergistic Effect of Cobalt and Iron in Layered Double Hydroxide Catalysts for the Oxygen Evolution Reaction. *ChemSusChem* **2017**, 10 (1), 156-165.
15. Li, H.; Chen, Y.; Xi, S.; Wang, J.; Sun, S.; Sun, Y.; Du, Y.; Xu, Z. J., Degree of geometric tilting determines the activity of FeO6 octahedra for water oxidation. *Chem. Mater*. **2018**, 30, 4313-4320.
16. Li, X.; Wang, H.; Cui, Z.; Li, Y.; Xin, S.; Zhou, J.; Long, Y.; Jin, C.; Goodenough, J. B., Exceptional oxygen evolution reactivities on $CaCoO_3$ and $SrCoO_3$. *Sci. Adv*. **2019**, 5 (8), eaav6262.
17. Suntivich, J.; Hong, W. T.; Lee, Y.-L.; Rondinelli, J. M.; Yang, W.; Goodenough, J. B.; Dabrowski, B.; Freeland, J. W.; Shao-Horn, Y., Estimating Hybridization of Transition Metal and Oxygen States in Perovskites from O K-edge X-ray Absorption Spectroscopy. *J. Phys. Chem. C* **2014**, 118 (4), 1856-1863.

18. Hong, W. T.; Welsch, R. E.; Shao-Horn, Y., Descriptors of Oxygen-Evolution Activity for Oxides: A Statistical Evaluation. *J. Phys. Chem. C* **2016**, 120, 78-86.
19. Yagi, S.; Yamada, I.; Tsukasaki, H.; Seno, A.; Murakami, M.; Fujii, H.; Chen, H.; Umezawa, N.; Abe, H.; Nishiyama, N.; Mori, S., Covalency-reinforced oxygen evolution reaction catalyst. *Nat. Commun.* **2015**, 6, 8249.
20. Yamada, I.; Fujii, H.; Takamatsu, A.; Ikeno, H.; Wada, K.; Tsukasaki, H.; Kawaguchi, S.; Mori, S.; Yagi, S., Bifunctional oxygen reaction catalysis of quadruple manganese perovskites. *Adv. Mater*. **2017**, 29, 1603004.
21. Yamada, I., Novel catalytic properties of quadruple perovskites. *Sci. Technol. Adv. Mater* **2017**, 18, 541-548.
22. Takamatsu, A.; Yamada, I.; Yagi, S.; Ikeno, H., Oxygen evolution via the bridging inequivalent dual-site reaction: first-principles study of a quadruple-perovskite oxide catalyst. *J. Phys. Chem. C* **2017**, 121, 28403-28411.
23. Hong, W. T.; Risch, M.; Stoerzinger, K. A.; Grimaud, A.; Suntivich, J.; Shao-Horn, Y., Toward the rational design of non-precious transition metal oxides for oxygen electrocatalysis. *Energ. Environ. Sci*. **2015**, 8, 1404-1427.
24. Momma, K.; Izumi, F., VESTA 3 for three-dimensional visualization of crystal, volumetric and morphology data. *J. Appl. Crystallogr.* **2011**, 44 (6), 1272-1276.
25. Jain, P.; Saha, J.; Gupta, L. C.; Patnaik, S.; Ganguli, A. K.; Chatterjee, R., Dramatic variation of the multiferroic properties in Sr doped $Ca_{1-x}Sr_xMn_7O_{12}$. *AIP Advances* **2017**, 7 (5), 055832.
26. Sławiński, W.; Przeniosło, R.; Sosnowska, I.; Bieringer, M.; Margiolaki, I.; Fitch, A. N.; Suard, E., Phase coexistence in $CaCu_xMn_{7-x}O_{12}$ solid solutions. *J. Solid State Chem*. **2006**, 179 (8), 2443-2451.

27. Glazkova, Y. S.; Terada, N.; Matsushita, Y.; Katsuya, Y.; Tanaka, M.; Sobolev, A. V.; Presniakov, I. A.; Belik, A. A., High-Pressure Synthesis, Crystal Structures, and Properties of $CdMn_7O_{12}$ and $SrMn_7O_{12}$ Perovskites. *Inorg. Chem.* **2015**, 54 (18), 9081-9091.

28. Kosugi, N.; Yokoyama, T.; Kuroda, H., Polarization dependence of XANES of square-planar Ni(CN)2−4 ion. A comparison with octahedral $Fe(CN)_{4-6}$ and $Fe(CN)_{3-6}$ ions. *Chem. Phys*. **1986**, 104, 449-453.

29. Shukla, D. K.; Mollah, S.; Kumar, R.; Thakur, P.; Chae, K. H.; Choi, W. K.; Banerjee, A., Effect of Ti substitution on multiferroic properties of $BiMn_2O_5$. *J. Appl. Phys.* **2008**, 104, 033707.

30. Gautam, K.; Shukla, D. K.; Choudhary, R. J.; Phase, D. M., Enroute to phase purity in CaMn7O12. *AIP Conf. Proc.* **2017**, 1832, 090041.

31. Mannella, N.; Rosenhahn, A.; Watanabe, M.; Sell, B.; Nambu, A.; Ritchey, S.; Arenholz, E.; Young, A.; Tomioka, Y.; Fadley, C. S., Temperature-dependent x-ray absorption spectroscopy of colossal magnetoresistive perovskites. *Phys. Rev. B* **2005**, 71, 125117.

32. Doyle, R. L.; Lyons, M. E. G., Kinetics and Mechanistic Aspects of the Oxygen Evolution Reaction at Hydrous Iron Oxide Films in Base. *J. Electrochem. Soc.* **2013**, 160 (2), H142-H154.

33. Liu, G.; Gao, X. S.; Wang, K. F.; He, D. Y.; Li, J. P., Uniformly mesoporous NiO/NiFe2O4 biphasic nanorods as efficient oxygen evolving catalyst for water splitting. *Int. J. Hydrogen Energy* **2016**, 41 (40), 17976-17986.

34. Mattioli, G.; Giannozzi, P.; Amore Bonapasta, A.; Guidoni, L., Reaction Pathways for Oxygen Evolution Promoted by Cobalt Catalyst. *J. Am. Chem. Soc.*

2013, 135 (41), 15353-15363.

35. Mavros, M. G.; Tsuchimochi, T.; Kowalczyk, T.; McIsaac, A.; Wang, L.-P.; Voorhis, T. V., What Can Density Functional Theory Tell Us about Artificial Catalytic Water Splitting? *Inorg. Chem*. **2014**, 53 (13), 6386-6397.
36. McCrory, C. C. L.; Jung, S.; Peters, J. C.; Jaramillo, T. F., Benchmarking heterogeneous electrocatalysts for the oxygen Evolution Reaction. *J. Am. Chem. Soc*. **2013**, 135, 16977-16987.

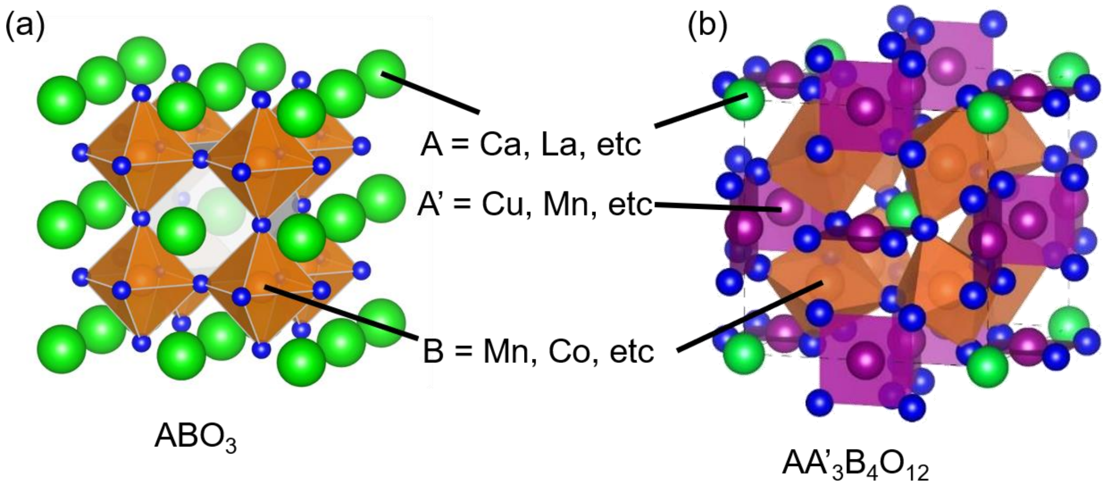

Figure 6.1. schematics of the crystal structures of (a) simple ABO_3 type and (b) quadruple $AA'_3B_4O_{12}$ type perovskites. Green, purple, orange and blue spheres represent A, A’, B, and O atoms, respectively. Both crystal structures were drown using the VESTA program[24].

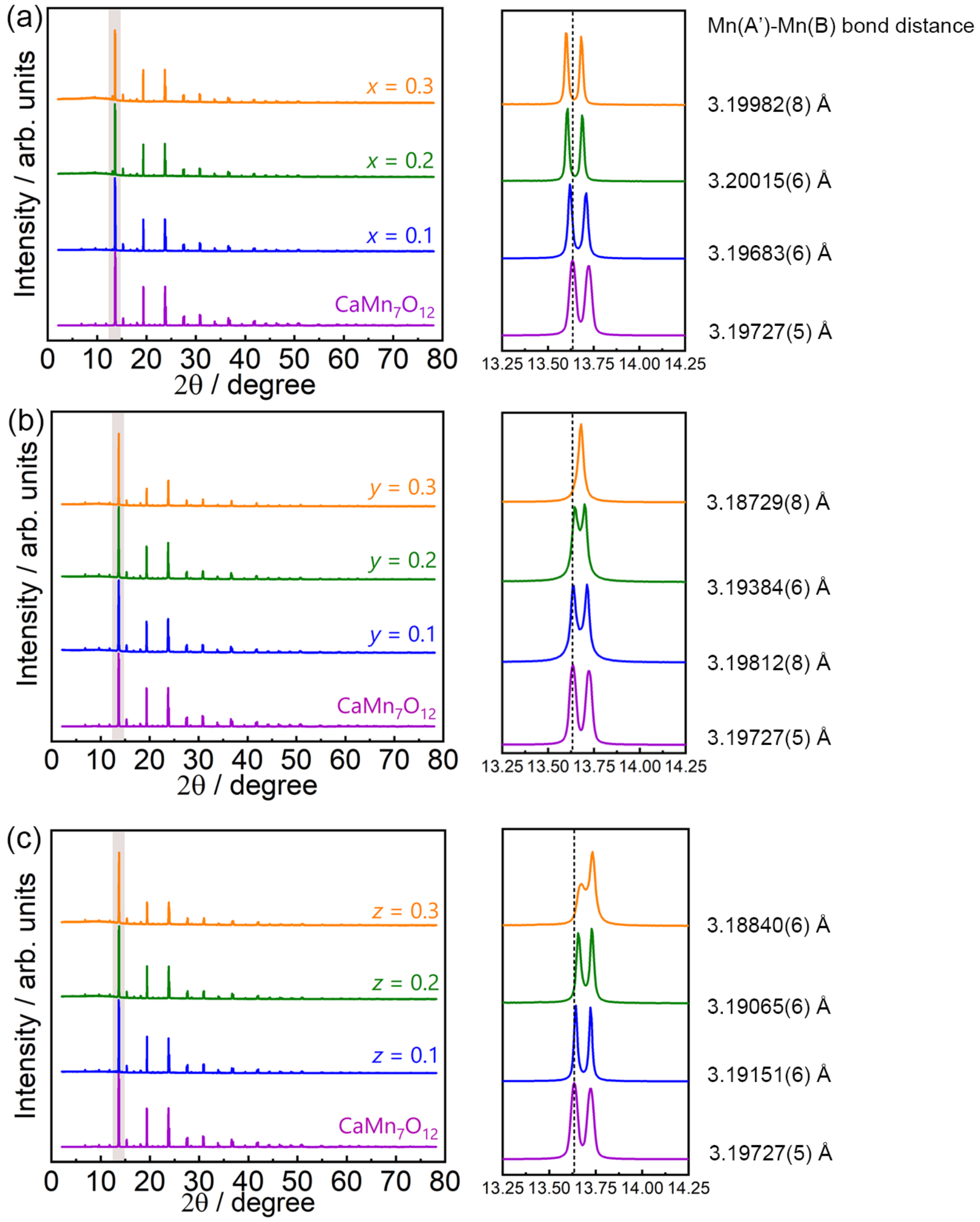

Figure 6.2. X-ray diffraction patterns of as-synthesized samples. (a) $Ca_{1-x}Sr_xMn_7O_{12}$ (b) $CaMn_{7-y}Cu_yO_{12}$ (c) $CaMn_{7-z}Al_z$O12

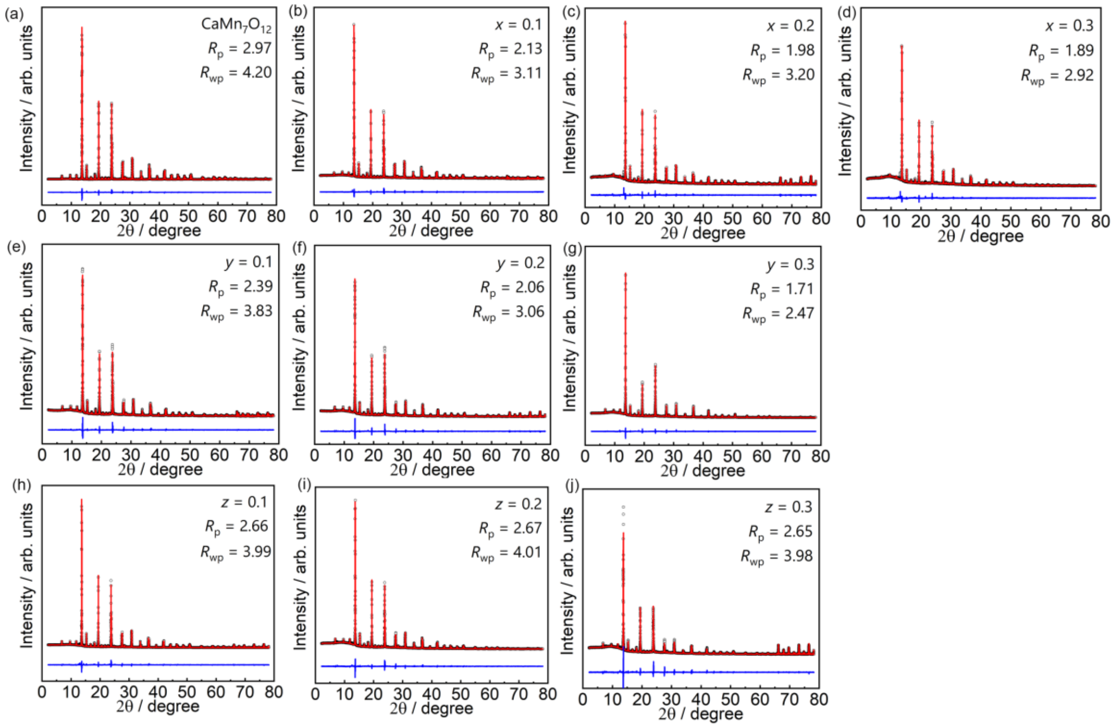

Figure 6.3. Rietveld refinement results for (a) CaMn$_7$O$_{12}$; (b)~(d) Ca$_{1-x}$Sr$_x$Mn$_7$O$_{12}$, x = 0.1, 0.2, 0.3 respectively; (e)~(g) CaMn$_{7-y}$Cu$_y$O$_{12}$, y = 0.1, 0.2, 0.3 respectively; (h)~(j) CaMn$_{7-z}$Al$_z$O$_{12}$, z = 0.1, 0.2, 0.3 respectively. The black circles and red lines represent observed and calculated diffraction patterns, respectively. The blue lines show the difference between observed and calculated patterns.

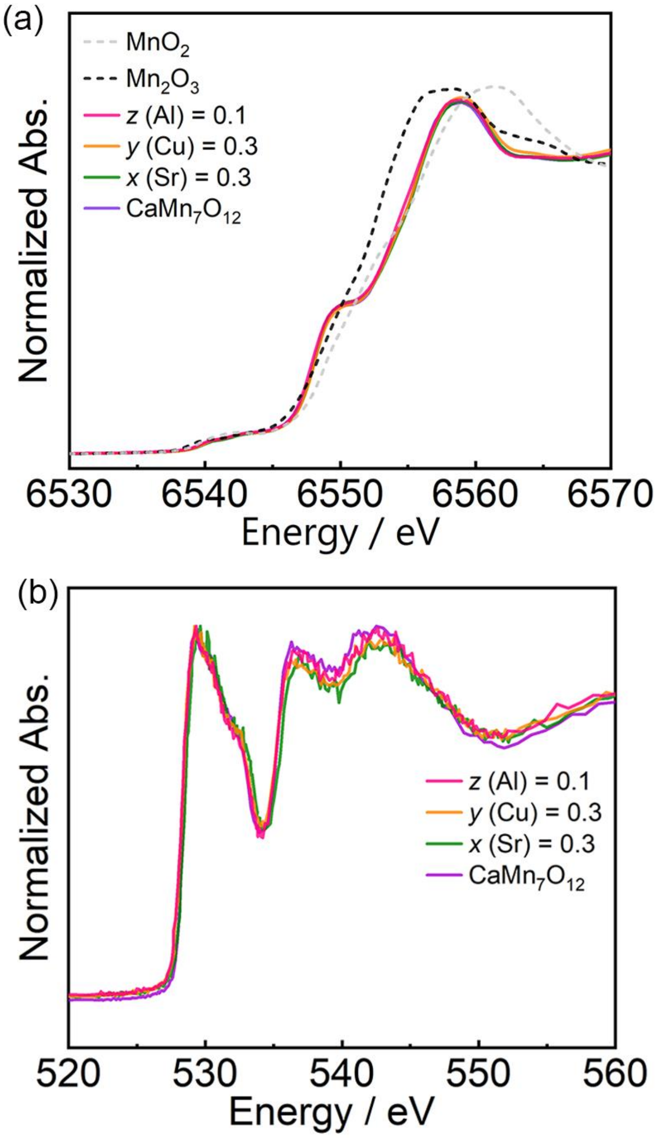

Figure 6.4. (a) Mn K-edge XANES spectra (b) O K-edge XAS spectra for $Ca_{1-x}Sr_xMn_7O_{12}$, $CaMn_{7-y}Cu_yO_{12}$ and $CaMn_{7-z}Al_zO_{12}$

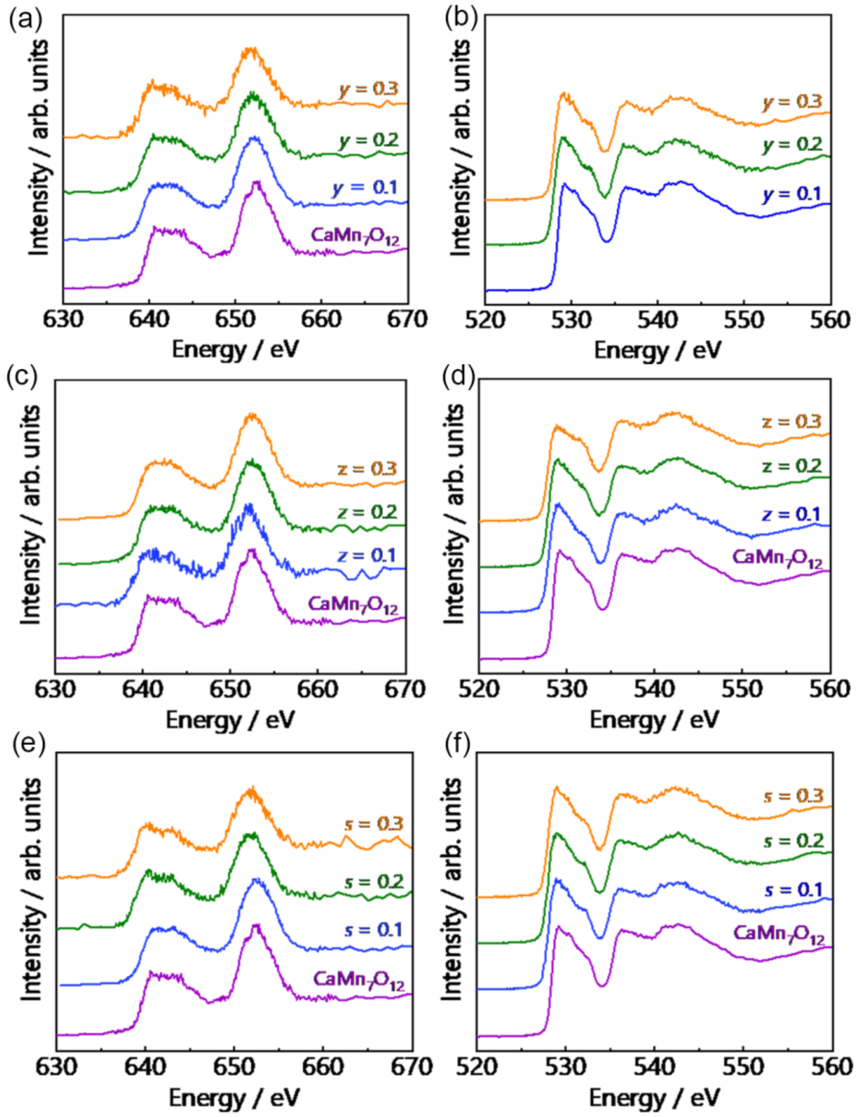

Figure 6.5. Mn L-edge (a, c, e) and O K-edge XAS (b, d, f) results for (a)(b) $Ca_{1-x}Sr_xMn_7O_{12}$ (c)(d) $CaMn_{7-y}Cu_yO_{12}$ (e)(f) $CaMn_{7-z}Al_zO_{12}$

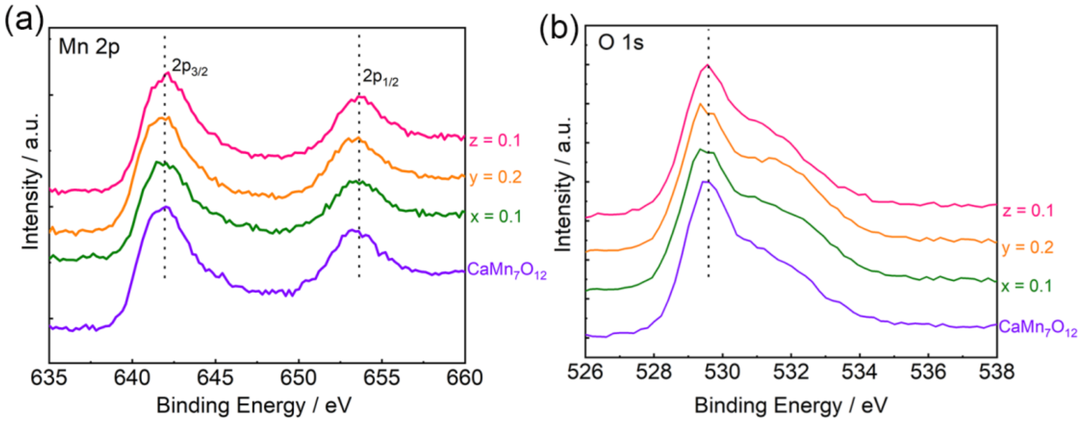

Figure 6.6. XPS core level spectra of (a) Mn 2p and (b) O 1s for pristine $CaMn_7O_{12}$ and typical Sr, Cu, Al doped catalysts.

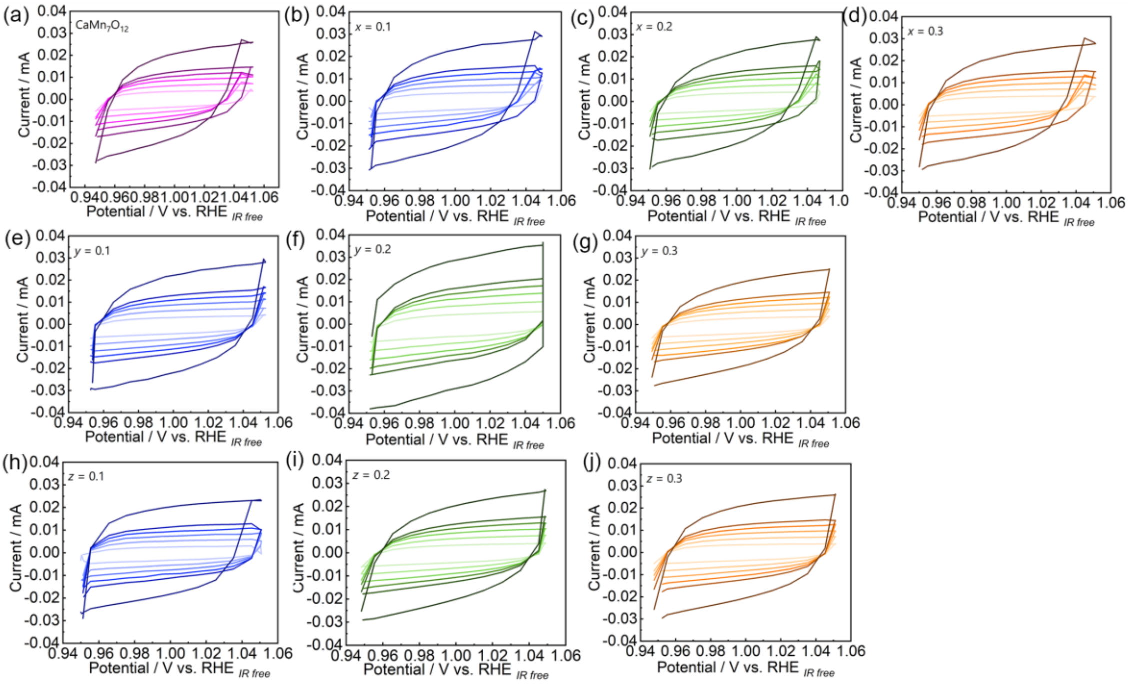

Figure 6.7. Cyclic voltammograms measured under different scan rates for (a) $CaMn_7O_{12}$; (b)~(d) $Ca_{1-x}Sr_xMn_7O_{12}$, x = 0.1, 0.2, 0.3 respectively; (e)~(g) $CaMn_{7-y}Cu_yO_{12}$, y = 0.1, 0.2, 0.3 respectively; (h)~(j) $CaMn_{7-z}Al_zO_{12}$, z = 0.1, 0.2, 0.3 respectively.

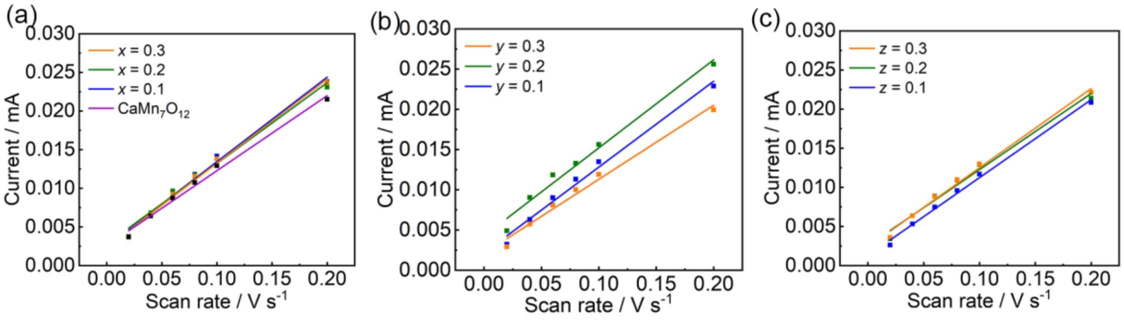

Figure 6.8. Double layer capacity measurement results for (a) $CaMn_7O_{12}$ and $Ca_{1-x}Sr_xMn_7O_{12}$, x = 0.1, 0.2, 0.3 respectively; (b) $CaMn_{7-y}Cu_yO_{12}$, y = 0.1, 0.2, 0.3 respectively; (c)$CaMn_{7-z}Al_zO_{12}$, z = 0.1, 0.2, 0.3 respectively.

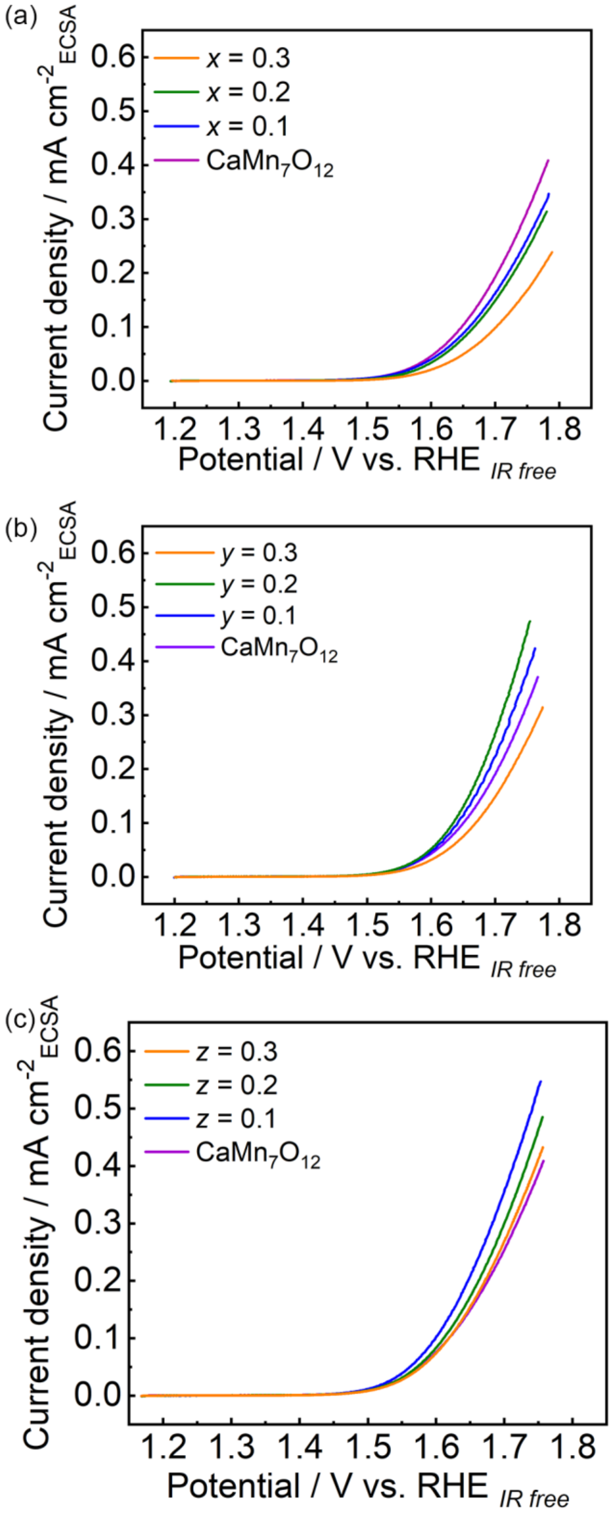

Figure 6.9. The result of electrochemical measurement on OER for (a) $Ca_{1-x}Sr_xMn_7O_{12}$ (b) $CaMn_{7-y}Cu_yO_{12}$ (c) $CaMn_{7-z}Al_zO_{12}$

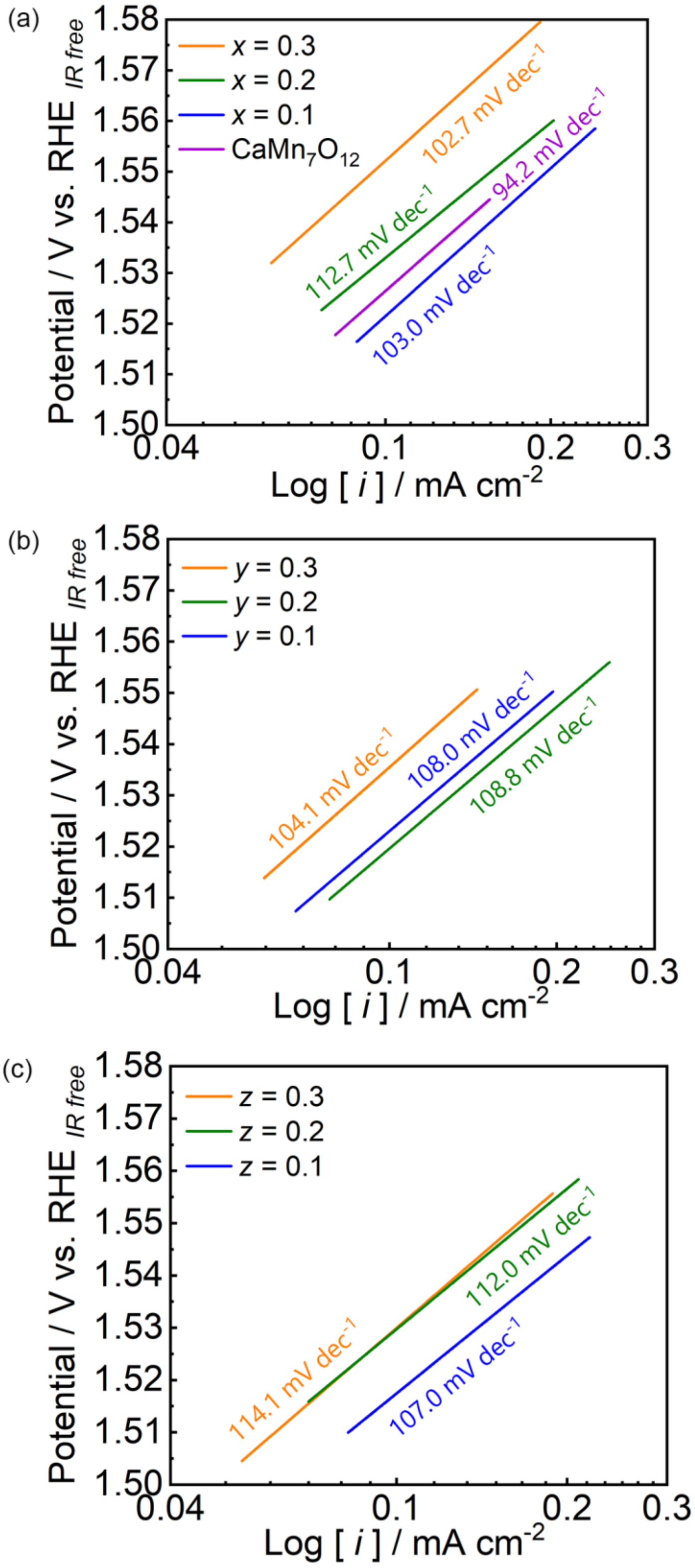

Figure 6.10. The results of Tafel plot for (a) $Ca_{1-x}Sr_xMn_7O_{12}$ (b) $CaMn_{7-y}Cu_yO_{12}$ (c) $CaMn_{7-z}Al_zO_{12}$

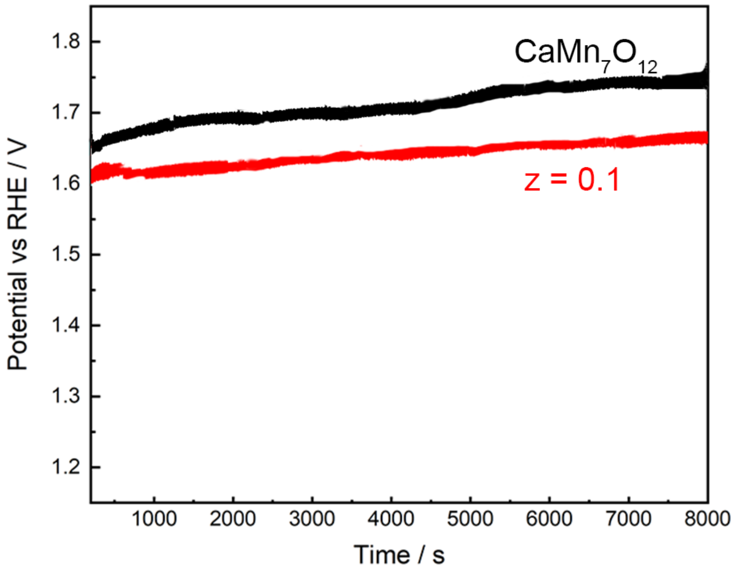

Figure 6.11. Galvanostatic measurement of mass activities of CaMn$_7$O$_{12}$ and the most active z =0.1 sample. The current density was kept at 10 A g^{-1} during the whole tests with the RDE rotating speed of 3600 rpm.

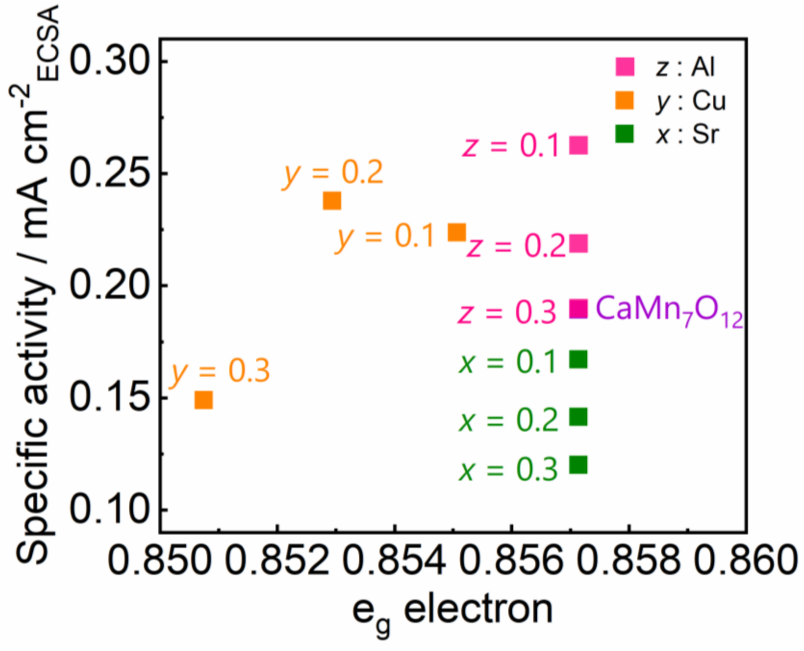

Figure 6.12. The relation between OER activities and the number of e_g electron of Mn

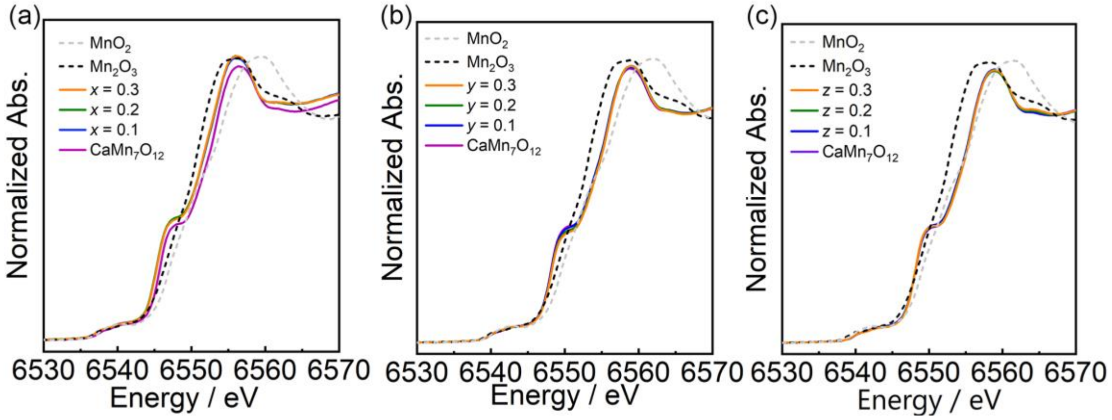

Figure 6.13. Mn K-edge XANES for (a) $CaMn_7O_{12}$ and $Ca_{1-x}Sr_xMn_7O_{12}$, x = 0.1, 0.2, 0.3 respectively; (b) $CaMn_{7-y}Cu_yO_{12}$, y = 0.1, 0.2, 0.3 respectively; (c)$CaMn_{7-z}Al_zO_{12}$, z = 0.1, 0.2, 0.3 respectively.

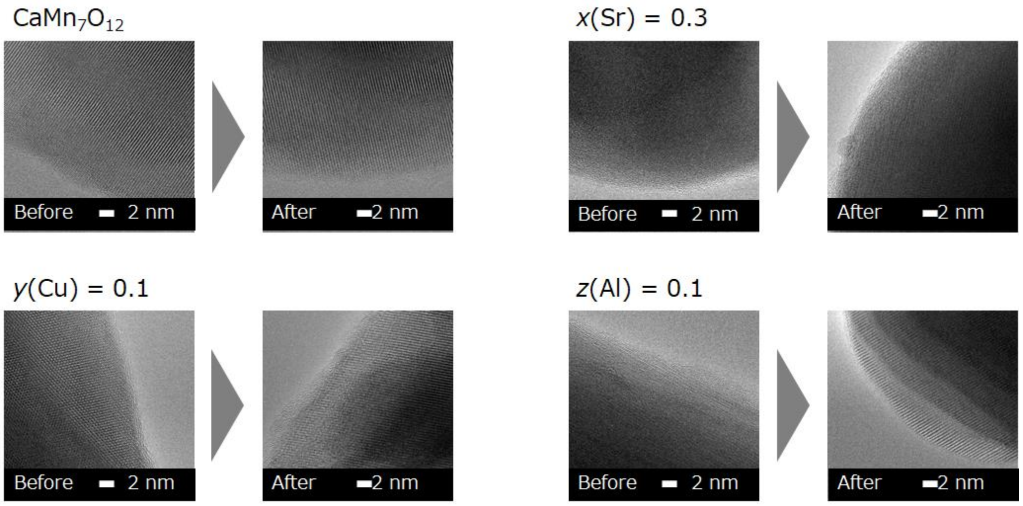

Figure 6.14. TEM image of synthesized samples before and after OER measurement.

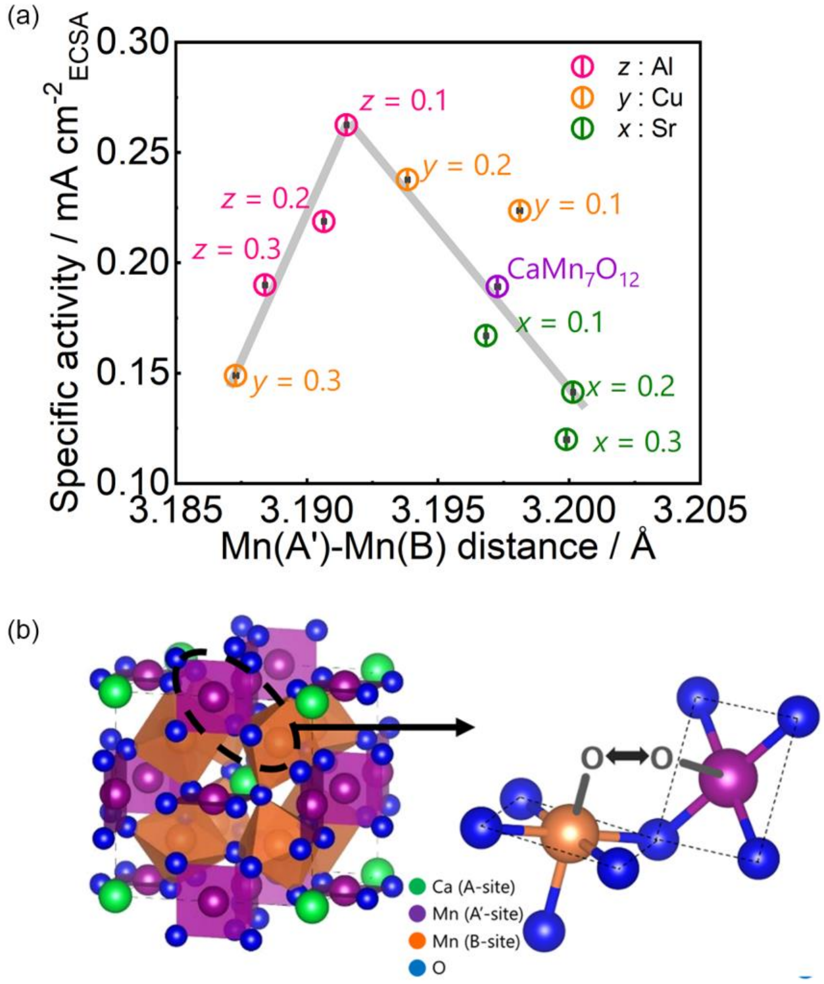

Figure 6.15. (a) The relationship between OER activity and Mn(A')-Mn(B) distance (b) Schematic illustration of Mn(A')-Mn(B) site (c) The relationship between OER activity and the number of e_g electron of Mn

Table 6.1. Rietveld refinement parameter for (a) $Ca_{1-x}Sr_xMn_7O_{12}$ (b) $CaMn_{7-y}Cu_yO_{12}$ (c) $CaMn_{7-z}Al_zO_{12}$

sample	Space group	Atom	Wyck	S.O.F	*x* / a	*y* / b	*z* / c	B_{iso} / Å^2
$CaMn_7O_{12}$	*R-3*	Ca	3a	1.000	0	0	0	0.644(22)
		Mn1	9e	1.000	0.5	0	0	0.389(16)
	a = 10.45331(18) Å	Mn2	9d	1.000	0.5	0	0.5	=Mn1(B)
		Mn3	*3b*	1.000	0	0	0.5	=Mn1(B)
	c = 6.34002(11) Å	O1	18f	1.000	0.22382(83)	0.27400(71)	0.08041(10)	0.476(60)
		O2	18f	1.000	0.34175(82)	0.52262(70)	0.34139(10)	=O2(B)

sample	Space group	Atom	Wyck	S.O.F	*x* / a	*y* / b	*z* / c	B_{iso} / Å^2
x = 0.1		Ca	3a	0.900	0	0	0	0.495(18)
	R-3	Sr	3a	0.100	0	0	0	= Ca(1)
		Mn1	9e	1.000	0.5	0	0	0.378(25)
	a = 10.45169(22) Å	Mn2	9d	1.000	0.5	0	0.5	=Mn1
		Mn3	3b	1.000	0	0	0.5	=Mn1
	c = 6.34009(13) Å	O1	18f	1.000	0.22471(11)	0.27463(96)	0.08062(17)	0.309(71)
		O2	18f	1.000	0.34121(94)	0.52275(87)	0.34204(46)	=O1

sample	Space group	Atom	Wyck	S.O.F	*x* / a	*y* / b	*z* / c	B_{iso} / Å^2
x = 0.2		Ca	3a	0.800	0	0	0	0.495(18)
	R-3	Sr	3a	0.200	0	0	0	= Ca(1)
		Mn1	9e	1.000	0.5	0	0	0.540(44)
	a = 10.46195(26) Å	Mn2	9d	1.000	0.5	0	0.5	=Mn1
		Mn3	3b	1.000	0	0	0.5	=Mn1
	c = 6.34927(16) Å	O1	18f	1.000	0.22322(18)	0.27434(16)	0.08024(89)	0.477(71)
		O2	18f	1.000	0.34363(57)	0.52331(42)	0.34792(43)	=O1

sample	Space group	Atom	Wyck	S.O.F	*x* / a	*y* / b	*z* / c	B_{iso} / Å^2
x = 0.3		Ca	3a	0.700	0	0	0	0.213(39)
	R-3	Sr	3a	0.300	0	0	0	= Ca(1)
		Mn1	9e	1.000	0.5	0	0	0.373(71)
	a = 10.46092(39) Å	Mn2	9d	1.000	0.5	0	0.5	=Mn1
		Mn3	3b	1.000	0	0	0.5	=Mn1
	c = 6.34878(24) Å	O1	18f	1.000	0.22297(30)	0.27340(79)	0.08053(46)	0.147(64)
		O2	18f	1.000	0.34190(20)	0.52545(20)	0.34603(40)	=O1

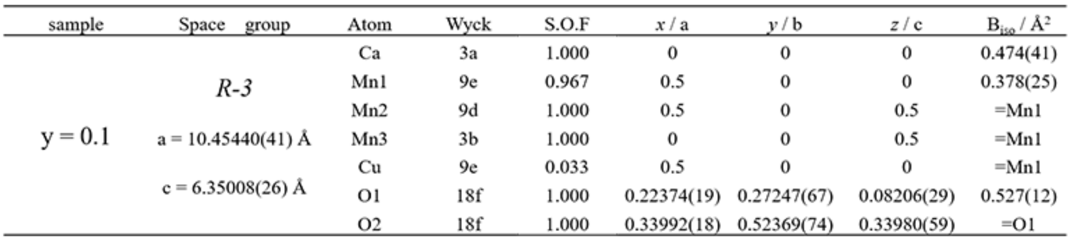

sample	Space group	Atom	Wyck	S.O.F	*x* / a	*y* / b	*z* / c	B_{iso} / Å^2
y = 0.1	*R-3* a = 10.45440(41) Å c = 6.35008(26) Å	Ca	3a	1.000	0	0	0	0.474(41)
		Mn1	9e	0.967	0.5	0	0	0.378(25)
		Mn2	9d	1.000	0.5	0	0.5	=Mn1
		Mn3	3b	1.000	0	0	0.5	=Mn1
		Cu	9e	0.033	0.5	0	0	=Mn1
		O1	18f	1.000	0.22374(19)	0.27247(67)	0.08206(29)	0.527(12)
		O2	18f	1.000	0.33992(18)	0.52369(74)	0.33980(59)	=O1

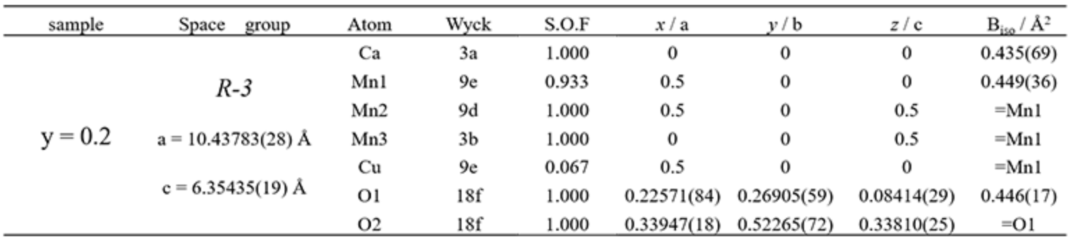

sample	Space group	Atom	Wyck	S.O.F	*x* / a	*y* / b	*z* / c	B_{iso} / Å^2
y = 0.2	*R-3* a = 10.43783(28) Å c = 6.35435(19) Å	Ca	3a	1.000	0	0	0	0.435(69)
		Mn1	9e	0.933	0.5	0	0	0.449(36)
		Mn2	9d	1.000	0.5	0	0.5	=Mn1
		Mn3	3b	1.000	0	0	0.5	=Mn1
		Cu	9e	0.067	0.5	0	0	=Mn1
		O1	18f	1.000	0.22571(84)	0.26905(59)	0.08414(29)	0.446(17)
		O2	18f	1.000	0.33947(18)	0.52265(72)	0.33810(25)	=O1

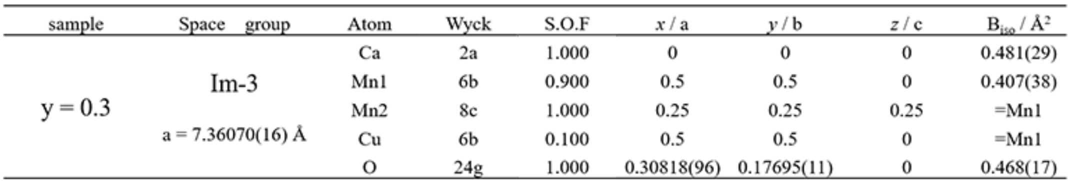

sample	Space group	Atom	Wyck	S.O.F	*x* / a	*y* / b	*z* / c	B_{iso} / Å^2
y = 0.3	Im-3 a = 7.36070(16) Å	Ca	2a	1.000	0	0	0	0.481(29)
		Mn1	6b	0.900	0.5	0.5	0	0.407(38)
		Mn2	8c	1.000	0.25	0.25	0.25	=Mn1
		Cu	6b	0.100	0.5	0.5	0	=Mn1
		O	24g	1.000	0.30818(96)	0.17695(11)	0	0.468(17)

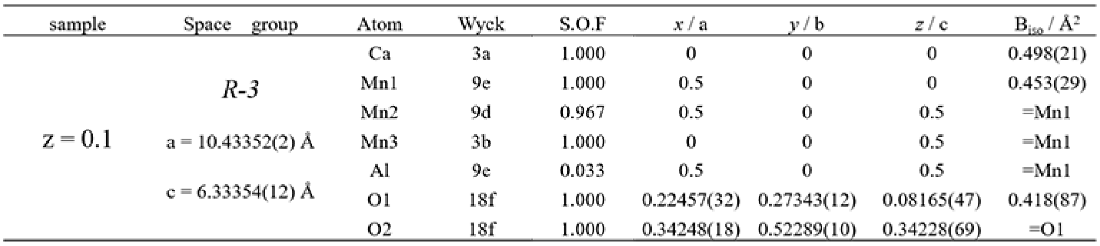

sample	Space group	Atom	Wyck	S.O.F	*x* / a	*y* / b	*z* / c	B_{iso} / Å^2
z = 0.1	*R-3* a = 10.43352(2) Å c = 6.33354(12) Å	Ca	3a	1.000	0	0	0	0.498(21)
		Mn1	9e	1.000	0.5	0	0	0.453(29)
		Mn2	9d	0.967	0.5	0	0.5	=Mn1
		Mn3	3b	1.000	0	0	0.5	=Mn1
		Al	9e	0.033	0.5	0	0.5	=Mn1
		O1	18f	1.000	0.22457(32)	0.27343(12)	0.08165(47)	0.418(87)
		O2	18f	1.000	0.34248(18)	0.52289(10)	0.34228(69)	=O1

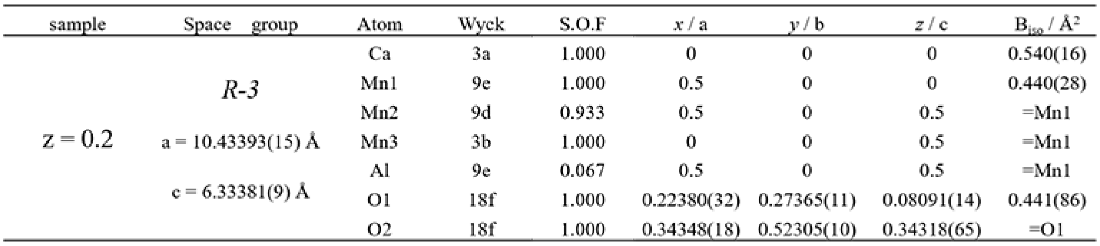

sample	Space group	Atom	Wyck	S.O.F	*x* / a	*y* / b	*z* / c	B_{iso} / Å^2
z = 0.2	*R-3* a = 10.43393(15) Å c = 6.33381(9) Å	Ca	3a	1.000	0	0	0	0.540(16)
		Mn1	9e	1.000	0.5	0	0	0.440(28)
		Mn2	9d	0.933	0.5	0	0.5	=Mn1
		Mn3	3b	1.000	0	0	0.5	=Mn1
		Al	9e	0.067	0.5	0	0.5	=Mn1
		O1	18f	1.000	0.22380(32)	0.27365(11)	0.08091(14)	0.441(86)
		O2	18f	1.000	0.34348(18)	0.52305(10)	0.34318(65)	=O1

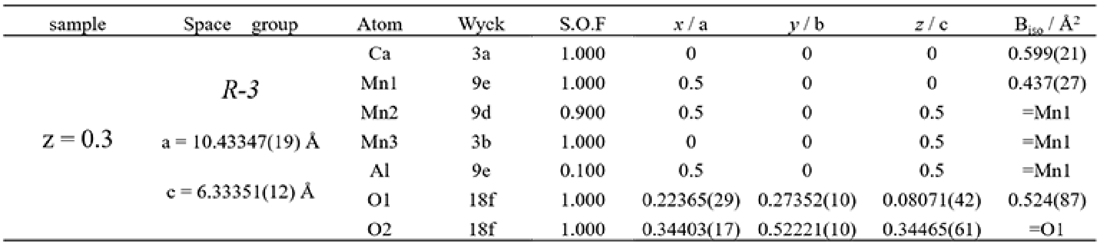

sample	Space group	Atom	Wyck	S.O.F	*x* / a	*y* / b	*z* / c	B_{iso} / Å^2
z = 0.3	*R-3* a = 10.43347(19) Å c = 6.33351(12) Å	Ca	3a	1.000	0	0	0	0.599(21)
		Mn1	9e	1.000	0.5	0	0	0.437(27)
		Mn2	9d	0.900	0.5	0	0.5	=Mn1
		Mn3	3b	1.000	0	0	0.5	=Mn1
		Al	9e	0.100	0.5	0	0.5	=Mn1
		O1	18f	1.000	0.22365(29)	0.27352(10)	0.08071(42)	0.524(87)
		O2	18f	1.000	0.34403(17)	0.52221(10)	0.34465(61)	=O1

Table 6.2. Mn(A')-Mn(B) distance values obtained from Rietveld refinement

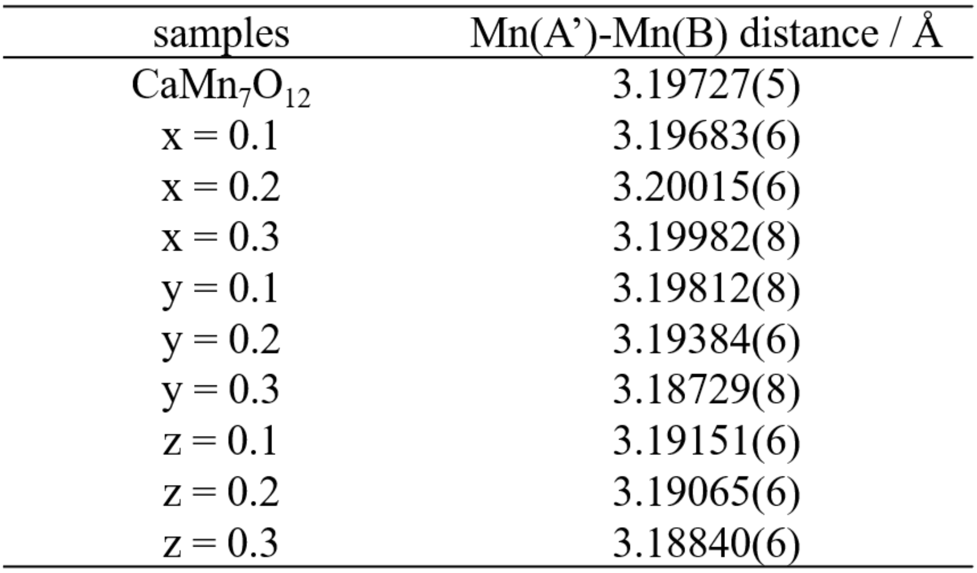

samples	Mn(A')-Mn(B) distance / Å
$CaMn_7O_{12}$	3.19727(5)
x = 0.1	3.19683(6)
x = 0.2	3.20015(6)
x = 0.3	3.19982(8)
y = 0.1	3.19812(8)
y = 0.2	3.19384(6)
y = 0.3	3.18729(8)
z = 0.1	3.19151(6)
z = 0.2	3.19065(6)
z = 0.3	3.18840(6)

Table 6.3. Double layer capacitance and ECSA of doped samples

Sample	Double layer capacitance / mF	Electrochemical surface area / cm^2
$CaMn_7O_{12}$	0.097	2.43
x = 0.1	0.109	2.73
x = 0.2	0.104	2.60
x = 0.3	0.109	2.73

Sample	Double layer capacitance / mF	Electrochemical surface area / cm^2
y = 0.1	0.107	2.68
y = 0.2	0.109	2.73
y = 0.3	0.092	2.30

Sample	Double layer capacitance / mF	Electrochemical surface area / cm^2
z = 0.1	0.100	2.50
z = 0.2	0.097	2.43
z = 0.3	0.101	2.53

Table 6.4. Summary of some recently reported OER electrocatalysts in alkaline electrolytes

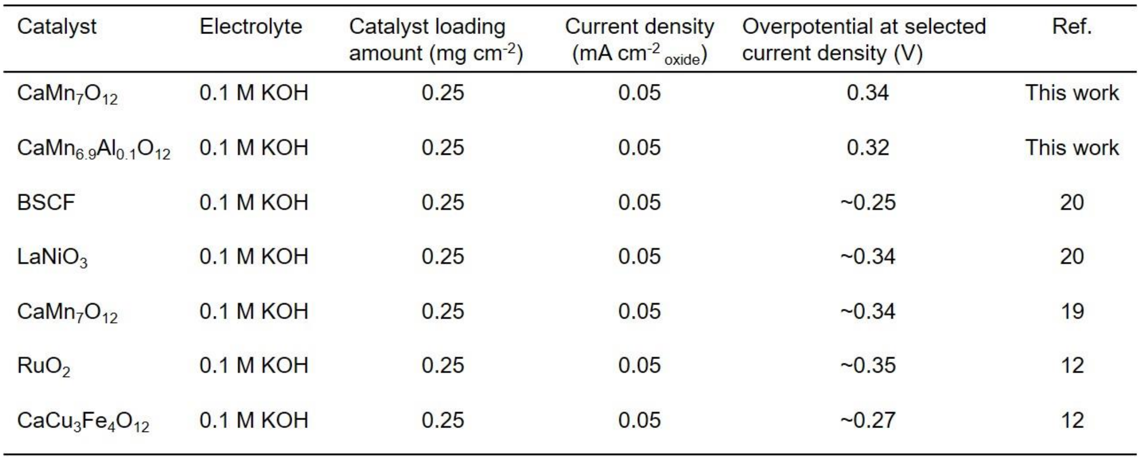

Catalyst	Electrolyte	Catalyst loading amount (mg cm^{-2})	Current density (mA cm^{-2} $_{oxide}$)	Overpotential at selected current density (V)	Ref.
$CaMn_7O_{12}$	0.1 M KOH	0.25	0.05	0.34	This work
$CaMn_{6.9}Al_{0.1}O_{12}$	0.1 M KOH	0.25	0.05	0.32	This work
BSCF	0.1 M KOH	0.25	0.05	~0.25	20
$LaNiO_3$	0.1 M KOH	0.25	0.05	~0.34	20
$CaMn_7O_{12}$	0.1 M KOH	0.25	0.05	~0.34	19
RuO_2	0.1 M KOH	0.25	0.05	~0.35	12
$CaCu_3Fe_4O_{12}$	0.1 M KOH	0.25	0.05	~0.27	12

Chapter 7. Understanding the key factors affecting OER activity of iridium oxides

Elucidation of the reaction mechanism of highly active iridium oxides is promising for the further development of cost-efficient PEM water electrolysis catalysts. However, the short life cycle of the reaction intermediates during the oxygen evolution reaction (OER) process makes it challenging to provide direct evidence for the reaction steps, putting the OER reaction mechanism still under debate. Herein, several iridium oxides catalysts were thoroughly investigated and the relationship between their structures and OER activities was revealed. Unlike the typical tetragonal symmetry of crystal IrO_2, the combination of orthorhombic symmetry and monoclinic symmetry was found in the amorphous IrOx through atomic pair distribution function analyses, and the ratio of monoclinic phase ratio corresponds well to the OER activity. The origin of high activity was further clarified using synchrotron hard and soft X-ray absorption spectroscopy under operando situation. The low symmetry of monoclinic phase resulted in the structure defection and thus lead to large amount of active electrophilic O^{I-} species, boosting the OER activity. The thorough investigation in this study is promising to deepen the understanding of high active OER catalysts and provide new inspiration towards the design of novel OER catalysts.

7.1 Introduction

With the increase in fossil energy consumption and the attendant pronounced climate changes, the call for sustainable energy forms has become urgent and has attracted more and more attention. Hydrogen[1], generated by the electricity-derived water electrolysis, is now considered the promising energy carrier for conversion between electricity and chemical, making the realization of hydrogen society promising in the future[2-4]. The most developed water electrolysis technology up to date is the proton-exchange membrane (PEM) water electrolysis, where commercial Pt/C works as the cathodic catalyst for hydrogen evolution reaction (HER) and noble metal-based materials serve as the anodic catalyst for oxygen evolution reaction (OER)[5]. Considering the sluggish four-electron reaction kinetics of OER and the harsh acidic environment of PEM water electrolysis, the selectivity of high-efficient OER catalysts is narrowed down to Ir-based catalysts because of their superior activity, long-term stability and corrosion resistance against acidic environment[6-8]. However, the scarcity of Ir on earth has impeded the wide application of PEM water electrolysis and has driven the research of cost-efficient OER catalysts[9-13].

Understanding the origin of the high activity of Ir-based oxides is essential for the design of novel OER catalysts. Recent research revealed that the morphology and structure of iridium oxide can significantly affect the OER activity, where catalysts with amorphous structure showed higher OER activity than crystallized ones[14-16]. Although the reaction mechanism of amorphous iridium catalysts is still under debate, the superior catalytic performance of amorphous oxides was attributed to extra active sites resulted from the defects in electronic structure[17, 18] and the irregular Ir-Ir and/or Ir-O bond interactions[19-23]. A recent work of Elmaalouf M. al. et. investigated a wide range of iridium-based catalysts by controllable stoichiometry and crystallinity, and demonstrated that higher OER activity originated from the amorphous crystalline with the smaller particle size rather than the initial Ir oxidation state[24]. Willinger E. and co-workers revealed that the high activity of amorphous catalysts is related to the corner- and edge-sharing IrO6 octahedra[21]. They proposed that the appearance of hollandite-like structure was responsible for the enhanced OER activity, indicating the possibility of catalyst design by rational structure arrangement. Such structure property was evidenced by further study, where orthorhombic symmetry and monoclinic symmetry appeared in amorphous iridium oxides[22] and the mixed phase of traditional tetragonal structure and orthorhombic structure was found to show the best OER activity[21, 22].

To elucidate the reaction mechanism of iridium oxide catalysts, advanced *ex situ* and *operando* measurements are demanded to disclose the intrinsic catalytic properties during the oxygen evolution process. Since the OER activity is determined by the structural/electronic structure of the catalyst surface, it is important to have an *operando* analysis method to obtain information on the catalyst surface under the OER process. Recently, several techniques such as *operando* O K-edge XAS and in situ X-ray photoemission (XPS) have been reported to obtain information on the catalytic interface during the oxygen evolution reaction. Nong. H. N. and co-workers distinguished two types of O 2*p* hole character (μ-O and μ-O oxyl) through operando O K-edge XAS[25]. Combining with the pulse voltammetry measurements and DFT calculations, they found a linear relationship between the activation free-energy and catalytic activity. Pfeifer V. et. al. also successfully captured the intermediate oxygen species by in situ X-ray photoemission (XPS), XAS and theoretical calculations[26-28]. Their work disclosed that the electrophilic O^{I-} species increased with the active oxygen evolution and disappeared with the absence of the applied potential, suggesting the O^{I-} species contribute to the OER activity. Although various *in situ* techniques are developed to unveil the intrinsic mechanism of high active iridium-based materials, the understanding between morphology, structure, electronic state, and catalytic performance is far from adequate and demands further research.

Herein, we thoroughly investigated several amorphous IrO_x catalysts and revealed the relation between their structures and OER activities. The amorphous structure of IrO_x was characterized through atomic pair distribution function (PDF) analyses. Different from the typical tetragonal symmetry of crystal IrO_2, the combination of orthorhombic symmetry and monoclinic symmetry was found in the amorphous IrO_x, and the ratio of monoclinic phase ratio corresponds well to the OER activity. The origin of high activity was further clarified that the low symmetry of monoclinic phase resulted in the structure defection and thus lead to more active sites through hard X-ray photoelectron spectra (HXPES), *ex situ* and *operando* X-ray absorption spectroscopy (XAS). The thorough investigation in this study is promising to deepen the understanding of high active OER catalysts and provide new inspiration towards the design of novel OER catalysts.

7.2 Experimental

7.2.1 Materials and Characterization

IrO_2 was provided by High Purity Chemical Laboratory Co., LTD. and used as the reference catalyst without further purification. Iridium oxides with different degree of crystallinity (SA103, SA58, SA14.6 and SA58) were provided by Tanaka Kikinzoku Kogyo K.K., Chemical & Refining Company and named after their BET surface areas.

X-ray diffraction (XRD) measurements were carried out using BL02B2 at SPring-8, Japan (Proposal No. 2021A1286). Transmission electron microscopy (TEM) experiments were conducted at 200 kV (JEM-2200FS, JEOL Ltd.). Scanning TEM

(STEM) analyses were carried out with an acceleration voltage of 200 kV using the JEM-ARM200F (JEOL Ltd.). *Ex situ* and *operando* Ir L_3-edge XAS was measured in the transmission mode using a Si (111) monochromator on BL14B2 at SPring-8, Japan (Proposal No. 2021A1645, No. 2021B1748). O K-edge XAS was conducted in partial fluorescence yield (PFY) mode on BL27SU at SPring-8 (Proposal No. 2021A1009). *Operando* O K-edge was measured in PFY mode on BL27SU at Spring-8 (Proposal No. 2021B1374), using a home-made *in situ* cell described previously[27]. All the XAS data were processed and analyzed using the Athena software package[29]. Atomic pair diffraction functional (PDF) analyses were conducted on BL04B2 at SPring-8 (Proposal No. 2021A1031) with the X-ray energy of 112.88 keV. The structure factor S(*Q*) was calculated from the scattering data with the background correction, absorption correction, multiple scattering and inelastic scattering correction, further Fourier transformed into reduced G(r). The structural fitting of G(r) was conducted using the PDFgui software[30]. Hard X-ray photoelectron spectroscopy (HAXPES) measurements were conducted at 7939 eV at beamline BL46XU at Spring-8, Japan (Proposal No. 2021B1051). X-ray emission spectroscopy (XES) measurements were conducted at beamline BL27XU at Spring-8, Japan (Proposal No. 2021A1029).

7.2.2 Electrochemical Measurements

All the catalyst inks were prepared by mixing the catalyst powder, 5 wt % Nafion solution (sigma-Aldrich) and ethanol (FUJIFILM Wako Pure Chemical Corporation) in deionized water (electrical resistivity of 18.2 MΩ.cm, Milli-Q®, Millipore A/S). The mass ratio of catalyst powder and Nafion was 0.1 mg: 1 mg to obtain good binder effect without impeding the catalytic performance. The volume ratio of ethanol and deionized water was

1:4. The catalyst inks were sonicated in an ice bath for 30 min and casted on the carefully polished Au rotating disk electrode (RDE, 5 mm diameter, Hokuto-denko). The catalyst loading on the RDE was 80 μg_{Ir} cm^{-2}. The electrochemical measurements were performed using a standard three-electrode cell connected to an MPG-205-NUC system (Bio-Logic) and ohmic drop of 21 Ω was compensated in all cases. A Pt mesh was used as the counter electrode, a reversible hydrogen electrode (RHE) was used as the reference electrode and the catalyst-coated Au RDE was used as the working electrode. The cyclic voltammograms (CV) were scanned from 0.1 V to 1.2 V vs. RHE at 50 mV s^{-1} in N_2-saturated 0.1 M $HClO_4$. The electrochemical activities of the catalysts were subsequently investigated using linear sweep voltammetry (LSV) in the range of 1.1 to 1.7 V vs RHE at 10 mV s^{-1}.

7.2.3 *Operando* Ir L-edge XAS Measurement

Operando Ir L_3-edge XAS were collected using a home-made flow-type cell, where Pt wire and RHE worked as counter and reference electrodes, respectively. The catalyst ink was coated onto an Au (50nm) sputtered polyetherimide film (Mitsubishi Chemical Corporation) to prepare both the X-ray window and working electrode. 0.1 M $HClO_4$ was used as the electrolyte and the flow rate of the electrolyte was controlled at 0.5 L min^{-1} using a non-pulsation pump to remove the accumulation of bubbles on the electrode surface. The XAS spectra were recorded at the applied potential of 0.5, 0.8, 1.2, 1.4, 1.5, 1.6, 1.8 V vs. RHE to obtain the catalytic electronic structure changes during OER process.

7.3 Results and Discussion

7.3.1 Morphology and Structure

Crystalline IrO_2 has the rutile structure of tetragonal symmetry (space group $P_{42}mnm$), where the Ir atom locates in the center of IrO_6 octahedra and each octahedra is densely connected through edge-sharing and corner-sharing (Figure 7.1a). The XRD patterns of all samples was shown in Figure 7.1b. IrO_2 showed the typical reflection of rutile structure, as further evidenced by the Rietveld refinement results (Figure 7.2, Table 7.1). The SA58 sample also showed the XRD patterns of tetragonal phase (Figure 7.3, Table 7.2), however, the reflection peaks were rather broad with low intensity, indicating the relatively weaker crystallinity. Moreover, the XRD patterns of SA103, SA14.6 and SA3.5 samples were significantly broad, making the structure analysis through Rietveld refinement impossible. The morphology of all the samples were revealed by TEM, as shown in Figure 7.1 c-g. All the samples had the particle size of around 10-30 nm. The ordered atomic arrangement of IrO_2 and SA58 could be observed, indicating the good crystallinity. In contrast, SA103, SA14.6 and SA3.5 showed the disordered and short-ranged structure, which is in accordance with their XRD patterns and indicated their unique structures different from crystalline IrO_2.

Since it is difficult to reveal the structural information of disordered samples through XRD refinement, the pair-distribution function (PDF) analyses were carried out to quantitively identify the structural properties. By the Fourier transform of high-energy X-ray diffraction data, the reduced pair distribution function G*(r)* expresses the probability of finding a pair of atoms at distance *r*, providing information such as the interatomic bond length and coordination number[21, 31, 32]. Therefore, PDF analysis is suitable to evaluate the structures of short-range ordered materials. The PDF results of all samples up to 10 Å were shown in Figure 7.4. The crystalline IrO_2 and SA58 showed well-defined peaks in the long-range distance, only the shape and peak intensity of SA58 sample is slightly different from IrO_2. However, the distribution peaks faded away from around 4 Å for SA103, SA14.6 and SA3.5 samples, indicating their long-range disordered structures. For the crystalline IrO_2, three discrete peaks at about 1.96 Å, 3.15 Å and 3.55 Å were observed within 4 Å, indicating the Ir-O bond, edge-sharing Ir-Ir bond and corner-sharing Ir-Ir bond respectively[21-23]. However, a sub-peak at around 2.13 Å appeared for Ir-O bond and the second Ir-Ir bond split into two peaks for SA103, SA14.6 and SA3.5 samples (Figure 7.5a), while the obvious shift to lower distance of the first Ir-Ir bond could also be observed, indicating the significant structure changes. To further identify the structure parameters, the PDF fitting was conducted for all samples. Based on the lattice parameters obtained from XRD Rietveld refinement results, the PDF of IrO_2 was fitted in the range of 20 Å, as shown in Figure 7.6 and Table 7.3. The fitting results showed the rutile structure of IrO_2 with the tetragonal symmetry, in good agreement of the Rietveld refinement results. Previous studies have reported the appearance of orthorhombic symmetry and monoclinic symmetry in IrOx[21, 22]. However, little studies mentioned about the space group of such different structures for iridium oxides. To better analyze the PDF, we investigated the materials within the space group of $P_{42}mnm$ of tetragonal symmetry and found that the titanium oxides and tin oxides have not only the typical rutile structure, but also cubic, orthorhombic, and monoclinic structures, while the space group and crystal information were provided in the previous research[33, 34]. Therefore, the crystal structure of the above-mentioned materials would be taken into consideration for the fitting of short-ranged samples. The G (r) of SA58 showed the peak shift to lower distance at the first Ir-Ir bond (around 3.14 Å) compared with IrO_2, which might indicate the structure changes. Figure 7.7 and Table 7.4 showed the fitting results of SA58, and the perfect fit was achieved after adding an extra orthorhombic phase. For the fitting of other samples, several plans were carried out and the results showed the typical tetragonal phase could not fit at all, while the combination of orthorhombic phase and monoclinic phase was proved to be the best fit (Figure 7.8- Figure 7.10, Table 7.5- Table 7.7). Moreover, the SA3.5 sample consisted of most monoclinic phase of approximately 34.8 % mass ratio (Table 7.7). The as-obtained different crystal structures were shown in Figure 7.5b-d. The appearance of orthorhombic and monoclinic phases in SA103, SA14.6 and SA3.5 samples lead to a totally different local atomic arrangement, which could further affect their electronic structures and electrochemical performances. The differences of local atomic arrangement were further confirmed by high-angle annular dark field (HAADF) STEM images, as shown in Figure 7.5e and f. The ordered atomic arrangement of SA58 sample indicates the main tetragonal phase of rutile structure, while the atomic arrangement of SA3.5 was short-range ordered and indicated the crystal structure of more than one phase.

7.3.2 Electronic Structure

The Ir oxidation state was investigated through the Ir L_3-edge X-ray absorption near-edge structure (XANES) spectra. As shown in Figure 7.11a, the white line position of SA58 shifted to the lower energy side compared with IrO_2, while for SA103, SA14.6 and SA3.5 samples, the white line positions were further shifted to lower energy side. Since the Ir L_3-edge XANES corresponds to the transition from occupied $2p$ to empty $5d$ states[12, 23], the white line position shifts indicated different d orbital states of different samples. The local ligand environment was further revealed by extending X-ray absorption fine structure (EXAFS) measurements and EXAFS simulations (Figure 7.11b, Figure 7.12). Compared with IrO_2 and SA58, SA103, SA14.6 and SA3.5 samples showed relative longer average Ir-O bond lengths (Figure 3a). Further EXAFS simulation parameters (Table 7.8) revealed appropriate fitting results of two Ir-O paths for SA103, SA14.6 and SA3.5 samples, in good agreement with PDF analyses (Figure 7.5a). The differences of Ir-O bonding and Ir-Ir bonding between different samples were further verified through EXAFS wavelet transforms (WT-EXAFS) analysis (Figure 7.11c, d, Figure 7.13). IrO_2 showed strong interaction of Ir-O bonding and Ir-Ir bonding, in good agreement with previous research[35, 36]. Moreover, SA58 showed a similar WT-EXAFS pattern with IrO_2, consistent with XRD, HAADF-STEM and PDF results. In contrast, SA103, SA14.6 and SA3.5 samples displayed the wider dispersion of Ir-O and the weakening of Ir-Ir of WT-EXAFS patterns, further confirming the different local atomic environments.

Hard X-ray photoelectron spectroscopy (HAXPES) measurements were conducted to provide detailed information of electronic structure. The rutile IrO_2 showed two sharp asymmetric peaks at 61.5 eV and 64.6 eV (Figure 7.14a), attributed to the deconvolution of Ir $4f_{7/2}$ and Ir $4f_{5/2}$, respectively[18, 37]. The peak positions for SA58 were similar to that of IrO_2, only the shape of peaks became broader. Furthermore, a significant shift to higher binding energy side and the broadening of peaks were observed for SA103, SA14.6 and SA3.5, while the Ir $4f_{7/2}$ and Ir $4f_{5/2}$ components located at 61.7 eV and 64.8 eV, respectively. This phenomenon is in line with recent research about short-rang ordered iridium oxides[18, 37, 38]. Pfeifer et al. demonstrated that the shift to higher energy sides of the amorphous IrOx was attributed to the Ir^{III} species due to coordination defects through their experiment and computational studies[18]. This was also verified in our fitting results of Ir 4f spectra (Figure 7.15) and PDF analyses (Figure 7.5a), since the SA103, SA14.6 and SA3.5 showed the phase of orthorhombic and monoclinic, and the local environments were less ordered than the rutile type IrO_2. The O 1s spectra and the fitting results are presented in Figure 7.14b and Figure 7.15b. Compared with the sharp peaks at around 530 eV for rutile IrO_2, the O 1s spectra for SA103, SA14.6 and SA3.5 were much broader and shifted to higher binding energy sides. The fitting results in Figure 7.15b revealed that SA103, SA14.6 and SA3.5 had higher contents of hydroxyl species, further verifying the appearance of Ir^{III} species in those samples as elucidated from Ir 4f spectra.

The electronic structures of all samples were further investigated through valence band spectra (VBS) and X-ray emission spectra (XES). As shown in Figure 7.14c, a shoulder peak near Fermi level was obvious observed in rutile IrO_2 (electron configuration $t_{2g}^5e_g^0$), which was attributed to the spin-orbital couple (SOC) effect in the IrO_6 coordination[39]. Moreover, this shoulder peak feature became vague for SA58 sample and even disappeared for SA103, SA14.6 and SA3.5 samples, indicating the total change of IrO_6 octahedral coordination environment as pointed out by PDF analyses (Figure 7.5a). The combination of the VBS with O K-edge XES results further shed light on the bonding environment. As shown in Figure 7.16, the four features in O K-edge XES were attributed to π-antibonding (feature I and II), π-bonding (feature III) and σ-bonding (feature IV) orbitals, well corresponding to the features in VBS[40]. The splitting of the π-antibonding states varied between rutile type IrO_2 and other samples, indicating the deviations from the perfect six coordinated octahedral symmetry. Since the photoionization cross section of Ir 5d electrons is much greater than that of the O 2p electrons at $h\nu = 7939$ eV, the HAXPES spectra are mostly dominated by Ir 5d states[40]. While feature III was much more intense than feature IV in the XES spectra, their intensities were similar in VBS, indicating the σ-bonding showed a relative greater 5d character than the π-bonding and the Ir-O hybridization was more effective in the σ-bonding states. Furthermore, the disappearance of feature I and the weakening of feature IV indicated the Ir 5d states changes and different degrees of Ir-O hybridization, corresponding well with the structural symmetry differences in different samples.

O K-edge XAS were measured to further elucidate the electronic information of iridium oxides. As shown in Figure 7.14d, rutile type IrO_2 showed the strong resonances at approximate 529.7 eV and 533 eV, indicating the ligand O^{II-}, in agreement with the previous research[18, 26]. Compared with perfect tetragonal symmetry IrO_2, SA58 sample showed a shift toward lower energy side at around 529.5 eV and the peak intensity decreased significantly, which could be attributed to the appearance of orthorhombic phase in the crystal structure. In contrast, the resonance peak for SA103, SA14.6 and SA3.5 further shifted to lower energy side, while a new resonance appeared at ca. 528.8 eV. In one previous study, Pfeifer et al. identified the new resonance peak for amorphous IrOx as O^{I-} species due to electronic defects through calculation[18]. In this study, the new resonance peak of SA3.5 sample showed the strongest peak intensity, which is in line with the fact that SA3.5 sample had the most monoclinic symmetry structure content. Interestingly, in a recent benchmarking work of Nong et al, the appearance of such new resonance peak (ca. 528.3 eV) was observed under operando O K-edge XAS measurements[25]. They found the peak intensity increased with the increasing applied OER potential and decreased with lower applied potential, claiming this phenomenon was related to the surface deprotonation and attributed to the OER activity. Therefore, the stable and intensive existence of O^{I-} species in the samples studied in this study might boost the OER activity significantly.

7.3.3 Electrochemical Performance

The electrochemical performance of SA58, SA103, SA14.6 and SA3.5 were investigated in a typical three-electrode system. The cyclic voltammetry results (Figure 7.17) showed obvious different redox behaviors between SA58 and other samples. When normalized using the BET surface area, SA3.5 samples showed the highest OER activity (Figure 7.18a). Meanwhile, the Tafel slope values of SA103, SA14.6 and SA3.5 were almost the same, slight smaller than that of SA58 samples (Figure 7.18b). The current density at 1.5 V vs. RHE was plotted against the phase ratio of monoclinic symmetry in each sample (Figure 7.18c). An obvious trend was observed that with the increasing of monoclinic phase ratio, the OER activity increased significantly, indicating the short-range ordered monoclinic symmetry boosted the catalytic dynamics toward OER.

7.3.4 Discussion of Reaction Mechanism

To further observe the electronic states changes during the OER process, *operando* Ir L_3-edge XANES were measured under different applied potential. As shown in Figure 7.19, with the increasing applied potential, SA58 sample showed little spectra changes, while the spectra of other samples shifted to higher energy side obviously. The spectra shift for SA3.5 sample was most significant especially at the potential OER occurred, indicating the oxidation state changes of Ir and active OER performance. However, it is worth noticing that the intensively increasing white line area of SA3.5 sample does not necessarily correspond to the constant oxidation of Ir, i.e., further oxidation to Ir^{V}. As pointed out by Pfeifer et. al., the further oxidation of Ir^{IV} to Ir^{V} is energetically less favorable for oxides than creating hole state (electrophilic character) in the O 2p states[27]. This was further verified by many other research groups[23, 25, 28].

Compared with the Ir 4f core line characters, the O K-edge is more sensitive to the electronic structural changes and might detect the intermediate O species in the OER process. Therefore, the *operando* O K-edge measurements were further conducted. As shown in Figure 7.20a, the CVs of SA58 and SA3.5 measured in *operando* cell corresponds well with the results obtained in the three electrode RDE cell (Figure 7.17), indicating the accuracy of the applied OER potential. Moreover, the relationship between the obtained current and as-applied potential was recorded in Figure 7.20b. The polarization curve was in line with the RDE results, making the *operando* measurements reliable to capture the intermediates during OER process. The OER potential was applied to the working electrode from 0.5 V vs. RHE (non-OER region, non-iR corrected) to 1.9 V vs RHE (active OER region, non-iR corrected). After the measurements at 1.9 V vs. RHE, the O K-edge spectra were recorded at the applied potential 0.5 V vs. RHE twice subsequently, to verify the time-dependent reversibility of intermediates. The O K-edge spectra of SA58 and SA3.5 were displayed in Figure 7.21. The spectra recorded at 0.5 V vs. RHE of both samples were in good agreement with the *ex situ* results (Figure 7.14d). With the increasing of the applied potential, a new resonance peak appeared at approximately 528.5 eV for SA58, while the peak intensity increased until 1.5 V vs. RHE and then stayed stable with the further applied high potential. This new feature for SA58 is similar to the new resonance peak identified in the *ex situ* O K-edge XAS of SA3.5, indicating that the electrophilic O^{I-} species appeared as the reaction intermediates for SA58. Meanwhile, the peak at ca. 529.5 eV (representing the lattice oxygen) showed negligible changes. For SA3.5 samples, the intensity of the resonance peak at ca. 528.5 eV increased significantly after 1.35 V vs. RHE and continued to increase with the increasing applied potentials, which is different from SA58 sample. Meanwhile, the peak position slightly shifted to lower energy side with increasing applied potentials. Furthermore, the peak at ca. 529.5 eV of SA3.5 also showed an increasing trend toward increasing applied potential, though not as significant as the previous peak at 528.5 eV, which is also different from that of SA38. When changing the potential from high active OER region 1.9 V vs. RHE to non-OER region 0.5 V, the related peak intensities of both samples faded away gradually, indicating the reversibility of those features.

According to the previous research, the OER process of iridium oxides could be described as follows[25, 27, 28, 41, 42]:

$$* + H_2O \rightarrow *OH + H^+ + e^- \tag{1}$$

$$*OH \rightarrow *O^{I-} + H^+ + e^- \tag{2}$$

$$*O^{I-} + H_2O \rightarrow *O^{I-}\,O^{I-}\,H + H^+ + e^- \tag{3}$$

$$*O^{I-}\,O^{I-}\,H \rightarrow * + O_2 + H^+ + e^- \tag{4}$$

where * denotes an active reaction site.

Nong et al. demonstrated that the O-O coupling requires higher activation energy than *OH deprotonation through DFT calculation, therefore, the water nucleophilic attack step (step 3) is supposed to be the rate-determining step[25]. This could also be verified through the findings of our *operando* O K-edge XAS. The detected O^{I-} originated from the deprotonation step and the signal increased with the increased applied OER potential, making the deprotonation step have little chance being the elementary step. Moreover, the nucleophilic attack of water is possible to occur due to the electrophilic nature of the increasingly populated O^{I-} species, as pointed out by Pfeifer et. al.[27]. Different from SA58, the peak at ca. 529.5 eV was observed to increase with the applied potential, which could be attributed to the detection of *OH species. The low symmetry structure of SA3.5 might benefit in a way that large amounts of electrophilic the increasingly populated O^{I-} species was continually formed through OER process and provide highly reactive sites for the water nucleophilic attack, leading to the superior OER activity.

Combing with the crystal structure characterization, electronic structures, and OER performance results, we can conclude that the highest content of monoclinic symmetry in the short-range ordered SA3.5 sample lead to the significantly and continuously formation of reaction active O^{I-} species, provided large number of reactive sites for the rate-determining water nucleophilic attack step, therefore boosted the OER dynamics.

7.4 Conclusion

In this research, several amorphous IrOx catalysts was thoroughly investigated and the relationship between their structures and OER activities was revealed. The amorphous structure of IrOx was characterized through PDF analyses. Different from the typical tetragonal symmetry of crystal IrO2, the combination of orthorhombic symmetry and monoclinic symmetry was found in the amorphous IrOx, and the ratio of monoclinic phase ratio corresponds well to the OER activity. The origin of high activity was further clarified that the low symmetry of monoclinic phase resulted in the structure defection and thus lead to more active sites through HAXPES analyses, ex situ and operando XAS. The thorough investigation in this study is promising to deepen the understanding of high active OER catalysts and provide new inspiration towards the design of novel OER catalysts.

Reference

1. Dincer, I.; Acar, C., Review and evaluation of hydrogen production methods for better sustainability. *Int. J. Hydrogen Energy* **2015,** *40* (34), 11094-11111.
2. Mazloomi, K.; Gomes, C., Hydrogen as an energy carrier: Prospects and challenges. *Renew. Sust. Energ. Revi.* **2012,** *16* (5), 3024-3033.
3. Turner, J.; Sverdrup, G.; Mann, M. K.; Maness, P.-C.; Kroposki, B.; Ghirardi, M.; Evans, R. J.; Blake, D., Renewable hydrogen production. *Int. J. Energy Res.* **2008,** *32* (5), 379-407.
4. Rosen, M. A.; Koohi-Fayegh, S., The prospects for hydrogen as an energy carrier: an overview of hydrogen energy and hydrogen energy systems. *Energy Ecol. Environ.* **2016,** *1* (1), 10-29.
5. Rashid, M. M.; Al Mesfer, M. K.; Naseem, H.; Danish, M., Hydrogen production by water electrolysis: a review of alkaline water electrolysis, PEM water electrolysis and high temperature water electrolysis. *Int. J. Eng. Adv. Technol* **2015,** *4* (3), 2249-8958.
6. Carmo, M.; Fritz, D. L.; Merge, J.; Stolten, D., A comprehensive review on PEM water electrolysis. *Int. J. Hydrogen Energy* **2013,** *38* (12), 4901-4934.
7. Millet, P.; Mbemba, N.; Grigoriev, S. A.; Fateev, V. N.; Aukauloo, A.; Etiévant, C., Electrochemical performances of PEM water electrolysis cells and perspectives. *Int. J. Hydrogen Energy* **2011,** *36* (6), 4134-4142.
8. An, L.; Wei, C.; Lu, M.; Liu, H.; Chen, Y.; Scherer, G. G.; Fisher, A. C.; Xi, P.; Xu, Z. J.; Yan, C.-H., Recent Development of Oxygen Evolution Electrocatalysts in Acidic Environment. *Adv. Mater.* **2021,** *33* (20), 2006328.
9. Zhao, F.; Wen, B.; Niu, W.; Chen, Z.; Yan, C.; Selloni, A.; Tully, C. G.; Yang, X.; Koel, B. E., Increasing Iridium Oxide Activity for the Oxygen Evolution

Reaction with Hafnium Modification. *J. Am. Chem. Soc.* **2021**, 143 (38), 15616-15623.

10. Zheng, Y.-R.; Vernieres, J.; Wang, Z.; Zhang, K.; Hochfilzer, D.; Krempl, K.; Liao, T.-W.; Presel, F.; Altantzis, T.; Fatermans, J.; Scott, S. B.; Secher, N. M.; Moon, C.; Liu, P.; Bals, S.; Van Aert, S.; Cao, A.; Anand, M.; Nørskov, J. K.; Kibsgaard, J.; Chorkendorff, I., Monitoring oxygen production on mass-selected iridium–tantalum oxide electrocatalysts. *Nat. Energy* **2021**.
11. Xu, J.; Li, J.; Lian, Z.; Araujo, A.; Li, Y.; Wei, B.; Yu, Z.; Bondarchuk, O.; Amorim, I.; Tileli, V.; Li, B.; Liu, L., Atomic-Step Enriched Ruthenium–Iridium Nanocrystals Anchored Homogeneously on MOF-Derived Support for Efficient and Stable Oxygen Evolution in Acidic and Neutral Media. *ACS Catal.* **2021**, 3402-3413.
12. Shi, Z.; Wang, Y.; Li, J.; Wang, X.; Wang, Y.; Li, Y.; Xu, W.; Jiang, Z.; Liu, C.; Xing, W.; Ge, J., Confined Ir single sites with triggered lattice oxygen redox: Toward boosted and sustained water oxidation catalysis. *Joule* **2021,** *5* (8), 2164-2176.
13. Zhao, G.; Li, P.; Cheng, N.; Dou, S. X.; Sun, W., An Ir/Ni(OH)$_2$ Heterostructured Electrocatalyst for the Oxygen Evolution Reaction: Breaking the Scaling Relation, Stabilizing Iridium(V), and Beyond. *Adv. Mater.* **2020,** *32* (24), 2000872.
14. Jang, H.; Lee, J., Iridium oxide fabrication and application: A review. *J. Energy Chem.* **2020,** *46*, 152-172.
15. Zhang, Y.; Zhu, X.; Zhang, G.; Shi, P.; Wang, A.-L., Rational catalyst design for oxygen evolution under acidic conditions: strategies toward enhanced electrocatalytic performance. *J. Mater. Chem. A* **2021**.9, 5890-5914.
16. Chen, Z.; Duan, X.; Wei, W.; Wang, S.; Ni, B.-J., Iridium-based nanomaterials for electrochemical water splitting. *Nano Energy* **2020,** *78*, 105270.
17. Pfeifer, V.; Jones, T. E.; Velasco Vélez, J. J.; Massué, C.; Arrigo, R.; Teschner, D.; Girgsdies, F.; Scherzer, M.; Greiner, M. T.; Allan, J.; Hashagen, M.;

Weinberg, G.; Piccinin, S.; Hävecker, M.; Knop-Gericke, A.; Schlögl, R., The electronic structure of iridium and its oxides. *Surf. Interface Anal.* **2016,** *48* (5), 261-273.

18. Pfeifer, V.; Jones, T. E.; Velasco Vélez, J. J.; Massué, C.; Greiner, M. T.; Arrigo, R.; Teschner, D.; Girgsdies, F.; Scherzer, M.; Allan, J.; Hashagen, M.; Weinberg, G.; Piccinin, S.; Hävecker, M.; Knop-Gericke, A.; Schlögl, R., The electronic structure of iridium oxide electrodes active in water splitting. *PCCP* **2016,** *18* (4), 2292-2296.
19. Czioska, S.; Boubnov, A.; Escalera-López, D.; Geppert, J.; Zagalskaya, A.; Röse, P.; Saraçi, E.; Alexandrov, V.; Krewer, U.; Cherevko, S.; Grunwaldt, J.-D., Increased Ir–Ir Interaction in Iridium Oxide during the Oxygen Evolution Reaction at High Potentials Probed by Operando Spectroscopy. *ACS Catal.* **2021,** *11* (15), 10043-10057.
20. Kwon, G.; Chang, S. H.; Heo, J. E.; Lee, K. J.; Kim, J.-K.; Cho, B.-G.; Koo, T. Y.; Kim, B. J.; Kim, C.; Lee, J. H.; Bak, S.-M.; Beyer, K. A.; Zhong, H.; Koch, R. J.; Hwang, S.; Utschig, L. M.; Huang, X.; Hu, G.; Brudvig, G. W.; Tiede, D. M.; Kim, J., Experimental Verification of Ir 5d Orbital States and Atomic Structures in Highly Active Amorphous Iridium Oxide Catalysts. *ACS Catal.* **2021,** *11* (15), 10084-10094.
21. Willinger, E.; Massué, C.; Schlögl, R.; Willinger, M. G., Identifying Key Structural Features of IrOx Water Splitting Catalysts. *J. Am. Chem. Soc.* **2017,** *139* (34), 12093-12101.
22. Sharma, R.; Karlsen, M. A.; Morgen, P.; Chamier, J.; Ravnsbæk, D. B.; Andersen, S. M., Crystalline Disorder, Surface Chemistry, and Their Effects on the Oxygen Evolution Reaction (OER) Activity of Mass-Produced Nanostructured Iridium Oxides. *ACS Appl. Energy Mater.* **2021,** *4* (3), 2552-2562.

23. Nong, H. N.; Reier, T.; Oh, H.-S.; Gliech, M.; Paciok, P.; Vu, T. H. T.; Teschner, D.; Heggen, M.; Petkov, V.; Schlögl, R.; Jones, T.; Strasser, P., A unique oxygen ligand environment facilitates water oxidation in hole-doped IrNiOx core–shell electrocatalysts. *Nat. Catal.* **2018,** *1* (11), 841-851.

24. Elmaalouf, M.; Odziomek, M.; Duran, S.; Gayrard, M.; Bahri, M.; Tard, C.; Zitolo, A.; Lassalle-Kaiser, B.; Piquemal, J.-Y.; Ersen, O.; Boissière, C.; Sanchez, C.; Giraud, M.; Faustini, M.; Peron, J., The origin of the high electrochemical activity of pseudo-amorphous iridium oxides. *Nat. Commun.* **2021,** *12* (1), 3935.

25. Nong, H. N.; Falling, L. J.; Bergmann, A.; Klingenhof, M.; Tran, H. P.; Spöri, C.; Mom, R.; Timoshenko, J.; Zichittella, G.; Knop-Gericke, A.; Piccinin, S.; Pérez-Ramírez, J.; Cuenya, B. R.; Schlögl, R.; Strasser, P.; Teschner, D.; Jones, T. E., Key role of chemistry versus bias in electrocatalytic oxygen evolution. *Nature* **2020,** *587* (7834), 408-413.

26. Pfeifer, V.; Jones, T. E.; Wrabetz, S.; Massué, C.; Velasco Vélez, J. J.; Arrigo, R.; Scherzer, M.; Piccinin, S.; Hävecker, M.; Knop-Gericke, A.; Schlögl, R., Reactive oxygen species in iridium-based OER catalysts. *Chem. Sci.* **2016,** *7* (11), 6791-6795.

27. Pfeifer, V.; Jones, T. E.; Velasco Vélez, J. J.; Arrigo, R.; Piccinin, S.; Hävecker, M.; Knop-Gericke, A.; Schlögl, R., In situ observation of reactive oxygen species forming on oxygen-evolving iridium surfaces. *Chem. Sci.* **2017,** *8* (3), 2143-2149.

28. Saveleva, V. A.; Wang, L.; Teschner, D.; Jones, T.; Gago, A. S.; Friedrich, K. A.; Zafeiratos, S.; Schlögl, R.; Savinova, E. R., Operando Evidence for a Universal Oxygen Evolution Mechanism on Thermal and Electrochemical Iridium Oxides. *J. Phys. Chem. Lett.* **2018,** *9* (11), 3154-3160.

29. Ravel, B.; Newville, M., ATHENA, ARTEMIS, HEPHAESTUS: data analysis for X-ray absorption spectroscopy using IFEFFIT. *J. Synchrotron Radiat.* **2005,** *12* (4), 537-541.

30. Farrow, C. L.; Juhas, P.; Liu, J. W.; Bryndin, D.; Božin, E. S.; Bloch, J.; Proffen, T.; Billinge, S. J. L., PDFfit2 and PDFgui: computer programs for studying nanostructure in crystals. *J. Phys.: Condens. Matter* **2007,** *19* (33), 335219.

31. Huang, J.; Blakemore, J. D.; Fazi, D.; Kokhan, O.; Schley, N. D.; Crabtree, R. H.; Brudvig, G. W.; Tiede, D. M., Domain structure for an amorphous iridium-oxide water-oxidation catalyst characterized by X-ray pair distribution function analysis. *PCCP* **2014,** *16* (5), 1814-1819.

32. Du, P.; Kokhan, O.; Chapman, K. W.; Chupas, P. J.; Tiede, D. M., Elucidating the Domain Structure of the Cobalt Oxide Water Splitting Catalyst by X-ray Pair Distribution Function Analysis. *J. Am. Chem. Soc.* **2012,** *134* (27), 11096-11099.

33. Grey, I. E.; Li, C.; Madsen, I. C., Phase Equilibria and Structural Studies on the Solid Solution MgTi2O5-Ti3O5. *J. Solid State Chem.* **1994,** *113* (1), 62-73.

34. Muller, E., RHEED-Untersuchungen einer Grenzschichtstruktur von SnO2 auf Quarz. *Acta Crystallogr. B* **1984,** *40* (4), 359-363.

35. Wen, Y.; Chen, P.; Wang, L.; Li, S.; Wang, Z.; Abed, J.; Mao, X.; Min, Y.; Dinh, C. T.; Luna, P. D.; Huang, R.; Zhang, L.; Wang, L.; Wang, L.; Nielsen, R. J.; Li, H.; Zhuang, T.; Ke, C.; Voznyy, O.; Hu, Y.; Li, Y.; Goddard Iii, W. A.; Zhang, B.; Peng, H.; Sargent, E. H., Stabilizing Highly Active Ru Sites by Suppressing Lattice Oxygen Participation in Acidic Water Oxidation. *J. Am. Chem. Soc.* **2021,** *143* (17), 6482-6490.

36. Liu, X.; Xi, S.; Kim, H.; Kumar, A.; Lee, J.; Wang, J.; Tran, N. Q.; Yang, T.; Shao, X.; Liang, M.; Kim, M. G.; Lee, H., Restructuring highly electron-deficient metal-metal oxides for boosting stability in acidic oxygen evolution reaction. *Nat. Commun.* **2021,** *12* (1), 5676.

37. Abbott, D. F.; Lebedev, D.; Waltar, K.; Povia, M.; Nachtegaal, M.; Fabbri, E.; Copéret, C.; Schmidt, T. J., Iridium Oxide for the Oxygen Evolution Reaction: Correlation between Particle Size, Morphology, and the Surface Hydroxo Layer from Operando XAS. *Chem. Mater.* **2016,** *28* (18), 6591-6604.
38. Siracusano, S.; Van Dijk, N.; Payne-Johnson, E.; Baglio, V.; Aricò, A. S., Nanosized IrOx and IrRuOx electrocatalysts for the O2 evolution reaction in PEM water electrolysers. *Appl. Catal. B* **2015,** *164*, 488-495.
39. Sun, W.; Liu, J.-Y.; Gong, X.-Q.; Zaman, W.-Q.; Cao, L.-M.; Yang, J., OER activity manipulated by IrO6 coordination geometry: an insight from pyrochlore iridates. *Sci. Rep.* **2016,** *6* (1), 38429.
40. Kahk, J. M.; Poll, C. G.; Oropeza, F. E.; Ablett, J. M.; Céolin, D.; Rueff, J. P.; Agrestini, S.; Utsumi, Y.; Tsuei, K. D.; Liao, Y. F.; Borgatti, F.; Panaccione, G.; Regoutz, A.; Egdell, R. G.; Morgan, B. J.; Scanlon, D. O.; Payne, D. J., Understanding the Electronic Structure of IrO_2 Using Hard-X-ray Photoelectron Spectroscopy and Density-Functional Theory. *Phys. Rev. Lett.* **2014,** *112* (11), 117601.
41. Lončar, A.; Escalera, D.; Cherevko, S.; Hodnik, N., Interrelations of Oxygen Evolution and Iridium Dissolution Mechanisms. *Angew. Chem. Int. Ed.* **2021**, e20214437.
42. Frevel, L. J.; Mom, R.; Velasco-Vélez, J.-J.; Plodinec, M.; Knop-Gericke, A.; Schlögl, R.; Jones, T. E., In Situ X-ray Spectroscopy of the Electrochemical Development of Iridium Nanoparticles in Confined Electrolyte. *J. Phys. Chem. C* **2019,** *123* (14), 9146-9152.

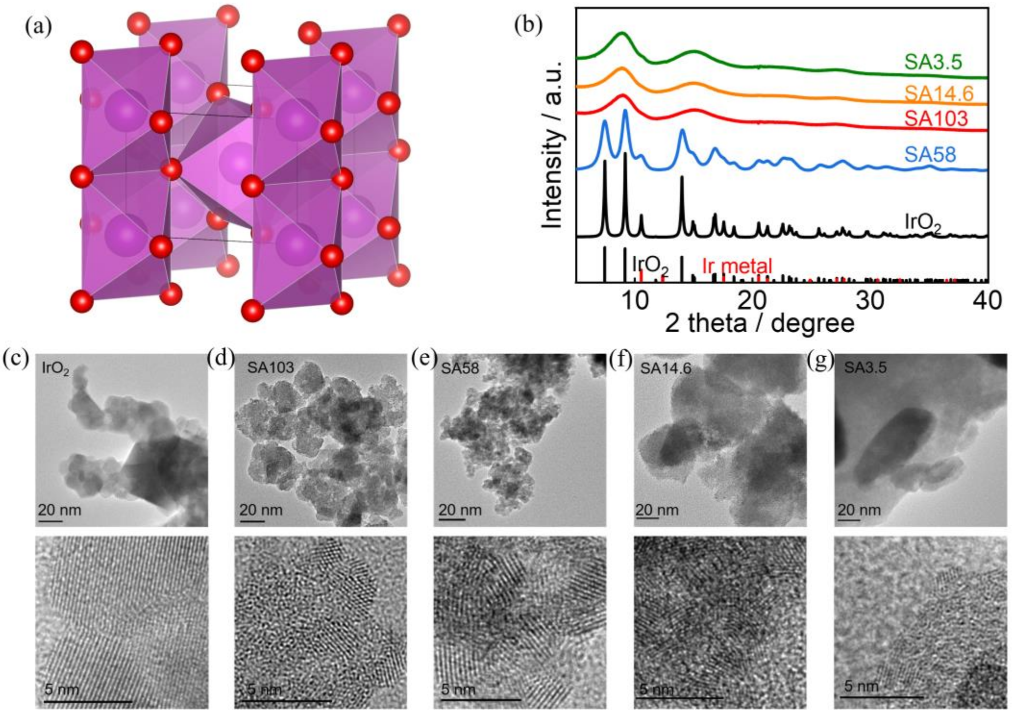

Figure 7.1. Crystal structure and morphology of as-studied catalysts. (a) the typical crystal structure of tetragonal iridium oxide of P42mnm space group, the red and purple spheres represent oxygen and iridium atoms, respectively; (b) XRD patterns, λ = 0.41401 Å; (c)-(g) TEM images of IrO2, SA103, SA58, SA14.6 and SA3.5 catalysts.

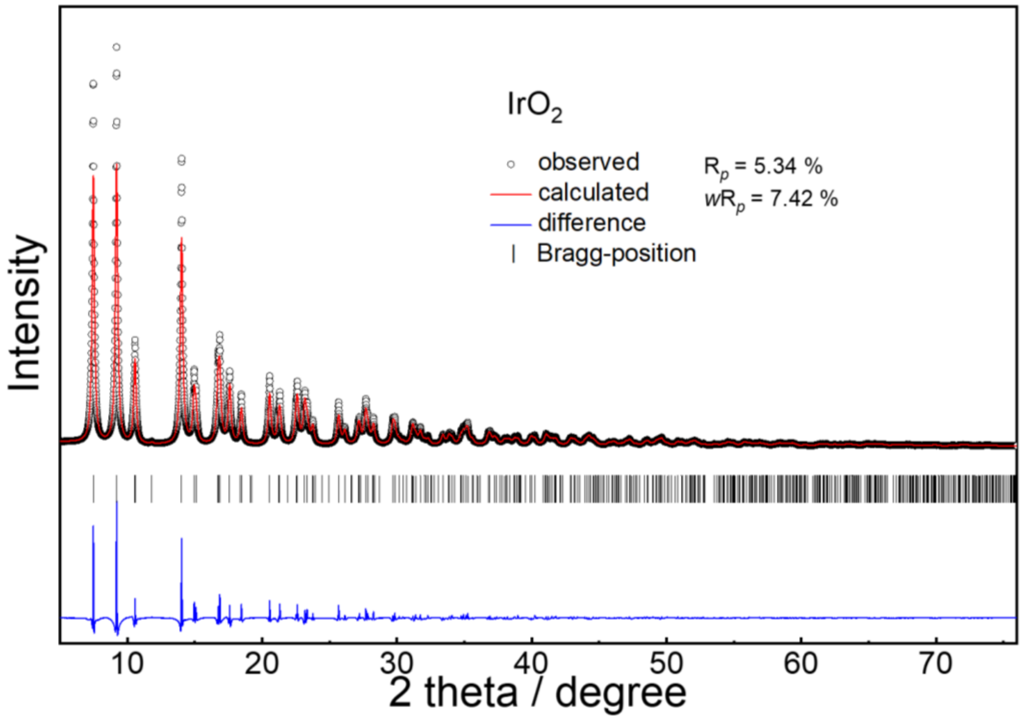

Figure 7.2. Rietveld refinement results of IrO_2

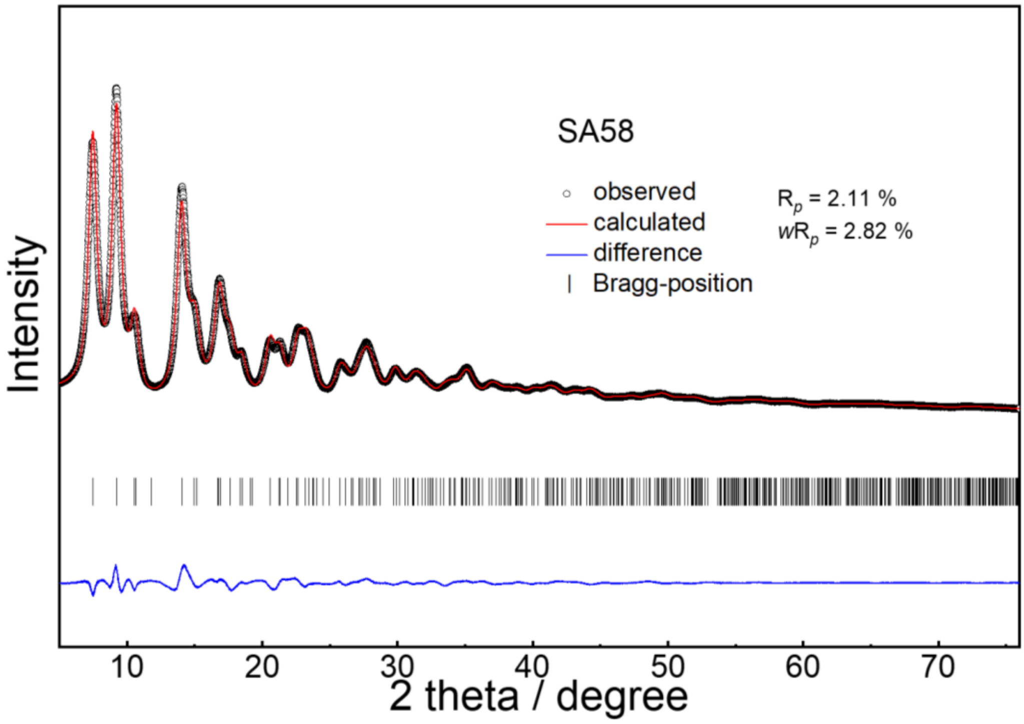

Figure 7.3. Rietveld refinement results of SA58

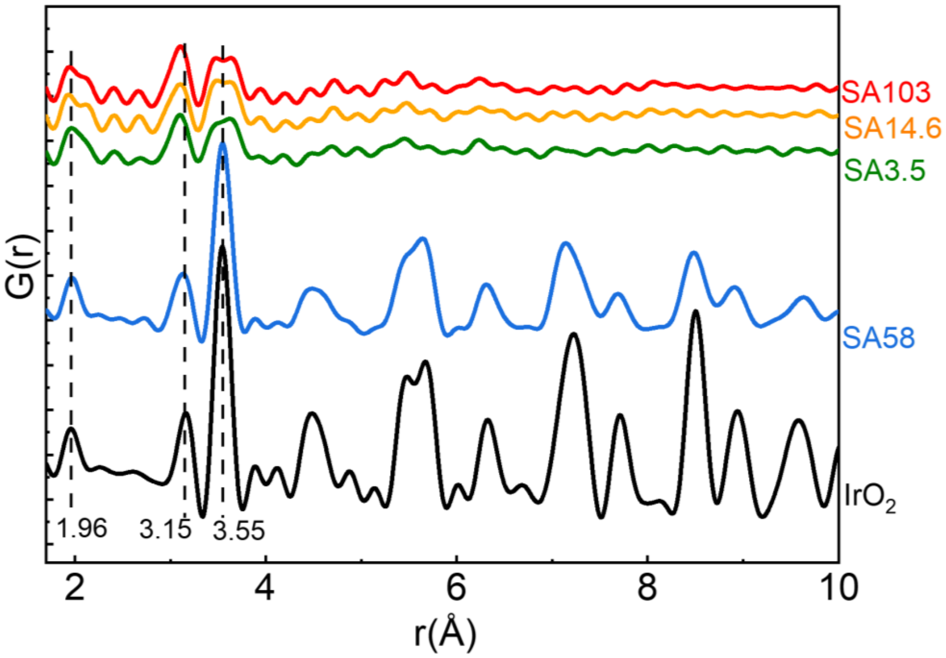

Figure 7.4. PDF G (r) of all samples up to 10 Å

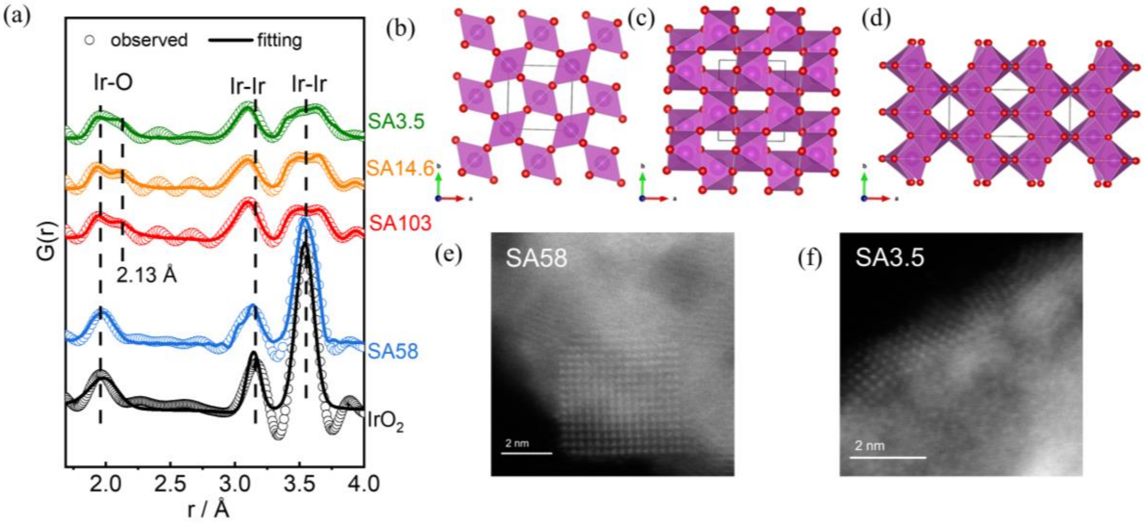

Figure 7.5. (a) PDF analyses of experimental and fitting results; (b)-(d) illustrations of crystal structures based on PDF fitting results, tetragonal, orthorhombic and monoclinic, respectively; STEM- HAAD images of (e) SA58 and (f) SA3.5 sample;

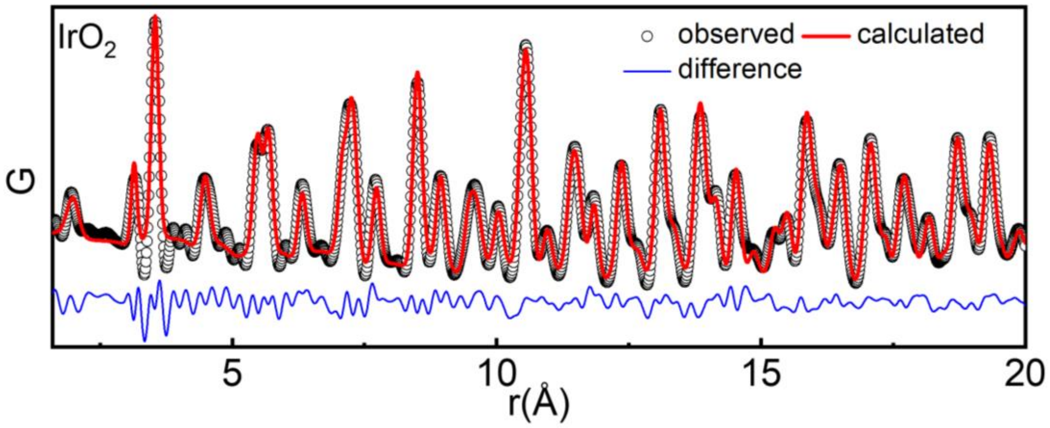

Figure 7.6. PDF fitting results for rutile type IrO$_2$.

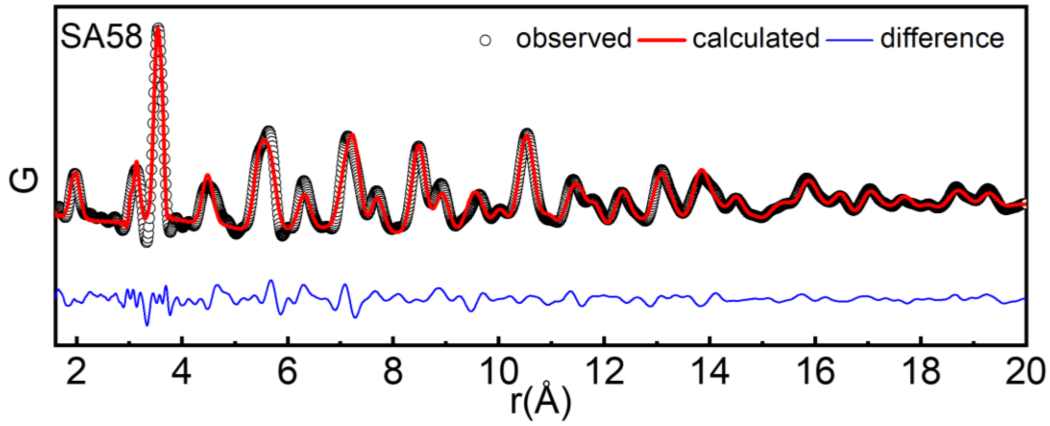

Figure 7.7. PDF fitting results for SA58.

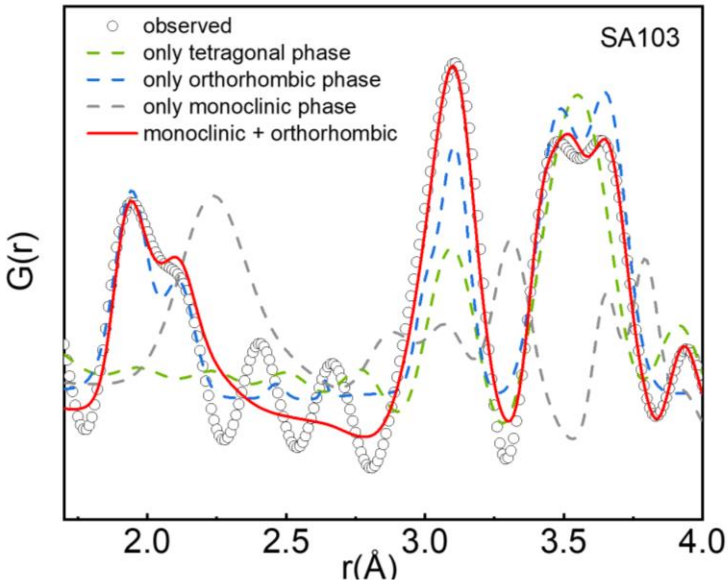

Figure 7.8. PDF fitting results for SA103.

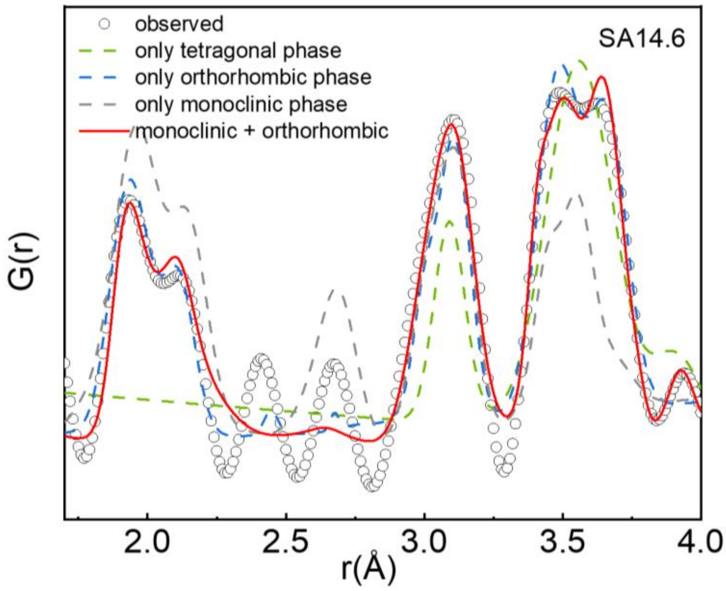

Figure 7.9. PDF fitting results for SA14.6.

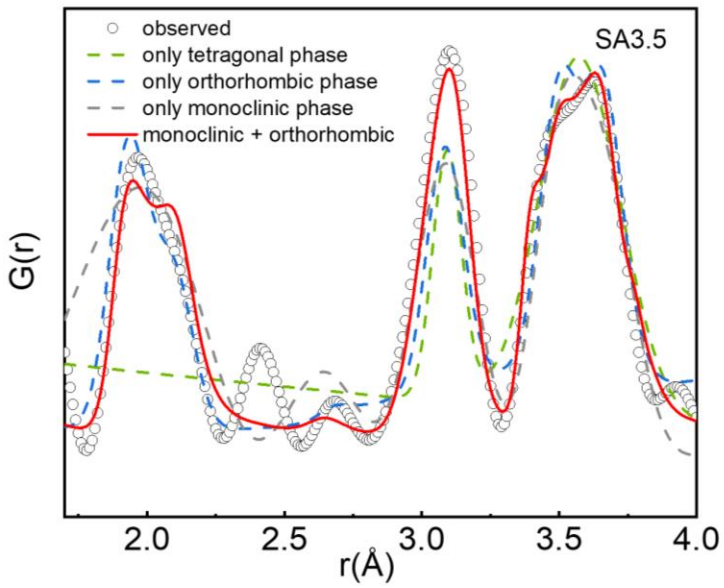

Figure 7.10. PDF fitting results for SA3.5.

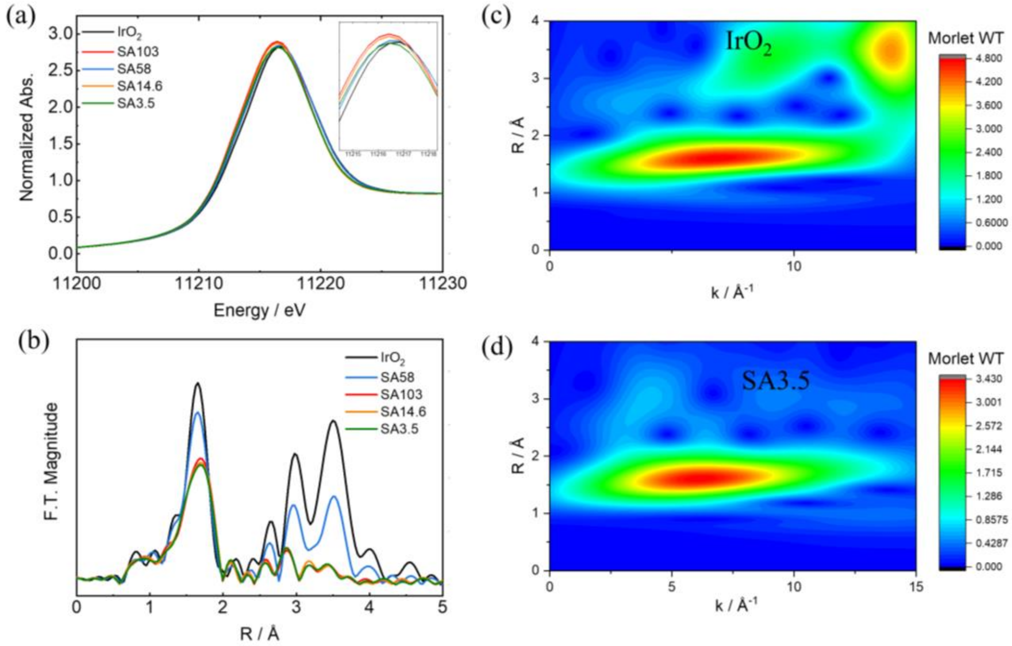

Figure 7.11. Electronic structures. (a) Ir L3-edge XANES (b) R-space and wavelet transforms for the k3-weighted Ir L_3-edge EXAFS signals of (c) IrO_2 and (d) SA3.5.

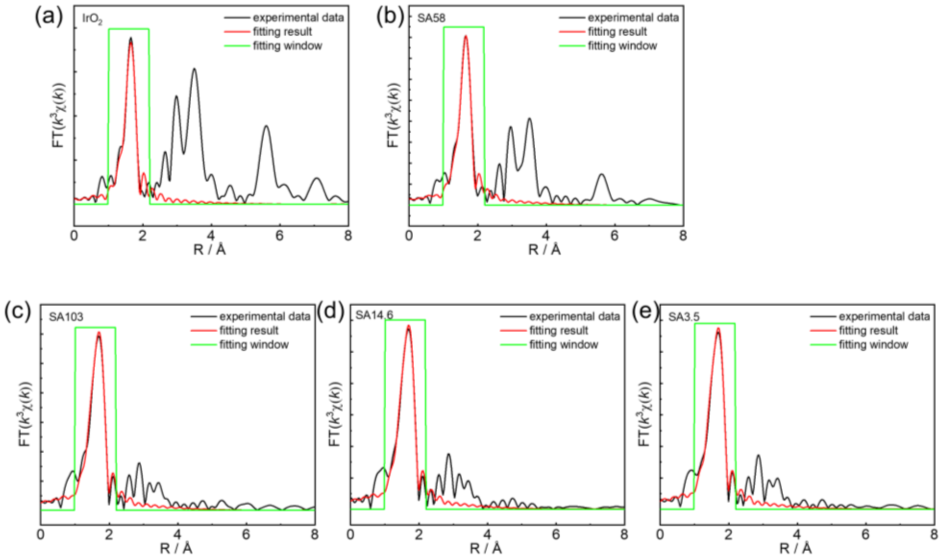

Figure 7.12. EXAFS fitting results of Ir-O path for all samples.

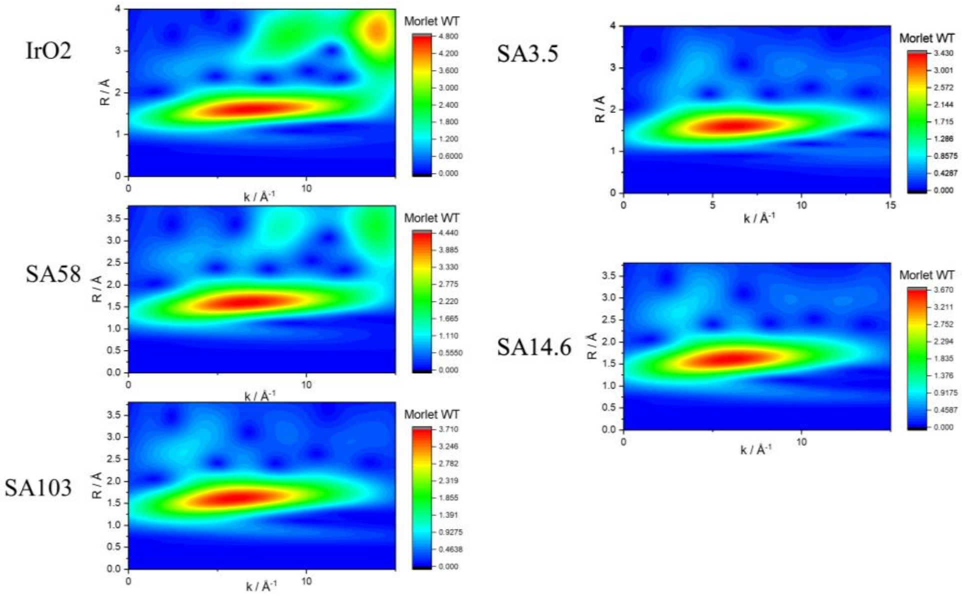

Figure 7.13. Wavelet transforms for the k3-weighted Ir L3-edge EXAFS signals

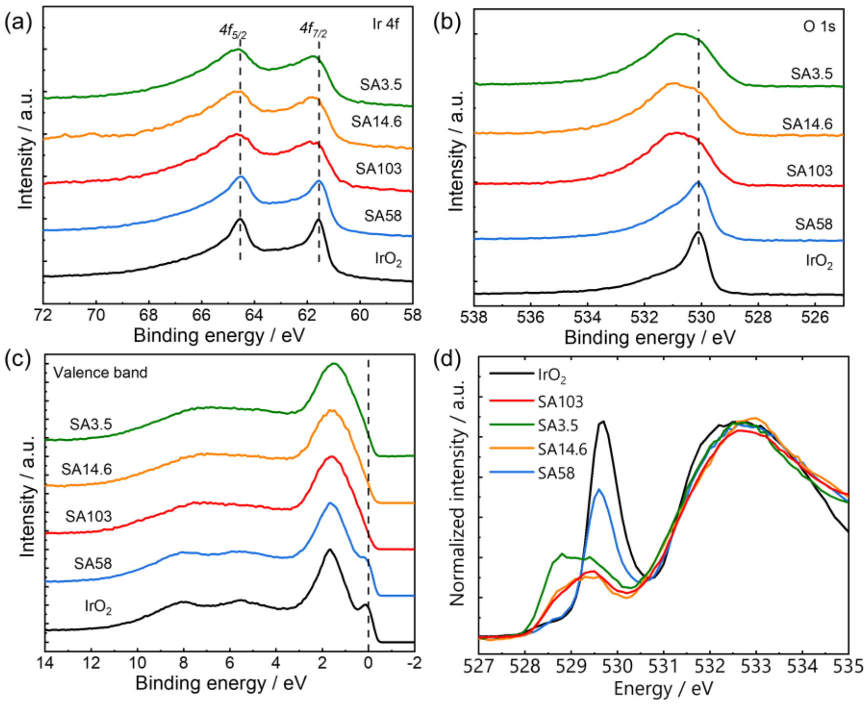

Figure 7.14. HAXPES results of (a) Ir 4f region; (b) O 1s region; (c) valence band spectra. (d) O K-edge XAS of all samples in PFY mode.

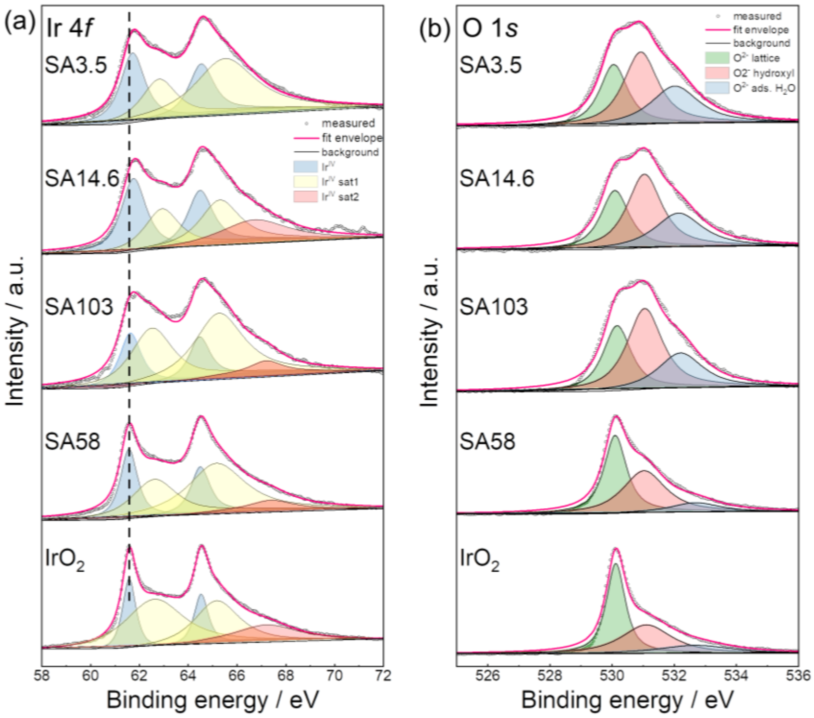

Figure 7.15. Fitting results of HAXPES. (a) Ir 4f region and (b) O 1s region.

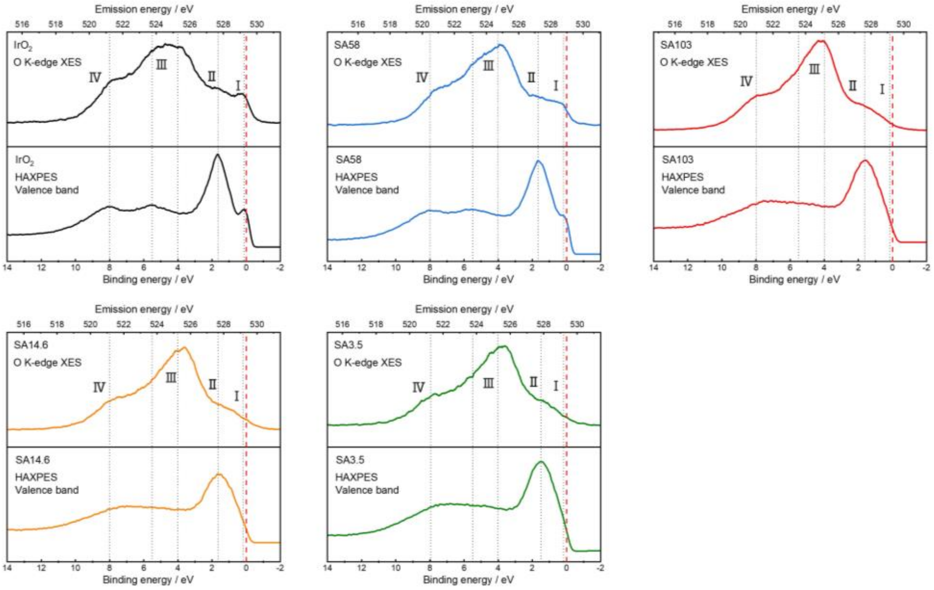

Figure 7.16. O K-edge XES results and HAXPES VBS of all samples.

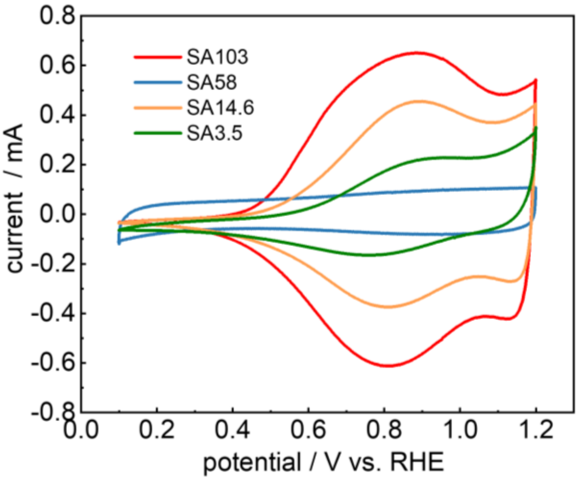

Figure 7.17. CV results at scan speed of 50 mV s^{-1} for all samples.

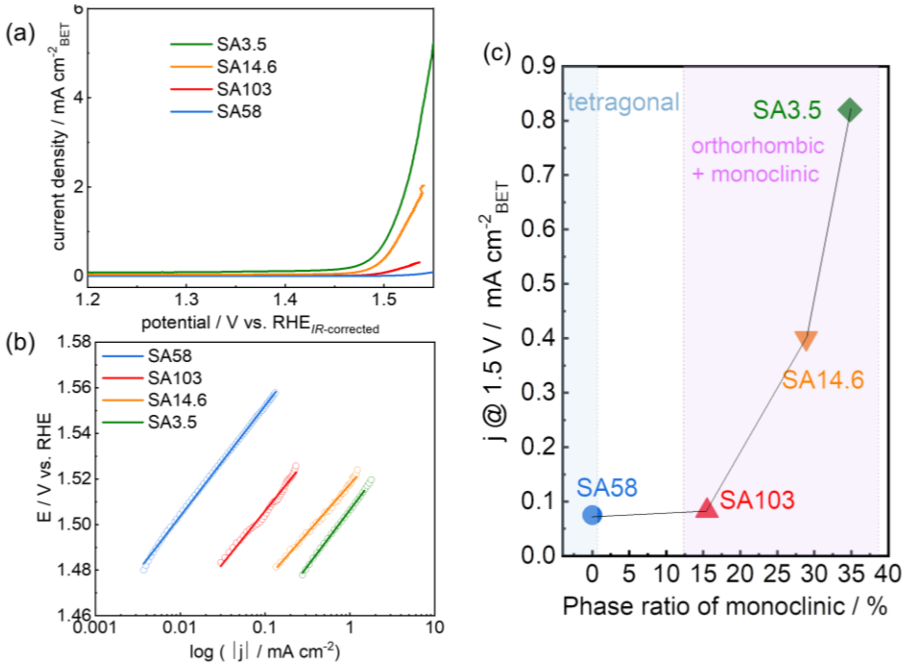

Figure 7.18. (a) OER activity normalized by BET surface area; (b) Tafel slopes; (c) the relationship between OER activity and monoclinic symmetry phase ratio.

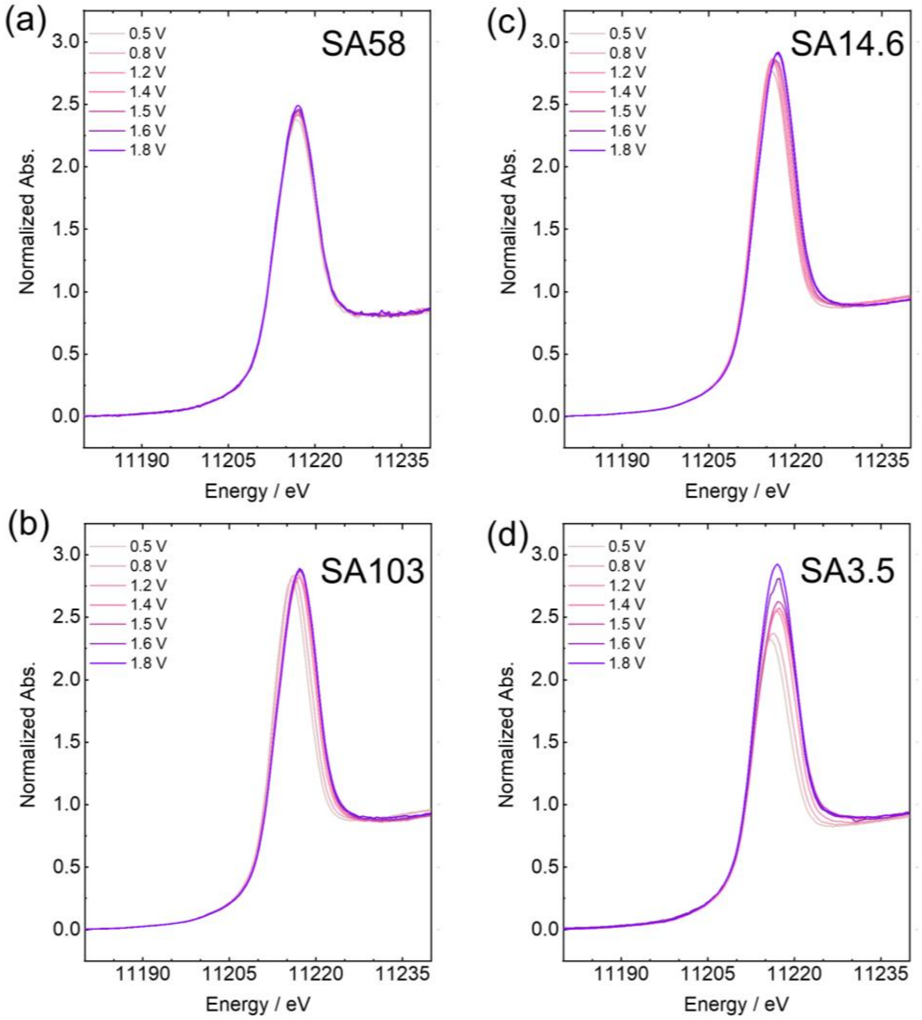

Figure 7.19. *Operando* Ir L_3-edge XANES under different applied potential of (a) SA58; (b) SA103; (c) SA14.6 and (d) SA3.5. All the potentials were versus RHE.

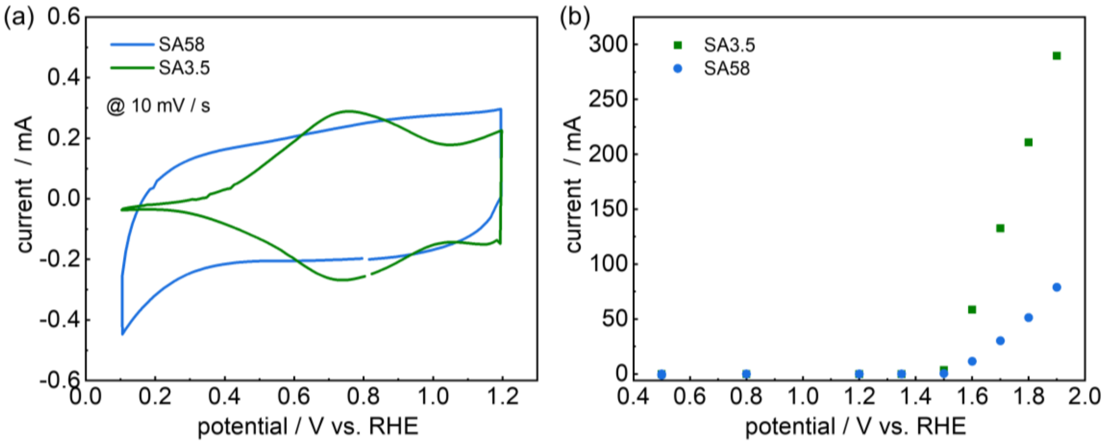

Figure 7.20. Electrochemical performance of SA58 and SA3.5 in the *operando* cell with the 0.1 M HClO4 as electrolyte. (a) CV obtained at the scan speed of 10 mV / s; (b) the relationship between OER current and the applied potential under steady-state *operando* O K-edge measurements.

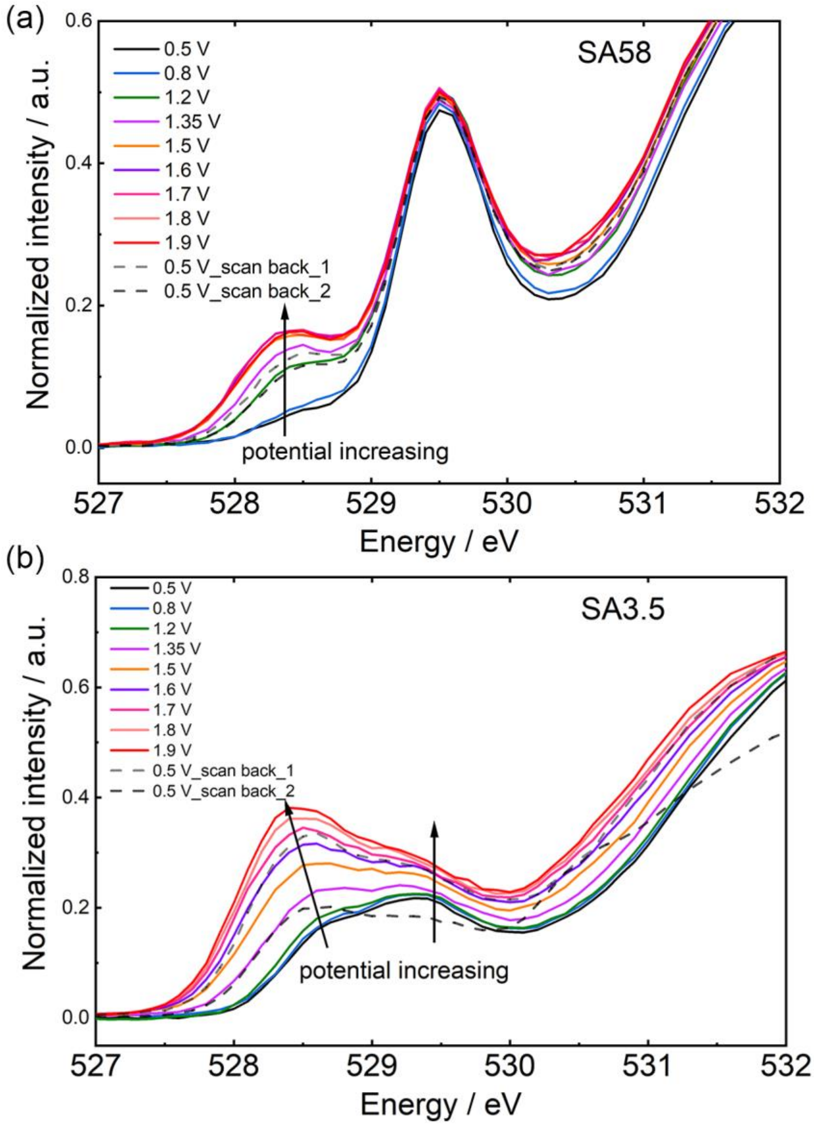

Figure 7.21. Steady-state *operando* O K-edge XAS of (a) SA58 and (b) SA3.5 at increasing potentials vs. RHE. Dashed lines show the reverse scan at 0.5 V vs. RHE in the order indicated.

Table 7.1. Crystal structural parameters obtained from Rietveld refinement for IrO_2.

Phase	Lattice parameter / Å	Space group	Atom	Site	Occupancy	*x*	*y*	*z*
Tetragonal	a = 4.500(1) c = 3.153(1)	$P4_2$mnm	Ir1	2a	1.000	0.000	0.000	0.000
			O1	4f	1.000	0.304	0.304	0.000

Table 7.2. Crystal structural parameters obtained from Rietveld refinement for SA58.

Phase	Lattice parameter / Å	Space group	Atom	Site	Occupancy	*x*	*y*	*z*
Tetragonal	a = 4.498(4) c = 3.141(3)	$P4_2$mnm	Ir1	2a	1.000	0.000	0.000	0.000
			O1	4f	1.000	0.258	0.258	0.000

Table 7.3. Crystal structural parameters obtained from PDF fitting results for IrO_2.

Phase	R_w	Lattice parameter / Å	Space group	Coherent domain size / Å	Scale factor
Tetragonal	0.16	a = 4.488(1) c = 3.144(1)	$P4_2$mnm	85.802(31)	1.000(3)

Table 7.4. Crystal structural parameters obtained from PDF fitting results for SA58.

Phase	Lattice parameter / Å	Space group	scale factor	Phase ratio in mass	R_w
Tetragonal	a = 4.485(1) c = 3.133(2)	$P4_2$mnm	0.833(5)	0.976(6)	0.20
Orthorhombic	a = 5.046(2) b = 5.274(1) c = 4.853(3)	*Pbcn*	0.020(5)	0.024(6)	

Table 7.5. Crystal structural parameters obtained from PDF fitting results for SA103.

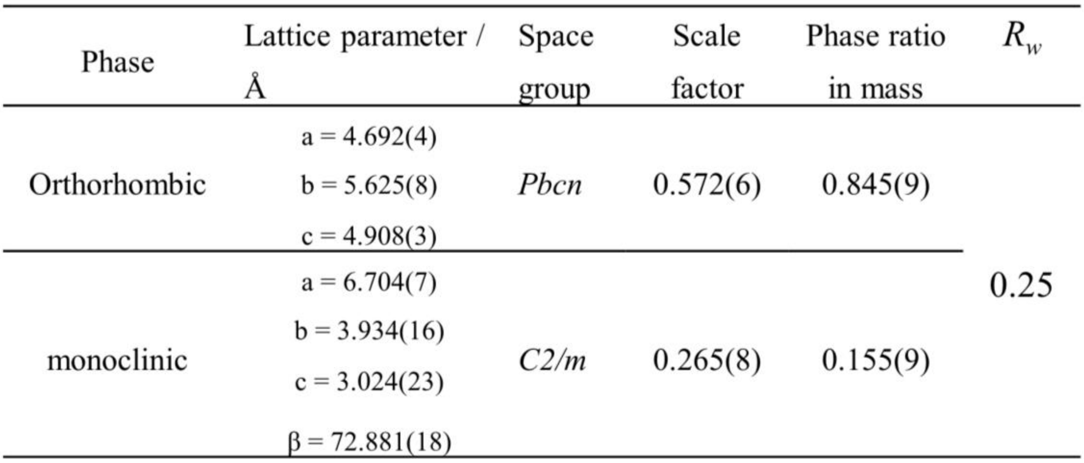

Phase	Lattice parameter / Å	Space group	Scale factor	Phase ratio in mass	R_w
Orthorhombic	a = 4.692(4) b = 5.625(8) c = 4.908(3)	*Pbcn*	0.572(6)	0.845(9)	0.25
monoclinic	a = 6.704(7) b = 3.934(16) c = 3.024(23) β = 72.881(18)	*C2/m*	0.265(8)	0.155(9)	

Table 7.6. Crystal structural parameters obtained from PDF fitting results for SA14.6.

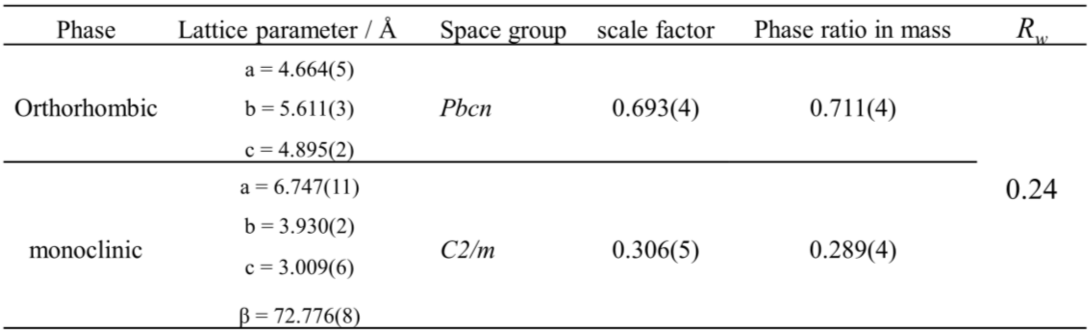

Phase	Lattice parameter / Å	Space group	scale factor	Phase ratio in mass	R_w
Orthorhombic	a = 4.664(5) b = 5.611(3) c = 4.895(2)	*Pbcn*	0.693(4)	0.711(4)	0.24
monoclinic	a = 6.747(11) b = 3.930(2) c = 3.009(6) β = 72.776(8)	*C2/m*	0.306(5)	0.289(4)	

Table 7.7. Crystal structural parameters obtained from PDF fitting results for SA3.5.

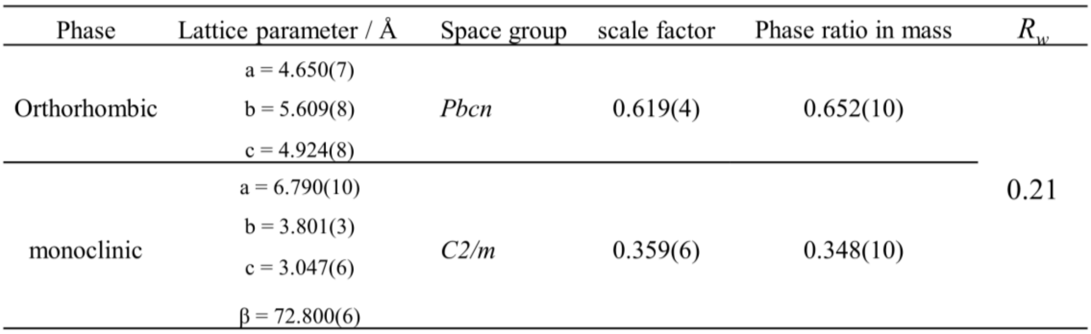

Phase	Lattice parameter / Å	Space group	scale factor	Phase ratio in mass	R_w
Orthorhombic	a = 4.650(7) b = 5.609(8) c = 4.924(8)	*Pbcn*	0.619(4)	0.652(10)	0.21
monoclinic	a = 6.790(10) b = 3.801(3) c = 3.047(6) β = 72.800(6)	*C2/m*	0.359(6)	0.348(10)	

Table 7.8. EXAFS fitting parameters of Ir-O bond

Entry	Path	N [a]	R [b] / Å	σ^2 [c] / Å^2	R_f [d] / %
IrO_2	Ir-O	6.00*	1.978	0.0027	1.9
SA58	Ir-O	6.00*	1.986	0.0037	1.3
SA103	Ir-O_1	2.20	1.936	0.0016	1.0
	Ir-O_2	3.80	2.045		
SA14.6	Ir-O_1	2.18	1.933	0.0018	0.70
	Ir-O_2	3.82	2.044		
SA35	Ir-O_1	2.14	1.927	0.0019	0.60
	Ir-O_2	3.86	2.039		

* Fixed Value
- Coordination Number
- Bond distance
- Debye-Waller factor
- Residual factor

$$R_f = \frac{\int \left| k^3 \chi^{obs}(k) - k^3 \chi^{calc}(k) \right|^2 dk}{\int \left| k^3 \chi^{obs}(k) \right|^2 dk} \times 100$$

Chapter 8. General Conclusions

The development of renewable energy storage technology is envisioned to replace the conventional fossil fuels to impede global warming and to meet the growing demand for energy sources. Among many proposed solutions, renewable source-derived water electrolysis is considered a promising mass production tool for generating O_2 and H_2 for the storage of chemicals as fuels. However, the complex four-electron transfer of the oxygen evolution reaction (OER) leads to a high overpotential and undisclosed reaction mechanism, further impeding the development of high performance OER catalysts. Therefore, it is of significance to investigate the reaction mechanism of OER, thus providing design principles for OER catalysts. In this study, a combination of electrochemical measurements and advanced X-ray based characterization were conducted to elucidate the reaction mechanism of the OER for water electrolysis.

In Chapter 1, the principles of water electrolysis, previously proposed OER reaction mechanisms, the present developments related to OER catalysts and the PEM water electrolyzer were reviewed.

In Chapter 2, the electronic structural changes of nickel at the electrode/electrolyte interface during OER were investigated using thin-film Li-doped NiO catalysts. *Operando* TRF-XAS revealed a distinct surface oxidation state change for $Li_{0.59}Ni_{0.41}O$, indicating the formation of high oxidation state Ni sites. The corresponding surface reconstruction resulted in an increased number of active sites on the reaction interface, thereby enhancing the OER activity. The founding in this chapter deepened the understanding about catalytic surface reconstruction behaviours.

In Chapter 3, the electrochemical performance and reaction kinetics of perovskite-type $La_{1-x}Sr_xCoO_{3-\delta}$ thin films as OER catalysts were investigated. The thin films were synthesized by the pulsed laser deposition method. Through the innovative combination of *ex situ* XAS and *operando* TRF-XAS, a significant oxidation state change on the surface of $La_{0.6}Sr_{0.4}CoO_{3-\delta}$ was observed. The formation of active surface sites resulting from surface reconstruction at the reaction interface enhanced the OER activity.

In chapter 4, the effect of cation mixing in $LiNiO_2$ on OER performance were discussed. The *ex situ* XAS revealed a strong hybridization state of Ni 3*d* and O 2*p* orbitals, which was believed to be the origin of the observed differences in catalytic activity behaviors. Moreover, it was found that the instability of $LiNiO_2$ originated from de-intercalation of Li ions and the irreversible structure change decreased performance. The intercalation/deintercalation of ions also occurred during the OER process, similar to lithium ion batteries. It was demonstrated that hindering the lithium diffusion path by cation mixing is useful for maintaining performance

In chapter 5, the activity of low-spin tetravalent Ni ion sites in OER was quantitively evaluated. The Ni valence was changed from divalent to tetravalent through the chemical delithiation of $Li_{0.96}Ni_{0.49}Mn_{1.51}O_4$, and the OER activity was found to increase with decreasing Li content. The high OER activity was attributed to the strong hybridization of the Ni 3*d*–O 2*p* orbital resulting from the downshift of the Ni conduction band, as confirmed through comprehensive XAS analyses. This chapter revealed the mechanism underpinning the high OER activity of high valence Ni(4+) and also provided a approach for the development of highly active catalyst materials, namely, topochemical delithiation.

In Chapter 6, the two-active-site OER mechanisms for quadruple perovskite oxides were discussed. The OER catalytic performance of $CaMn_7O_{12}$ quadruple perovskite oxides with different Mn(A')–Mn(B) distances were carefully examined. Mn(A')–Mn(B) distances were precisely controlled through doping with Sr, Cu, and Al. The crystal structure and state of cations and O was investigated using XRD with Rietveld refinement and XAS. The OER catalytic activity was clearly correlated to the Mn(A')–Mn(B) distance, while the e_g states of both the Mn and O 2p band centers remained unchanged. A shrinkage of the A'–B distance affected the stability of the O–O bond on the A'–B site and accelerated the OER kinetics.

In Chapter 7, the origin of the high OER activity of amorphous iridium oxide was thoroughly investigated. A PDF analysis revealed that the short-range-ordered iridium oxides have two different structure phases. Further *ex situ* and *operando* XAS measurements demonstrated that the mixed phases contributed to an increase in active sites, thus enhancing the OER activity.

In chapter 8, the results of the thesis were summarized.

Acknowledgement

First and foremost, I would like to thank my supervisor, Prof. Yoshiharu Uchimoto for providing me the research opportunities and walking me through difficulties over the past 3 years with his extensive research experience. The work presented in this thesis would not have been possible without his kind support and encouragement.

I would like to thank Dr. Tomoki Uchiyama for his guidance of various X-ray based measurements and useful suggestions during our countless discussions. Prof. Toshiyuki Matsunaga are due special gratitude for his help in guiding the crystal structural analyses. I would like to thank Prof. Kentaro Yamamoto, Dr. Toshiki Watanabe and Prof. Tsuyoshi Takami for their kind help over the past 3 years.

Similarly, I would like to thank all the members of Prof. Uchimoto's laboratory. The helps, discussions, and encouragement from them generated inspirations and supported me throughout this study.

Finally, a special thank you is addressed towards my family who have been my side all the time. Although the worldwide pandemic prevents us from seeing each other, their unconditional love and support always warm my heart and keep me going on.

※著作権等

1. The effect of cation mixing in LiNiO2 toward oxygen evolution reaction

Yadan Ren, Yamaguchi Ryusei, Tomoki Uchiyama, Yuki Orikasa, Toshiki Watanabe, Kentaro Yamamoto, Toshiyuki Matsunaga, Yoshinori Nishiki, Shigenori Mitsushima, Yoshiharu Uchimoto ("ChemElectroChem" July 2020, Volume 8, p70 – 76).

doi: 10.1002/celc.202001207

The final publication is available at Wiley Publishing via

http://dx.doi.org/10.1002/celc.202001207

2. Quantitative Evaluation of the Activity of Low Spin Tetravalent Nickel Ion Site for Oxygen Evolution Reaction: Yadan Ren, Tomoya Horiguchi, Tomoki Uchiyama, Yuki Orikasa, Toshiki Watanabe, Kentaro Yamamoto, Tsuyoshi Takami, Toshiyuki Matsunaga, Yoshinori Nishiki, Shigenori Mitsushima, Yoshiharu Uchimoto

("ACS Appl. Energy Mater." September 2021, Volume4, p10731-10738).

doi:10.1021/acsaem.1c01719

The final publication is available at ACS Publishing via

http://dx.doi.org/10.1021/acsaem.1c01719

3. Quadruple perovskite oxides CaMn7O12 proceed by two-active-site reaction mechanism for oxygen evolution reaction: Yadan Ren, Kodai Kashihara, Tomoki Uchiyama, Yuki Orikasa, Toshiki Watanabe, Kentaro Yamamoto, Tsuyoshi Takami, Toshiyuki Matsunaga, Yoshinori Nishiki, Shigenori Mitsushima, Yoshiharu Uchimoto

("ChemElectroChem." October 2021, Volume 8, p4605 – 4611).

doi: 10.1002/celc.202101228

The final publication is available at Wiley Publishing via

https://doi.org/10.1002/celc.202101228